Imperial College London

MICRO-CHANNEL ENHANCED ALUMINA MEMBRANES – DESIGNING AND TAILORING THEIR PROPERTIES FOR WIDENED APPLICATIONS

By

Melanie Wei Ting Lee

A Thesis Submitted for the Degree of Doctor of Philosophy and the Diploma of Imperial College London

April 2016

Faculty of Engineering

Department of Chemical Engineering

Declaration of Originality

I hereby declare that this thesis and the work reported herein was composed by and originated entirely from me. Information derived from the published and unpublished work of others has been acknowledged in the text and the relevant references are included in this thesis.

Melanie Wei Ting Lee

Imperial College London, April 2016

Copyright Declaration

The copyright of this thesis rests with the author and is made available under a Creative Commons Attribution Non-Commercial No Derivatives license. Researchers are free to copy, distribute or transmit the thesis on the condition that they attribute it, that they do not use it for commercial purposes and that they do not later, transform or build upon it. For any reuse or redistribution, researchers must make clear to others the license terms of this work.

Melanie Wei Ting Lee

Imperial College London, April 2016

Abstract

Ceramic membranes have the potential to replace polymeric membranes in existing membrane processes as well as expanding their applications to unexplored territories. However, they only hold a small market share out of all the other membrane materials, and the main deterrents are high capital costs, lower performance, and brittleness. Hereby, in this thesis, significant progress has been made addressing the above-mentioned bottlenecks. By using the micro-channel inducing combined phase inversion and sintering method, ceramic asymmetric membranes with greatly enhanced performance and widened applications were fabricated.

Firstly, improved understanding of the formation mechanisms of these micro-channels was achieved by fabricating alumina disc membranes. Parameters such as: suspension composition, membrane width, and coagulation temperature were manipulated and a wide range of different micro-channels were formed. The microfiltration membranes with the long and cylindrical micro-channels exhibited the highest water permeation flux and can be potentially used in water treatments. Furthermore, the micro-channel properties were mimicked using the Rayleigh-Taylor Instability.

Next, six hollow fibre cross-section morphologies were designed and delivered via the use of different bore fluids, air gap, and polymer sacrificial layers in order to control the surface at which the micro-channels are open at. Apart from improving permeation flux, the opening of the micro-channels allows access to these pockets of space, which can be used to store and pack functional materials to form highly compact systems. The presence of micro-channels compensates the membranes' mechanical stability, and therefore, a method for improving mechanical stability was put forward: to form multi-channel hollow fibres, tubes or monoliths with a plurality of micro-channels and increased cross-section area. The resultant membranes exhibited improved bending strengths. Finally, a potential new application of the hollow fibre with open micro-channels was studied. Adsorbents were packed into the micro-channels, to form a hollow fibre GC column perform oxygen and nitrogen separation, and an 8 m long column managed to separate the two components.

Acknowledgements

There are many people who I would like to thank for getting me through this journey. First of all, I would like to thank Professor Kang Li, my supervisor, who gave me not only research-related suggestions, but also support and an often-needed pushing hand. Discussing issues with him always led to fruitful consequences and he has given me encouragements on countless occasions. I would not have been able to enjoy my studies without his wisdom, support, and patience.

In terms of my direct research I am extremely grateful to my postdoctoral fellows, Dr. Bo Wang and Dr. Zhentao Wu. Dr. Wang was always generous in sharing his knowledge and expertise, and was there whenever I needed advice and help during the fabrication, characterisation, and publication processes. He was a great teacher and it was both fun and exciting working with him. Dr. Wu was always there to give advice from a different point of view, and showed me a lighter side to research.

Throughout the three years in the college, there is also a long list of people who assisted and influenced my research. I am grateful to all my colleagues from the same research group, who often gave me great advice and assisted me in various experiments, and my office mates in room 116, who often dampened my worries and stress during our meals and outings.

Finally, I am forever grateful to my family and close friends, who were there to support and accept me as who I am, and whatever decision I make. My parents showed me unconditional love and encouragements, and continuously made sacrifices to ensure that I can carry out my studies in the utmost comfort. I would also like to thank my brother, who reminded me to be thankful to all the people and opportunities around me, and my close friends, who alleviated my stress by reminding me that there is a world outside of my Ph.D. studies. Finally, I would like to thank Chris, who did not only give great advice and support, but was also a great sponge when I faced tough and challenging situations, and lightened my research days with positivity and energy.

Table of Contents

Declaration of Originality i

Copyright Declaration ii

Abstract iii

Acknowledgements iv

Table of Contents v

List of Figures xi

List of Tables xviii

Nomenclature xxi

Chapter 1: Introduction 1

1.1 Background 1

1.2 PhD Objectives 2

1.2.1 Fundamental Study on the formation of micro-channels in disc membranes – Spatial structure, simulation, and potential use in water treatment 3

1.2.2 High flux micro-channelled ceramic disc membranes for water treatments and spinning of microfibres 4

1.2.3 Micro-structured alumina hollow fibre membranes – Potential applications in wastewater treatment 4

1.2.4 New open micro-channelled alumina hollow fibre membrane structures toward broadened applications 5

1.2.5 Micro-structured alumina multi-channel capillary tubes and monoliths 5

1.2.6 A high-capacity open bore GC column based on alumina hollow fibres with open micro-channels 5

1.3 Thesis structure and presentation 6

Chapter 2: Literature Review 7

2.1 Membrane Principles and processes 7

2.2 Development in ceramic membranes and their fabrication processes 8

2.2.1 Brief history of ceramic membrane developments over the past 50 years 8
2.2.2 Desirable membrane characteristics and their design 12
2.2.3 Material and microstructure 12
2.2.4 Membrane configurations 18
2.2.5 Development in membrane modules and units 22
2.2.6 Fabrication techniques 27
2.2.7 Ceramic membrane materials 49
2.3 Ceramic membranes for Microfiltration and Ultrafiltration applications 51
2.3.1 Drinking water production 51
2.3.2 Municipal wastewater/sewage treatment 53
2.3.3 Industrial wastewater treatment 54
2.3.4 Produced water 55
2.3.5 Food and beverage industries 55
2.3.6 Commercial ceramic applications 56
2.3.7 Emerging research areas related to porous ceramic membranes 59
2.4 Prospects and challenges 61
References 62

Chapter 3: Experimental 93

3.1 Materials 93
3.2 Preparation of ceramic suspensions 93
3.3 Preparation of alumina discs 94
3.4 Preparation of alumina hollow fibres 94
3.5 Heat treatment 95
3.6 Characterisation 96
3.6.1 Viscosity 96
3.6.2 Microscopy 96
3.6.3 Porosimetry 96
3.6.4 Micro-channel characterisation 97
3.6.5 Mechanical strength 97
3.6.6 Pure water permeation 98
References 100

Chapter 4: Fundamental Study of micro-channels in ceramic membranes – spatial structure and simulation 101

Abstract 101
4.1 Introduction 102
4.2 Experimental 105
4.2.1 Materials and membrane preparation 105
4.2.2 Characterisation 105
4.3 Results 106
4.3.1 Rheology of ceramic suspensions 106
4.3.2 Characteristics of micro-channels 107
4.3.3 Water permeation and pore structure 115
4.4 Discussions 119
4.4.1 The hierarchical micro-channel structure and linear stability theory 119
4.4.2 The Rayleigh-Taylor Instability hypothesis 121
4.4.3 Mimicking the experimental results with the RTI theory 128
4.4.4 The shape of micro-channels 133
4.5 Conclusions 136
References 138

Chapter 5: High flux micro-channelled ceramic disc membranes for water treatments and spinning of microfibres 145

Abstract 145
5.1 Introduction 145
5.2 Experimental 146
5.2.1 Materials and Preparation of ceramic suspensions 146
5.2.2 The preparation of alumina discs 147
5.2.3 Spinning of YSZ microfibres 148
5.2.4 Characterisation 148
5.3 Results 149
5.3.1 Morphological characteristics 149
5.3.2 Water permeation and pore size 157
5.3.3 Mechanical stability 159
5.4 Discussion 160

5.4.1 Influencing factors 160
5.4.2 Simulation 161
5.4.3 Potential new application of micro-channel enhanced ceramic disc membranes - continuous and facile spinning of microfibres 165
5.5 Conclusions 166
References 168

Chapter 6: Micro-structured alumina hollow fibre membranes 170

Abstract 170
6.1 Introduction 171
6.2 Experimental 172
6.2.1 Materials and alumina suspension preparation 172
6.2.2 Preparation of alumina hollow fibres 172
6.2.3 Characterisation 173
6.3 Results and Discussion 174
6.3.1 Morphology and microstructure of Membrane 1 174
6.3.2 Morphology and microstructure of Membrane 2 177
6.3.3 Morphology and microstructure of Membrane 3 180
6.3.4 Mechanical Strength and Water Permeation Flux 183
6.4 Conclusions 187
References 188

Chapter 7: New open micro-channelled alumina hollow fibre membrane structures toward broadened applications 190

Abstract 190
7.1 Introduction 191
7.2 Experimental 192
7.2.1 Materials and preparation of alumina suspensions 192
7.2.2 Preparation of alumina hollow fibres 193
7.2.3 Preliminary application experiments 195
7.2.4 Characterisation 196
7.3 Results 197
7.3.1 Cross-sectional morphology of the micro-structured hollow fibre membranes 197
7.3.2 Pore size, pore size distribution and micro-channel size 203

7.3.3 Water permeation 205
7.3.4 Mechanical property 206
7.4 Discussions **207**
7.4.1 Propagation of micro-channels at the two-layer interface 207
7.4.2 Potential applications of the three unique structured hollow fibres 209
7.5 Conclusions **213**
References **214**

Chapter 8: Micro-structured alumina multi-channel capillary tubes and monoliths **218**

Abstract **218**
8.1 Introduction **218**
8.2 Experimental **221**
8.2.1 Materials and alumina suspension preparation 221
8.2.2 Preparation of alumina hollow fibres, multi-channel tubes and monoliths 221
8.2.3 Characterisation 223
8.3 Theoretical analysis of the geometrical influence to the fractural loading **223**
8.4 Results and discussions **226**
8.4.1 Structure of the multi-channel alumina tubes 226
8.4.2 The mechanical property 233
8.4.3 Water permeation 234
8.5 Conclusions **237**
References **238**

Chapter 9: A high-capacity open bore GC column based on alumina hollow fibres **239**

Abstract **239**
9.1 Introduction **240**
9.2 Experimental **241**
9.2.1 Materials and alumina hollow fibre preparation 241
9.2.2 Deposition of 5Å particles into the micro-channels of alumina hollow fibres 242
9.2.3 Gas chromatograph experiment 244
9.2.4 Characterisation 245
9.3 Results **245**

9.3.1 GC column morphology 245
9.3.2 Separation performance of nitrogen and oxygen 247
9.4 Discussion 250
9.5 Conclusions 252
References 253

Chapter 10: Conclusions and future works 255

10.1 Introduction 255
10.2 General conclusions 256
10.3 Chapter by chapter conclusions 257
10.3.1 Chapter 4 257
10.3.2 Chapter 5 257
10.3.3 Chapter 6 258
10.3.4 Chapter 7 258
10.3.5 Chapter 8 259
10.3.6 Chapter 9 259
10.4 Future work 260
10.4.1 Morphology design 260
10.4.2 Other membrane materials 261
10.4.3 Potential applications 264
References 265

List of Publications 266

List of Figures

Figure 2.1	Scanning Electron Micrograph of the cross-section of a) a symmetric alumina substrate [116], b) three-layered alumina membrane/support composite [117], and c) an asymmetric integral alumina membrane [86]	14
Figure 2.2	Product photograph of a commercial multi-channeled alumina flat sheet membrane (CFM Systems®) from ItN Nanovation AG [141]	19
Figure 2.3	Product photograph of a) Pall Corporation Membralox® multi-channeled alumina membranes [131], b) LiqTech International, Inc's SiC SteriMem® products [128], and c) Veolia Water Ltd CeraMem® element [134]	20
Figure 2.4	Product photograph of alumina hollow fibre alumina membranes from Hyflux Ltd [121]	21
Figure 2.5	Product photograph of a ceramic flat sheet module from a), ItN Nanovation AG; and b), a ceramic flat sheet system from Meidensha Corporation [144]	24
Figure 2.6	Product photograph a) of an immersed ceramic tubular membrane module from Kubota Corporation [145]; and b) a contained module from Pall Corporation [146]	25
Figure 2.7	Product photograph of the CeraMem® contained module and housing from Veolia Water Ltd [112]	26
Figure 2.8	Schematic drawing of a dual-layer spinneret. The ceramic suspension and bore fluid are extruded simultaneously through the concentric orifices with no contact with one another until they leave the spinneret	32
Figure 2.9	Scanning Electron Micrograph of the cross-section morphology of a), a symmetric alumina hollow fibre; and (b-d), different asymmetric alumina hollow fibres formed by combined phase inversion and sintering [86, 115, 171]	33
Figure 2.10	Schematic of the different sub-structures that can be found in ceramic membranes made via the combined phase inversion and sintering method	35

Figure 3.1	Schematic of the ceramic disc membrane preparation set-up	94
Figure 3.2	Schematic of the ceramic hollow fibre membrane preparation set-up	95
Figure 3.3	Schematic of the dead-end pure water permeation experiment set-up for ceramic disc membranes	99
Figure 3.4	Schematic of the dead-end pure water permeation experiment set-up for hollow fibre membranes in the out-in configuration	99
Figure 4.1	Cross-sectional SEM images of a) Membrane-DMSO, b) Membrane-NMP, c) Membrane-DMAc, d) Membrane-DMF, e) Membrane-TEP	108
Figure 4.2	Cross-sectional SEM images of the upper region of a) Membrane-DMSO, b) Membrane-NMP and c) Membrane-DMAc	110
Figure 4.3	Cross-sectional image of Membrane-DMSO with the labelled hierarchical levels	111
Figure 4.4	A SEM image of a polished section showing the distribution and the multi-level feature of micro-channels. The image was taken from a section close to the top surface of a Membrane-DMSO specimen.	111
Figure 4.5	SEM images of the sections close to the membrane upper and lower surfaces. The sections were exposed after polishing off 20-30 % of the membrane thickness. (a-b) Membrane-DMSO, (c-d) Membrane-NMP and (e-f) Membrane-DMAc, respectively	112
Figure 4.6	The rate of change of micro-channels density with respect to the depth of the membrane. The data were extracted from Table 4.3	114
Figure 4.7	Two-dimensional perturbations on the interface of the suspension/solvent/non-solvent system during phase inversion	123
Figure 4.8	An example of the k-n curve showing the solution of the R-T Instability equation (Equation 4.9). Parameters used for the calculation: ρ_c=1000 (Kg/m^3), ρ_s=1500 (Kg/m^3), μ_c=0.001 (Pa·s), μ_s=10.000 (Pa·s), T=0.02 (N/m), and a=1×104 (m/s^2)	126
Figure 4.9	Cross-sectional schematic of a membrane formed via phase inversion with micro-channels visualising the solution in Figure 4.8	127
Figure 4.10	An example of the k-n curve showing the solution of the R-T Instability equation (Equation 4.9). Parameters used for the calculation: ρ_c=1000 (Kg/m^3), ρ_s=1500 (Kg/m^3), μ_c=0.001 (Pa·s), μ_s=10.000 (Pa·s), T=0.02 (N/m), and a=1×107 (m/s^2)	127

Figure 4.11 Simulation growth number vs wavenumber for Membrane-DMSO. Parameters used for the calculation: ρ_c = 1000 (kg/m^3), ρ_s = 1820 (kg/m^3), μ_c = 0.001 (Pa.s), μ_s = 7.58 (Pa.s), T = 0.02 (N/m) and a = 4x106 (m/s^2) 131

Figure 4.12 Simulation Growth number vs wavenumber for Membrane-DMAc. Parameters used for the calculation: ρ_c = 1000 (kg/m^3), ρ_s = 1650 (kg/m^3), μ_c = 0.001 (Pa.s), μ_s = 3.64 (Pa.s), T = 0.02 (N/m) and a = 5x106 (m/s^2) 133

Figure 5.1 Schematic of the set-up for fabricating thin fibres by spinning through micro-channelled ceramic membranes 148

Figure 5.2 SEM images of membranes made from suspensions with different alumina loadings of 30 wt.% (a, f, k), 36 wt.% (b, g, l), 45 wt.% (c, h, m), 55 wt.% (d, I, n), and 65 wt.% (e, j, o). The left column (a-e) shows the whole view of cross-section, the middle column (f-j) shows the micro-channel openings on a section parallel to the surface after removal of 500μm from the top of membranes, and the right column (k-o) gives high-resolution SEM images of the top surface 150

Figure 5.3 Close up cross section SEM images of (left) the top regions and (right) the bottom regions of membranes made from suspensions of different alumina loadings (a-b) 30 wt.%, (c-d) 36 wt.%, (e-f) 45 wt.%, (g-h) 55 wt.%, and (i-j) 65 wt.% 151

Figure 5.4 Cross-section SEM images of the alumina membranes made from the 55 wt.% suspension with different membrane thicknesses. a) 30 mm, b) 4 mm, c) 1 mm, d) 380 μm and e) 250 μm 154

Figure 5.5 Cross-section SEM images of the alumina membranes with different coagulation temperatures a) 20 °C, b) 30 °C, c) 50 °C 156

Figure 5.6 Gas-liquid displacement porosimetry data for the membranes made from suspensions of different loadings after the removal of the bottom sponge layer 158

Figure 5.7 Simulation growth number vs wavenumber for 3 different alumina suspension loadings. Parameters used for the calculation: ρ_c = 1000 (kg/m^3), ρ_s = 1440, 1660 and 1850 (kg/m^3), μ_c = 0.001, (Pa.s), μ_s = 0.309, 1.38 and 37.8 (Pa.s), T = 0.02 (N/m) and a = 4x10^6 (m/s^2) for 162

loadings 30, 45, and 65 wt.%, respectively

Figure 5.8 Simulation Growth number vs wavenumber for 3 different alumina suspension loadings. Parameters used for the calculation: ρ_c = 1000 (kg/m^3), ρ_s = 1660 (kg/m^3), μ_c = 0.001 (Pa.s), μ_s = 1.38 (Pa.s), T = 0.02 (N/m) and a = 1x10^6, 2x10^6 and 4x10^6 (m/s^2) 162

Figure 5.9 SEM image of YSZ microfibres sintered at 1300 °C fabricated by extrusion through alumina disc membranes with open micro-channels 166

Figure 6.1 Photograph of the double-orifice spinneret for extruding single-layered hollow fibre membranes 173

Figure 6.2 SEM images of a) whole view, b) close-up cross-sectional view, c) inner surface at low magnification, d) outer surface at low magnification, e) inner surface at high magnification and f) outer surface at high magnification of Membrane 1 sintered at 1342 °C 175

Figure 6.3 Bubble point method data a) and mercury intrusion data b) for Membrane 1 sintered at 1342 and 1455 °C 176

Figure 6.4 SEM images of a) whole view, b) close-up cross-sectional view, c) inner surface at low magnification, d) outer surface at low magnification, e) inner surface at high magnification and f) outer surface at high magnification of Membrane 2 sintered at 1342 °C 178

Figure 6.5 Bubble point method data a) and mercury intrusion data b) for Membrane 2 sintered at 1342 and 1455 °C 179

Figure 6.6 SEM images of a) whole view, b) close-up cross-sectional view, c) inner surface at low magnification, d) outer surface at low magnification, e) inner surface at high magnification and f) outer surface at high magnification of Membrane 3 sintered at 1342 °C 181

Figure 6.7 a) Bubble point method data and b) mercury intrusion data for Membrane 3 sintered at 1342 and 1455 °C 182

Figure 6.8 Mercury intrusion data for Membrane 2 sintered at 5 different temperatures 185

Figure 6.9 Peak loading and mechanical strength data for Membrane 2 sintered at 5 different temperatures with standard deviations of within 35 % 186

Figure 6.10 Water permeation flux data measured at 1 bar difference and the outer diameters of Membrane 2 sintered at 5 different temperatures with 187

standard deviations of within 25 %

Figure 7.1 Schematic of the three types of hollow fibre cross-section structural designs achievable through co-extrusion of ceramic and polymeric layers 192

Figure 7.2 Photographs of the triple-orifice and quadruple-orifice spinnerets for extruding dual-layered and triple-layered hollow fibre membranes 195

Figure 7.3 Schematic of the set-up for the hollow fibre membrane emulsion experiment 196

Figure 7.4 SEM cross-section images of the Design 4's dual-layered membrane precursor (a-b), sintered fibre at 1500 °C (c-d) and the inner and outer surfaces of the sintered fibre at 1500 °C (e-f), respectively 199

Figure 7.5 SEM cross-section images of Design 5's dual-layered membrane precursor (a-b), sintered fibre at 1500 °C (c-d) and the inner and outer surfaces of the sintered fibre at 1500 °C (e-f), respectively 201

Figure 7.6 SEM cross-section images of Design 6's triple-layered membrane precursor (a-b), sintered fibre at 1500 °C (c-d) and the inner and outer surfaces of the sintered fibre at 1500 °C (e-f), respectively 203

Figure 7.7 Gas-liquid displacement porosimetry data for membrane Design 4 204

Figure 7.8 Gas-liquid displacement porosimetry data for membrane Design 5 205

Figure 7.9 Mercury intrusion porosimetry data for membrane Design 6 205

Figure 7.10 Schematic of a membrane emulsification process that can be realised with Design 4 210

Figure 7.11 SEM of PAN spheres formed from membrane emulsification using Design 4 followed by phase inversion 210

Figure 7.12 Schematic of membrane Design 5 with deposited functional material in the micro-channels 211

Figure 7.13 Schematic of a combined methanol reforming and water shift reaction process that can be realised with Design 6 213

Figure 8.1 Photograph and schematic of the multi-channel spinnerets for extruding multi-channel hollow fibre/tubular/monolithic membranes 222

Figure 8.2 The effect of the distance between the channel centre and the tube centre on the relative fractural loading of a 7-channel capillary tube listed in 226

Table 8.3. The outer diameter of the tube is 4 mm and the internal diameter of the channels is 0.945 mm.

Figure 8.3 Photographic pictures of 19-channel alumina monolith a) with cylindrical geometry, b) with hexagonal geometry, and SEM images of the c) wall structure between channels and d) wall structure between channel and outer surface of the hexagonal alumina monolith 227

Figure 8.4 Pore size distribution of 19-channel alumina monoliths sintered at 1350 °C for 4 h 229

Figure 8.5 Photographic pictures of (a, c, e) the single-channel, 3-channel hollow fibres and 7-channel capillary tube respectively and SEM images of (b, d, f) close-up of the cross section of single-channel, 3-channel hollow fibres and 7-channel capillary tube respectively 231

Figure 8.6 Pore size distribution of the single-channel hollow fibre sintered at different temperatures between 1300 – 1450 °C for 4 h 232

Figure 8.7 Fracture load of the single-channel hollow fibre and multi-channel monoliths sintered at different temperatures between 1300 – 1450 °C with standard deviations of within 35 % 233

Figure 8.8 Pressure dependent dead-end water permeation of the single-channel hollow fibre and multi-channel monoliths sintered at 1300 °C carried out in the out-in configuration with standard deviations of within 25 % 235

Figure 8.9 Fracture load (standard deviation 35 %) and water permeation flux (standard deviation 25 %) of the 7-channel capillary tube sintered at different temperatures between 1300 – 1450 °C 236

Figure 8.10 Stepwise decrease and subsequent increase in trans-membrane pressure on dead-end water permeation (standard deviation 25 %) of the 7-channel capillary tube with a selectively sealed channel sintered at 1350 °C and carried out in the out-in configuration. Note: For the selected sealing patterns, red lines indicate physical regions of feed side, blue lines indicate physical regions of permeate side, shadows indicate the blockage to the channel ends of feed side 237

Figure 9.1 Common gas chromatography configurations (a-b), and the proposed new configuration using packed micro-channels in hollow fibres c) 241

Figure 9.2	Schematic of the deposition process for loading zeolite particles into the hollow fibres' micro-channels	243
Figure 9.3	Photograph of the gas chromatography column	243
Figure 9.4	Gas chromatography column paired with a mass spectrometer using argon as the carrier gas and air as the sample gas	244
Figure 9.5	SEM of the hollow fibres a) the hollow fibre cross-sectional overview, the dashed line highlights the inner skin layer; b) the outer surface of the hollow fibre with micro-channel openings, the arrows indicates open micro-channels; c) a schematic of the deposition process to pack the 5Å molecular sieve particles into the micro-channels; d) an illustration of the hollow fibre with packed molecular sieve particles; e) the cross-sectional view in which the dashed line highlights a micro-channel capsuling molecular sieve; and f) a close-up cross-sectional view, the dashed line highlights the open shell side of the hollow fibre, and the pink shading highlights the example of an area where molecular sieve particles were deposited	246
Figure 9.6	Pore size distribution of the hollow fibre membrane obtained by the gas-liquid displacement method	247
Figure 9.7	Mass spectrographs of nitrogen and oxygen through a a) 2 m, b) 4 m, c) 6 m and d) 8 m long GC columns with 10 mL min^{-1} argon carrier gas and 90 µL air injection volume	248
Figure 9.8	Mass spectrographs of nitrogen and oxygen through an 8 m column with 45 µL air injection volume and argon carrier flow rates of a) 10 mL min-1, b) 20 mL min-1, c) 30 mL min-1 and d) 40 mL min^{-1}	249
Figure 10.1	Schematic of the quadruple-orifice spinneret and the different layers that are spun for very smooth ceramic membranes	261
Figure 10.2	Schematic of a) the cross sectional structure of the hollow fibre potentially suitable for microbial fuel cells and b) the processes happening across the membrane layers to generate electricity	264

List of Tables

Table 2.1	List of commercially available ceramic membranes for MF/UF	15
Table 4.1	Alumina suspension composition for the disc membranes with the solvents: DMSO, NMP, DMAc, DMF and TEP	105
Table 4.2	The effect of solvent choice in the ceramic suspension on their measured viscosities and densities	107
Table 4.3	The density of micro-channels on sections of different depths with standard deviations of within 15 %	113
Table 4.4	Water permeation flux, thickness and average pore size of the 5 membranes with standard deviations of within 25 %	115
Table 4.5	The correlation of water permeation (standard deviations within 25 %) and macrostructure for Membranes-DMSO, NMP and DMAc.	117
Table 4.6	Comparison of the properties between the alumina membranes with micro-channels formed in this study and commercial ceramic membranes	118
Table 4.7	Mechanical stability of the alumina disc membranes made from different solvents with standard deviations of within 35 %	119
Table 4.8	Wavelength converted from the density of micro-channels in Table 4.3	130
Table 4.9	Comparison between the experimental and the simulation results of the micro-channel structure of Membrane-DMSO	132
Table 4.10	Hansen Solubility parameters for the five solvents and their relative energy difference with PESf	135
Table 5.1	Alumina suspension compositions for disc membranes	147
Table 5.2	YSZ suspension composition for making thin nanofibres	147
Table 5.3	Micro-channel densities from different strata of the membranes made with different alumina loadings with standard deviations of within 20 %	152
Table 5.4	Micro-channel densities from different strata of the membranes of different thicknesses with standard deviations of within 30 %	155
Table 5.5	Micro-channel densities for membranes made in different coagulation temperatures after removing 40 μm of the membranes' top surfaces	156

with standard deviations of within 30 %

Table 5.6	Dead-end water permeation fluxes of 5 membranes made from different ceramic loadings under 1 bar trans-membrane pressure with standard deviations of within 25 %	158
Table 5.7	Mechanical stability of the membranes made from different ceramic loadings under 3-point bending configuration with standard deviations of within 35 %	159
Table 5.8	Comparison between the experimental and simulation results of the micro-channel structure of membranes made from different alumina loadings	164
Table 6.1	Alumina suspension composition for single-layered hollow fibre membrane Designs 1, 2 and 3	172
Table 6.2	Fabrication parameters for hollow fibre designs 1, 2 and 3 by changing the bore fluid and air gap	173
Table 6.3	Mechanical properties of the three membranes sintered at different temperatures with standard deviations of within 35 %	184
Table 6.4	Water permeation of the three membranes sintered at different temperatures with standard deviations of within 25 %	184
Table 7.1	Alumina suspension composition for hollow fibre membranes Designs 4, 5 and 6	193
Table 7.2	Polymer dope composition for membrane emulsion experiment	193
Table 7.3	Fabrication parameters for hollow fibre designs 4, 5 and 6	194
Table 7.4	Water permeation flux of Design 5 sintered at different temperatures under 1 bar trans-membrane pressure operated under dead-end filtration mode with standard deviations of within 25 %	206
Table 7.5	3-point bending strength of the 3 designs sintered at different temperatures with standard deviations of within 35 %	207
Table 8.1	Alumina suspension composition for multi-channel membranes	221
Table 8.2	Fabricating parameters of micro-structured multi-channel alumina tubes	222
Table 8.3	Relative fractural loading of multi-channel tubes.	224

Table 9.1 Comparing the properties and performance of the packed micro-channel hollow fibres and commercial GC columns using 5Å molecular sieve as the stationary phase 252

Nomenclature

Symbol	Definition	Units
A_m	Membrane area	m^2
a	Acceleration of the interface	$m\ s^{-2}$
b	Sample width	
d_f	Micro-channel density	m^{-2}
D	Diffusion coefficient	$m^2\ s^{-1}$
d_i	Inner diameter of fibre	m
d_o	Outer diameter of fibre	m
F	Breaking force	N
h	Sample thickness	m
I	Second moment of area	m^4
J	Membrane flux	$m^3\ m^{-2}\ s^{-1}$
J^{ϕ}	Volume flux	$m^3\ m^2\ s^{-1}$
K	Carman-Kozeny constant	-
k	Wavenumber	m^{-1}
L	Distance between centre of supporting rollers	m
M	Bending moment	N m
N	Number of theoretical plates	-
n	Growth number	-
p_n	Number of pores	-
R_{AB}	Resolution	-
S	Specific surface area	$m^2\ m^{-3}$
T	Surface tension	$N\ mm^{-2}$
t	Time	s
t_R	Retention time	s
w_h	Peak width at half-height	s
x	Membrane thickness	m
Greek letters		
δ_d	Dispersion cohesion solubility parameter	$MPa^{1/2}$

δ_h	Hydrogen bonding cohesion solubility parameter	$MPa^{1/2}$
δ_p	Polar cohesion solubility parameter	$MPa^{1/2}$
ε	Porosity	-
η_0	Initial amplitude	m
η	Growth rate	s^{-1}
λ	Wavelength, $\lambda = 2\pi/k$	m
λ_c	Critical wavelength	m
λ_m	Wavelength of the fastest growth	m
μ	Dynamic viscosity	Pa s
μ_r	Relative viscosity	-
v	Kinematic viscosity	$m^2 s^{-1}$
ρ	Density	$kg\ m^{-3}$
Φ	Volume fraction of inorganic particles in suspension	-
Φ_{max}	Maximum volume fraction	-
σ	Breaking strength	Pa
Subscripts		
c	External coagulant	-
s	Suspension solution	-

Chapter 1: Introduction

Chapter 1 *provides some background knowledge of ceramic membranes, followed by the objectives for each chapter and an overview for the thesis*

1.1 Background

In recent years there has been a steady growth in the applications of membranes across a wide range of sectors, such as: water treatment, food, beverage, biotechnology, pharmaceutical, oil and gas industries, reaction engineering, energy generation, and more. The most sought after features of membranes are their flexible selectivity and permeability, allowing only what you want through at the rate desired. In particular, membranes have anchored themselves a firm position in separation processes, which can be in the liquid, gas or mixed phases. Furthermore, the general trend of transitioning to more energy efficient technologies, meeting the increasingly stringent emission standards, striving for more and more compact systems, and reducing the total amount of waste produced act as main drivers for the development of membranes and membrane processes.

In both the past and today, polymeric membranes have dominated the membrane market, and due to their expanded applications, many other sectors' awareness and interest in membrane technology have also increased. This brought forth widened challenges that these membranes must face, including a greater range of environments and conditions to operate in, and they must be more specifically tailored for optimised performance. As the environments and conditions that the membranes are desired to operate in become harsher and more extreme, the drive for alternative, more robust membrane materials began to rise. Membranes with good chemical, thermal, and mechanical stabilities are desired, which led to the development of inorganic ceramic membranes. These membranes provide long-term stable performances, and can operate in extreme conditions.

However, research for ceramic membranes was slower and less widespread when compared with organic membranes. Their main drawbacks include: high capital

costs, brittleness, and lower packing densities when arranged in modules. Although the rate of development was slower, significant progresses have been made in the past 40 years. The development of various different deposition techniques such as chemical vapour deposition (CVD) and sol-gel, etc, have allowed the fabrication of higher performing membranes for expanded applications in nanofiltration, reverse osmosis, gas separation, reaction, pervaporation, and more. For many advanced applications, the same bottlenecks are hindering their industrialisation and larger-scale uses, such as: high capital cost, long and tedious fabrication process, low packing densities and high mass transfer resistances due to thick membrane thicknesses.

On the other hand, the emergence of the combined phase inversion and sintering method has created highly asymmetric membrane substrates that have superior performance as well as shortened and cheaper fabrication processes. In particular, the ability to manipulate the finger-like macrovoids, which has been traditionally seen as a disadvantage in polymeric membranes, is the main feature that enhanced the membrane performance as well as potentially debottling the limitations. After careful manipulation of fabrication parameters, their identity was transformed from a redundant void of space that weakens the membrane mechanically, to a pocket of space that extends the surface area of the membrane and can act as storage space, which can further expand their applications.

This study focuses on negating all of the abovementioned issues associated with ceramic membranes in order to easily reproduce high performing and economic ceramic membranes for expanded applications. The study is split into four main categories: fundamental study on the formation of micro-channels in alumina membrane systems, the manipulation of the micro-channels in alumina disc and hollow fibre membranes, the improvement of mechanical stability by adjusting membrane geometry, and finally, a possible broadened application of the newly developed membranes.

1.2 PhD Objectives

The objective of this thesis is to design and fabricate tuneable micro-channel enhanced ceramic membranes via the combined phase inversion and sintering method

for tailored and widened applications. Firstly, a fundamental study is carried out to investigate the factors that affect and influence micro-channel growth and characteristics in flat disc membranes. In this study, preliminary simulation attempts are used to predict and control the types of micro-channels that can be formed more quantitatively. The knowledge gained from this study is then transferred to ceramic hollow fibre membranes, and distinctively different micro-channelled membranes are fabricated using different bore fluids and air gap, and subsequently, characterised and tested for water filtration. The membrane structures are further expanded by the formation of multi-layer membrane precursors with sacrificial layers, to form open micro-channels at the surfaces desired. The potential applications of these membranes are discussed. Then, a study is carried out to improve the mechanical stability of micro-channelled membranes, by developing multi-channel hollow fibre, tubular, and monolithic membranes. Finally, gas chromatography, a potential application of the micro-channelled ceramic membrane whereby the stationary phase is deposited and packed into the micro-channels, is studied.

1.2.1 Fundamental Study on the formation of micro-channels in ceramic membranes – Spatial structure and simulation

The purpose of this chapter is to gain an improved fundamental understanding behind the formation of micro-channels in ceramic membranes systems. This is achieved by first simplifying the phase inversion process by forming alumina flat disc membranes to reduce the amount of variables that can affect the development of micro-channels. The effects of 5 different solvents in the ceramic suspension on the macro- and microstructures of the disc membranes are studied. Membrane characteristics such as pore size, pore size distribution, mechanical strength and pure water permeation flux are studied and the stratified micro-channel densities and periodic distances are also quantified. The effect of the membrane skin layers on pure water permeation flux are studied. The Rayleigh-Taylor instability phenomenon is also proposed as the cause for the formation of micro-channels and preliminary simulations were carried out to mimic the micro-channel characteristics.

1.2.2 High flux micro-channelled ceramic disc membranes for water treatments and spinning of microfibres

This chapter further studies the different fabrication parameters that can affect the formation of micro-channels based on the knowledge gained from the previous chapter, in effort to improve membrane performance in terms of water permeation flux. The effects of alumina loading in the ceramic suspension, membrane thickness, and coagulation temperature on the macro- and microstructures of the membranes are studied and the stratified micro-channel densities and periodic distances are quantified. The membranes made with different alumina loadings are further characterised in terms of pore size, pore size distribution, mechanical strength, and pure water permeation flux and the micro-channel characteristics are explained with preliminary simulations. A potential application of using micro-channelled disc membranes for the spinning of microfibers is also tested successfully to fabricate YSZ fibres.

1.2.3 Micro-structured alumina hollow fibre membranes

This chapter applies the knowledge gained from the previous two chapters onto hollow fibre membranes for improved packing density. Three distinctly different asymmetric alumina hollow fibre membrane morphologies are designed and fabricated by manipulating the spinning conditions, such as bore fluid choice and air gap. The membranes are characterised in terms of cross-section morphology, pore size, pore size distribution, mechanical strength, and pure water permeation flux. Effects of sintering temperature on these membrane properties are also studied and the most promising design for potential applications in aqueous microfiltration are discussed and studied further.

1.2.4 New open micro-channelled alumina hollow fibre membrane structures toward broadened applications

This chapter is focused on improving the performance and expanding the applications of asymmetric ceramic membranes, by forming open micro-channels in a single step through using polymer sacrificial layers during spinning. 3 types of alumina hollow fibres with open micro-channels at the desired surface(s) are designed and fabricated. The membranes are characterised in terms of cross-sectional morphology, pore size, pore size distribution, mechanical stability, and pure water permeation flux. Potential applications of these new designs are also briefly discussed.

1.2.5 Micro-structured alumina multi-channel capillary tubes and monoliths

This chapter aims to improve the mechanical stability of the micro-channelled ceramic membranes by fabricating multi-channel capillary and monolith tubes. 1-channel, 3-channel hollow fibres and 7-channel and 19-channel capillary/monolith tubes are fabricated with micro-channels in the cross-section. The membranes are characterised in terms of cross-sectional morphology, pore size, pore size distribution, mechanical property, and pure water permeation flux. The water permeation flux of the multi-channel tubes are further improved by selectively sealing channels.

1.2.6 A high-capacity open bore GC column based on alumina hollow fibres

This chapter looks into detail a potential application of ceramic hollow fibres with open micro-channels: as a gas chromatography column. The alumina hollow fibres with open micro-channels are used as the support to hold 5Å molecular sieve particles to separation oxygen and nitrogen in air. Factors such as column length and carrier gas flow rate and their effects on separation performance are studied. The performance of this new type of GC column is compared with conventional packed and capillary columns.

1.3 Thesis structure and presentation

This thesis consists of 10 chapters in total; to design and develop micro-channelled ceramic membranes for more broadened applications. Chapter 1 introduces the topic of membrane processes and why ceramic membranes should be researched into, and in particular, ceramic membranes with micro-channels. It also includes the main objectives of this thesis. Chapter 2 reviews the literature available on ceramic membranes, with emphasis on the combined phase inversion and sintering fabrication method and water treatment applications. Chapter 3 describes all the materials that were used, as well as the experimental procedures and characterisation techniques that were carried out. Chapter 4 is for improving the fundamental understanding of the micro-channel formation mechanisms, by studying simplified flat disc systems and developing preliminary simulations to mimic the micro-channel characteristics. Chapter 5 builds from the knowledge gained in Chapter 4 and further improves on the fundamental understanding by testing a series of fabrication parameters in effort to develop high flux micro-channelled membranes. Chapter 6 transfers and applies the knowledge gained from disc membranes onto hollow fibre membranes for much improved packing densities and develops 3 types of different asymmetric structures by using different bore fluids and air gap. Chapter 7 concentrates on developing ceramic hollow fibre membranes that can have open micro-channel at any desired membrane surface by spinning with polymer sacrificial layers to expand the application of asymmetric membranes. Chapter 8 describes a method for increasing the asymmetric membranes' mechanical strength, by producing multi-channel tubes and monoliths. Chapter 9 looks in more detail into a potential new application for asymmetric ceramic hollow fibres with open micro-channels: as a gas chromatography column. Chapter 10 concludes the thesis, with regards to the achievements made and future works that can be carried out.

Chapter 2: Literature Review

Chapter 2 *reviews the development of inorganic membranes in terms of fabrication methods, geometry designs, micro-structural designs, as well as their applications*

2.1 Membrane Principles and processes

A membrane can be defined as a semi-permeable active or passive barrier, which when placed under a certain driving force, separates one or more selected species or components of a mixture whilst the rest is rejected [1]. Most of the existing membrane process can be categorised into the following: microfiltration (MF), ultrafiltration (UF), nanofiltration (NF), reverse osmosis (RO), gas separation, pervaporation, and electrodialysis. The processes differ in terms of the pore size, the separation mechanism, as well as the driving force for separation. Micro- and ultrafiltration separate via sieving through pores, and reverse osmosis separates via the commonly accepted solution-diffusion model and they are driven by partial pressure differences across the membrane. Gas separation is the separation of selected gas species through a membrane that is selectively permeable to certain species of gases via a partial pressure difference across the membrane. Pervaporation is when permeate is passed as a gas through the membrane, whereby one side contains a liquid and the other side vapour and is driven by the vapour pressure difference. Finally, electrodialysis separates ions in aqueous solutions via a charged membrane driven by electrical potential differences. The emphasis of this review will be on the pressure-driven processes, mostly micro- and ultrafiltration and water treatment.

Due to the large range of membrane processes available today, it is difficult to pinpoint specific research priorities, as they vary from industry to industry, as well as application. In 1989, the Membrane Technology and Research, Inc (MTR) performed a study addressing the research priorities in the membrane separation industry [2]. For MF and UF, the highest priority research topics include: fouling-resistant long-life membranes that are high temperature, solvent, wide pH, and oxidant resistant, low-cost membrane modules and low energy module designs. Although the study was

performed more than 20 years ago, many of the issues still remain as important research areas today. Most of the progress was concentrated on organic membranes and operating systems, and inorganic membranes were not given as much attention mostly because they were much more expensive. The development of cheap asymmetric inorganic membranes with high packing densities and permeation fluxes can be seen as a possible solution to most of the challenges listed above.

2.2 Development in ceramic membranes and their fabrication processes

Ceramic materials can be made into membranes; which can be both porous and dense. Using ceramic materials as membranes have advantages of high chemical, thermal, and mechanical stabilities over organic membranes. Below is a brief overview of the history of ceramic membranes, describing the loose trends and major developments.

2.2.1 Brief history of ceramic membrane developments over the past 50 years

The earliest uses of ceramic membranes dated back to the 1940s for enriching uranium in nuclear power plants [3]. In the entire 60s and 70s there was little growth in ceramic membranes, and they were mostly used in very niche fields and in the food and dairy industry, for carrying out micro- and ultrafiltration functions. The research interest in ceramic membranes began to grow in the 80s, whereby more durable and chemically and thermally stable membrane materials were desired due to the increase in general membrane applications. The first tubular and monolithic membranes were also available for commercial use [4], and ceramic membranes became increasingly popular in the emerging food, dairy, and biological industries [5-8]. The main attractions that brought ceramic membranes to these industries include robustness, sterilisability, and their ability to be cleaned in harsh conditions. In order to reduce costs, monolithic hexagonal configurations were developed [4]. However, the applications of ceramic membranes stayed almost entirely in aqueous MF, UF, and some gas separation processes [9, 10].

From the 1990s onwards, there was a rapid increase in research and development of ceramic membranes, including a large expansion in applications, and the development of additional materials and fabrication methods. Ceramic membranes were no longer viewed solely as separation barriers, but carried out other tasks such as reactions and energy generation and researchers concentrated on integrated processes. There was a boom in research on membrane reactors, such as the enzyme immobilised membrane reactor and catalytic membrane reactor. Applications included the dehydrogenation of organic compounds such as ethylbenzene to styrene [11, 12], steam reforming and water gas shift to produce H_2 [13-15], and partial oxidation of methane to synthesis gas [16-18], etc. This development was much facilitated by the fabrication of hydrogen permeable palladium membranes supported on porous ceramic substrates [19-21], and mixed ion conducting membranes for oxygen transport [22-24]. Solid-oxide fuel cells were also popular topics to provide electricity with high efficiency and low emissions [25]. There was also an increase in the application of ceramic membranes in water treatment; in particular, the appearance of membrane hybrid systems such as coagulation-microfiltration and adsorption-ultrafiltration [26], and photodegradation of organic materials with TiO_2 [27]. There were larger scale studies for treating and reusing wastewater from buildings [28], and in treating primary sewage effluent [29]**.** Membrane bioreactors using ceramic membranes were popular studies [30-33], mainly for the treatment of wastewater. A newer field that received increasing attention was membrane emulsification [34-36].

In terms of development in fabrication, the CVD method was introduced to make UF ceramic membranes with thin functional layers [37, 38]. Improvements in the sol-gel technique was achieved, for the formation of smaller pores and controlled porosity [39, 40], as well as other new deposition techniques such as slipcasting, filtration, coating, and permformation [41]. Phase inversion was also first introduced in the 90s, to form the first asymmetric ceramic membranes via wet-spinning with a polymer in suspension [42].

Ceramic membranes started appearing in a wider range of configurations, and the hollow fibre configuration was fabricated in effort to increase the packing density of the modules [42, 43]. Some research efforts have also been paid to improve the membrane modules [44], so that they can handle the high temperature conditions that

are required by the new applications. However, the main deterrent for using ceramic membranes industrially and commercially remained the investment costs.

The 2000s saw an expansion in applications, fabrication techniques, and materials for ceramic membranes. Much research on membrane reactors were continued from the 90s, but there was little attempt at industrial use, and the main deterrent was the cost of the microporous membranes, which would require radical changes to membrane and module design to improve [45]. It was recognised that affordable, efficient, long term reliable membranes and optimised reactor design and up-scale process analysis were needed for further growth of membrane reactors. There was some increasing attention on renewable energy sources, such as the direct solar thermal splitting of water using ceramic membranes [46, 47], and using ceramic membranes to refine biodiesel [48]. Much attention was given to oxygen separation [49, 50], and hydrogen technology to make rechargeable batteries or for hydrogen energy sources [51, 52]. There was more attention on hybrid systems for wastewater treatment and drinking water production [53-55], and a growth on membrane emulsification [56-58]. Other applications concerning ceramic membranes included hollow fibre membrane contactors [59, 60], hydrophobic ceramic membranes from grafting for membrane distillation [61-63], and using ceramic monoliths as the stationary phase in chromatography [64].

In terms of fabrication, the combined phase inversion and sintering technique became more studied [65, 66], which can achieve the fabrication of asymmetric multi-layered membranes in a single step [67]. This method was also explored for a range of ceramic materials, such as YSZ hollow fibres [68, 69] and composite membranes [70].

In terms of membrane materials, researchers doped ceramic materials for ion-conducting membranes [71-73], and other materials studied include SiC [74-76] and anodic aluminium oxide [77, 78]. A lot of zeolite studies were carried out for applications such as pervaporation and heavy metal removal from wastewater [79-81].

From 2010 onwards to now, there is still a rapid expansion in ceramic membrane research and development, particularly for integrated systems to form synergies with other technologies. In particular, hybrid systems with advance materials have received a lot of attention. Emerging areas include using ceramic membranes to treat oily wastewater and oil field wastewater, etc [82-84]. A rise in attention on membrane reactors is experienced, due to the rise of dual-layer

membrane reactor [85], multifunctional catalytic membrane reactors [86], and membrane hollow fibre micro-reactors etc [87]. Asymmetric hollow fibre membranes are attractive as they have lower mass transfer resistances and higher packing densities compared with older membrane reactors. There has been an increase in researches for carbon dioxide separation using dual-phase membranes [88], as well as carbon dioxide capture [89, 90], as power plants aim for zero-emission and sustainable fuel production [91, 92]. Renewable methods for producing electricity with ceramic membranes is still studied, with developments such as the microbial fuel cell for converting organic biomass into electricity [93].

One particular area that is receiving on-going increasing attention is the use of nanoparticles in ceramic membrane structures for enhanced performance and widened applications. Application examples include water treatment [94], hydrogen recovery from hydrocarbons and gas separation using ZIF-8 particles in membranes [95, 96], and graphene oxide membranes on ceramic supports for pervaporation, nanofiltration, or oil and water separation [97-100].

Research on the combined phase inversion and sintering method continued with promising progress. The method can produce micro-channels, which are opening up the applications for ceramic membranes. A wider variety of materials have been used with this method to fabricate hollow fibre porous membranes, such as stainless steel [101]. Other novel fabrication methods include centrifugal casting [102], and the emulsion-templated method for making porous membrane materials [103]. The quest for cheaper membrane materials continues, and from 2010 onwards, much research was carried out on making membranes from low cost clay [104-107].

As can be seen from the developments, many achievements have been made over the past half-century, and the applications of ceramic membranes have spread extensively and are projected to continue doing so. As ceramic membranes become more and more competitive cost wise, there should be increasing situations whereby they will be chosen over or replace polymeric membranes, due to their robustness and great chemical and thermal stabilities. The focus of this literature review will be mainly on pressure-driven membrane processes, such as micro- and ultrafiltration in aqueous conditions.

2.2.2 Desirable membrane characteristics and their design

To understand the type of membrane properties desired for pressure-driven membrane processes, it is important to first understand the membrane transport mechanisms. Transport models can help to identify the structural parameters that affect the membrane performance. Different pore geometries exist depending on the fabrication processes and hence different models can be used to describe the transport through these different geometries. For example, the pores can be depicted as parallel cylinders, or a network of tightly packed spheres. For pores formed from voids between tightly packed spheres, the Carman- Kozeny relationship can be used to describe membrane flux assuming no interaction between the fluids and surface of the membrane [1]:

$$J = \frac{\varepsilon^3}{\kappa \mu S^2 (1-\varepsilon)^2} \frac{\Delta p}{\Delta x} \quad (2.1)$$

where J is the membrane flux ($m^3/(m^2 \cdot s)$), K is the Carman- Kozeny constant (depends on pore shape and tortuosity), ε is the porosity, S the specific surface area (m^2/m^3), μ is the permeate viscosity ($N \cdot s/m^2$), ΔP is the pressure difference (N/m^2) and Δx is the membrane thickness (m). Membrane selectivity and permeation flux are major indicators of membrane performance and from Equation 2.1, it can be seen that structural parameters such as high porosity and thin membrane thickness can lead to higher membrane fluxes. The different characteristics of the membrane can be designed and tailored by using different fabrication techniques and controlling the related fabricating parameters during the course of production.

2.2.3 Material and microstructure

Various membrane materials are available for MF/UF processes. The choice of the membrane material affects the practicality and sustainability of the filtration operation and hence can be chosen based on the specific application requirements.

Some examples of ceramic materials include alumina (γ-Al2O3, α- Al2O3), zirconia (ZrO2), titania (TiO2), glass (SiO2), and silicon carbide (SiC), etc. Ceramic membranes offer superior temperature and chemical tolerances, leading to an

extensive range of applications across many industries. They can be an important and environmentally friendly component in helping companies achieve “zero discharge” state. However, the main drawback from using ceramic membranes for water treatment is their high capital cost, hence large-scale membrane applications or less challenging water purification processes are still dominated by polymeric membranes. As shown from Table 2.1, commercial ceramic membranes for MF/UF processes consist mainly of α-Al_2O_3 as the substrate, and α-Al_2O_3, TiO_2, or ZrO_2 as the selective separation layer. According to experiments from the literature there is a general consensus that chemical stability (in highly acidic or basic environments) decreases in the following trend: TiO_2, ZrO_2, α-Al_2O_3, Υ-Al_2O_3, SiO_2 [108-110]. Generally, inorganic membranes can withstand organic solvents, chlorine and other oxidants, are less susceptible to microbial attack than polymeric membranes, and can be used from pH values 0 to 14 (TiO_2 and α- Al_2O_3) [108, 111].

Ceramic membranes are generally accepted to have high mechanical strength in terms of compressibility. They can be backwashed at elevated pressures operated over a longer period of time compared to polymer membranes [112, 113]. However a disadvantage of ceramic membranes is their brittleness, hence they must be handled with care and choice of housing and sealing should be carefully considered. The pressure required to drive MF is from 0.1 to 2 bar, and much higher for UF [114]. The maximum operating pressure specified by a hollow fibre ceramic membrane manufacturer is 6 bar. [115].

As mentioned before in Section 2.2.2, the microstructure across the membrane cross-section and surfaces are the key properties that dictate the performance and usability of a membrane for a certain application. In terms of the cross-section morphology, a membrane can be categorized into symmetric and asymmetric structures. A symmetric membrane has a uniform cross-section, whereas an asymmetric membrane does not, as shown in Figure 2.1a and Figure 2.1b (or Figure 2.1c), respectively.

For MF and UF processes asymmetric membranes consisting of a thin skin layer on top of a porous sub-layer are desired. The top layers of UF membranes are much denser than MF membranes; hence they require higher trans-membrane pressures and generally have lower permeability. The asymmetric structures are associated with higher permeation flux, as the effective membrane thickness can be much thinner than in symmetric membranes. The porous sub-layer acts to provide

adequate mechanical strength. This type of structure combines high selectivity of the skin layer with good permeation fluxes.

An asymmetric membrane can be either integral or made of several layers, known as a composite. The top and porous layers of an integral asymmetric membrane are normally made of the same material (Figure 2.1c) and for composite membranes the top skin layer and the porous sub-layer can be made of different materials (Figure 2.1b).

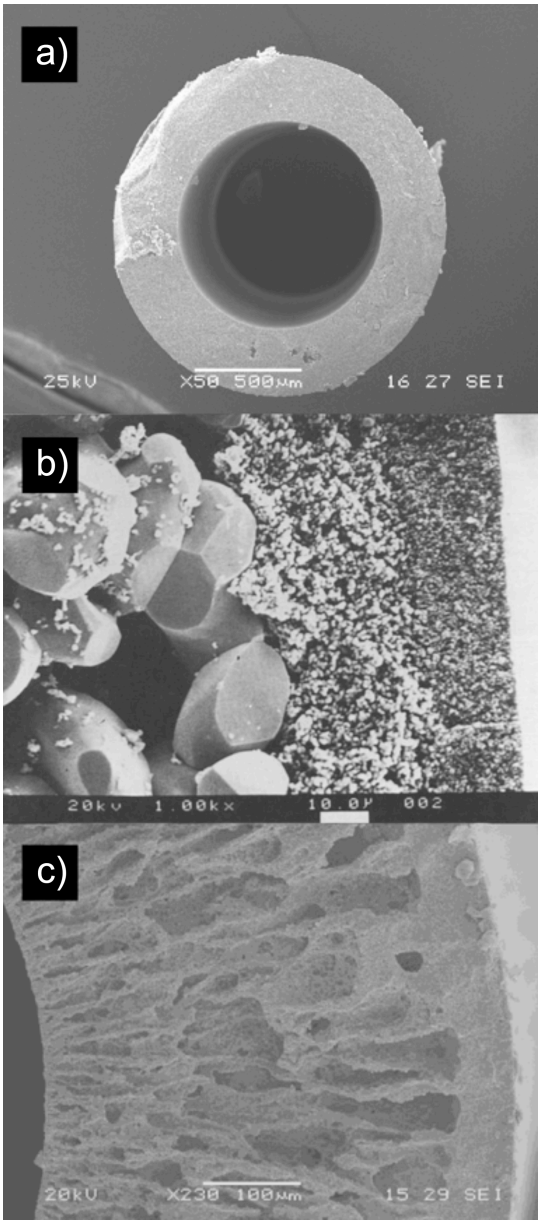


Figure 2.1 Scanning Electron Micrograph of the cross-section of a) a symmetric alumina substrate [116], b) three-layered alumina membrane/support composite [117], and c) an asymmetric integral alumina membrane [86]

Table 2.1 List of commercially available ceramic membranes for MF/UF

	Company	Product	Material	Technical Specifications			
				Pore Size (μm)	Channel diameter/Outer diameter (mm)	Packing density (m^2/m^3)	Pure water flux ($L \cdot m^{-2} \cdot h^{-1} \cdot bar^{-1}$))
Flat Sheet	ItN Nanovation AG	CFM Systems® [118-120]	Substrate: α-Al_2O_3 Selective layer: α- Al_2O_3/ZrO_2	0.2	3.0	91.8	-
	Meidensha Corporation	Ceramic Membrane Unit [121]	α-Al_2O_3	0.1	-	36.1	1,670
	LiqTech International, Inc	Silicon Carbide Flat Sheet Membrane [122]	SiC	0.2	-	37.7	-
	LiqTech	Silicon Carbide	SiC	0.04, 0.1,	-	-	3,000 4,000

Flat Disc	International, Inc	Flat Disc Membrane [123]		1.0			10,000
Tubular/ Monolith	Tami Industries	CéRAM™ [124] ISOFLUX™ [125]	TiO_2	0.002 – 1.4	-	-	-
	Atech Innovations gmbh	Ceramic membranes [126]	MF: α-Al_2O_3 UF: TiO_2	MF: 0.1 – 1.2 UF: up to 0.05 and MWCO: 5 kD	2.5 – 8.0/10.0 – 52.0	-	-
	Kubota Corporation	Filcera® [127]	Al_2O_3	0.1	9.0/13.0	68.2	-
	LiqTech International, Inc	SteriMem® [128], CoMem® [65], CoMem® Conduit [129], and Aquasolution® [130]	SiC	0.04, 0.1, 1.0	3.0 – 17.0/25.0 – 146.0	-	-
	Pall Corporation	Membralox® [131,	Substrate: Al_2O_3	MF: 0.1 –	3.0 – 6.0	285	-

		132]	Selective layer MF: Al_2O_3 or ZrO_2 UF: TiO_2	5.0 UF: 1.0 and MWCO: 0.1 kD			
	Veolia Water Ltd	Ceramem® [133-135]	MF: α-Al_2O_3, SiC, TiO_2 UF: SiC, SiO_2, TiO_2	0.2 – 0.5	2.0 – 5.0/142.0	MF: 1,200 UF: 800	-
Hollow Fibre	Hyflux Ltd	InoCep® [136, 137]	α-Al_2O_3	0.02 – 1.4	3.0/4.0	157	250 – 4,500
	Media & Prcoess Technology Inc	MPT hollow fibre membranes [138]	α-Al_2O_3	0.004 – 0.2	1.0 – 3.5	502	-

A composite membrane's properties and performance can be tailored by using different materials in different layers. Some disadvantages of composite membranes include the high complexity of the membrane fabrication process, which requires many steps, and the possibility of membrane failure due to delamination of the separation layer, which occurs during the sintering or variation of filtration pressures [139]. Integral membranes are homogenous in composition, but can also be highly structurally varied in layers or distinct regions, depending on their fabrication methods.

As shown in Figure 2.1c and Figure 2.1b, the cross-sectional microstructure of the integral membrane and the composite membrane vary significantly, despite both being asymmetric membranes. The integral membrane in Figure 2.1c is normally achieved by the combined phase inversion/sintering method [140], whereas the composite in Figure 2.1b is made by skin deposition on top of a multi-layer substrate support. The integral membrane consists of two different types of sub-structures: sponge-like structures and micro-channel structures. The sponge-like structure can provide the membrane with the desired selectivity and the micro-channel structures can reduce the overall membrane resistance to permeate flow. On the other hand, the composite membrane consists of pores formed by the voids between the particle packing only and the membrane selectivity is provided by the finer particles at the top layer and at a lower magnification the entire cross-section will appear like a sponge-like structure.

Integral and composite ceramic membranes can be made via different fabrication methods, and the choice of method will largely depend on the membrane configuration and microstructures that are desired.

2.2.4 Membrane configurations

There are a wide variety of membrane geometries available, depending on the shape formation technique chosen in the fabrication process. Ceramic membranes come in two main types of element configurations, i.e. flat and cylindrical membranes. The choice of the membrane configuration depends largely on the application, such as the required operating and feed conditions.

2.2.4.1 Flat membranes

Flat ceramic membranes can come in a disc or sheet form. The packing density of disc membranes is generally low and hence they are limited to use in small scale industrial, medical, and laboratory applications. Commercial ceramic flat sheet membranes may have thicknesses of around 6 mm and can be multi-channeled across their cross-section, as shown in Table 2.1 and Figure 2.2. Flat sheet membranes are easy to replace when packed in modules and can also handle high turbidity feeds. Mechanical cleaning of ceramic flat sheet membranes is also most versatile; it can withstand air scrubbing, backwashing, and high-pressure water jet cleaning.

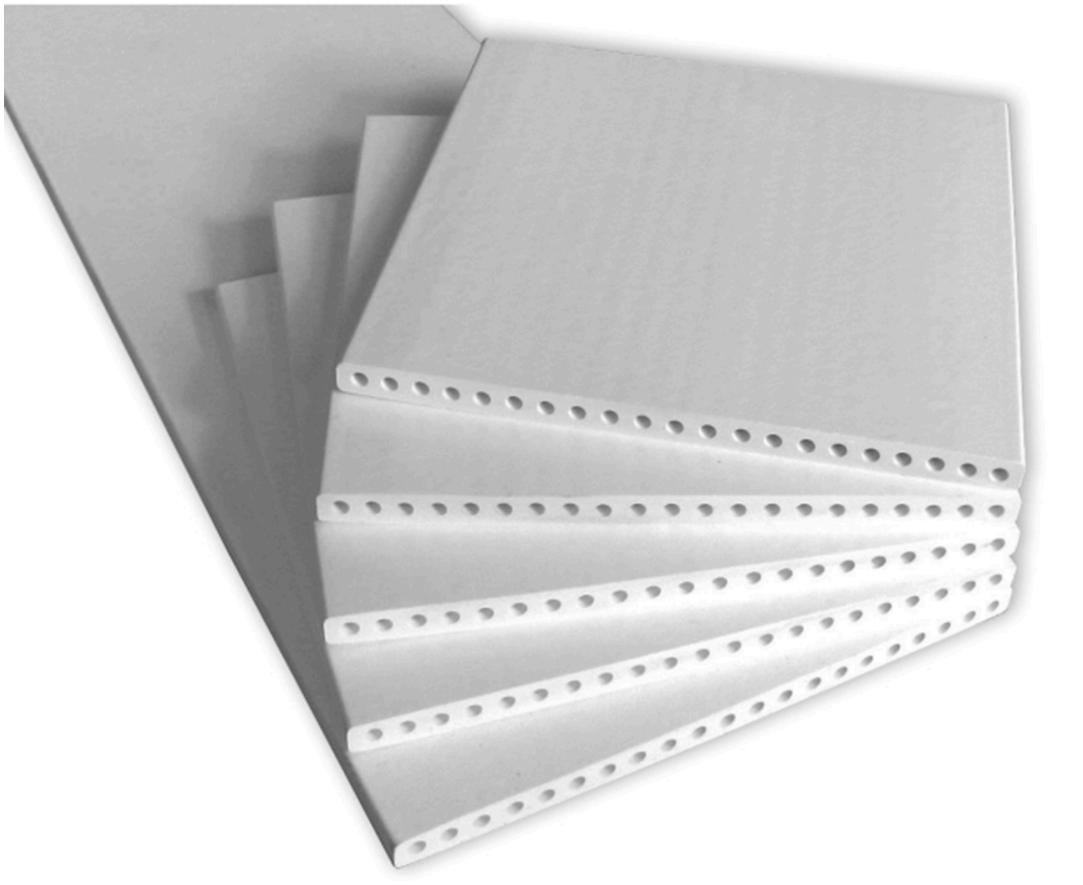


Figure 2.2 Product photograph of a commercial multi-channeled alumina flat sheet membrane (CFM Systems®) from ItN Nanovation AG [141]

2.2.4.2 Cylindrical membranes

Single-channel tubular membranes have diameters of generally between 10 – 25 mm, shown in Table 2.1 and Figure 2.3. They are more suitable for the separation of feeds that have high turbidity and large amount of suspended solids. Due to their larger diameters and robustness they can be more easily cleaned mechanically, and high cross-flow velocities can also be used to control fouling. To further improve the packing density of the tubular membranes, they can be fabricated as multi-channel tubes, called monoliths, with surface area to volume ratio of up to 782 m^2/m^3, as shown from Table 2.1. In effort to improve the packing density, hexagonal monoliths have also been developed (Figure 2.3a). Monolith membranes offer the same advantages as the singular tubular membranes. However, when running in the inside-out configuration, the pressure drop of the permeate flow across the monolith could be quite high due to the long and tortuous path that it has to travel to reach the outer surface of the monolith, hence, limiting the size of the outer diameter that can be used. The patented CeraMem® from Veolia Water Ltd. solves this problem by adding multiple conduits across the monolith through which the permeate will flow through and then collected at the end of the module (Figure 2.3c).

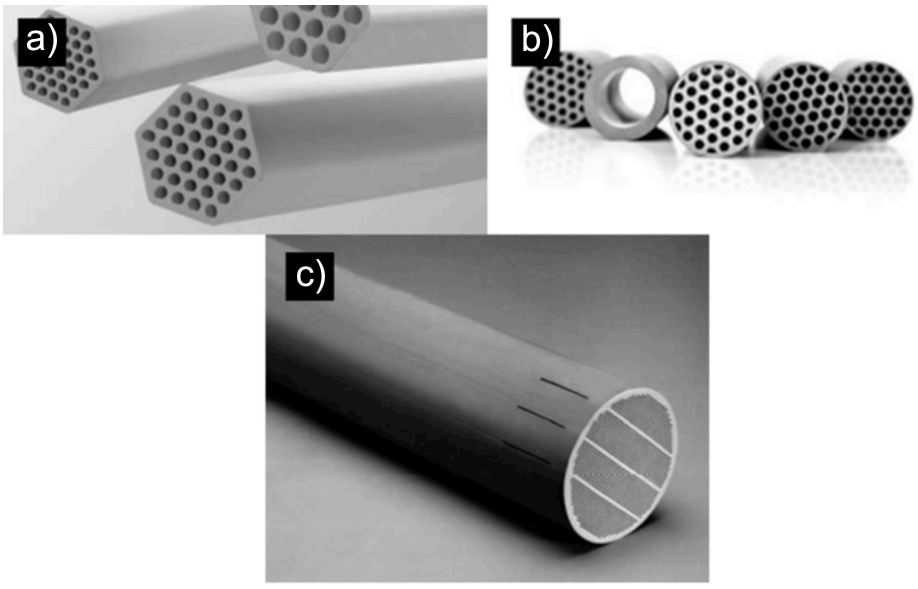


Figure 2.3 Product photograph of a) Pall Corporation Membralox® multi-channeled alumina membranes [131], b) LiqTech International, Inc's SiC SteriMem® products [128], and c) Veolia Water Ltd CeraMem® element [134]

Ceramic hollow fibre membranes have diameters of between 2.0 to 4.0 mm [65, 66, 116, 142] (Figure 2.4), meaning compact modules with high effective membrane surface areas can be achieved. Furthermore, Fraunhofer IGB, Ltd stated that ceramic hollow fibres of down to 0.5 mm outer diameter have been fabricated via combined phase inversion and sintering [113], potentially increasing the packing density that can be achieved further. In addition, they require lower trans-membrane pressures to drive permeate flow due to the thinner membrane, and can be cleaned easily, using methods such as backwashing and forward flushing.



Figure 2.4 Product photograph of alumina hollow fibre alumina membranes from Hyflux Ltd [121]

2.2.5 Development in membrane modules and units

The design of the membrane module is important in achieving the highest packing density possible for the particular membrane element whilst offering effective filtration. The different membrane elements are packed in a unit called the module and these modules are often arranged and connected in a specific way to form a unit, offering great efficiencies. The unit(s) is then integrated with other components such as pumps, pipes, control systems, etc, to form a membrane system and part of the water or wastewater treatment plant. The following section describes the ceramic MF/UF modules and units available commercially.

2.2.5.1 Module and unit designs

There are many different module designs available for the different ceramic membranes and their choice depends largely on the application, the demand of the process, and any spatial limitations and economical factors. The arrangement and packing of the membrane elements can be divided into two main types, i.e. flat membranes and cylindrical membranes.

The membrane elements may be contained in pressure vessels or immersed in a fluid medium at atmospheric pressure. For the contained modules the ceramic membranes are packed and fitted inside a pressure vessel and trans-membrane pressure is applied at one end of the vessel with the feed. The immersed unit allows easier replacement of the membrane elements or modules and is also more flexible to tailor to specific needs and demands. Furthermore, they enable air sparging in the unit to improve permeation and reduce fouling by promoting turbulence. Both flat sheet and cylindrical membranes can be packed in this way and this type of system requires less energy to operate than the contained units.

2.2.5.2 Flat membranes

Ceramic flat membranes can come in the form of flat sheets or flat discs, as described in Section 2.2.4, and can both be packed into plate-and-frame modules. The contained

plate-and-frame configuration consists of stacking the flat membranes on top of one another with porous spacers in between. The size of the spacing depends on the amount and size of suspended solids in the feed. The feed enters the module from one end and is collected at the membrane support plates. Such a module is easy to operate and membrane defects can be detected and replaced simply. However, their packing density is low and so most of the time they are limited to use for small-scale applications.

The flat sheet membranes with multiple channels can be stacked next to one another and form an immersed module, as shown in Figure 2.5. These flat sheet membranes are connected at the two ends to permeate collector(s) and then packed together and supported by a metal framework that is then immersed in the feed medium. The permeate enters from the membrane's outer surface into the channels inside the flat sheets and are then collected at the end(s) of the membrane. These modules can then be further stacked together to easily increase productivity. The energy consumption of the immersed module is lower than that of the contained module, due to the lower pressure driving force requirements. The membranes can also be replaced easily as they are produced and sealed sheet by sheet. In addition, their ability to handle feeds with high contents of suspended solids means that they are commonly used in MBRs for treating wastewater. Packing densities of around 52.6 m^2/m^3 is reached using the CFM Systems® from ItN Nanovation AG, by stacking units on top of one another (Table 2.1). However, this is still significantly lower than the packing densities offered by polymeric flat sheet membranes that are spiral wound (700 – 1000 m^2/m^3) [143].

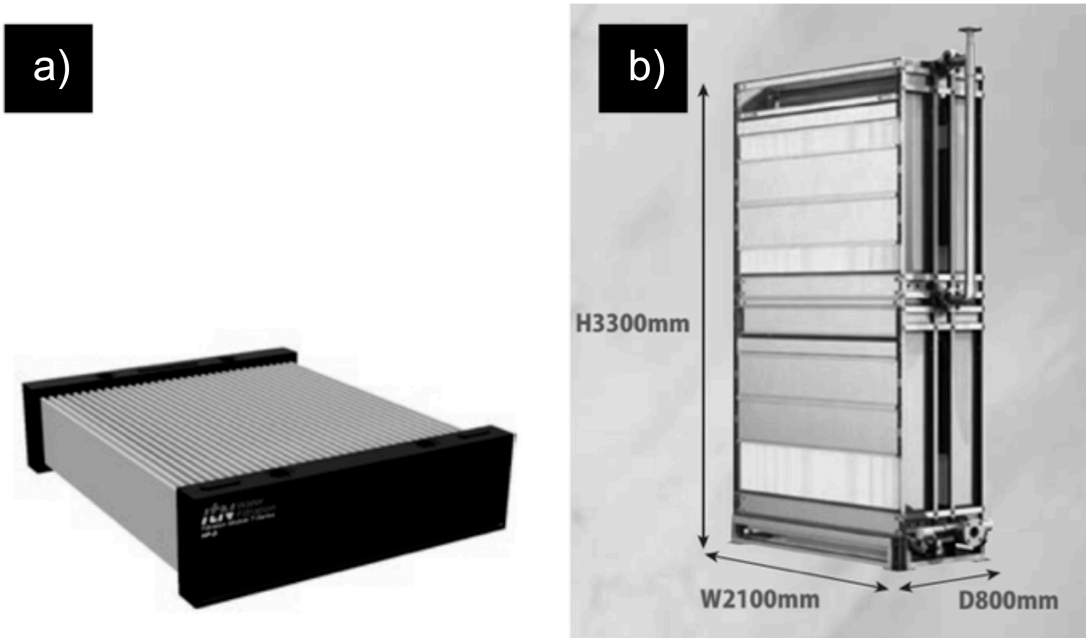


Figure 2.5 Product photograph of a ceramic flat sheet module from a), ItN Nanovation AG; and b), a ceramic flat sheet system from Meidensha Corporation [144]

2.2.5.3 Cylindrical membranes

Tubular membranes are often packed as a bundle inside a casing which could be a contained vessel or an open vessel, as shown in Figure 2.6. The feed solution may be fed though the centre of the tubular or monolith membranes, and the permeate is collected outside the tube in the module casing. This operating mode requires high operating flow rates and the pressure drop can be quite large and hence, the energy consumption is highest compared to the other module designs. However, due to the relatively large channel diameters of tubular and monolith membranes, they are suitable for feed streams with larger particles, and cleaning of these membranes is also more facile. The tubular or monolith membranes can also be packed and supported by a partly open housing support and operated by immersion into the feed solution, similar to the immersed flat sheet modules, offering similar advantages and disadvantages. The immersed tubular modules are commonly used in MBRs for larger scale applications and also for treating harsh feed streams.

Hollow fibre membranes can also be packed in a similar way in their modules, as shown in Figure 2.4. Ceramic hollow fibre membranes are generally packed together and immobilised at both ends and then placed in a cylindrical housing. The

fully contained module is more suited for small-scale applications, such as for domestic scale drinking water treatment. Hollow fibre modules can potentially offer a much higher packing density and form more compact systems, saving space and improving productivity. As shown in Table 2.1, the packing density offered by commercial ceramic hollow fibre modules is still not as competitive (502 m^2/m^3 offered by Media and Process Technology Inc) as some of the multi-channel tubular module designs (up to 782 m^2/m^3 offered by Ceramem® module from Veolia Water Ltd). This is mainly attributed to the relatively large ceramic hollow fibre outer diameters from most of the suppliers (3-4 mm from Table 2.1). Furthermore, their intrinsic brittleness makes them more difficult to be packed into bundles, as well as limiting their lengths. Hence cassette-style modules for ceramic hollow fibre membranes are not available, whereby the hollow fibres are supported at the top and bottom only and are immersed fully into the feed solution with no housing. In addition, the lack of open vessel designs for the hollow fibre membrane elements mean that their application for immersed MBR is still limited.

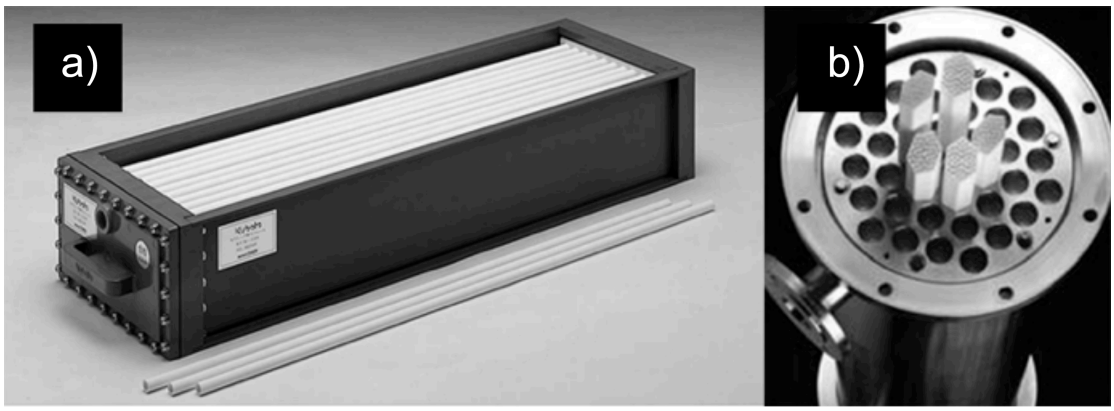


Figure 2.6 Product photograph a) of an immersed ceramic tubular membrane module from Kubota Corporation [145]; and b) a contained module from Pall Corporation [146]

2.2.5.4 Housing, sealing and operation

The membrane modules consist of the housing, sealing materials and the membrane. The type of housing used for the membrane varies depending on the membrane, module type, and operating configuration. For contained cylindrical membranes the membrane is packed and enclosed in a vessel, shown in Figure 2.7. For outside-in

feed configuration or immersed cylindrical membranes, the housing may have openings that expose certain areas of the membrane element. Kubota Corporation's Filcera® ceramic membrane filtration system uses a rectangular housing that is open at the upper surface (Figure 2.6a). Flat sheet ceramic membranes are normally sealed at the top and bottom to a permeate collector. They are then stacked together and supported by a stainless steel frame into modules such as the Meidensha Corporation's ceramic membrane unit, and ItN nanovation AG's CFM System® (Figure 2.5).

Typical module housing materials include stainless steel, titanium, and plastic. Stainless steel is most commonly used for its good chemical and thermal stability, as well as great robustness. Although plastic housing is a cheaper choice, it often limits the conditions within which the membranes can operate.



Figure 2.7 Product photograph of the CeraMem® contained module and housing from Veolia Water Ltd [112]

The type of seal used on the membranes varies depending on the membrane and module type. They are important as they prevent contaminant leakage into the permeate stream. Mostly O-rings and gaskets are used to cover the perimeter of the membrane ends where both the feed and permeates are exposed. The material used for sealing the membranes depends on the required operating conditions of the MF/UF, which will change depending on the application. Typical sealing material includes rubber, silicon, PTFE, and PVC.

There are many different module designs for the flat sheet and tubular (single and multi-channel) ceramic membranes. However, due to the much larger dimensions of the flat sheet and tubular elements, their packing density is still lower than the polymeric membrane modules offered, making them less competitive for large scale applications, or when space is limited in a treatment plant. Hollow fibre membrane modules have the potential to improve the packing density significantly, but most of the ones offered on the market have relatively large outer diameters, leading to lower packing densities. The commercially available hollow fibre modules are limited, for example, there are limited open-vessel modules and no cassette-style ceramic hollow fibre modules for large-scale immersion applications, and so limits their applications to small-scale MF/UF applications.

2.2.6 Fabrication techniques

The fabrication of ceramic membranes is generally a multi-step process, and can be broken up into 3 different stages: the preparation of the ceramic powder paste or suspension, the shaping of the ceramic powder into the desired goemetry, and then heat treatment which includes calcination and sintering [140]. After these main steps, additional layer deposition followed by further heat treatment steps can tailor the membrane selectivity as well as other membrane properties. The choice of method for each step depends on the desired membrane configuration, quality, morphology, mechanical and chemical stability, and the selectivity of the final membranes. However, the fabrication method should also be easy to replicate and economical without compromising the quality of the final membrane.

2.2.6.1 Ceramic powder paste and suspension preparation

The ceramic powder preparation stage processes the raw inorganic material into the shape and size distribution desired for the membrane fabrication. This can be in the form of milling or chemical particle preparation. Often, the ceramic powder is made into a paste or suspension for shape formation to be possible. During this step additives can also be added to the ceramic material. The choice of suspension

medium, additives, and powder are important in affecting the membrane microstructures and quality. Deflocculants or dispersants, often in the form of various fatty acids and esters, can be added to stabilize the ceramic particles in suspension, in order to achieve high particle loadings and continuously high quality ceramic membranes [140, 147-149]. Magnesium oxide has been used as a sintering additive to lower the sintering temperature required for the formation of alumina hollow fibre membranes via combined phase inversion and sintering method [150]. Other additives, such as the polymer binder is used to maintain the shape of the ceramic membrane precursor, and plasticizers can be used to increase flexibility and ease of handling of the suspensions, for tape casting or extrusion methods [151].

2.2.6.2 Shaping

The shaping step is the physical process whereby the ceramic material is transformed from a suspension or powder paste form into the membrane geometry. Methods that can create ceramic membranes and substrates include: pressing, tape casting, slip casting, extrusion, phase inversion, foam techniques, and leaching techniques.

Pressing is a simple and quick method for producing flat ceramic membranes [152-154]. A force is applied over an area of ceramic powder (varies from 10 MPa-100 MPa [155]) until the particles are consolidated. This method produces membranes of a symmetric structure, due to the uniform force applied across the area of ceramic material, and are commonly used for making disc membranes. Meanwhile, this method is not very flexible in fine-tuning microstructures and there is a limitation on the thickness to diameter ratio of the membrane that can be achieved. In addition, it is a batch fabrication process, and has been used primarily for making membranes to use in laboratories, rather than commercially.

The tape casting method is used for the formation of flat sheet ceramic membranes [156-158]. A tape cast suspension is first prepared with the ceramic material, a liquid dispersing medium, and organic additives to provide the suspension with pseudo-plastic behaviour. Then the suspension is transferred into a reservoir controlled by a blade that can be height adjusted over a mobile carrier film. Subsequently, the suspension film is dried in a controlled environment. Tape casting

is a more flexible method that can make flat sheet membranes as well as coating layers onto membrane supports.

Slip casting uses a porous mould to form the shape of the ceramic membrane [159, 160]. When the ceramic suspension is poured into the mould, the solvent is extracted into the pores of the mould due to the capillary force, leaving ceramic particles on the surface of the mould. Slip casting is commonly used to form tubular membranes with high surface quality, density, and uniformity. Important factors that affect the final quality of the membranes created via this method include slip density and viscosity.

Extrusion is a method popular for the fabrication of tubular, monolithic, and hollow fibre/capillary membranes [9, 161-164]. It is a process whereby an inorganic stiff paste is forced through an orifice of a designed shape and compacted by applying high pressure. The paste must have plastic properties to form and maintain the shape of the membrane precursors; hence additives are added to the ceramic powder. The paste is then forced through a die at high pressure (around 20 MPa) to produce hollow tubes.

Combined phase-inversion/sintering [65, 66, 116] is a relatively new method for fabricating microstructured ceramic hollow fibre membranes. Solvent-non-solvent exchange induced precipitation of the polymeric binder and micro-channelling phenomenon occur during the membrane fabrication, distinguishing this method from conventional ram-extrusion, and will be further introduced in Section 2.2.6.5.

2.2.6.3 Heat treatment

After the forming step, the ceramic membrane precursors are produced. They are then dried and treated with heat. This heat treatment step consists of three main steps [140]: presintering, thermolysis, and final sintering with the purpose of removing any components other than the ceramic material, to strengthen the membrane, and to consolidate the microstructure and dimensions of the final membrane.

Presintering occurs at around 200 °C. Presintering is used to remove any water from the membrane precursors, which may be in the form of water chemically bonded to the ceramic particle surfaces, or as water of crystallization within the inorganic phases. The thermolysis, or calcination step, is the process whereby all the organic

components in the membrane precursor are removed. The sintering stage is where the major changes to the porosity and pore size occur, the final shape of the ceramic membrane consolidated, and mechanical strength improved. In general, the higher the sintering temperature, the higher the mechanical strength but the porosity of the final membrane is lowered.

Important parameters that affect thermal stability of ceramic membranes are the sintering activity and phase transformation of the membrane material and the support [108]. During sintering, the ceramic material is kept at a certain temperature long enough for the material to approach its equilibrium structure. The final membrane structure can be maintained for temperatures up to 100-150 °C below the sintering temperature, which is normally extremely high (over 1000 °C) [151].

2.2.6.4 Layer deposition for composite membranes

Additional layer deposition can be used to alter or enhance the ceramic membrane properties, for example, to change the membrane selectivity, porosity, hydrophilicity, conductivity, permeability, bio-compatibility, etc. In order to form composite membranes, layer deposition methods are required to add additional layers onto a symmetric substrate. Each layer normally consists of ceramic particles of different sizes, to achieve a gradient pore structure across the membrane cross-section. Multiple layers are normally required to reach the desired selectivity at the end.

Dip or spin coating is the most commonly used method for layer deposition onto a support [156, 165, 166]. Dip coating method is when a support is dipped into and then withdrawn from a ceramic powder suspension. Upon withdrawal from the suspension, the liquid will be sucked into the support pores along with the ceramic particles due to the capillary forces, if they are small enough in size. Spin coating rotates the substrate while the suspension is deposited over the substrate surface.

Sol-gel method can be used to fabricate membranes with high selectivity with pores from 100 nm down to a few nanometres, and is commonly used to form ceramic ultrafiltration membranes [157, 167-171]. A colloidal (consists of alkoxide) or polymeric solution is first deposited over a membrane substrate, by means of dip coating, whilst it is being converted into a gel form by hydrolysis and condensation or

polymerisation. Afterwards, it is heat treated to form a thin and uniform skin over the membrane. There are many other coating techniques such as chemical vapour deposition (CVD), neutron sputtering, plasma, etc., and details of these can be found elsewhere [111, 140, 151].

2.2.6.5 Combined phase inversion and sintering technique

As described by the previous section, the traditional and common method for the production hollow fibre membranes is to use extrusion followed by sintering. However, this would give rise to symmetric membranes and additional layer deposition and heat treatment steps are required to produce the required selectivity, as shown in Figure 2.1b. An alternative and innovative method for producing ceramic hollow fibre membranes is the combined phase inversion and sintering technique [65, 66, 86, 116, 120, 134, 150, 172, 173]. It is a flexible technique that can produce both symmetric and a wide range of asymmetric ceramic membranes in one step for both flat sheet and hollow fibre geometries, as shown in Figure 2.1a and Figure 2.1c. Due to the presence of the large micro-channel structures, they can reduce mass transfer resistance to achieve permeation fluxes that are highly competitive to the membranes formed via the conventional methods.

A suspension consisting of ceramic particles and polymer binder in a solvent is first prepared, then through solvent-non-solvent exchange induced phase inversion of the polymer binder, the ceramic particles are immobilised in their desired geometry by casting (flat membrane), or spinning (hollow fibre membrane). This method can easily tailor and form membrane precursors with various specific morphologies. Then, similar to all the other ceramic fabrication methods, the membrane precursors undergo a heat treatment session (Section 2.2.5.3) to remove all the organics as well as consolidating the final membrane structure and mechanical strength.

The spinning process is achieved via tube-in-orifice spinnerets. These spinnerets can deliver simultaneous extrusions of the ceramic suspension, bore liquid, and any other components in separate layers with tailored thicknesses. Figure 2.8 is a schematic of a typical dual-layer spinneret for the spinning of single-layered ceramic hollow fibres. Here, two separated streams can be extruded simultaneously through

the spinneret, and once they leave the spinneret, they come into contact with one another, as well as with the external coagulation bath, whereby solvent and non-solvent exchange and phase inversion occurs. These spinnerets can be designed to simultaneously extrude multiple layers or multiple channels, and can be specifically tailored for a wide range of hollow fibres.

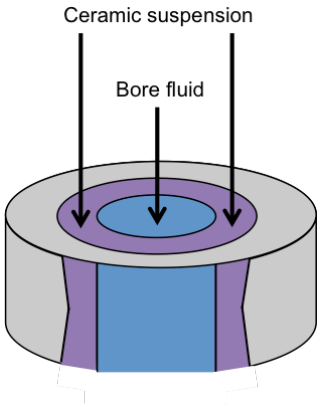


Figure 2.8 Schematic drawing of a dual-layer spinneret. The ceramic suspension and bore fluid are extruded simultaneously through the concentric orifices with no contact with one another until they leave the spinneret

Although the process of spinning ceramic hollow fibre membranes is similar to the spinning of polymeric ones, the rules and optimisation of the polymeric spinning system cannot be applied directly to the ceramic spinning process, due to the significantly different composition of the spinning suspension. The presence of a large amount of ceramic particles also changes the mechanisms behind the formation of the different membrane sub-structures. Two basic sub-structures have been achieved within the membrane cross-section: sponge-like denser structures, and micro-channels, which can be closed or open, as shown in Figure 2.9. The positioning and dimensions of these different sub-structures can be tailored mainly by changing the parameters during spinning.

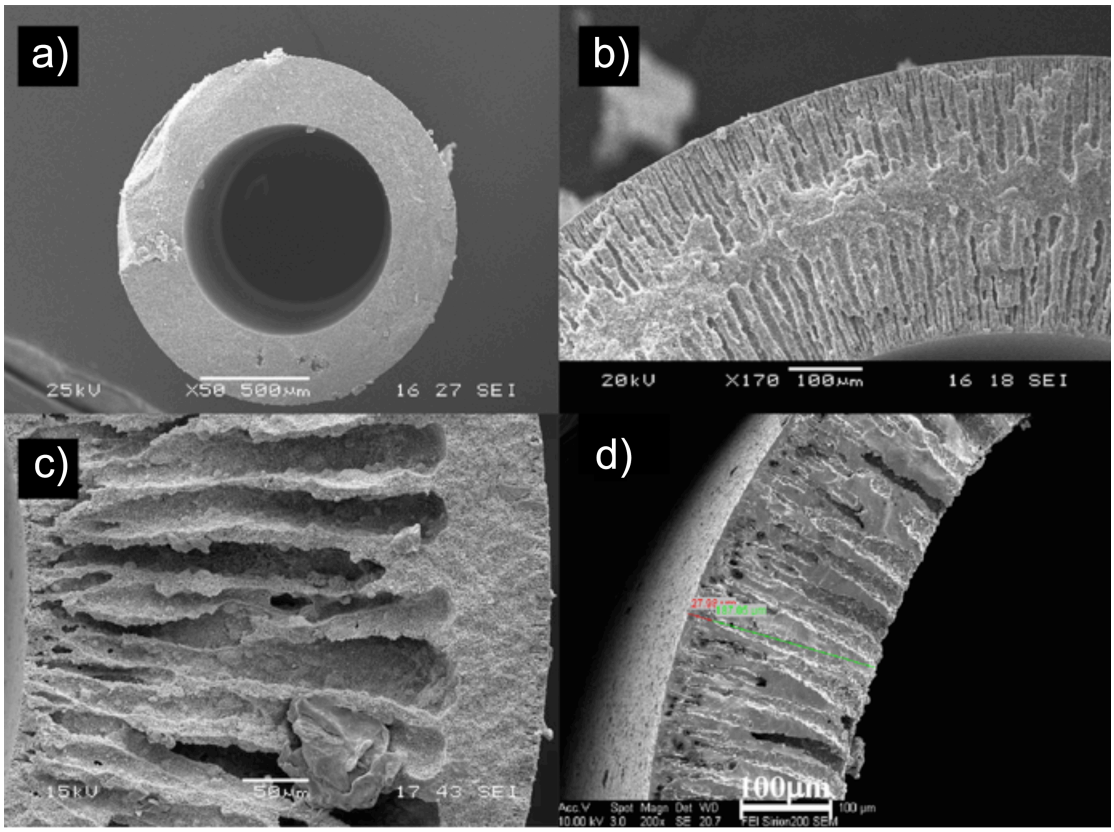


Figure 2.9. Scanning Electron Micrograph of the cross-section morphology of a), a symmetric alumina hollow fibre; and (b-d), different asymmetric alumina hollow fibres formed by combined phase inversion and sintering [86, 116, 127]

The combined phase inversion and sintering method was first introduced in the early 90s [42], and it was not until the early 2000s that more researchers embarked on developing this technique [66]. Initial studies looked mainly at the alumina suspension composition, to find the best formulation, and investigated the effects of alumina particle size, particle size distribution, alumina particle to polymer ratios, and sintering temperatures on the membrane structure and performance [65, 66]. Then, the research expanded to tailoring the membranes for expanded applications, such as gas separation [174, 175], multi-layered ceramic membranes, [67, 70] and other ceramic materials [176, 177]. The morphology was quite commonly studied, and the effects of various parameters on the morphology of these membranes from the literature is reviewed in the following section.

2.2.6.5.1 Micro-channel structures in the phase inversion ceramic membranes

The unique and flexible morphology of the ceramic membranes fabricated by the combined phase inversion and sintering technique is one of the key properties that gave rise to their broadened applications and improved performances. Here are the explanations of the terminology adopted for the different sub-structures used in this review. A common asymmetric ceramic membrane made via this method consists of two main components: finger-like structures and sponge-like structures (Figure 2.10), loosely like those typically found in polymeric membranes. The entire ceramic membrane scaffold consists of ceramic particles packed and sintered together. The structure at regions whereby ceramic particles are stacked on top of one another, forming a uniform porous structure, is named the sponge-like region. The gaps between the ceramic particles become the pores of the membrane, and the continuous layer of packed ceramic particles with the smallest pore size becomes the separation layer. Another type of structure commonly found in phase inversion membranes is the finger-like macrovoids. These are large empty spaces in the membrane that are isolated, and for polymeric membranes, mainly act to reduce the membrane's mechanical stability. In polymeric membranes they are undesirable, but in ceramic membranes, they are the component that can improve and offer potentially increased functionalities. They can be tailored and fabricated to be intensely packed, long, and cylindrical. Hence, in this review, they are not named finger-like macrovoids, but instead, denoted as micro-channels.

Higher performances are normally expected with these asymmetric membranes, as the effective membrane thickness can be much thinner than in symmetric membranes. Furthermore, these micro-channels can be potentially used to load functional materials, such as adsorbents or catalysts, forming highly compact systems. Therefore, the design and control of the micro-channels is highly important in order to tailor membranes specifically for enhanced performance. To begin with, a fundamental understanding of the formation mechanism is highly desired, and below are some of the theories that have been used to explain the formation of the micro-channels.

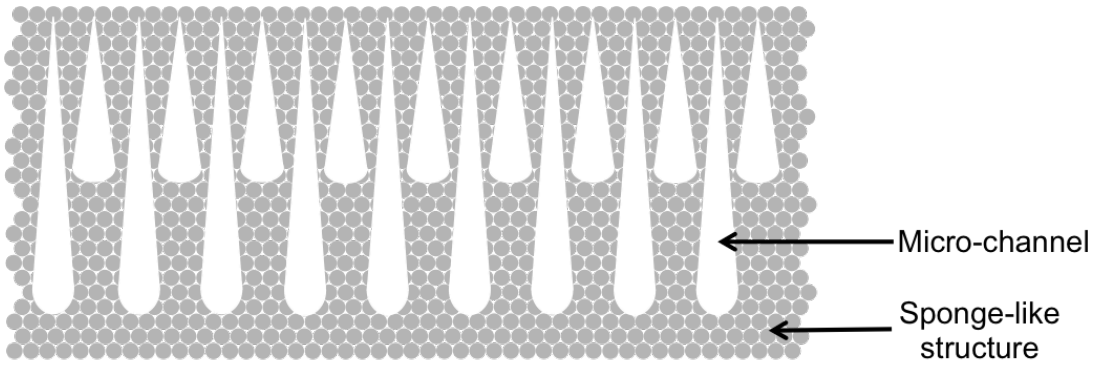


Figure 2.10 Schematic of the different sub-structures that can be found in ceramic membranes made via the combined phase inversion and sintering method

2.2.6.5.2 Fundamental Study on the formation of micro-channels

There is very little research available that looks at the fundamentals behind the formation process of the micro-channels in ceramic systems. Within the polymeric membrane research community, there is a wider range of theories available to explain the formation of the finger-like macrovoids. Possible origins of these structures are interfacial instabilities, which can arise from many different sources, such as: interfacial tension gradients (marangoni instability) [178], viscosity gradients (viscous fingering) [179], or density gradients (Rayleigh-Taylor Instability (RTI) [180-182], and so on.

It has been noticed that the micro-channels or finger-like macrovoids mostly have a regular and periodic placement in the membranes, which have therefore led researchers to connect them to periodical surface disturbing waves [183]. The theories that have been put forth used linear stability analysis to find the wavelengths most likely to grow into micro-channels from the surface disturbances [184]. These surface disturbing waves have been linked to various different sources, ranging from surface tension gradients (the Marangoni effect) [178], the difference in viscosity or density between two contact fluids [179, 182], or the gradient of solidification and shrinkage rate along the interface [185]. Frommer et al. provided some qualitative explanation using the Marangoni instability [186], which Ray et al. mentioned was unlikely to cause the finger-like structures, due to the slow speed of the finger growth caused by the Marangoni instability [183]. He proposed that the excess intermolecular potential is more likely to cause the growth of these fingers. In his study he derived the distance

between the longest fingers to be 4.2 times the membrane thickness. On the other hand, Addad and Panine suggested that a "diffusional shock" at the interface between the polymer solution and coagulation bath can lead to the growth of finger-like structures due to hydrodynamic instabilities, such as the Rayleigh-Taylor instability [187]. Although there is no consensus on the specific physical phenomenon that causes the formation of micro-channels, it can be agreed that they are generated by one or more interfacial instability between the ceramic suspension and the coagulant.

Although there is little research on the fundamentals behind the formation of micro-channels in ceramic systems, there are plenty of studies on the effect of suspension preparation and phase inversion process parameters on the ceramic membrane morphologies, and they are reviewed below.

2.2.6.6 Effect of Fabrication Parameters on Membrane Morphology

2.2.6.6.1 Effect of Ceramic Suspension Preparation Parameters

a) Effect of Ceramic Particle Size

Zhang et al. studied the effects of cordierite particle size on the hollow fibre membrane morphology formed by the combined phase inversion and sintering method [176]. It was observed that when the larger particle size (7.8 μm) was used, the morphology consisted of a macrovoid inner region and a thin sponge-like outer region. When smaller particles were used (1.6 μm), the membrane consisted of large enclosed micro-channel structures.

b) Effect of Non-solvent Additives

The presence of non-solvent additives in the ceramic suspension can dramatically affect the morphology of the inorganic membranes. The effect of suspension viscosity on the hollow fibre morphology was studied in more detail by Kingsbury, using water as a non-solvent additive in the ceramic suspension to increase suspension viscosity [116]. Overall, it was found that as the water content in the ceramic suspension was increased, the viscosity of the suspension also increased, and micro-channel length was reduced as a result. At a certain weight percentage of water, all of the micro-

channels can be eliminated. It was concluded that the formation of these enclosed micro-channel structures could be avoided if the suspension viscosity is above a certain threshold before non-solvent influx occurs [116].

Choi et al. studied the effects of using 1,4-dioxane in the ceramic suspension as a non-solvent additive on the morphology of the alumina hollow fibre membrane [150]. It was observed that a closely packed sponge-like structure was formed in place of the enclosed micro-channels.

2.2.6.6.2 Effect of Spinning Parameters

a) Effect of Air Gap

Kingsbury and Wang et al. studied the effect of air gap distance on membrane morphology [188, 189]. Results showed that micro-channel lengths from the shell side decreased as air gap is increased. During the time that the nascent fibre traveled through the air gap, micro-channels were already initiated from the lumen side, and grew towards the shell side in parallel to polymer precipitation from the lumen surface. Therefore, upon immersion into the coagulant bath, polymer precipitation from the shell side commenced and the micro-channel started to grow, but this growth was terminated shortly due to the micro-channels that have already grown and immobilised from the lumen side. The greater the air gap, the more time the micro-channels had to propagate from the lumen towards the shell side.

b) Effect of Bore Fluid Choice

Tan et al. controlled perovskite hollow fibre morphologies by using different bore fluids in a study [127]. They added NMP solvent to the bore fluid, which was water or ethanol in different weight percentages, and discovered that the denser separation layer at the lumen side reduces with increasing solvent content, and can be fully eliminated, leaving open micro-channels. This result was corroborated by Othman et al. [125].

c) Effect of Bore Fluid Flow Rate

Kingsbury et al. studied the effects of the internal coagulant flow rate on the morphology of hollow fibre membranes [86]. It was observed that as the internal coagulant flow rate is decreased, the thickness of the sponge-like region increased. At the lowest coagulant flow rate the sponge-like structure was seen to dominate the inner fibre surface, with isolated micro-channels within the sponge-like region. This was because at lower coagulant flow rates, the driving force was insufficient to overcome the interfacial tension and hence micro-channels were not formed. Increasing the internal coagulant flow rate encouraged the growth of micro-channels due to an increase in the interface velocity. It was also observed that the increase of the internal coagulant flow rate eliminated the formation of isolated voids [116].

d) Effect of Immersion Method

Wang et al. studied the effects of different immersion methods of the casting solution on the morphology of the flat sheet alumina membranes [189]. When the casting film was immersed slowly, the morphology consisted of a symmetric structure with no visible voids. When the casting film was immersed from sliding at a height, the structure was asymmetric with long micro-channels of different sizes. This highlighted the importance of an interface moving velocity and the presence of a critical moving velocity that initiated the micro-channel formation process. The microstructure of the top layer of the membrane immersed horizontally and slowly showed no evidence of polymers in the top layer, whereas when the flat sheet was slid from a height of 10 cm, one can see the network of fibrous polymer surrounding the tightly packed alumina particles.

Immersion time also had an affect on the final membrane morphology [189]. The flat sheet membrane that was immersed for 1 minute in the coagulant water showed no evidence of micro-channels whereas the membrane that was immersed for 5 minutes had much longer micro-channels. Water accumulation was observed on the membrane top surface after removing from the coagulation bath for short immersion times. This showed that the micro-channel formation process was faster than the phase inversion process. The one-minute immersion time in the coagulant was not enough for the shape of the micro-channels to be consolidated and reversal of the

micro-channels occurred. Therefore, the difference in micro-channel lengths represented the position of the phase inversion front.

e) Effect of External Coagulant Choice

Wang et al studied the effect of different external coagulants on the membrane morphology [189]. When the casting film was slid into the ethanol coagulation bath, much longer micro-channel lengths were observed compared to when combined NMP and water was used. Similar to the effect of bore liquid choice, this was explained by the difference in precipitation rates of the polymer solution.

2.2.6.6.3 Effect of Heat Treatment Parameters

It was observed by Kingsbury that the sponge-like region of alumina hollow fibre membranes densified after sintering whereas the micro-channels were retained, which was also agreed by Zhang et al. in cordierite hollow fibres [116, 176].

2.2.6.7 Ceramic membrane selective layer properties

The selective layer of the ceramic membrane is the layer of continuously stacked and sintered ceramic particles that provides the membrane with its separation function. For filtration processes the size of the voids between the ceramic particles (pore size) denotes the cut off of the membrane, and the amount of these voids affect the porosity and performance of the membrane. As mentioned in Section 2.2.2, in order to maximise the volumetric flux of the MF and UF membranes, structural parameters such as surface porosity should be maximised, pore size distribution as narrow as possible, and the membrane thickness minimised. This section reviews the studies on how various fabrication parameters can affect the selective layer properties of ceramic membranes. First, the different properties that are core to the selective property as well as membrane performance are described and explained.

2.2.6.7.1 Pore Size and Pore Size Distribution

Filtration through a porous membrane works by size exclusion and its effectiveness depends highly on the pore size of the membrane [1]. Therefore, the pore size determines the size from which the particles will be filtered out and the process application that the membrane falls into. For MF applications, the membranes are rated in micrometre units, and for UF applications the membranes are rated in terms of Molecular Weight Cut Off. The MWCO is the molecular weight of the macromolecule of which 90 % will be retained on the upstream side [190].

The pore size also plays an important role in determining the permeation rate through the membrane, as can be seen in Equation 2.1. A membrane's resistance to fluid flow depends on both the diameter of the smallest pores and the thickness of the active separation layer. In addition, a narrow pore distribution is desired in order to provide high selectivity.

2.2.6.7.2 Volumetric Porosity

Volumetric porosity or overall porosity, is the volume of air in the three dimensional membrane structures and it is usually given as a percentage of the membrane's total volume. It is generally independent to pore size and thickness, instead, depends on the ceramic/polymer ceramic suspension, spinning process and the thermal treatment.

2.2.6.7.3 Surface Porosity

Surface porosity is the fractional pore area, which is the ratio of the pore area to effective membrane area A_m multiplied by the number of pores, as described by Equation 2.2 [1]. Together with the effective membrane thickness, they are very important parameters that determine the membrane flux. Porous membranes should have a high enough number of pores for transporting mass but at the same time the lowest trans-membrane fluid resistance possible [177]. MF membranes exhibit a wide variation in surface porosity, ranging from 5 to 70 % but should be at least 35 % in order to reduce the ceramic membrane's resistance to fluid flow [177]. UF membranes have much lower surface porosity due to their much smaller pore sizes and are

normally in the range of 0.1 to 10 % for polymeric membranes, and 10 to 50 % for ceramic membranes [191].

$$\varepsilon = \frac{p_n \cdot \pi r^2}{A_m} \quad (2.2)$$

where A_m is the membrane area (m^2), and p_n the number of pores.

2.2.6.7.4 Effective Skin Thickness

The effective membrane thickness is an important factor in determining the membrane flux and resistance to fluid flow. It is desired for the membrane to be as thin as possible to reduce the resistance to fluid flow.

2.2.6.7.5 Surface Roughness

The surface roughness is an important factor in determining the thickness of the additional coating layers that can be attained on top. This is particularly significant in applications where the ceramic membrane acts as a porous support. In addition, surface roughness can also affect the fouling tendency of the ceramic membranes during MF/UF applications. Microscopic roughness on the surface of the membranes increases the surface area and thus increases the area available for adsorption. It also deteriorates the hydrodynamics near the surface thus increases the likelihood of concentration polarization [191]. Many factors such as: ceramic powder particle size, sintering temperature, and sintering time can affect the surface roughness of the final membrane substrate [140].

Similarly to membrane morphology, many different factors affect the surface microstructure of the final inorganic membrane across the entire membrane fabrication process. The following section reviews the different factors that affect the surface membrane properties.

2.2.6.7.6 Effect of Ceramic Suspension Preparation Parameters on surface properties

a) Effect of Ceramic Particle loading

Choi et al. studied the effect of the alumina content in the ceramic suspension on the surface microstructure of the hollow fibre membrane formed by the combined phase inversion and sintering method [150]. At an alumina concentration of 65 wt.% (0.4 μm particle size), the pore size of the hollow fibre was 0.2 μm, porosity 40 %, and the pore size distribution was narrow and sharp. At alumina concentrations below 65 wt.% the pore size distribution was very broad.

b) Effect of Ceramic to Polymer Ratio

The weight ratio between ceramic to polymer is an important factor in determining the pore size and porosity of the hollow fibres. Tan et al. studied the effect of the Al_2O_3 to PES ratio on the alumina hollow fibre membrane performance and morphology [66]. It was found that as the Al_2O_3: PES ratio was increased, the pore size of the membrane increased but surface porosity was reduced. The pure water flux, porosity, and maximum pore size were found to have decreased as the Al_2O_3: PES ratio increased [173]. As the ratio was increased, the packing of the particles improved, and the interspace between the particles became smaller and the overall hollow fibre became more compact.

c) Effect of Ceramic Particle Size

Dobo et al. stated in his patent that using smaller sized inorganic particles in the ceramic suspension leads to the formation of smaller pores and defect free hollow fibre, regardless of the inorganic powder used [192]. Tan et al. also investigated the effect of using different sized alumina particles on the surface microstructure of the hollow fibre membranes, but found difficulties in forming spinnable ceramic suspensions with 0.01 μm only [66]. Porous alumina hollow fibre membranes have selectivity in the microfiltration range when 1 μm particles were used [116].

d) Effect of Particle Size Distribution

Liu et al. studied the effect of using different particle size and size distribution on the alumina hollow fibre membranes' surface microstructure [65]. Different ratios of 1, 0.3 and 0.01 μm alumina particles were used. The membrane formed from the 0.3 μm particles was much denser than when 1 μm particles were used, and as a result gas permeation decreased as the particle size of the alumina was decreased.

Tan et al. also studied the effect of ceramic particle size distribution on the surface microstructure of the membrane formed [66]. As the amount of 0.01 μm particles was increased in a blend with 1 μm particles, the maximum pore size decreased but average pore size increased, and indicated that blending led to increased uniformity. Membranes in the ultrafiltration range were made when mixtures of 0.01 and 1 μm particles were used. The results were matched the results of other studies [65, 173]. The same results were obtained when other ceramic materials were used, such as YSZ and cordierite [120, 176]. Also, it was observed that the surface and volumetric porosity increased as the weight percentage of 0.01 μm was increased. The phenomenon was not explained due to the complexity of the pore forming process, which occurred during coagulation and sintering. However, this was contrary to the theoretical prediction by Lu, whereby porosity is predicted to decrease when smaller particles are used alone [193].

e) Effect of non-solvent Additives in ceramic suspension

Kingsbury et al. studied the effects of adding different non-solvent additives in the ceramic suspension on the membrane surface microstructure.[188] Addition of water led to an increase in the proportion of sponge-like region in the hollow fibre. The peak pore size for the shell side was around 0.1 – 0.2 μm, representing the pores formed from the sponge-like region. The peak pore sizes on the lumen side formed by the entrances to the micro-channels were dramatically reduced (from 5 to 1 μm with water content of 2 and 4 wt.%, respectively). Further addition of water led to elimination of the peak representing the micro-channel entrances. When ethanol was added, the suspension viscosity underwent an initial decrease and only increased at higher ethanol concentrations. The membrane pore size was observed to have decreased significantly (down to 1 μm), despite the reduction in suspension viscosity.

This showed that polymer precipitation rate is also important in determining the pore size of the entrances to the micro-channels.

2.2.6.7.7 Effect of Phase Inversion Process Parameters on surface properties

The phase inversion step is the process whereby the pores of the membranes are initially formed. In ceramic hollow fibre membranes two types of pores have been observed: primary and secondary pores. The primary pores are formed by the spaces between the tightly packed ceramic spheres, whereas the secondary pores are larger and are entrances to the micro-channels in the membrane bulk, which can be partially open, or fully open. In addition, the presence of pores formed on the sides of micro-channels have been confirmed by Wang et al, which were believed to be formed by finger splitting during the micro-channel formation process and phase inversion [189].

a) Effect of Air Gap

Kingsbury did an extensive study on the effect of the membrane fabrication parameters on the surface microstructure of alumina hollow fibre membranes [188]. The pore sizes that were the entrances to micro-channels (lumen side) were found to fluctuate greatly when a lower bore flow rate was used (7 ml/min) and calcined at 1450 °C. When air gaps of 3, 7, 9, and 13 cm were used, the lumen side pore sizes were between 4 - 5 μm. For air gaps of 5 and 11 cm, the lumen side pore sizes were 0.4 and 1.3 μm, respectively. However, at 12 ml/min, the pore size of the micro-channel entrances stayed in the range of 7-9 μm.

b) Effect of Internal Precipitant Flow Rate

Kingsbury studied the effect of precipitation flow rate on the surface microstructure of alumina hollow fibre membranes [188]. Bore fluid flow rates of 3 - 15 ml/min were used with an air gap of 15 cm and were calcined at 1450 °C. The pores formed by the micro-channel entrances at the lumen side were found to increase considerably with increasing bore flow rate (from 1.2 μm with 6 ml/min to 9 μm with 15 ml/min). At a

bore fluid flow rate of 3 ml/min, there was insufficient driving force for the formation of micro-channels and therefore there were no pores from micro-channels observed.

c) Effect of Immersion Methods

Wang et al. studied the effect of different immersion methods of flat sheet membranes during casting on the microstructure of alumina flat sheet membranes [189]. When the membrane was immersed for 30 s, small packing pores between the alumina particles of the membrane precursor surface were observed. For the membrane immersed for 1 minute, bigger secondary pores were observed on the surface, believed to be the entrances to the micro-channels in the bulk membrane.

2.2.6.7.8 Effect of Thermal Treatment Parameters

The multi-stage heat treatment processing stage is when the most dramatic changes occur to the surface microstructure of the membrane. The sintering step is where the final shape, size, distribution and amount of pores are determined.

a) Sintering Mechanisms

The sintering process consists of three stages: the initial stage; the intermediate stage, and the final stage [194]. These different stages have different characteristics and features and occur at different sintering temperatures. During the initial stage, the predominant mass transport mechanism is diffusion. During this stage there is rapid interparticle neck growth, whereby the surface of particles are smoothened and porosity decreases slowly and interconnected open pores are rounded. The intermediate stage follows after the pores have reached their equilibrium shape and takes up most of the sintering process and can be affected by multiple mechanisms. Shrinkage occurs during this stage and the mean porosity decreases significantly and grain growth is slow. During the final stage the pores shrink continuously and may reach a limited size or be eliminated completely. The grains of much larger size disappear rapidly and pores within the larger grains shrink relatively slowly. The following section describes the observations made from literature in regards to the effect of sintering conditions on the membrane microstructure.

b) Effect of Sintering Temperature

Tan et al. found that as sintering temperature is increased, the maximum pore size is reduced, but the average pore size remained unchanged [66]. Therefore, increasing the sintering temperature encourages uniformity of the membrane pores, but at the same time both the surface and volumetric porosity undergo reductions. Liu et al. observed that pore quantity and pore size changed after sintering and they depend on sintering temperature, as well as the alumina particle size and the composition of the ceramic suspension [65].

Wang et al. observed that the pore quantity and size changed after sintering from SEM images, but the general structure was maintained [173]. Sintering temperatures between 1200 °C to 1600 °C were used on alumina. Both the pure water flux and porosity underwent a dramatic decrease as sintering was increased to 1400 °C, but from 1400 °C to 1600 °C, the rate of decrease was much slower. Maximum pore size was also found to decrease with increasing sintering temperature. At a sintering temperature of 1600 °C, the pure water flux, porosity, and maximum pore size of the final membrane was found to be 2398 $L/m^2.h$, 40.8 %, and 1.5 μm respectively. The final membrane fell under the performance range of a microfiltration membrane. The appropriate sintering temperature was suggested to be between 1400 °C and 1600 °C for alumina, but at least 1500 °C is required to achieve membranes with good mechanical strength.

Kingsbury also studied the effect of sintering temperature on the pore size distribution of alumina hollow fibre membranes fabricated with 15 cm air gap [188]. From mercury intrusion data it was found that a bimodal pore distribution exists, one representing the pores due to the sponge-like region, and the other for the pores that were the entrances to the micro-channels. The peak pore size from the sponge-like region increased from 0.12 μm to 0.18 μm when calcination temperature increased from 1200 to 1400 °C. Above 1500 °C the sponge-like region densified due to particle growth during sintering. Pore size increased whereas the porosity decreased for the pores at the shell side, and at 1500 °C, the extent of membrane shrinkage was sufficient to eliminate the voids. The pore size at the lumen side was observed to have increased by a small amount from 6 to 7 μm (1200 to 1600 °C). Although particle growth also occurred on the lumen side, the extent of shrinkage was insufficient to reduce the pore size significantly.

2.2.6.8 Mechanical Properties

It is important for the ceramic hollow fibre membranes to exhibit adequate mechanical strength for packing into a module without breakage, as well as to enable long-term and continuous operation. As mentioned in Section 2.2.3, a disadvantage of ceramic membranes is their brittleness. This section reviews the different factors that the mechanical strength of the ceramic membranes made via the combined phase inversion and sintering method depend on. Due to the asymmetric structure, hollow fibres made by this method generally have lower mechanical strengths when compared with the symmetric ceramic membranes. Commercially available alumina capillary membranes have bending strengths of up to 125 MPa [195]. Asymmetric alumina membranes made via combined phase inversion and sintering have reached bending strengths of 91.4 MPa (1550 °C) [196], which is noticeably lower. The mechanical stability of the membrane made via this method is affected by many different factors, such as the ceramic suspension, sintering conditions, and the membrane morphology. Below is a review of the literature available which studied the various fabrication parameters on membrane mechanical strength.

2.2.6.8.1 Effect of Suspension Particle Size Distribution

Increasing the packing of the alumina suspension by blending the particles of different sizes allowed for higher solid loadings of the suspension. Early on, Liu et al. studied the effects of different alumina powder size combinations in the suspension on the bending strength of the final membranes [65]. It was found that by adding smaller nano-sized alumina particles (mixture of 1.0, 0.3 0.01 μm) into the suspension, the 3-point bending strength increased from 76.1 MPa to 107 MPa at 1550 °C. Kingsbury also found similar results [188]. The difference in mechanical strength was greater at higher sintering temperatures. This is because adding smaller particles can improve the packing in the suspension, and hence there is improved contact between each particle during sintering.

2.2.6.8.2 Effect of reinforcing additives in ceramic suspension

Improving the mechanical stability of ceramics by reinforcement with fibres or particles have been commonly studied [197]. The presence of these whiskers or fibres can deflect cracks by acting as bridges between cracks. Commonly used materials for reinforcing ceramics are: silicon carbide, titanium carbide, carbon, carbon nanotubes, stainless steel, etc. In ceramic hollow fibres made via the combined phase inversion and sintering method, SiC nanofibres have been added to the membranes, which led to an improvement of 40 % in bending strength [198].

2.2.6.8.2 Effect of Membrane Morphology

Sponge-like structures provide higher mechanical strength than micro-channels. Therefore, by varying the ratio of micro-channels to sponge-like structures, the mechanical strength can be altered [116]. When the thickness of one of the sponge-like layer at the lumen side was reduced [127], the bending strength decreased significantly as well, and when this sponge-like layer was eliminated completely, the bending strength of LSCF membranes dropped from around 150 MPa to 115 MPa.

2.2.6.8.3 Effect of Sintering Temperature

Sintering temperature is the most important factor that determines the mechanical strength of the final hollow fibre membrane. During the first step of sintering, surface and grain boundary diffusion causes the formation of grain boundaries, and surface of the particles in the particle compact smoothens. Strong interconnected porous microstructure forms and mechanical stability is increased [155]. Then, at higher temperatures, grain growth will occur, during which larger grains will grow by consuming the surrounding smaller grains. During this stage, the mean pore size will increase whereas porosity decreases.

Wang et al. studied the effect of sintering temperature on the final alumina hollow fibre properties [173]. It was observed from cross-sectional SEM images that the alumina particles become more and more compact with increasing sintering

temperature, and suggested that the higher sintering temperature must be maintained in order to produce membranes with good mechanical strength and permeability. An appropriate sintering temperature of between 1400 °C and 1600 °C was recommended. This is because the fusion and bonding of particles that is essential to increasing membrane strength occurred at high temperatures. A similar trend has been observed with other ceramic materials [138, 177]. Liu et al. tested a range of sintering temperatures from 1500 °C to 1600 °C and the bending strength increased from 48.6 MPa to 182.4 MPa [65].

However, a compromise always has to be made between the porosity and mechanical strength when a high sintering temperature is involved. A study suggested the use of a controlled sintering process by using PESf as not just a polymer binder, but also a pore structure "stabilizer" [199]. By thermally treating the membrane precursors, the PESf is not completely removed during the first stage of heat treatment. Instead, some of the PESf is converted to carbon at 1450 °C in an environment devoid of oxygen, which allows mechanical strengthening of the alumina membranes without losing significant porosity.

2.2.7 Ceramic membrane materials

The combined phase inversion and sintering technique has been successfully applied to a wide range of ceramics as well as metals with a range of different pore sizes [65, 138, 176, 200-202]. The common ceramic materials such as alumina, titania [203], and zirconia [68] have been used to make ceramic hollow fibre membranes via this fabrication method. Different materials were studied in effort to expand and cater to new application needs, as well as to negate current bottlenecks. Titania membranes have been fabricated mainly due to their photocatalytic properties, and can be used to perform simultaneous physical separation and photocatalytic oxidation to treat wastewater [203]. YSZ was used to produce high mechanical strength hollow fibre membranes, due to their intrinsic hardness [69, 177], and have expanded applications as the electrolyte material for solid oxide fuel cells and ceramic support for catalytic reactions, etc. SiC have been used in phase inversion to form highly mechanically robust and permeable hollow fibre membranes [204]. Also, SiC nanofibre reinforced alumina hollow fibre membranes were made to improve mechanical stability without

increasing the fabrication costs too much and had a maximum bending strength of up to 218 MPa with 5 wt.% SiC and sintering temperature of 1450 °C [198]. Perovskite membranes, on the other hand, were developed for their super conducting properties, for oxygen or hydrogen permeation in catalytic reactions [127, 205, 206]. Different sources for ceramic materials have also been looked at, such as using waste fly ash for its mullite content [207], cordierite [176] and kaolin [142].

An improved understanding of the fabrication parameters on the ceramic membrane morphology, performance, and properties has been achieved. The designing and engineering of the two types of sub-structures have led to distinctively different membrane morphologies (Figure 2.9), and generated a string of potential applications. These applications include: hollow fibre membrane micro-reactors, membrane contactors, solid-oxide fuel cells, gas separation, etc [60, 86, 141, 146, 208]. In particular, the morphology consisting of one sponge-like skin layer on top of a layer of micro-channels (Figure 2.9d) is expected to dramatically reduce the trans-membrane resistance to permeate flow. The single thin separation layer provides the membrane with its selectivity and the micro-channels can reduce the mass transfer resistance significantly. This morphology is expected to excel in aqueous MF/UF applications compared to the conventional composite asymmetric ceramic membranes.

On the other hand, the fundamental mechanisms behind the formation of the different sub-structures need further research efforts. A clearer understanding of the mechanisms behind the formation of the unique sub-structures would allow easier and more advanced designing of the different morphologies and engineering of the production process.

All in all, the combined phase inversion and sintering method can potentially open the opportunity for ceramic membranes in large-scale water and wastewater treatments, by offering a hugely reduced fabrication process and cost, and great flexibilities in microstructure design. However, further improvements are still required before this method can be fully commercialized, for example, to improve pure water permeation without sacrificing its mechanical strength, and to have a better fundamental understanding of the microstructure formation mechanisms to enable a reliable and reproducible fabrication process at large scales.

2.3 Ceramic membranes for Microfiltration and Ultrafiltration applications

Due to the high chemical, thermal stabilities, and robustness of ceramic membranes, they have been commonly applied in applications whereby polymeric membranes cannot be used. For example, ceramics can be used in harsh environments such as at high temperatures, in aggressive chemicals (solvents, highly acidic or caustic solutions), and oily water. Unlike polymeric membranes, ceramic membranes do not swell in solvent and can be treated with strong cleaning agents and sterilized at high temperatures, as well as withstanding high pressures for backwashing. All these advantages have made long-term flux stability possible for ceramic membranes, and encourage commercial scale usage [108]. Recently, ceramic membranes have also been garnering increasing attention for applications in milder operating conditions whereby polymeric membranes dominate, due to the increase in packing density of the membrane modules and reductions in capital costs.

2.3.1 Drinking water production

MF and UF membranes are used extensively in producing drinking water, and can handle both small- and large-scale capacities [209]. Small-scale MF/UF applications include transportable membrane systems, and in large scale applications MF/UF membranes can be used as standalone or hybrid systems in a water treatment process train. This market has been and is still currently dominated by polymeric membranes, but recently the incorporation of ceramic membranes for producing drinking water has been increasing [210-213]. Water sources used to produce drinking water can vary considerably from groundwater, lakes and rivers, municipal wastewater, to seawater. The final water that is safe to drink must fulfil standards set by the World Health Organisation or by the European Union, free of suspended solids, microorganisms, and harmful chemicals.

Small-scale ceramic membrane MF/UF systems can serve several purposes, such as to: improve the quality of tap water, reduce the volume or recycle household wastewater, provide safe drinking water in remote areas with limited resources such

as during camping or hiking, and provide safe drinking water in developing nations or during humanitarian crises.

To produce drinking water from surface water for a large community, or in other words, for municipal use, large systems are required. The water purification process will consist of a process train of different steps. As the design of the process depends on the feed quality and the final water quality, preparing drinking water from surface water is much more expensive as it requires more purification steps. A typical process train for purifying surface water consists of: a prefiltration unit, addition of chemicals, natural filtration, disinfection, fine filtration, and preservation and storage. Ceramic MF/UF membrane units may be used to replace conventional particle removal units such as coagulation and sedimentation, as well as disinfection unit(s). Furthermore, the ability to reject microorganisms, bacteria, and viruses can reduce the amount of chemicals required to be added to drinking water, overall saving considerable space. For the production of drinking water from seawater, ceramic MF/UF units may be used to provide pretreatment to reverse osmosis.

Studies in literature have shown that ceramic MF/UF membranes alone can provide permeate turbidity low enough for drinking standards, as well as being effective in removing microorganisms, organic matter, and disinfection by-product (DBP) precursors [210, 211, 214]. Due to the hydrophilic and inorganic characters of the ceramic membranes, they are less affected by organic fouling when compared to polymeric membranes [215]. However, high turbidity water (up to 80 NTU) can lead to membrane fouling and significant permeate flux declination, which can be recovered via chemical cleaning. The membrane pore size also appears to affect the rate of flux decline, as Harman et al. suggested that the smaller 4 nm pore size membrane fouls mainly by the formation of a cake layer, whereas pore clogging may dominate in the larger 10 nm pore size membrane [214].

To minimise the effect of fouling, much research has been carried out to analyse the performance of hybrid ceramic membrane systems, such as the combination of ceramic membrane MF/UF with activated carbon for natural organic matter (NOM) removal [216-219], coagulation for reducing organics and viruses [55, 220-222], photocatalytic reactions [223-225], and ozonation to remove NOM [226, 227] and subsequent formation of DBPs [228]. The use of the coagulation and MF/UF hybrid system is preferred from an economic point of view.

2.3.2 Municipal wastewater/sewage treatment

The treatment and recycling of municipal wastewater is common and a highly important part of today's water management. Municipal wastewater consists of household, commercial and institutional wastewater. A typical sewage treatment plant consists of the following steps: pretreatment for the removal of large and heavy debris, followed by primary treatment, used to remove the suspended inorganic and some organic particles, then secondary treatment for the biological conversion of dissolved and colloidal organics into biomass and then tertiary treatment for the further removal of suspended solids or nutrients and disinfection.

MF/UF can be incorporated in the treatment train as standalone processes or combined with the activated sludge process to form hybrid systems such as the membrane bioreactor (MBR). This can reduce the steps in secondary and tertiary treatment, for example, eliminating the need for sedimentation and secondary disinfection, saving space as well as reducing wastes such as disinfection by-products (DBPs) that need to be treated and disposed of. Ceramic membranes can be used to replace the traditional polymeric membranes for sewage treatment as the quick fouling of the polymeric membranes limits them to shorter operating lifetimes. They can be cleaned under harsher cleaning conditions and therefore offer longer and more reliable operation, as well as less servicing and maintenance, reducing long term operating costs. The flat sheet and cylindrical membrane elements are suitable to be combined with MBRs and the modules can be operated in the immersed mode or as a separate external unit. The immersed mode consists of the membrane module immersed in the aeration basin, and permeate is extracted via suctioning. The external configuration consists of pumping the mixed liquor at high pressure through the membrane from one surface. Due to the higher trans-membrane pressure required for the external configuration, their permeate flux is also generally higher [229]. However, the energy and space consumption of the immersed configuration tends to be lower, making them more suited for large-scale wastewater treatments.

Many studies have been carried out to analyse the effectiveness of ceramic MBR systems for treating municipal wastewater [230-233]. Xing et al. [104] looked at using external cross-flow ceramic ultrafiltration membrane bioreactor for urban wastewater reclamation. The system provided a high removal efficiency, removing carbon oxygen demand (COD) of an average of 97 % and the reclaimed water could

be reused directly for municipal or industrial purposes after additional treatment [230]. The lab-scale immersed ceramic membrane bioreactor has offered COD removal of more than 92 % during the course of a prolonged sludge retention time (142 days) for the treatment of simulated high strength wastewater (consisting of glucose and protein) [234]. Using longer sludge retention times can reduce the amount of sludge produced and cut down the cost of sludge treatment.

Fouling was found to be mainly affected by the membrane's microstructure, surface roughness and pore sizes in immersed ceramic bioreactor systems [235]. The ceramic membrane with the roughest surface and largest pore size (0.3 μm) has the highest fouling potential whereas the membrane with the smoothest surface and smallest pore size (0.08 μm) fouls the least. Using air sparging has been found to be an effective, simple and economical method to improve permeate flux and reduce concentration polarisation and fouling in external-loop air lift ceramic membrane bioreactors and the immersed ceramic membrane bioreactor [233, 234, 236]. Anaerobic membrane bioreactors may have lower energy consumptions [237]. However, inorganic fouling in anaerobic membrane bioreactors by struvite has been observed in ceramic membranes [238] and requires periodic alkaline backflushing to recover the permeate flux.

2.3.3 Industrial wastewater treatment

The composition of industrial wastewater varies dramatically across the industries, and the choice of membrane technology will vary according to the contaminants. Due to increasingly stringent regulations on waste discharge and the increasing costs of clean water, industries are more motivated on treating and recycling wastewater, which can potentially save significant amounts of the operating costs.

Typical contaminants in industrial wastewater are: suspended solids, particulates, colloids, bacteria and viruses, dissolved inorganics such as heavy metals, salts, nuclear wastes, acids or alkalis, volatile organics such as aromatics, aliphatics, alcohols, halogenated hydrocarbons and non-volatile organics such as phenolics, polyaromatic compounds, pesticides, insecticides, surfactants and dyes. Similar to sewage treatment, MBRs are a popular treatment unit in the treatment train. Upstream and downstream treatment units will vary depending on the desired quality of the final

effluent (ultra pure water, process water, etc). Ceramic MBRs are commonly used for small-scale treatment of high strength industrial wastewater, as they are more robust, stable, and reliable.

2.3.4 Produced water

Produced water is the largest waste stream generated from oil and gas operations. MF/UF is a promising technology to use as one of the units to treat produced water, as it is a low energy consumption process and can cut down the amount of harsh and expensive chemicals required to treat the wastewater. Polymeric membranes have been commonly used to remove organic contaminants as well as suspended particles prior to desalination so that the water can be reused. However, as the feed has a high composition of organic contaminants, oil, and grease, the polymeric membranes can be degraded and fouled quite easily, requiring regular replacements. Ceramic membranes offer higher stability in such conditions and may prolong the lifetime of the membrane and can also be cleaned more easily.

Many studies have been carried out to investigate the performance of ceramic membranes in oil/water treatments in laboratory or pilot-scale [84, 239-241]. Studies showed that the using MF/UF ceramic membranes can give permeate streams of very high quality, with less than 6 ppm total hydrocarbons, and perform better than polymeric membranes. However, an important limitation is the permeate flux decline due to fouling by waxes and asphaltenes. Backwashing was found to be a useful cleaning method to prevent the permeate flux decline [242].

2.3.5 Food and beverage industries

Microfiltration and ultrafiltration are important processes in the food and beverage industries. They can be used to achieve clarification, sterilisation, concentration, and purification of the final product in place multiple traditional process units. For the diary industry MF can be used to clarify the cheese whey [243], concentrating and defatting milk as well as sterilising it by rejecting microorganisms [244]. In the sugar refining and beverages industry, MF and UF membranes are used to clarify the products such as maple syrup, wine, beer, juices, and vinegar [245-250]. Wastewater

generated in these industries can also be recycled with the help of MF/UF membranes in order to save operating costs. Ceramic porous MF/UF membranes have demonstrated success in the food and beverage industries, offering superior long-term performance in these applications over polymeric membranes.

2.3.6 Commercial ceramic applications

Ceramic membranes have been implemented commercially in the industries mentioned in Section 2.3.1 to 2.3.5 for the treatment of aqueous feeds. In terms of producing drinking water, there are far fewer ceramic membrane drinking production systems than polymeric ones, mainly due to their high capital costs. However, Veolia Water Ltd has developed a mobile ceramic UF system for providing emergency drinking water [140, 251]. The system consists of a treatment train in the order of coagulation, adsorption, prefiltration, ultrafiltration using ceramic monolith elements, and UV and chlorination disinfection, providing up to 360 m^3/day permeate flow fit for drinking purposes.

For large-scale drinking water production the cost of ceramic membranes can be somewhat recuperated by their reliable performance and long operating lifetimes, for example, a ceramic MF system by Metawater Co., Ltd has been operating for 15 years [252]. Metawater Co., Ltd's systems typically consist of coagulation, dead-end microfiltration using ceramic monolith elements, followed by disinfection with chlorine, and has the treatment capacity of between 1,000 to 100,000 m^3/day for the treatment of clear raw water.

Due to the superior stability and operating lifetimes of ceramic MF/UF membranes, they can also be used as a pretreatment step prior to reverse osmosis for desalination. A drinking water plant in Qassim replaced their polymeric UF pretreatment membranes with ceramic flat sheet membranes, which has reduced the membrane replacement frequency dramatically and has a treatment capacity of 42,000 m^3/day [253].

For the treatment of municipal wastewater or sewage, the performance of ceramic MBRs are highly competitive compared to the polymeric systems. Similar to the drinking water production plants, implementation of ceramic membranes is mainly limited by their high cost. There are examples of commercial ceramic MBR

systems being implemented in small-scale wastewater treatments, such as in a school and an airport by Likuid Nanotek [148]. They use external cross-flow configuration to treat domestic wastewater with capacities ranging from 38 to 50 m^3/day and the permeate flux is recovered solely by periodic chemical cleaning. For larger-scale wastewater treatments the ceramic immersed MBR is more commonly used, for example, ItN Nanovation AG has installed the immersed ceramic flat sheet membrane modules with a capacity to treat 150 and 1,300 m^3/day of sewage feed in two different sewage treatment plants [149, 150]. No membrane servicing or maintenance has been required since operation began in 2011 for one of the plants, and chemical cleaning is used once a year (oxidant and chelating agent) to maintain the permeation flux.

Ceramic membranes have found more frequent uses in the treatment of industrial wastewater, as they are normally more challenging to treat. Examples of ceramic MBRs include an external MBR using ceramic tubular membranes from Likuid Nanotech to treat industrial waste of between 3 to 300 m^3/day, which has been commercially used in an olive oil, wine and narcotics production plants. For all of their ceramic MBRs, the quality of the final effluent is clean enough to be directly discharged [148]. Another application includes the ceramic MBR installed for treatment and recycling of up to 1,400 m^3/day of highly pigmented wastewater by Pall Corporation [151]. Complete retention of the insoluble pigments is achieved using the monolith ceramic membranes running in external configuration, and up to 50 % of the wastewater can be recycled. A larger-scale ceramic MBR has been scheduled for installation in a demonstration plant by Meidensha Corporation to treat and recycle up to 4,550 m^3/day of industrial wastewater by combining the upflow anaerobic sludge blanket technology with the 0.1 μm alumina flat sheet MBR system [254].

Commercial operations of ceramic membranes in produced water treatment are much more limited, compared to other application areas such as the food and beverage industry and industrial wastewater treatment. For treatment of produced water, the ceramic membranes typically run in cross-flow configuration [255]. An example is the full-scale facility in Colorado, which uses ceramic membranes as one of the units to treat oily wastewater [153]. The process train consists of dissolved air floatation, pre-filtration, ceramic microfiltration, activated carbon adsorption and then the water is supplied to a reverse osmosis plant, providing municipal drinking water. In addition, Veolia Water Ltd has developed a system consisting of ceramic monolith membranes to treat produced water, which has so far been installed at 60 locations

[154]. Their typical performance includes removal of 98.7 % turbidity and effluent has less than 1 ppm oil and grease [155][151][154][158]. Furthermore, a ceramic (SiC) membrane module will be installed for commercial use in Columbia and Venezuela, after the trial period offered consistent reductions of oil concentration from 20 – 100 ppm to less than 5 ppm [256].

Ceramic membranes are most commonly used in the food and beverage industry [244]. One commercial system for the removal of bacteria and spores from milk using MF is the Tetra Alcross® Bactocatch. The raw milk is first separated into skim milk and cream, then the former undergoes microfiltration leaving the concentration of bacteria in the permeate to be less than 0.5 % of the original value [257]. Ceramic membranes were also chosen and installed by Atech Innovations gmbh over polymeric membranes in a commercial citrus fruit juice production plant due to their high performance as well as resistance to essential oils from the fruit skins. Another commercialisation includes the use of tubular ceramic monolith membranes at high velocity cross-flow configuration in a glucose production plant to minimise gel layer formation, and is able to produce 180 m^3/day of glucose [258].

Ceramic MF/UF membranes have been used across a wide range of different applications involving water and wastewater treatment. They are most commonly used in the food and beverage industry and the treatment small-scale industrial wastewater. Laboratory, pilot and some commercial case studies have shown potential and advantages of using ceramic membranes for large-scale municipal wastewater treatment and the provision of safe drinking water. Due to the many benefits offered by ceramic membranes, their global incorporation into more drinking water treatment plants is anticipated. Promising developments include the installation of ceramic flat sheet membranes from ItN Nanovation AG in Saudi Arabia to pretreat seawater in 2013 [259]. In addition, three pilot plants using ceramic membrane hybrid systems with suspended ion exchange and ozone for drinking water treatment plants will be installed in the United Kingdom, Australia and Singapore by PWN Technologies [147]. The incorporation of ceramic membranes in MBRs also clearly offers many advantages such as ease of maintenance and long-term reliability. High capital membrane costs along with the energy consumption by continuous aeration contributes to a large proportion of the MBR's operating costs, and both deter the growth of ceramic MBRs for large-scale sewage treatment. Therefore, further research and optimisation of the immersed membrane bioreactor will be anticipated to

widen the use of ceramic membranes. The main overriding limitation to the commercial implementation of ceramic membranes for most large-scale water treatments is their high capital cost, despite their overall longer lifetimes and ease of maintenance.

2.3.7 Emerging research areas related to porous ceramic membranes

In the past 20 years, increasing attention has been paid to the formation of synergetic systems, known as integrated membrane hybrid systems. This is the combination of multiple processes into one system to perform multiple tasks simultaneously, with improved performance when compared with using any one of the technologies by themselves.

Much of the recent research efforts on ceramic membrane synergetic technologies have circled around the integration of functional nanoparticles with membranes. The various nanoparticles can be mainly categorised into sorbents and catalysts, and they work to expand the functionality of the membranes, making the membrane systems much more powerful. In terms of sorbents, a few of the state-of-the-art materials include: carbanaceous materials such as carbon nanotubes and graphene, zeolites, metal organic frameworks, amine solid sorbents, silica sorbents, etc. Photocatalytic nanoparticles include titania and graphene.

Carbonaceous sorbents have been investigated extensively on ceramic substrates. Carbon nanotubes have high surface area, thermal and electrical conductivity, and great mechanical strength, and have exhibited extremely high gas and water permeation [260-262]. In water treatment applications, they have been effective in removing a range of organic contaminants, such as bacteria, phenol, and dyes through adsorption [263, 264]. Their main drawbacks today are the high cost and complicated preparation processes for CNTs, which make them very difficult to produce on a larger scale. Similarly, graphene and its derivatives, such as graphene oxide, have shown to have both high selectivity and good fluxes for gas [265]. They have potential to be applied in nanofiltration, pervaporation, and gas separation but are unstable in the dry state on ceramic hollow fibre substrates. Research on composite graphene-ceramic membranes is still at an early stage and attention is

focused on improving the fabrication process, and in particular, for forming defect free, thin, and air-stable graphene oxide composite layers [98, 100, 266, 267].

Zeolite-coated ceramic membranes have been fabricated that can achieve high fluxes similar to those of ultrafiltration membranes, with increased selectivity comparable to nanofiltration and reverse osmosis processes [268]. The zeolites are coated on top of the ceramic membranes as a thin layer and have been studied to treat wastewater and brackish water for reverse osmosis desalination [269, 270]. They have been more commonly used in applications such as pervaporation and gas separation [271, 272]. Current limitations with zeolite composite membranes are low fluxes due to the thick zeolite membrane layer, high cost of the ceramic membrane support, as well as difficulty to up-scale.

In the past decade, porous metal-organic-frameworks (MOFs) have been becoming increasingly popular as a research topic. They have exhibited powerful adsorption capabilities, can be customised, and also be synthesised under milder conditions. In terms of water treatment, there is a study which used a water-stable UiO-66 polycrystalline membrane on top of ceramic substrates in potential desalination applications with very promising results [273]. There are far more studies on MOF-integrated ceramic membranes in gas separation and pervaporation [274-276]. Existing challenges include developing water stable MOFs, and the practical application of thin-film MOF membranes is still a considerable distance away due to the expensive, time consuming, and low-yield MOF synthesis methods.

On the other hand, titania, zinc oxide, and ferric oxide have been applied to a range of ceramic membranes, whereby they can be coated as an additional functional layer on top of the membranes to photocatalyse organic components in wastewater [268]. Graphene oxide has also been combined with titania to form composites for photocatalysis, which can perform in both near-UV/Vis and visible light irradiation [277]. Silver particles have been used to mitigate biofouling during filtration processes [278, 279].

Straying away from water treatment applications, catalytic nanoparticles have also been used with ceramic membranes to form membrane reactors. For the common symmetric hollow fibre reactors, catalysts are layered on the membrane surface by solution technologies, such as sol-gel and impregnation [280, 281]. Dual-layer ceramic membranes have also been fabricated through co-extrusion and co-sintering for partial oxidation of methane as well as micro-tubular solid oxide fuel cells [259,

282, 283]. There are also a few studies that dispersed the catalyst into the membrane micro-channels open from the lumen side to form a microstructured catalytic hollow fibre reactor for methane steam reforming with improved productivity rates [284], and for oxidative coupling of methane with increased yield [285]. The micro-channels offer additional volumes whereby catalysts can be deposited.

One of the main challenges that currently exist is the difficulty in immobilising nanoparticles in ceramic membranes. Currently, almost all of the related studies have applied the nanoparticles as an additional layer on the ceramic support structures, using methods such as sol-gel, dip coating [165, 286, 287], electrophorectic deposition [288, 289], and chemical vapour deposition [290], etc. Existing challenges include ensuring that the membrane layers are defect free, continuous, and as thin as possible. Furthermore, the lower packing densities of ceramic membranes, as well as high substrate costs have hindered their larger-scale industrial uses.

2.4 Prospects and challenges

From a technical viewpoint, the outstanding robustness and integrity of ceramic membranes have secured their positions in dealing with the wastewater systems where at least an aggressive environment is involved, and contribute to a sustainable and strong growth towards wider applications. Technical innovations in promoting separation performance and engineering designs keep driving the development of ceramic membrane products towards an application-orientated pattern. In particular, new membrane fabrication techniques such as the combined phase inversion and sintering method is expected to see wider applications in membrane production facilities. They offer a much simpler fabrication cycle and can make highly microstructurally varied membrane morphologies that can be tailored according to the application. In terms of membrane design, the presence of hollow fibre membranes is expected to grow in the ceramic membrane market, to offer much greater treatment capacities for larger scale applications. The potential of a wider range of ceramic materials other than the commonly used alumina membranes and membrane substrates, as well as membrane hybrid systems, are also expected. In terms of applications, there is a trend in increasing use of ceramic membranes for larger-scale,

wastewater treatments, especially in MBRs, as the cost of ceramic membranes is reduced. Anticipated cheaper ceramic membrane prices combined with higher packing densities of hollow fibre configuration will increase applications in municipalities, and more space-efficient module designs, especially for hollow fibre membranes are expected to penetrate the market to meet the higher demands.

The widespread use of ceramic MF/UF membranes in water treatments is still limited by many challenges. A key challenge is to reduce the capital cost of ceramic membranes, which can be met by reducing the steps in the fabrication process and lowering the sintering temperature. The emergence of cheaper fabrication processes, such as the combined phase inversion and sintering method, can potentially reduce the fabrication costs of ceramic membranes. The performance of the porous membranes formed by this method needs to be improved so that both good mechanical strength and high porosity can be achieved simultaneously. Improved fundamental understanding of the formation mechanisms of ceramic membrane microstructures can help to improve the reliability and reproducibility of the fabrication process, particularly useful when producing membranes from different ceramic materials and when production is scaled up. The micro-channels have been shown to improve the performance of membranes due to reduced mass transfer resistance, and can have already widened the ceramic membrane applications. So far, there is little research on how these micro-channels are formed as well as which factors affect their characteristics. In order to expand their applications, it would be highly useful to be able to design and control the micro-channel properties, such as their density, length, and shape, etc. Although the presence of micro-channels in the ceramic membranes can enhance performance and expand applications, their presence compromises the mechanical stability of the hollow fibres. This limits their potential to be industrialised and therefore research is required to improve this aspect of the membranes whilst maintaining the micro-channel structures.

References

1. Mulder, M., *Basic Principles of Membrane Technology*. 1996: Springer
2. Ruutenhuch, R., *Membrane Separation Systems - Recent Developments and Future Directions. Von R. W. Baker u.a. Noyes Data Corp., Park Ridge 1991.*

XV, 451 S., zahlr. Abb. u. Tab., geb., US-$64. Chemie Ingenieur Technik, 1992. **64**(6): p. 584-584.10.1002/cite.330640633

3. Hilal, N., A.F. Ismail, and C. Wright, *Membrane Fabrication*. 2015: CRC Press
4. Kimura, S., *Proceedings of the Symposium on Membrane TechnologyResearch and development of membrane technologies and their applications in Japan.* Desalination, 1985. **53**(1): p. 279-287.http://dx.doi.org/10.1016/0011-9164(85)85067-0
5. Merson, R., G. Paredes, and D. Hosaka, *Concentrating fruit juices by reverse osmosis*, in *Ultrafiltration membranes and applications*. 1980, Springer. p. 405-413
6. Finnigan, T. and P. SKUDDER, *Using ceramic microfiltration for the filtration of beer and recovery of extract.* Filtration & separation, 1989. **26**(3): p. 198-200
7. Gekas, V., B. Hallström, and G. Träg→rdh, *Proceedings of the Symposium on Membrane TechnologyFood and dairy applications: the state of the art.* Desalination, 1985. **53**(1): p. 95-127.http://dx.doi.org/10.1016/0011-9164(85)85054-2
8. Shackleton, R., *The application of ceramic membranes to the biological industries.* Journal of Chemical Technology & Biotechnology, 1987. **37**(1): p. 67-69.10.1002/jctb.280370108
9. Terpstra, R.A., B.C. Bonekamp, and H.J. Veringa, *Preparation, characterization and some properties of tubular alpha alumina ceramic membranes for microfiltration and as a support for ultrafiltration and gas separation membranes.* Desalination, 1988. **70**(1–3): p. 395-404.http://dx.doi.org/10.1016/0011-9164(88)85069-0
10. Niwa, M., et al., *Separation of gaseous mixtures of CO2 and CH4 using a composite microporous glass membrane on ceramic tubing.* Journal of Membrane Science, 1988. **39**(3): p. 301-314.http://dx.doi.org/10.1016/S0376-7388(00)80936-9
11. Wu, J., et al., *Dehydrogenation of ethylbenzene to styrene using commercial ceramic membranes as reactors.* Separation Science and Technology, 1990. **25**(13-15): p. 1489-1510

12. Becker, Y.L., et al., *Modelling of ethylbenzene dehydrogenation in a catalytic membrane reactor.* Journal of Membrane Science, 1993. **77**(2–3): p. 233-244.http://dx.doi.org/10.1016/0376-7388(93)85072-5
13. Kikuchi, E., S. Uemiya, and T. Matsuda, *Hydrogen production from methane steam reforming assisted by use of membrane reactor.* Studies in Surface Science and Catalysis, 1991. **61**: p. 509-515
14. 菊地英一, *Steam Reforming and Related Reactions in Hydrogen-permselective Membrane Reactor.* 石油学会誌, 1996. **39**(5): p. 301-313
15. Kikuchi, E., *Membrane reactor application to hydrogen production.* Catalysis Today, 2000. **56**(1–3): p. 97-101.http://dx.doi.org/10.1016/S0920-5861(99)00256-4
16. Balachandran, U., et al., *Development of dense ceramic membranes for methane conversion.* Studies in Surface Science and Catalysis, 1997. **107**: p. 409-414
17. Balachandran, U., et al., *Dense ceramic membranes for partial oxidation of methane to syngas.* Applied Catalysis A: General, 1995. **133**(1): p. 19-29.http://dx.doi.org/10.1016/0926-860X(95)00159-X
18. Santos, A., et al., *Catalytic partial oxidation of methane to synthesis gas in a ceramic membrane reactor*. Vol. 30. 189-199.10.1007/bf00813685
19. Uemiya, S., T. Matsuda, and E. Kikuchi, *Hydrogen permeable palladium-silver alloy membrane supported on porous ceramics.* Journal of Membrane Science, 1991. **56**(3): p. 315-325.http://dx.doi.org/10.1016/S0376-7388(00)83041-0
20. Jayaraman, V. and Y.S. Lin, *Synthesis and hydrogen permeation properties of ultrathin palladium-silver alloy membranes.* Journal of Membrane Science, 1995. **104**(3): p. 251-262.http://dx.doi.org/10.1016/0376-7388(95)00040-J
21. Lun Yeung, K. and A. Varma, *Novel preparation techniques for thin metal-ceramic composite membranes.* AIChE Journal, 1995. **41**(9): p. 2131-2139.10.1002/aic.690410912
22. Tsai, C.-Y., et al., *Dense Perovskite, La1-xA′ xFe1-yCoyO3- δ (A′ = Ba, Sr, Ca), Membrane Synthesis, Applications, and Characterization.* Journal of

the American Ceramic Society, 1998. **81**(6): p. 1437-1444.10.1111/j.1151-2916.1998.tb02501.x

23. Stiegel, G., *Mixed conducting ceramic membranes for gas separation and reaction.* Membrane Technology, 1999. **1999**(110): p. 5-7.http://dx.doi.org/10.1016/S0958-2118(00)80068-3
24. Balachandran, U., et al., *Development of mixed-conducting oxides for gas separation.* Solid State Ionics, 1998. **108**(1–4): p. 363-370.http://dx.doi.org/10.1016/S0167-2738(98)00064-2
25. Singhal, S.C., *Advances in solid oxide fuel cell technology.* Solid State Ionics, 2000. **135**(1–4): p. 305-313.http://dx.doi.org/10.1016/S0167-2738(00)00452-5
26. Yuasa, A., *Drinking water production by coagulation-microfiltration and adsorption-ultrafiltration.* Water Science and Technology, 1998. **37**(10): p. 135-146.http://dx.doi.org/10.1016/S0273-1223(98)00308-4
27. Tunesi, S. and M. Anderson, *Influence of chemisorption on the photodecomposition of salicylic acid and related compounds using suspended titania ceramic membranes.* The Journal of Physical Chemistry, 1991. **95**(8): p. 3399-3405.10.1021/j100161a078
28. Ahn, K.-H., J.-H. Song, and H.-Y. Cha, *Application of tubular ceramic membranes for reuse of wastewater from buildings.* Water Science and Technology, 1998. **38**(4–5): p. 373-382.http://dx.doi.org/10.1016/S0273-1223(98)00521-6
29. Gan, Q. and S.J. Allen, *Crossflow microfiltration of a primary sewage effluent–solids retention efficiency and flux enhancement.* Journal of Chemical Technology & Biotechnology, 1999. **74**(7): p. 693-699.10.1002/(SICI)1097-4660(199907)74:7<693::AID-JCTB93>3.0.CO;2-R
30. Yamagiwa, K., et al., *Activated sludge treatment of small-scale wastewater by a plunging liquid jet bioreactor with cross-flow filtration.* Bioresource Technology, 1991. **37**(3): p. 215-222.http://dx.doi.org/10.1016/0960-8524(91)90186-N
31. Beaubien, A., et al., *Design and operation of anaerobic membrane bioreactors: development of a filtration testing strategy.* Journal of Membrane

Science, 1996. **109**(2): p. 173-184.http://dx.doi.org/10.1016/0376-7388(95)00199-9

32. Tardieu, E., et al., *Hydrodynamic control of bioparticle deposition in a MBR applied to wastewater treatment.* Journal of Membrane Science, 1998. **147**(1): p. 1-12.http://dx.doi.org/10.1016/S0376-7388(98)00091-X
33. Defrance, L. and M.Y. Jaffrin, *Comparison between filtrations at fixed transmembrane pressure and fixed permeate flux: application to a membrane bioreactor used for wastewater treatment.* Journal of Membrane Science, 1999. **152**(2): p. 203-210.http://dx.doi.org/10.1016/S0376-7388(98)00220-8
34. Schröder, V., O. Behrend, and H. Schubert, *Effect of Dynamic Interfacial Tension on the Emulsification Process Using Microporous, Ceramic Membranes.* Journal of Colloid and Interface Science, 1998. **202**(2): p. 334-340.http://dx.doi.org/10.1006/jcis.1998.5429
35. Schröder, V. and H. Schubert, *Production of emulsions using microporous, ceramic membranes.* Colloids and Surfaces A: Physicochemical and Engineering Aspects, 1999. **152**(1–2): p. 103-109.http://dx.doi.org/10.1016/S0927-7757(98)00688-8
36. Joscelyne, S.M. and G. Trägårdh, *Food emulsions using membrane emulsification: conditions for producing small droplets.* Journal of Food Engineering, 1999. **39**(1): p. 59-64.http://dx.doi.org/10.1016/S0260-8774(98)00146-0
37. Xomeritakis, G. and Y.S. Lin, *Fabrication of a thin palladium membrane supported in a porous ceramic substrate by chemical vapor deposition.* Journal of Membrane Science, 1996. **120**(2): p. 261-272.http://dx.doi.org/10.1016/0376-7388(96)00149-4
38. Cao, G.-z., et al., *Pore Narrowing and Formation of Ultrathin Yttria-Stabilized Zirconia Layers in Ceramic Membranes by Chemical Vapor Deposition/Electrochemical Vapor Deposition.* Journal of the American Ceramic Society, 1993. **76**(9): p. 2201-2208.10.1111/j.1151-2916.1993.tb07755.x

39. Xu, Q. and M.A. Anderson, *Synthesis of porosity controlled ceramic membranes.* Journal of Materials Research, 1991. **6**(05): p. 1073-1081.doi:10.1557/JMR.1991.1073

40. Julbe, A., et al., *The sol-gel approach to prepare candidate microporous inorganic membranes for membrane reactors.* Journal of Membrane Science, 1993. **77**(2–3): p. 137-153.http://dx.doi.org/10.1016/0376-7388(93)85065-5

41. Peterson, R.A., et al., *Ceramic membranes for novel separations.* Separation Science and Technology, 1995. **30**(7-9): p. 1689-1709.10.1080/01496399508010370

42. Lee, K.H. and Y.M. Kim, *Asymmetric hollow inorganic membranes.* Key Engineering Materials, 1991. **61-62**: p. 17-22

43. Okubo, T., et al., *Preparation of a sol-gel derived thin membrane on a porous ceramic hollow fiber by the filtration technique.* Journal of Membrane Science, 1991. **59**(1): p. 73-80.http://dx.doi.org/10.1016/S0376-7388(00)81222-3

44. Velterop, F. and K. Keizer. *Development of a high temperature resistant module for ceramic membranes*. in *Key Engineering Materials*. 1992. Trans Tech Publ

45. Mohanty, K. and M.K. Purkait, *Membrane Technologies and Applications*. 2011: CRC Press

46. Kogan, A., E. Spiegler, and M. Wolfshtein, *Direct solar thermal splitting of water and on-site separation of the products. III.: Improvement of reactor efficiency by steam entrainment.* International Journal of Hydrogen Energy, 2000. **25**(8): p. 739-745.http://dx.doi.org/10.1016/S0360-3199(99)00102-0

47. Kogan, A., *Direct solar thermal splitting of water and on-site separation of the products — IV. Development of porous ceramic membranes for a solar thermal water-splitting reactor.* International Journal of Hydrogen Energy, 2000. **25**(11): p. 1043-1050.http://dx.doi.org/10.1016/S0360-3199(00)00024-0

48. Nandi, B.K., R. Uppaluri, and M.K. Purkait, *Preparation and characterization of low cost ceramic membranes for micro-filtration applications.* Applied

Clay Science, 2008. **42**(1–2): p. 102-110.http://dx.doi.org/10.1016/j.clay.2007.12.001

49. Sunarso, J., et al., *Mixed ionic–electronic conducting (MIEC) ceramic-based membranes for oxygen separation.* Journal of Membrane Science, 2008. **320**(1–2): p. 13-41.http://dx.doi.org/10.1016/j.memsci.2008.03.074
50. Wang, H., et al., *Perovskite Hollow-Fiber Membranes for the Production of Oxygen-Enriched Air.* Angewandte Chemie International Edition, 2005. **44**(42): p. 6906-6909.10.1002/anie.200501914
51. Norby, T., *Ceramic proton and mixed proton-electron conductors in membranes for energy conversion applications.* Journal of Chemical Engineering of Japan, 2007. **40**(13): p. 1166-1171
52. Wronski, Z.S., *Materials for rechargeable batteries and clean hydrogen energy sources.* International Materials Reviews, 2001. **46**(1): p. 1-49.doi:10.1179/095066001101528394
53. Schlichter, B., V. Mavrov, and H. Chmiel, *Study of a hybrid process combining ozonation and microfiltration/ultrafiltration for drinking water production from surface water.* Desalination, 2004. **168**: p. 307-317.http://dx.doi.org/10.1016/j.desal.2004.07.014
54. Sartor, M., et al., *Demonstration of a new hybrid process for the decentralised drinking and service water production from surface water in Thailand.* Desalination, 2008. **222**(1–3): p. 528-540.http://dx.doi.org/10.1016/j.desal.2007.03.013
55. Lerch, A., et al., *Direct river water treatment using coagulation/ceramic membrane microfiltration.* Desalination, 2005. **179**(1–3): p. 41-50.http://dx.doi.org/10.1016/j.desal.2004.11.054
56. Zhou, J.-e., et al., *Separation of stable oil–water emulsion by the hydrophilic nano-sized ZrO2 modified Al2O3 microfiltration membrane.* Separation and Purification Technology, 2010. **75**(3): p. 243-248.http://dx.doi.org/10.1016/j.seppur.2010.08.008
57. Vladisavljević, G.T., et al., *Production of O/W emulsions using SPG membranes, ceramic α-aluminium oxide membranes, microfluidizer and a silicon microchannel plate—a comparative study.* Colloids and Surfaces A:

Physicochemical and Engineering Aspects, 2004. **232**(2–3): p. 199-207.http://dx.doi.org/10.1016/j.colsurfa.2003.10.026

58. Joscelyne, S.M. and G. Trägårdh, *Membrane emulsification — a literature review.* Journal of Membrane Science, 2000. **169**(1): p. 107-117.http://dx.doi.org/10.1016/S0376-7388(99)00334-8
59. Luis, P., A. Garea, and A. Irabien, *Zero solvent emission process for sulfur dioxide recovery using a membrane contactor and ionic liquids.* Journal of Membrane Science, 2009. **330**(1–2): p. 80-89.http://dx.doi.org/10.1016/j.memsci.2008.12.046
60. Koonaphapdeelert, S., Z. Wu, and K. Li, *Carbon dioxide stripping in ceramic hollow fibre membrane contactors.* Chemical Engineering Science, 2009. **64**(1): p. 1-8.http://dx.doi.org/10.1016/j.ces.2008.09.010
61. Picard, C., et al., *Grafting of ceramic membranes by fluorinated silanes: hydrophobic features.* Separation and Purification Technology, 2001. **25**(1–3): p. 65-69.http://dx.doi.org/10.1016/S1383-5866(01)00091-0
62. Lu, J., et al., *FAS grafted superhydrophobic ceramic membrane.* Applied Surface Science, 2009. **255**(22): p. 9092-9099.http://dx.doi.org/10.1016/j.apsusc.2009.06.112
63. Krajewski, S.R., et al., *Application of fluoroalkylsilanes (FAS) grafted ceramic membranes in membrane distillation process of NaCl solutions.* Journal of Membrane Science, 2006. **281**(1–2): p. 253-259.http://dx.doi.org/10.1016/j.memsci.2006.03.039
64. Valle, E.M.d., M.A.G. Serrano, and R.L. Cerro, *Use of Ceramic Monoliths as Stationary Phase in Affinity Chromatography.* Biotechnology Progress, 2003. **19**(3): p. 921-927.10.1021/bp0340234
65. Liu, S., K. Li, and R. Hughes, *Preparation of porous aluminium oxide (Al2O3) hollow fibre membranes by a combined phase-inversion and sintering method.* Ceramics International, 2003. **29**(8): p. 875-881.http://dx.doi.org/10.1016/S0272-8842(03)00030-0
66. Tan, X., S. Liu, and K. Li, *Preparation and characterization of inorganic hollow fiber membranes.* Journal of Membrane Science, 2001. **188**(1): p. 87-95.http://dx.doi.org/10.1016/S0376-7388(01)00369-6

67. de Jong, J., et al., *Towards single step production of multi-layer inorganic hollow fibers.* Journal of Membrane Science, 2004. **239**(2): p. 265-269.http://dx.doi.org/10.1016/j.memsci.2004.02.039

68. Liu, L., X. Tan, and S. Liu, *Yttria Stabilized Zirconia Hollow Fiber Membranes.* Journal of the American Ceramic Society, 2006. **89**(3): p. 1156-1159.10.1111/j.1551-2916.2005.00901.x

69. Yin, W., et al., *Highly asymmetric yttria stabilized zirconia hollow fibre membranes.* Journal of Alloys and Compounds, 2009. **476**(1–2): p. 566-570.http://dx.doi.org/10.1016/j.jallcom.2008.09.079

70. Liu, S. and K. Li, *Preparation TiO2/Al2O3 composite hollow fibre membranes.* Journal of Membrane Science, 2003. **218**(1–2): p. 269-277.http://dx.doi.org/10.1016/S0376-7388(03)00184-4

71. Matus, Y.B., et al., *Metal-supported solid oxide fuel cell membranes for rapid thermal cycling.* Solid State Ionics, 2005. **176**(5–6): p. 443-449.http://dx.doi.org/10.1016/j.ssi.2004.09.056

72. Mori, M., Y. Liu, and T. Itoh, *La0. 6Sr0. 4Co0. 2Fe0. 8O3− δ current collectors via Ag infiltration for microtubular solid oxide fuel cells with intermediate temperature operation.* Journal of The Electrochemical Society, 2009. **156**(10): p. B1182-B1187

73. Zuo, C., et al., *Effect of Zr-Doping on the Chemical Stability and Hydrogen Permeation of the Ni−BaCe0.8Y0.2O3-α Mixed Protonic−Electronic Conductor.* Chemistry of Materials, 2006. **18**(19): p. 4647-4650.10.1021/cm0518224

74. Elyassi, B., M. Sahimi, and T.T. Tsotsis, *A novel sacrificial interlayer-based method for the preparation of silicon carbide membranes.* Journal of Membrane Science, 2008. **316**(1–2): p. 73-79.http://dx.doi.org/10.1016/j.memsci.2007.09.044

75. Elyassi, B., M. Sahimi, and T.T. Tsotsis, *Silicon carbide membranes for gas separation applications.* Journal of Membrane Science, 2007. **288**(1–2): p. 290-297.http://dx.doi.org/10.1016/j.memsci.2006.11.027

76. Suwanmethanond, V., et al., *Porous Silicon Carbide Sintered Substrates for High-Temperature Membranes.* Industrial & Engineering Chemistry Research, 2000. **39**(9): p. 3264-3271.10.1021/ie0000156

77. Brevnov, D.A., et al., *Fabrication of Anisotropic Super Hydrophobic/Hydrophilic Nanoporous Membranes by Plasma Polymerization of C 4 F 8 on Anodic Aluminum Oxide.* Journal of the Electrochemical Society, 2004. **151**(8): p. B484-B489

78. Xiong, G., et al., *Effect of Atomic Layer Deposition Coatings on the Surface Structure of Anodic Aluminum Oxide Membranes.* The Journal of Physical Chemistry B, 2005. **109**(29): p. 14059-14063.10.1021/jp0503415

79. Caro, J., et al., *Zeolite membranes – state of their development and perspective.* Microporous and Mesoporous Materials, 2000. **38**(1): p. 3-24.http://dx.doi.org/10.1016/S1387-1811(99)00295-4

80. Chiang, A.S.T. and K.-j. Chao, *Membranes and films of zeolite and zeolite-like materials.* Journal of Physics and Chemistry of Solids, 2001. **62**(9–10): p. 1899-1910.http://dx.doi.org/10.1016/S0022-3697(01)00122-6

81. Blöcher, C., et al., *Hybrid flotation—membrane filtration process for the removal of heavy metal ions from wastewater.* Water Research, 2003. **37**(16): p. 4018-4026.http://dx.doi.org/10.1016/S0043-1354(03)00314-2

82. Abbasi, M., M. Reza Sebzari, and T. Mohammadi, *Enhancement of Oily Wastewater Treatment by Ceramic Microfiltration Membranes using Powder Activated Carbon.* Chemical Engineering & Technology, 2011. **34**(8): p. 1252-1258.10.1002/ceat.201100108

83. Weschenfelder, S.E., C.P. Borges, and J.C. Campos, *Oilfield produced water treatment by ceramic membranes: Bench and pilot scale evaluation.* Journal of Membrane Science, 2015. **495**: p. 242-251.http://dx.doi.org/10.1016/j.memsci.2015.08.028

84. Ebrahimi, M., et al., *Investigations on the use of different ceramic membranes for efficient oil-field produced water treatment.* Desalination, 2010. **250**(3): p. 991-996.http://dx.doi.org/10.1016/j.desal.2009.09.088

85. Wu, Z., B. Wang, and K. Li, *A novel dual-layer ceramic hollow fibre membrane reactor for methane conversion.* Journal of Membrane Science, 2010. **352**(1–2): p. 63-70.http://dx.doi.org/10.1016/j.memsci.2010.01.062

86. Kingsbury, B.F.K., Z. Wu, and K. Li, *A morphological study of ceramic hollow fibre membranes: A perspective on multifunctional catalytic membrane*

reactors. Catalysis Today, 2010. **156**(3–4): p. 306-315.http://dx.doi.org/10.1016/j.cattod.2010.02.039

87. García-García, F.R., et al., *Asymmetric ceramic hollow fibres applied in heterogeneous catalytic gas phase reactions.* Catalysis Today, 2012. **193**(1): p. 20-30.http://dx.doi.org/10.1016/j.cattod.2012.01.006
88. Anderson, M. and Y.S. Lin, *Carbonate–ceramic dual-phase membrane for carbon dioxide separation.* Journal of Membrane Science, 2010. **357**(1–2): p. 122-129.http://dx.doi.org/10.1016/j.memsci.2010.04.009
89. Ku, A.Y., et al., *Membrane performance requirements for carbon dioxide capture using hydrogen-selective membranes in integrated gasification combined cycle (IGCC) power plants.* Journal of Membrane Science, 2011. **367**(1–2): p. 233-239.http://dx.doi.org/10.1016/j.memsci.2010.10.066
90. Leo, A., et al., *High performance perovskite hollow fibres for oxygen separation.* Journal of Membrane Science, 2011. **368**(1–2): p. 64-68.http://dx.doi.org/10.1016/j.memsci.2010.11.002
91. Czyperek, M., et al., *Gas separation membranes for zero-emission fossil power plants: MEM-BRAIN.* Journal of Membrane Science, 2010. **359**(1–2): p. 149-159.http://dx.doi.org/10.1016/j.memsci.2010.04.012
92. Hashim, S.S., A.R. Mohamed, and S. Bhatia, *Oxygen separation from air using ceramic-based membrane technology for sustainable fuel production and power generation.* Renewable and Sustainable Energy Reviews, 2011. **15**(2): p. 1284-1293.http://dx.doi.org/10.1016/j.rser.2010.10.002
93. Ieropoulos, I.A., et al., *Waste to real energy: the first MFC powered mobile phone.* Physical Chemistry Chemical Physics, 2013. **15**(37): p. 15312-15316.10.1039/C3CP52889H
94. Kim, J. and B. Van der Bruggen, *The use of nanoparticles in polymeric and ceramic membrane structures: Review of manufacturing procedures and performance improvement for water treatment.* Environmental Pollution, 2010. **158**(7): p. 2335-2349.http://dx.doi.org/10.1016/j.envpol.2010.03.024
95. Huang, A., et al., *Molecular-Sieve Membrane with Hydrogen Permselectivity: ZIF-22 in LTA Topology Prepared with 3-Aminopropyltriethoxysilane as*

Covalent Linker. Angewandte Chemie International Edition, 2010. **49**(29): p. 4958-4961.10.1002/anie.201001919

96. Pan, Y., B. Wang, and Z. Lai, *Synthesis of ceramic hollow fiber supported zeolitic imidazolate framework-8 (ZIF-8) membranes with high hydrogen permeability.* Journal of Membrane Science, 2012. **421–422**: p. 292-298.http://dx.doi.org/10.1016/j.memsci.2012.07.028
97. Huang, K., et al., *A Graphene Oxide Membrane with Highly Selective Molecular Separation of Aqueous Organic Solution.* Angewandte Chemie International Edition, 2014. **53**(27): p. 6929-6932.10.1002/anie.201401061
98. Lou, Y., et al., *A facile way to prepare ceramic-supported graphene oxide composite membrane via silane-graft modification.* Applied Surface Science, 2014. **307**: p. 631-637.http://dx.doi.org/10.1016/j.apsusc.2014.04.088
99. Hu, X., et al., *The improved oil/water separation performance of graphene oxide modified Al2O3 microfiltration membrane.* Journal of Membrane Science, 2015. **476**: p. 200-204.http://dx.doi.org/10.1016/j.memsci.2014.11.043
100. Aba, N.F.D., et al., *Graphene oxide membranes on ceramic hollow fibers – Microstructural stability and nanofiltration performance.* Journal of Membrane Science, 2015. **484**: p. 87-94.http://dx.doi.org/10.1016/j.memsci.2015.03.001
101. Luiten-Olieman, M.W.J., et al., *Porous stainless steel hollow fiber membranes via dry–wet spinning.* Journal of Membrane Science, 2011. **370**(1–2): p. 124-130.http://dx.doi.org/10.1016/j.memsci.2011.01.004
102. Dong, X., J. Ortiz Landeros, and Y.S. Lin, *An asymmetric tubular ceramic-carbonate dual phase membrane for high temperature CO2 separation.* Chemical Communications, 2013. **49**(83): p. 9654-9656.10.1039/C3CC45949G
103. Silverstein, M.S., *PolyHIPEs: Recent advances in emulsion-templated porous polymers.* Progress in Polymer Science, 2014. **39**(1): p. 199-234.http://dx.doi.org/10.1016/j.progpolymsci.2013.07.003
104. Zhou, J., et al., *Elaboration and characterization of tubular macroporous ceramic support for membranes from kaolin and dolomite*. Vol. 17. 2008. 1-9.10.1007/s10934-008-9258-z

105. Monash, P. and G. Pugazhenthi, *Development of Ceramic Supports Derived from Low-Cost Raw Materials for Membrane Applications and its Optimization Based on Sintering Temperature.* International Journal of Applied Ceramic Technology, 2011. **8**(1): p. 227-238.10.1111/j.1744-7402.2009.02443.x

106. Vasanth, D., G. Pugazhenthi, and R. Uppaluri, *Fabrication and properties of low cost ceramic microfiltration membranes for separation of oil and bacteria from its solution.* Journal of Membrane Science, 2011. **379**(1–2): p. 154-163.http://dx.doi.org/10.1016/j.memsci.2011.05.050

107. Guo, H., W. Li, and F. Ye, *Low-cost porous mullite ceramic membrane supports fabricated from kyanite by casting and reaction sintering.* Ceramics International, 2016. **42**(4): p. 4819-4826.http://dx.doi.org/10.1016/j.ceramint.2015.11.167

108. Mallada, R. and M. Menéndez, *Inorganic Membranes: Synthesis, Characterization and Applications: Synthesis, Characterization and Applications*. 2008: Elsevier Science

109. Hofman-Züter, J.M., *Chemical and Thermal Stability of (modified) Mesoporous Ceramic Membranes*. 1995

110. Van Gestel, T., et al., *Corrosion properties of alumina and titania NF membranes.* Journal of Membrane Science, 2003. **214**(1): p. 21-29.http://dx.doi.org/10.1016/S0376-7388(02)00517-3

111. Hsieh, H.P., *Inorganic Membranes for Separation and Reaction*. 1996: Elsevier Science

112. Guerra, K., J. Pellegrino, and J.E. Drewes, *Impact of operating conditions on permeate flux and process economics for cross flow ceramic membrane ultrafiltration of surface water.* Separation and Purification Technology, 2012. **87**(0): p. 47-53.http://dx.doi.org/10.1016/j.seppur.2011.11.019

113. Sondhi, R. and R. Bhave, *Role of backpulsing in fouling minimization in crossflow filtration with ceramic membranes.* Journal of Membrane Science, 2001. **186**(1): p. 41-52.http://dx.doi.org/10.1016/S0376-7388(00)00663-3

114. Van Der Bruggen, B., et al., *A review of pressure-driven membrane processes in wastewater treatment and drinking water production.* Environmental Progress, 2003. **22**(1): p. 46-56.10.1002/ep.670220116

115. Huang, H., et al., *Facile one-step forming of NiO and yttrium-stabilized zirconia composite anodes with straight open pores for planar solid oxide fuel cell using phase-inversion tape casting method.* Journal of Power Sources, 2015. **274**: p. 1114-1117.http://dx.doi.org/10.1016/j.jpowsour.2014.10.190

116. Kingsbury, B.F.K. and K. Li, *A morphological study of ceramic hollow fibre membranes.* Journal of Membrane Science, 2009. **328**(1–2): p. 134-140.http://dx.doi.org/10.1016/j.memsci.2008.11.050

117. Hsieh, H.P., R.R. Bhave, and H.L. Fleming, *Microporous alumina membranes.* Journal of Membrane Science, 1988. **39**(3): p. 221-241.http://dx.doi.org/10.1016/S0376-7388(00)80931-X

118. Abdulgader, H.A., V. Kochkodan, and N. Hilal, *Hybrid ion exchange – Pressure driven membrane processes in water treatment: A review.* Separation and Purification Technology, 2013. **116**: p. 253-264.http://dx.doi.org/10.1016/j.seppur.2013.05.052

119. Ang, W.L., et al., *A review on the applicability of integrated/hybrid membrane processes in water treatment and desalination plants.* Desalination, 2015. **363**: p. 2-18.http://dx.doi.org/10.1016/j.desal.2014.03.008

120. Wei, C.C., et al., *Ceramic asymmetric hollow fibre membranes—One step fabrication process.* Journal of Membrane Science, 2008. **320**(1–2): p. 191-197.http://dx.doi.org/10.1016/j.memsci.2008.04.003

121. Corporation, M. *Ceramic Membrane Unit*. 2013 [cited 2014 04/02]; Available from: http://water-solution.meidensha.co.jp/download/img/bb60-3163.pdf.

122. Singh, R., *Chapter 3 - Hybrid Membrane Systems – Applications and Case Studies*, in *Membrane Technology and Engineering for Water Purification (Second Edition)*, R. Singh, Editor. 2015, Butterworth-Heinemann: Oxford. p. 179-281.http://dx.doi.org/10.1016/B978-0-444-63362-0.00003-3

123. Lee, M., et al., *Formation of micro-channels in ceramic membranes – Spatial structure, simulation, and potential use in water treatment.* Journal of

Membrane Science, 2015. **483**: p. 1-14.http://dx.doi.org/10.1016/j.memsci.2015.02.023

124. Lee, M., et al., *Micro-structured alumina multi-channel capillary tubes and monoliths.* Journal of Membrane Science, 2015. **489**: p. 64-72.http://dx.doi.org/10.1016/j.memsci.2015.03.091
125. Othman, N.H., Z. Wu, and K. Li, *A micro-structured La0.6Sr0.4Co0.2Fe0.8O3−δ hollow fibre membrane reactor for oxidative coupling of methane.* Journal of Membrane Science, 2014. **468**: p. 31-41.http://dx.doi.org/10.1016/j.memsci.2014.05.051
126. Lee, M., et al., *Micro-structured alumina hollow fibre membranes – Potential applications in wastewater treatment.* Journal of Membrane Science, 2014. **461**: p. 39-48.http://dx.doi.org/10.1016/j.memsci.2014.02.044
127. Tan, X., et al., *Morphology control of the perovskite hollow fibre membranes for oxygen separation using different bore fluids.* Journal of Membrane Science, 2011. **378**(1–2): p. 308-318.http://dx.doi.org/10.1016/j.memsci.2011.05.012
128. Liu, N., et al., *Honeycomb-structured perovskite hollow fibre membranes with ultra-thin densified layer for oxygen separation.* Separation and Purification Technology, 2011. **80**(2): p. 396-401.http://dx.doi.org/10.1016/j.seppur.2011.04.014
129. Liu, C., J. Wang, and B. Li, *Preparation and characterization of ordered mesoporous silica membrane.* Journal of Non-Crystalline Solids, 2005. **351**(5): p. 409-412.10.1016/j.jnoncrysol.2005.01.006
130. Drioli, E., A. Ali, and F. Macedonio, *Membrane distillation: Recent developments and perspectives.* Desalination, 2015. **356**: p. 56-84.http://dx.doi.org/10.1016/j.desal.2014.10.028
131. Fang, H., et al., *Hydrophobic porous alumina hollow fiber for water desalination via membrane distillation process.* Journal of Membrane Science, 2012. **403–404**: p. 41-46.http://dx.doi.org/10.1016/j.memsci.2012.02.011
132. Wang, P. and T.-S. Chung, *Recent advances in membrane distillation processes: Membrane development, configuration design and application exploring.* Journal of Membrane Science, 2015. **474**: p. 39-56.http://dx.doi.org/10.1016/j.memsci.2014.09.016

133. Ltd, V.W. *CeraMem® Full-size Membrane Modules*. 2013 [cited 2013 21/08]; Available from: http://www.veoliawaterst.com/ceramem/en/fullsizemodulesceramem.htm.

134. Koonaphapdeelert, S. and K. Li, *Preparation and characterization of hydrophobic ceramic hollow fibre membrane.* Journal of Membrane Science, 2007. **291**(1–2): p. 70-76.http://dx.doi.org/10.1016/j.memsci.2006.12.039

135. Wei, C.C. and K. Li, *Preparation and Characterization of a Robust and Hydrophobic Ceramic Membrane via an Improved Surface Grafting Technique.* Industrial & Engineering Chemistry Research, 2009. **48**(7): p. 3446-3452.10.1021/ie801639d

136. Smart, S., et al., *8 - Porous ceramic membranes for membrane reactors*, in *Handbook of Membrane Reactors*, A. Basile, Editor. 2013, Woodhead Publishing. p. 298-336.http://dx.doi.org/10.1533/9780857097330.2.298

137. Yacou, C., S. Smart, and J.C. Diniz da Costa, *Mesoporous TiO2 based membranes for water desalination and brine processing.* Separation and Purification Technology, 2015. **147**: p. 166-171.http://dx.doi.org/10.1016/j.seppur.2015.04.028

138. Luiten-Olieman, M.W.J., et al., *Towards a generic method for inorganic porous hollow fibers preparation with shrinkage-controlled small radial dimensions, applied to Al2O3, Ni, SiC, stainless steel, and YSZ.* Journal of Membrane Science, 2012. **407-408**: p. 155-163.10.1016/j.memsci.2012.03.030

139. wang, I.-F.D., Jerome F; Morris, Richard A; Kesting, Robert, *Highly asymmetric ultrafiltration membranes*, 1999, USF Filtration and Separations Group Inc.

140. Li, K., *Ceramic Membranes for Separation and Reaction*. 2007: Wiley

141. Rahman, M.A., et al., *Development of a catalytic hollow fibre membrane micro-reactor for high purity H2 production.* Journal of Membrane Science, 2011. **368**(1–2): p. 116-123.http://dx.doi.org/10.1016/j.memsci.2010.11.025

142. Han, L.-F., et al., *Preparation, characterization and permeation property of Al2O3, Al2O3–SiO2 and Al2O3–kaolin hollow fiber membranes.* Journal of

Membrane Science, 2011. **372**(1–2): p. 154-164.http://dx.doi.org/10.1016/j.memsci.2011.01.065

143. Crittenden, J.C., et al., *MWH's Water Treatment: Principles and Design*. 2012: Wiley

144. *Ceramic Membrane Unit*. 2013 [cited 2014 04/02]; Available from: http://water-solution.meidensha.co.jp/download/img/bb60-3163.pdf.

145. membranes, H. *Module Specifications*. InoCep® [cited 2014 10/01]; Available from: http://www.hyfluxmembranes.com/inocep_module.html.

146. Othman, M.H.D., et al., *Dual-layer hollow fibres with different anode structures for micro-tubular solid oxide fuel cells.* Journal of Power Sources, 2012. **205**: p. 272-280.10.1016/j.jpowsour.2012.01.002

147. Calvert, P.D., et al., *Dispersion of Ceramic Particles in Organic Liquids.* MRS Online Proceedings Library, 1986. **73**: p. null-null.doi:10.1557/PROC-73-579

148. Zürcher, S. and T. Graule, *Influence of dispersant structure on the rheological properties of highly-concentrated zirconia dispersions.* Journal of the European Ceramic Society, 2005. **25**(6): p. 863-873.http://dx.doi.org/10.1016/j.jeurceramsoc.2004.05.002

149. Sushumna, I., R. Gupta, and E. Ruckenstein, *Effective dispersants for concentrated, nonaqueous suspensions.* JOURNAL OF MATERIALS RESEARCH-PITTSBURGH-, 1992. **7**: p. 2884-2884

150. Choi, I.-H., et al., *Preparation and characterization of ultrathin alumina hollow fiber microfiltration membrane.* Desalination, 2006. **193**(1–3): p. 256-259.http://dx.doi.org/10.1016/j.desal.2005.07.051

151. Burggraaf, A.J. and L. Cot, *Fundamentals of Inorganic Membrane Science and Technology*. 1996: Elsevier Science

152. Xin, X., et al., *Fabrication of dense YSZ electrolyte membranes by a modified dry-pressing using nanocrystalline powders.* Journal of Materials Chemistry, 2007. **17**(16): p. 1627-1630.10.1039/B615548K

153. Wang, Y.H., et al., *Preparation and Sintering of Macroporous Ceramic Membrane Support from Titania Sol-Coated Alumina Powder.* Journal of the American Ceramic Society, 2008. **91**(3): p. 825-830.10.1111/j.1551-2916.2007.02207.x

154. Silva, L.L.O., et al., *Processing, structural characterization and performance of alumina supports used in ceramic membranes.* Ceramics International, 2012. **38**(3): p. 1943-1949.http://dx.doi.org/10.1016/j.ceramint.2011.10.025

155. Drioli, E. and L. Giorno, *Comprehensive Membrane Science and Engineering*. 2010: Elsevier Science

156. Lindqvist, K. and E. Lidén, *Preparation of alumina membranes by tape casting and dip coating.* Journal of the European Ceramic Society, 1997. **17**(2–3): p. 359-366.http://dx.doi.org/10.1016/S0955-2219(96)00107-0

157. Das, N. and H.S. Maiti, *Ceramic membrane by tape casting and sol–gel coating for microfiltration and ultrafiltration application.* Journal of Physics and Chemistry of Solids, 2009. **70**(11): p. 1395-1400.http://dx.doi.org/10.1016/j.jpcs.2009.08.016

158. Das, N., et al., *Tape-cast ceramic membranes for microfiltration application.* Journal of Materials Science, 1996. **31**(19): p. 5221-5225.10.1007/BF00355928

159. Falamaki, C. and M. Beyhaghi, *Slip casting process for the manufacture of tubular alumina microfiltration membranes.* Materials Science-Poland, 2009. **27**(2)

160. Lin, P.-K. and D.-S. Tsai, *Preparation and Analysis of a Silicon Carbide Composite Membrane.* Journal of the American Ceramic Society, 1997. **80**(2): p. 365-372.10.1111/j.1151-2916.1997.tb02839.x

161. Smid, J., et al., *Preparation and characterization of microporous ceramic hollow fibre membranes.* Journal of Membrane Science, 1996. **112**(1): p. 85-90.http://dx.doi.org/10.1016/0376-7388(95)00274-X

162. Wang, H.-t., et al., *Kinetics and Mechanism of a Sintering Process for Macroporous Alumina Ceramics by Extrusion.* Journal of the American Ceramic Society, 1998. **81**(3): p. 781-784.10.1111/j.1151-2916.1998.tb02412.x

163. Castillon, R. and J.P. Laveniere, *Monolithic ceramic supports for filtration membranes*, 1995, Google Patents

164. Feenstra, F.K., R.A. Terpstra, and J.P.G.M. Van Eijk, *Method for the production of ceramic hollow fibres*, 1998, Google Patents

165. Gu, Y. and G. Meng, *A model for ceramic membrane formation by dip-coating.* Journal of the European Ceramic Society, 1999. **19**(11): p. 1961-1966.http://dx.doi.org/10.1016/S0955-2219(99)00013-8

166. Babaluo, A.A., et al., *A modified model for alumina membranes formed by gel-casting followed by dip-coating.* Journal of the European Ceramic Society, 2004. **24**(15–16): p. 3779-3787.http://dx.doi.org/10.1016/j.jeurceramsoc.2004.01.007

167. Larbot, A., et al., *Inorganic membranes obtained by sol-gel techniques.* Journal of Membrane Science, 1988. **39**(3): p. 203-212.http://dx.doi.org/10.1016/S0376-7388(00)80929-1

168. Agoudjil, N., S. Kermadi, and A. Larbot, *Synthesis of inorganic membrane by sol–gel process.* Desalination, 2008. **223**(1–3): p. 417-424.http://dx.doi.org/10.1016/j.desal.2007.01.187

169. Kim, J. and Y.S. Lin, *Sol-gel synthesis and characterization of yttria stabilized zirconia membranes.* Journal of Membrane Science, 1998. **139**(1): p. 75-83.http://dx.doi.org/10.1016/S0376-7388(97)00250-0

170. Hao, Y., et al., *Preparation of ZrO2–Al2O3 composite membranes by sol–gel process and their characterization.* Materials Science and Engineering: A, 2004. **367**(1–2): p. 243-247.http://dx.doi.org/10.1016/j.msea.2003.10.321

171. Wu, J.C.-S. and L.-C. Cheng, *An improved synthesis of ultrafiltration zirconia membranes via the sol–gel route using alkoxide precursor.* Journal of Membrane Science, 2000. **167**(2): p. 253-261.http://dx.doi.org/10.1016/S0376-7388(99)00294-X

172. Wang, Z., et al., *Preparation and Oxygen Permeation Properties of Highly Asymmetric La0.6Sr0.4Co0.2Fe0.8O3−α Perovskite Hollow-Fiber Membranes.* Industrial & Engineering Chemistry Research, 2008. **48**(1): p. 510-516.10.1021/ie8010462

173. Wang, T., et al., *Preparation and characterization of alumina hollow fiber membranes.* Frontiers of Chemical Engineering in China, 2009. **3**(3): p. 265-271.10.1007/s11705-009-0010-2

174. Jiansheng, L., et al., *Preparation and characterization of Al2O3 hollow fiber membranes.* Journal of Membrane Science, 2005. **256**(1–2): p. 1-6.http://dx.doi.org/10.1016/j.memsci.2004.07.014

175. Liu, S., et al., *Ba0.5Sr0.5Co0.8Fe0.2O3-δ ceramic hollow-fiber membranes for oxygen permeation.* AIChE Journal, 2006. **52**(10): p. 3452-3461.10.1002/aic.10966

176. Zhang, X., et al., *Asymmetric porous cordierite hollow fiber membrane for microfiltration.* Journal of Alloys and Compounds, 2009. **487**(1–2): p. 631-638.http://dx.doi.org/10.1016/j.jallcom.2009.08.028

177. Zhang, X., et al., *Highly permeable porous YSZ hollow fiber membrane prepared using ethanol as external coagulant.* Journal of Alloys and Compounds, 2010. **494**(1–2): p. 366-371.http://dx.doi.org/10.1016/j.jallcom.2010.01.048

178. Sternling, C.V. and L.E. Scriven, *INTERFACIAL TURBULENCE - HYDRODYNAMIC INSTABILITY.* AIChE Journal, 1959. **5**(4): p. 514-523

179. Saffman, P., *Viscous Fingering in Hele-Shaw Cells.* J Fluid Mech, 1986. **173**: p. 73-94

180. Lewis, D., *The instability of liquid surfaces when accelerated in a direction perpendicular to their planes. II.* Proceedings of the Royal Society of London. Series A, Mathematical and Physical Sciences, 1950: p. 81-96

181. Taylor, G., *The Instability of Liquid Surfaces when Accelerated in a Direction Perpendicular to their Planes. I.* Proceedings of the Royal Society of London. Series A. Mathematical and Physical Sciences, 1950. **201**(1065): p. 192-196.10.1098/rspa.1950.0052

182. Sharp, D.H., *An Overview of Rayleigh-Taylor Instability.* Physica D, 1984. **12**(1-3): p. 3-18.Doi 10.1016/0167-2789(84)90510-4

183. Ray, R., W. Krantz, and R. Sani, *Linear-stability Theory Model for Finger Formation in Asymmetric Membranes.* Journal of Membrane Science, 1985. **23**(2): p. 155-182

184. Normand, C., Y. Pomeau, and M.G. Velarde, *Convective Instability - Physicists Approach.* Reviews of Modern Physics, 1977. **49**(3): p. 581-624.DOI 10.1103/RevModPhys.49.581

185. Neogi, P., *Mechanism of Pore Formation in Reverse-Osmosis Membranes during the Casting Process.* Aiche Journal, 1983. **29**(3): p. 402-410.DOI 10.1002/aic.690290309

186. Frommer, M.A. and R.M. Messalem, *Mechanism of membrane formation. VI. Convective flows and large void formation during membrane precipitation.*

Industrial & Engineering Chemistry Product Research and Development, 1973. **12**(4): p. 328-333

187. Addad, J.P.C. and P. Panine, *Pore generation in asymmetric polymeric membranes - Correlation with solvent mobilities.* Polymer Bulletin, 1999. **42**(3): p. 345-352
188. Kingsbury, B., *A Morphological Study of Ceramic Hollow Fibre Membranes: A Perspective on Multifunctional Catalytic Membrane Reactors*, in *Department of Chemical Engineering and Chemical Technology*2010, Imperial College London. p. 191
189. Wang, B. and Z. Lai, *Finger-like voids induced by viscous fingering during phase inversion of alumina/PES/NMP suspensions.* Journal of Membrane Science, 2012. **405–406**(0): p. 275-283.http://dx.doi.org/10.1016/j.memsci.2012.03.020
190. Miao, X., *Porous mullite ceramics from natural topaz.* Materials Letters, 1999. **38**(3): p. 167-172.http://dx.doi.org/10.1016/S0167-577X(98)00153-0
191. Cuperus, F. and C. Smolders, *Characterization of UF membranes: membrane characteristics and characterization techniques.* Advances in Colloid and Interface Science, 1991. **34**(2): p. 135-173
192. Dobo, E.J., *Process to produce inorganic hollow fibers*, 1980, Monsanto Company
193. Lu, G.Q., *Evolution of the pore structure of a ceramic powder compact during sintering.* Journal of Materials Processing Technology, 1996. **59**(4): p. 297-302.http://dx.doi.org/10.1016/0924-0136(95)02171-X
194. Reed, J.S., *Principles of Ceramics Processing*. 1995: Wiley
195. IGB, F. *Ceramic capillary membranes*. [cited 2016 28/01]; Available from: http://www.igb.fraunhofer.de/en/competences/interfacial-materials/membranes/capillary-membranes.html.
196. Zhang, X.Z., et al. *Preparation of Highly Permeable Al2O3 Hollow Fiber Membrane via Phase Inversion Method with Ethanol as External Coagulant*. in *Advanced Materials Research*. 2012. Trans Tech Publ

197. Xia, K. and T.G. Langdon, *The toughening and strengthening of ceramic materials through discontinuous reinforcement*. Vol. 29. 5219-5231.10.1007/bf01171532

198. Xu, G., et al., *SiC nanofiber reinforced porous ceramic hollow fiber membranes.* Journal of Materials Chemistry A, 2014. **2**(16): p. 5841-5846.10.1039/C3TA15348G

199. Wu, Z., et al., *A controlled sintering process for more permeable ceramic hollow fibre membranes.* Journal of Membrane Science, 2013. **446**(0): p. 286-293.http://dx.doi.org/10.1016/j.memsci.2013.05.040

200. Yang, N., X. Tan, and Z. Ma, *A phase inversion/sintering process to fabricate nickel/yttria-stabilized zirconia hollow fibers as the anode support for micro-tubular solid oxide fuel cells.* Journal of Power Sources, 2008. **183**(1): p. 14-19.http://dx.doi.org/10.1016/j.jpowsour.2008.05.006

201. Luiten-Olieman, M.W.J., et al., *Porous stainless steel hollow fibers with shrinkage-controlled small radial dimensions.* Scripta Materialia, 2011. **65**(1): p. 25-28.http://dx.doi.org/10.1016/j.scriptamat.2011.03.023

202. Zhang, J.-W., et al., *Preparation of silicon nitride hollow fibre membrane for desalination.* Materials Letters, 2012. **68**: p. 457-459.10.1016/j.matlet.2011.11.041

203. Zhang, X., et al., *Fabrication of nanostructured TiO2 hollow fiber photocatalytic membrane and application for wastewater treatment.* Chemical Engineering Journal, 2014. **236**: p. 314-322.http://dx.doi.org/10.1016/j.cej.2013.09.059

204. de Wit, P., et al., *Highly permeable and mechanically robust silicon carbide hollow fiber membranes.* Journal of Membrane Science, 2015. **475**: p. 480-487.http://dx.doi.org/10.1016/j.memsci.2014.10.045

205. Tan, X., et al., *La0.7Sr0.3FeO3−α perovskite hollow fiber membranes for oxygen permeation and methane conversion.* Separation and Purification Technology, 2012. **96**: p. 89-97.http://dx.doi.org/10.1016/j.seppur.2012.05.012

206. Liao, Q., et al., *U-Shaped BaCo0.7Fe0.2Ta0.1O3−δ Hollow-Fiber Membranes with High Permeation for Oxygen Separation.* Industrial &

Engineering Chemistry Research, 2012. **51**(46): p. 15217-15223.10.1021/ie301789t

207. Zhu, L., et al., *A low-cost mullite-titania composite ceramic hollow fiber microfiltration membrane for highly efficient separation of oil-in-water emulsion.* Water Research, 2016. **90**: p. 277-285.http://dx.doi.org/10.1016/j.watres.2015.12.035
208. Kanawka, K., et al., *A dual layer Ni/Ni-YSZ hollow fibre for micro-tubular SOFC anode support with a current collector.* Electrochemistry Communications, 2011. **13**(1): p. 93-95.http://dx.doi.org/10.1016/j.elecom.2010.11.022
209. Staff, A., *Microfiltration and Ultrafiltration Membranes for Drinking Water (M53)*. 2011: American Water Works Association
210. Bottino, A., et al., *Water treatment for drinking purpose: ceramic microfiltration application.* Desalination, 2001. **141**(1): p. 75-79.http://dx.doi.org/10.1016/S0011-9164(01)00390-3
211. Muhammad, N., et al., *Ceramic filter for small system drinking water treatment: Evaluation of membrane pore Size and importance of integrity monitoring.* Journal of Environmental Engineering, 2009. **135**(11): p. 1181-1191
212. Li, M., et al., *Treatment of river water by a hybrid coagulation and ceramic membrane process.* Desalination, 2011. **280**(1–3): p. 114-119.http://dx.doi.org/10.1016/j.desal.2011.06.059
213. Mahesh Kumar, S., G.M. Madhu, and S. Roy, *Fouling behaviour, regeneration options and on-line control of biomass-based power plant effluents using microporous ceramic membranes.* Separation and Purification Technology, 2007. **57**(1): p. 25-36.http://dx.doi.org/10.1016/j.seppur.2007.03.002
214. Harman, B., et al., *The removal of disinfection by-product precursors from water with ceramic membranes.* 2010
215. Hofs, B., et al., *Comparison of ceramic and polymeric membrane permeability and fouling using surface water.* Separation and Purification Technology, 2011. **79**(3): p. 365-374.http://dx.doi.org/10.1016/j.seppur.2011.03.025

216. Karnik, B., et al., *The effects of combined ozonation and filtration on disinfection by-product formation.* Water Research, 2005. **39**(13): p. 2839-2850

217. Konieczny, K. and G. Klomfas, *Using activated carbon to improve natural water treatment by porous membranes.* Desalination, 2002. **147**(1–3): p. 109-116.http://dx.doi.org/10.1016/S0011-9164(02)00584-2

218. Lee, H.C., J.Y. Park, and D.-Y. Yoon, *Advanced water treatment of high turbid source by hybrid module of ceramic microfiltration and activated carbon adsorption: Effect of organic/inorganic materials.* Korean Journal of Chemical Engineering, 2009. **26**(3): p. 697-701

219. Stoquart, C., et al., *Hybrid Membrane Processes using activated carbon treatment for drinking water: A review.* Journal of Membrane Science, 2012. **411–412**: p. 1-12.http://dx.doi.org/10.1016/j.memsci.2012.04.012

220. Fiksdal, L. and T. Leiknes, *The effect of coagulation with MF/UF membrane filtration for the removal of virus in drinking water.* Journal of Membrane Science, 2006. **279**(1–2): p. 364-371.http://dx.doi.org/10.1016/j.memsci.2005.12.023

221. Konieczny, K., M. Bodzek, and M. Rajca, *A coagulation–MF system for water treatment using ceramic membranes.* Desalination, 2006. **198**(1–3): p. 92-101.http://dx.doi.org/10.1016/j.desal.2006.09.014

222. Matsushita, T., et al., *Effect of membrane pore size, coagulation time, and coagulant dose on virus removal by a coagulation-ceramic microfiltration hybrid system.* Desalination, 2005. **178**(1–3): p. 21-26.http://dx.doi.org/10.1016/j.desal.2004.11.026

223. Chin, S.S., et al., *Factors affecting the performance of a low-pressure submerged membrane photocatalytic reactor.* Chemical Engineering Journal, 2007. **130**(1): p. 53-63.http://dx.doi.org/10.1016/j.cej.2006.11.008

224. Alem, A., H. Sarpoolaky, and M. Keshmiri, *Sol-gel preparation of titania multilayer membrane for photocatalytic applications.* Ceramics International, 2009. **35**(5): p. 1837-1843

225. Mozia, S., *Photocatalytic membrane reactors (PMRs) in water and wastewater treatment. A review.* Separation and Purification Technology, 2010. **73**(2): p. 71-91.http://dx.doi.org/10.1016/j.seppur.2010.03.021

226. Karnik, B.S., et al., *Effects of ozonation on the permeate flux of nanocrystalline ceramic membranes.* Water research, 2005. **39**(4): p. 728-734
227. Kim, J., et al., *Effect of ozone dosage and hydrodynamic conditions on the permeate flux in a hybrid ozonation–ceramic ultrafiltration system treating natural waters.* Journal of Membrane Science, 2008. **311**(1): p. 165-172
228. Karnik, B.S., et al., *The effects of combined ozonation and filtration on disinfection by-product formation.* Water Research, 2005. **39**(13): p. 2839-2850.http://dx.doi.org/10.1016/j.watres.2005.04.073
229. Marrot, B., et al., *Industrial wastewater treatment in a membrane bioreactor: A review.* Environmental Progress, 2004. **23**(1): p. 59-68.10.1002/ep.10001
230. Xing, C.H., et al., *Ultrafiltration membrane bioreactor for urban wastewater reclamation.* Journal of Membrane Science, 2000. **177**(1–2): p. 73-82.http://dx.doi.org/10.1016/S0376-7388(00)00452-X
231. Waeger, F., T. Delhaye, and W. Fuchs, *The use of ceramic microfiltration and ultrafiltration membranes for particle removal from anaerobic digester effluents.* Separation and Purification Technology, 2010. **73**(2): p. 271-278.http://dx.doi.org/10.1016/j.seppur.2010.04.013
232. Xu, N., et al., *Study on ceramic membrane bioreactor with turbulence promoter.* Separation and Purification Technology, 2003. **32**(1–3): p. 403-410.http://dx.doi.org/10.1016/S1383-5866(03)00073-X
233. Zhang, F., et al., *Experiment and calculation of filtration processes in an external-loop airlift ceramic membrane bioreactor.* Chemical Engineering Science, 2009. **64**(12): p. 2859-2865.http://dx.doi.org/10.1016/j.ces.2009.02.046
234. Sun, D., J. Zeng, and J. Tay, *A submerged tubular ceramic membrane bioreactor for high strength wastewater treatment.* Water Science & Technology, 2003. **47**(1): p. 105-111
235. Jin, L., S.L. Ong, and H.Y. Ng, *Comparison of fouling characteristics in different pore-sized submerged ceramic membrane bioreactors.* Water Research, 2010. **44**(20): p. 5907-5918.http://dx.doi.org/10.1016/j.watres.2010.07.014

236. Fan, Y., et al., *Treatment and reuse of toilet wastewater by an airlift external circulation membrane bioreactor.* Process Biochemistry, 2006. **41**(6): p. 1364-1370.http://dx.doi.org/10.1016/j.procbio.2006.01.023

237. Liao, B.-Q., J.T. Kraemer, and D.M. Bagley, *Anaerobic Membrane Bioreactors: Applications and Research Directions.* Critical Reviews in Environmental Science and Technology, 2006. **36**(6): p. 489-530.10.1080/10643380600678146

238. Kang, I.-J., S.-H. Yoon, and C.-H. Lee, *Comparison of the filtration characteristics of organic and inorganic membranes in a membrane-coupled anaerobic bioreactor.* Water Research, 2002. **36**(7): p. 1803-1813.http://dx.doi.org/10.1016/S0043-1354(01)00388-8

239. Chen, A., et al., *Removal of oil, grease, and suspended solids from produced water with ceramic crossflow microfiltration.* SPE production engineering, 1991. **6**(2): p. 131-136

240. Li, L. and R. Lee, *Purification of produced water by ceramic membranes: material screening, process design and economics.* Separation Science and Technology, 2009. **44**(15): p. 3455-3484

241. Ashaghi, K.S., M. Ebrahimi, and P. Czermak, *Ceramic Ultra- and Nanofiltration Membranes for Oilfield Produced Water Treatment: A Mini Review.* The Open Environmental Journal, 2007. **1**: p. 1-8

242. Abadi, S.R.H., et al., *Ceramic membrane performance in microfiltration of oily wastewater.* Desalination, 2011. **265**(1–3): p. 222-228.http://dx.doi.org/10.1016/j.desal.2010.07.055

243. Skrzypek, M. and M. Burger, *Isoflux® ceramic membranes — Practical experiences in dairy industry.* Desalination, 2010. **250**(3): p. 1095-1100.http://dx.doi.org/10.1016/j.desal.2009.09.116

244. Fernández García, L., S. Álvarez Blanco, and F.A. Riera Rodríguez, *Microfiltration applied to dairy streams: removal of bacteria.* Journal of the Science of Food and Agriculture, 2013. **93**(2): p. 187-196.10.1002/jsfa.5935

245. *Ceramic membranes and their application in food and beverage processing.* Filtration & Separation, 2000. **37**(3): p. 36-38.http://dx.doi.org/10.1016/S0015-1882(00)88497-9

246. Fukumoto, L.R., P. Delaquis, and B. Girard, *Microfiltration and Ultrafiltration Ceramic Membranes for Apple Juice Clarification.* Journal of Food Science, 1998. **63**(5): p. 845-850.10.1111/j.1365-2621.1998.tb17912.x

247. Li, M., et al., *Clarification of raw rice wine by ceramic microfiltration membranes and membrane fouling analysis.* Desalination, 2010. **256**(1–3): p. 166-173.http://dx.doi.org/10.1016/j.desal.2010.01.018

248. Gan, Q., et al., *Synergetic cleaning procedure for a ceramic membrane fouled by beer microfiltration.* Journal of Membrane Science, 1999. **155**(2): p. 277-289.http://dx.doi.org/10.1016/S0376-7388(98)00320-2

249. van der Horst, H.C. and J.H. Hanemaaijer, *Cross-flow microfiltration in the food industry. State of the art.* Desalination, 1990. **77**(0): p. 235-258.http://dx.doi.org/10.1016/0011-9164(90)85028-9

250. Hinkova, A., et al., *Potentials of separation membranes in the sugar industry.* Separation and Purification Technology, 2002. **26**(1): p. 101-110.http://dx.doi.org/10.1016/S1383-5866(01)00121-6

251. Corporation, P. *Pall® Membralox® Ceramic Membranes and Modules*. [cited 2014 10/01]; Available from: http://www.pall.com/pdfs/Fuels-and-Chemicals/PIMEMBRAEN.pdf.

252. Ltd, V.W. *CeraMem® Ceramic Membrane Technology*. Technology Brief [cited 2014 10/01]; Available from: http://www.tundrasolutions.ca/files/TechnologyBriefVWSCeramicMembranes.pdf.

253. Fraunhofer IGB, L. *Ceramic capillary membranes*. [cited 2014 10/01]; Available from: http://www.igb.fraunhofer.de/en/competences/interfacial-materials/membranes/capillary-membranes.html.

254. *PUB and Meiden Singapore collaborate on ceramic membrane MBR demonstration plant.* Membrane Technology, 2012. **2012**(9): p. 1-16.http://dx.doi.org/10.1016/S0958-2118(12)70171-4

255. Elshorbagy, W., *Water Treatment*. 2013: InTech

256. *Success for LiqTech ceramic membranes in oil & gas trial.* Filtration Industry Analyst, 2012. **2012**(11): p. 4.http://dx.doi.org/10.1016/S1365-6937(12)70350-7

257. Peinemann, K.V., S.P. Nunes, and L. Giorno, *Membrane Technology: Volume 3: Membranes for Food Applications*. 2011: Wiley

258. Bolduan, P. and M. Latz, *Filtration by Means of Ceramic Membranes - Practical Examples from the Chemical and Food Industries*, 2005, Atech innovations gmbh

259. Othman, N.H., Z. Wu, and K. Li, *Bi1.5Y0.3Sm0.2O3-δ-based ceramic hollow fibre membranes for oxygenseparation and chemicalreactions.* Journal of Membrane Science, 2013. **432**: p. 58-65.http://dx.doi.org/10.1016/j.memsci.2013.01.004

260. Hinds, B.J., et al., *Aligned Multiwalled Carbon Nanotube Membranes.* Science, 2004. **303**(5654): p. 62-65.10.1126/science.1092048

261. Holt, J.K., et al., *Fast mass transport through sub-2-nanometer carbon nanotubes.* Science, 2006. **312**(5776): p. 1034-1037.10.1126/science.1126298

262. Kim, S., et al., *Fabrication of flexible, aligned carbon nanotube/polymer composite membranes by in-situ polymerization.* Journal of Membrane Science, 2014. **460**: p. 91-98.10.1016/j.memsci.2014.02.016

263. Vecitis, C.D., G. Gao, and H. Liu, *Electrochemical Carbon Nanotube Filter for Adsorption, Desorption, and Oxidation of Aqueous Dyes and Anions.* The Journal of Physical Chemistry C, 2011. **115**(9): p. 3621-3629.10.1021/jp111844j

264. Pan, B. and B. Xing, *Adsorption Mechanisms of Organic Chemicals on Carbon Nanotubes.* Environmental Science & Technology, 2008. **42**(24): p. 9005-9013.10.1021/es801777n

265. Kim, H.W., et al., *Selective gas transport through few-layered graphene and graphene oxide membranes.* Science, 2013. **342**(6154): p. 91-95.10.1126/science.1236098

266. Chong, J.Y., et al., *UV-enhanced sacrificial layer stabilised graphene oxide hollow fibre membranes for nanofiltration.* Scientific Reports, 2015. **5**.10.1038/srep15799

267. Huang, K., et al., *A graphene oxide membrane with highly selective molecular separation of aqueous organic solution.* Angewandte Chemie - International Edition, 2014. **53**(27): p. 6929-6932.10.1002/anie.201401061

268. Pendergast, M.M. and E.M.V. Hoek, *A review of water treatment membrane nanotechnologies.* Energy & Environmental Science, 2011. **4**(6): p. 1946-1971.10.1039/C0EE00541J

269. Li, L., J. Dong, and T.M. Nenoff, *Transport of water and alkali metal ions through MFI zeolite membranes during reverse osmosis.* Separation and Purification Technology, 2007. **53**(1): p. 42-48.http://dx.doi.org/10.1016/j.seppur.2006.06.012

270. Liu, N., et al., *Removal of organics from produced water by reverse osmosis using MFI-type zeolite membranes.* Journal of Membrane Science, 2008. **325**(1): p. 357-361.http://dx.doi.org/10.1016/j.memsci.2008.07.056

271. Bowen, T.C., R.D. Noble, and J.L. Falconer, *Fundamentals and applications of pervaporation through zeolite membranes.* Journal of Membrane Science, 2004. **245**(1–2): p. 1-33.http://dx.doi.org/10.1016/j.memsci.2004.06.059

272. Kosinov, N., et al., *Recent developments in zeolite membranes for gas separation.* Journal of Membrane Science, 2016. **499**: p. 65-79.http://dx.doi.org/10.1016/j.memsci.2015.10.049

273. Liu, X., et al., *Highly Water-Stable Zirconium Metal–Organic Framework UiO-66 Membranes Supported on Alumina Hollow Fibers for Desalination.* Journal of the American Chemical Society, 2015. **137**(22): p. 6999-7002.10.1021/jacs.5b02276

274. Huang, A., W. Dou, and J. Caro, *Steam-Stable Zeolitic Imidazolate Framework ZIF-90 Membrane with Hydrogen Selectivity through Covalent Functionalization.* Journal of the American Chemical Society, 2010. **132**(44): p. 15562-15564.10.1021/ja108774v

275. Huang, A. and J. Caro, *Covalent Post-Functionalization of Zeolitic Imidazolate Framework ZIF-90 Membrane for Enhanced Hydrogen Selectivity.* Angewandte Chemie International Edition, 2011. **50**(21): p. 4979-4982.10.1002/anie.201007861

276. Liu, X.-L., et al., *An Organophilic Pervaporation Membrane Derived from Metal–Organic Framework Nanoparticles for Efficient Recovery of Bio-Alcohols.* Angewandte Chemie International Edition, 2011. **50**(45): p. 10636-10639.10.1002/anie.201104383

277. Pastrana-Martínez, L.M., et al., *Graphene oxide based ultrafiltration membranes for photocatalytic degradation of organic pollutants in salty water.* Water Research, 2015. **77**: p. 179-190.http://dx.doi.org/10.1016/j.watres.2015.03.014

278. Lee, H.J., S.Y. Yeo, and S.H. Jeong, *Antibacterial effect of nanosized silver colloidal solution on textile fabrics.* Journal of Materials Science, 2003. **38**(10): p. 2199-2204.10.1023/A:1023736416361

279. Ma, L.F., et al., *Synthesis, structures and properties of Mn(II) coordination frameworks based on R-isophthalate (R = -CH3 or -C(CH3)3) and various dipyridyl-type co-ligands.* CrystEngComm, 2009. **11**(1): p. 109-117.10.1039/b811725j

280. Gallegos-Suárez, E., et al., *Ceramic hollow fibres catalytic enhanced reactors for glycerol steam reforming.* Catalysis Today, 2014. **233**: p. 21-30.http://dx.doi.org/10.1016/j.cattod.2014.02.040

281. García-García, F.R. and K. Li, *New catalytic reactors prepared from symmetric and asymmetric ceramic hollow fibres.* Applied Catalysis A: General, 2013. **456**: p. 1-10.http://dx.doi.org/10.1016/j.apcata.2013.01.031

282. Wu, Z., B. Wang, and K. Li, *Functional LSM-ScSZ/NiO-ScSZ dual-layer hollow fibres for partial oxidation of methane.* International Journal of Hydrogen Energy, 2011. **36**(9): p. 5334-5341.10.1016/j.ijhydene.2011.01.167

283. Othman, M.H.D., et al., *Electrolyte thickness control and its effect on electrolyte/anode dual-layer hollow fibres for micro-tubular solid oxide fuel cells.* Journal of Membrane Science, 2010. **365**(1-2): p. 382-388.10.1016/j.memsci.2010.09.036

284. Gouveia Gil, A., et al., *Microstructured Catalytic Hollow Fiber Reactor for Methane Steam Reforming.* Industrial & Engineering Chemistry Research, 2015. **54**(21): p. 5563-5571.10.1021/ie504953j

285. Othman, N.H., Z. Wu, and K. Li, *An oxygen permeable membrane microreactor with an in-situ deposited Bi1.5Y0.3Sm0.2O3−δ catalyst for oxidative coupling of methane.* Journal of Membrane Science, 2015. **488**: p. 182-193.http://dx.doi.org/10.1016/j.memsci.2015.04.027

286. Lv, Y., et al., *Silver nanoparticle-decorated porous ceramic composite for water treatment.* Journal of Membrane Science, 2009. **331**(1–2): p. 50-56.http://dx.doi.org/10.1016/j.memsci.2009.01.007

287. Lv, Y., et al., *Silver nanoparticle-decorated porous ceramic composite for water treatment.* Journal of Membrane Science, 2009. **331**(1-2): p. 50-56.10.1016/j.memsci.2009.01.007

288. Zhou, S., et al., *Preparation of titania microfiltration membranes supported on porous Ti–Al alloys.* Journal of Membrane Science, 2008. **325**(2): p. 546-552.http://dx.doi.org/10.1016/j.memsci.2008.08.024

289. Boccaccini, A.R., et al., *Electrophoretic deposition of carbon nanotube-ceramic nanocomposites.* Journal of the European Ceramic Society, 2010. **30**(5): p. 1115-1129.10.1016/j.jeurceramsoc.2009.03.016

290. Hayashi, J.I., et al., *Pore size control of carbonized BPDA-pp'ODA polyimide membrane by chemical vapor deposition of carbon.* Journal of Membrane Science, 1997. **124**(2): p. 243-251.10.1016/S0376-7388(96)00250-5

Chapter 3: Experimental

Chapter 3 *lists and describes the common materials used, experimental procedures and characterisation methods employed in this thesis*

3.1 Materials

Aluminium oxide powders of 1 μm (alpha, 99.9% metals basis, surface area 6–8 m^2/g) were purchased from Alfa Aesar (Chapters 4 – 6) and Inframat Corporation (Chapters 7 – 9) and used as supplied. 3-YSZ powders of < 0.5 μm were purchased from Inframat Corporation and used as supplied. Polyethersulfone (PESf, Radal A300, Ameco Performance, USA) and Arlacel P135 (polyethyleneglycol 30–dipolyhydroxystearate, Uniqema) were used as binder and dispersant, respectively. Dimethyl Sulphoxide (HPLC grade, VWR International), N-Methyl-2-pyyrolidone (HPLC grade, VWR International), Dimethylacetamide (HPLC grade, Sigma Aldrich), dimethylformamide (HPLC grade, Sigma Aldrich) and triethyl phosphate (HPLC grade, Sigma Aldrich) were used as the solvents and deionized water or ethanol (HPLC grade, VWR) were used as the non-solvents. Hexane was used as the immiscible bore fluid (HPLC grade, Sigma Aldrich).

3.2 Preparation of ceramic suspensions

First the dispersant Arlacel P135 was weighed and dissolved in the chosen solvent. Then the ceramic powder was added to the solvent. This mixture was then rolled/milled with 20 mm agate grinding balls for 48 h. PESf was then added and the suspension was milled for a further 48 h. The continuous suspension was then transferred to a gas tight reservoir and degassed under vacuum until bubbles were no longer visible.

3.3 Preparation of alumina discs

Once the suspensions have been degassed, they were poured into a stainless steel mould of 2 mm thickness and 30 mm diameter and then horizontally placed in a coagulation bath of deionized water (Figure 3.1). A continuous deionised water flow was applied across the water bath to ensure constant fresh non-solvent supply. The moulds were left in the coagulation bath for 2 h and the alumina disc precursors were removed.

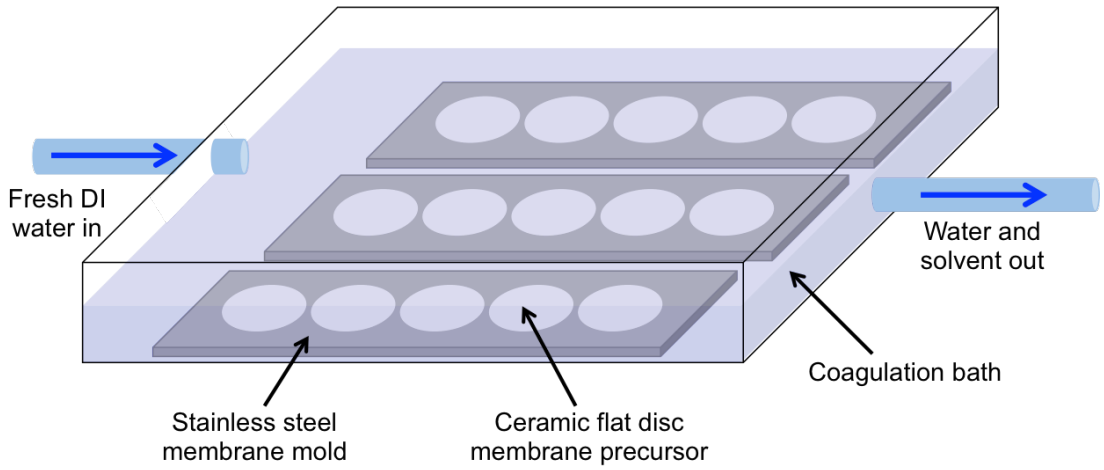


Figure 3.1 Schematic of the ceramic disc membrane preparation set-up

3.4 Preparation of alumina hollow fibres

Once the suspensions have been degassed, they were transferred to 200 ml Harvard Stainless steel syringes. The suspension was then extruded through the designated tube-in-orifice spinnerets, and their designs are described in the corresponding Chapters 4-8. The suspension was extruded into a coagulation bath that contained deionised water (Figure 3.2). The extrusion rates of the different layers of the spinnerets were controlled and monitored by two Harvard PHD 22/2000 Hpsi syringe pumps. The hollow fibre membrane precursors were left in the external coagulation bath overnight for phase inversion to complete. To remove traces of the solvent, the

membrane precursors were immersed in an excess of DI water, replaced every 48 h. They were then straightened in room temperature.

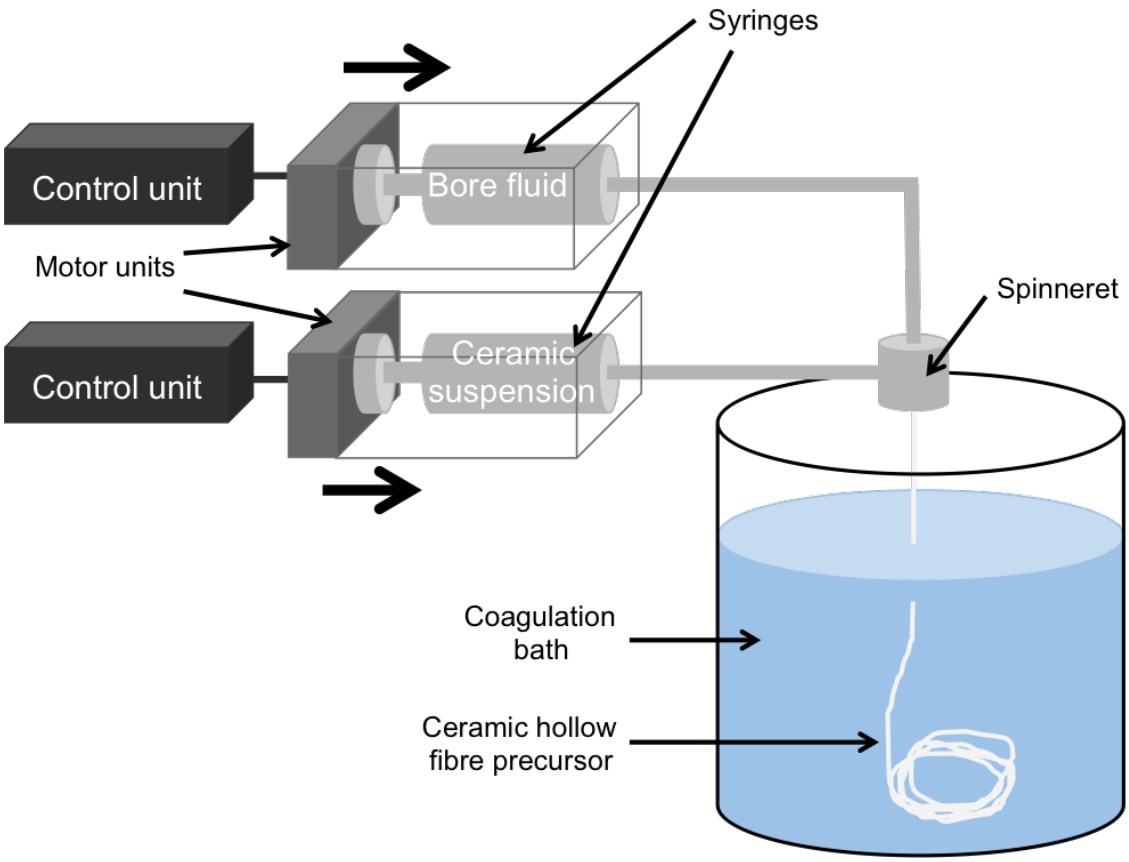


Figure 3.2 Schematic of the ceramic hollow fibre membrane preparation set-up

3.5 Heat treatment

The membrane precursors were calcined and sintered in air (CARBOLITE furnace) to form the final membranes. The temperature was increased from room temperature to 600 °C at a rate of 2 °C/min and held for 2 h, and then to the target temperature (changes depending on the experiment) at a rate of 5 °C/min and held for 4 h. The temperature was then reduced to room temperature at a rate of 5 °C/min.

3.6 Characterisation

3.6.1 Viscosity

For viscosity measurements samples were first degassed and then collected using the Model 2020 Rotary Viscometer from Cannon Instrument Company from 1–60 rpm at 20 °C. The viscometer uses concentric cylinder geometry and a sample volume of 5 ml, spindle diameter of 7 mm, and adaptor diameter of 13 mm.

3.6.2 Microscopy

Morphological characterisation was conducted with scanning electron microscopes (SEM, JEOL JSM-5610 LV for low resolution, and LEO Gemini 1525 FEGSEM for high resolution) for the membranes which were flexed at ambient temperature until a fracture occurred prior to being mounted on an SEM slide. Samples were gold coated under vacuum for 2 min at 20 mA (EMITECH Model K550) before SEM images at varying magnifications were collected. Optical microscope (Dino-Lite AM2111) was used for low magnification images.

3.6.3 Porosimetry

For pore size determination mercury intrusion data was collected at absolute pressures of between 1.38×10^{-2} and 2.28×10^{3} bar (Micromeritics Autopore IV) with an equilibration time of 10 s and assuming a mercury contact angle of 130°. The flat disc membranes were broken into sections of approximately 4 mm in diameter prior to mercury intrusion analysis.

Gas–liquid displacement measurements were taken using the PoroLux 1000 Porometer. Samples of no more than 3 cm in height were first fitted onto the sample holders with epoxy resin. The samples were then wetted with Porefil wetting liquid (perfluoroether) and data was collected. Nitrogen test gas was used between pressures of 0 to 10 bar with 30 steps.

3.6.4 Micro-channel characterisation

For assessing the micro-channels at the different strata of the membranes, a fraction of the membranes was sanded off from the top or the bottom to expose the micro-channels using 800, 1200 and 2000 grit sanding papers. SEM images were taken for each sanded stratum and the density of micro-channels was counted using the ImageJ software.

3.6.5 Mechanical strength

The mechanical property was evaluated by an Instron materials testing system (Model 5544) with a 5 kN load cell, using a three-point bending method where the samples were positioned onto a sample holder with a span of 20 mm for disc membranes and 30 mm for hollow fibres. For disc membranes they were first cut into rectangular strips of approximately 5 mm x 1.5 mm x 25 mm. 5 samples were used for each type of membrane with standard deviation of within 35 %.

The bending strength (σ) of the disc membranes were calculated using the following equation[1]:

$$\sigma = \frac{3FL}{2bh^2} \tag{3.1}$$

where F denotes the measured force when a fracture occurs (N), L is the distance between the centres of the supporting rollers (m) and b and h (m) are the sample width and thickness, respectively.

The bending strength (σ) for hollow fibres was calculated using the following equation[2]:

$$\sigma = \frac{8FLd_0}{\pi({d_o}^4 - {d_i}^4)} \tag{3.2}$$

where F denotes the measured force when a fracture occurs (N), L is the fibre length (m), D_o and D_i are the outer and inner diameters of the fibre (m), respectively.

3.6.6 Pure water permeation

3.6.6.1 Flat discs

Water permeation tests were carried out using a home designed dead-end system. Flat disc membranes were sealed at one side to a stainless steel tube of 17 mm internal diameter and 80 mm length with epoxy resin. The membranes were then fully wetted by water under vacuum. A constant trans-membrane pressure (1 bar) is applied and the water permeated through was collected and its weight measured every 5 min over a duration of 2 h (Figure 3.8). Three samples were tested for each type of membrane and the sample deviation is less than 25 %.

3.6.6.2 Hollow fibres

For hollow fibres, the membranes were first potted into ¼ inch NPT male connectors and sealed with epoxy resin at both the connector and at the hollow fibre end. They were then connected onto a stainless steel vessel and a pressure is applied across the membrane. Water is collected and its weight measured every 5 minutes over a duration of 2 h (Figure 3.9). The dead-end permeation tests were conducted with an out-in mode. Three samples were tested for each type of membrane and the sample deviation is less than 25 %.

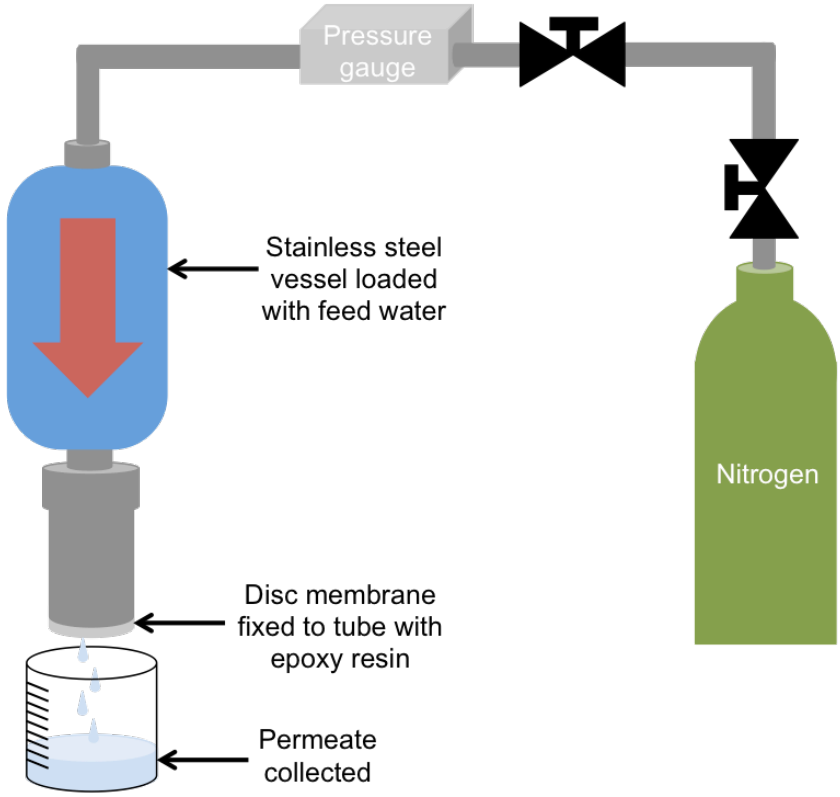


Figure 3.3 Schematic of the dead-end pure water permeation experiment set-up for ceramic disc membranes

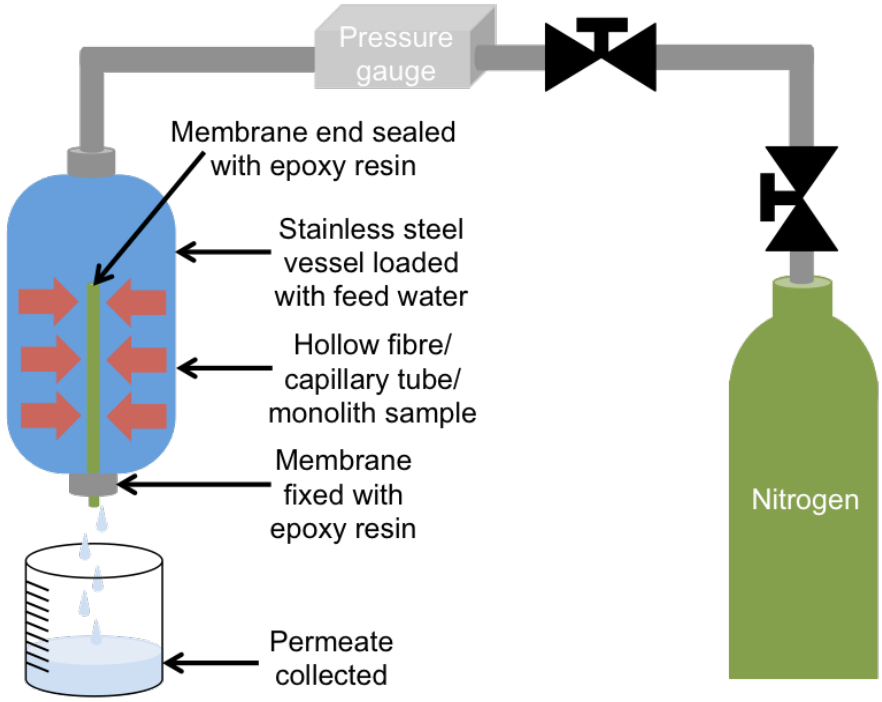


Figure 3.4 Schematic of the dead-end pure water permeation experiment set-up for hollow fibre membranes in the out-in configuration

References

1. Oberg, E., *Section 03. Properties, Treatment, and Testing of Materials – Machinery's Handbook 29*. 2012: Industrial Press
2. Liu, S., K. Li, and R. Hughes, *Preparation of porous aluminium oxide (Al2O3) hollow fibre membranes by a combined phase-inversion and sintering method.* Ceramics International, 2003. **29**(8): p. 875-881.http://dx.doi.org/10.1016/S0272-8842(03)00030-0

Chapter 4: Fundamental Study of micro-channels in ceramic membranes – spatial structure and simulation

Chapter 4 *This chapter provides a fundamental study into the effect of solvent choice in the alumina suspension on the formation of micro-channels in disc membranes with preliminary simulation attempts to mimic the micro-channels*

Abstract

In this chapter, alumina membranes with distinct types of micro-channels have been developed via a micro-channel inducing phase inversion and sintering technique. The designed membrane morphologies were achieved by using five different solvents: DMSO, NMP, DMAc, DMF and TEP, which led to unique changes in the macro- and microstructures of the membranes. The micro-channel shapes vary from long, straight, cylindrical and densely packed (DMSO) to pear-shaped conical structures (NMP and DMAc). When DMF and TEP were used, symmetric membranes with sponge-like structure were formed. These micro-channels display a regular and periodic distribution and also have a hierarchical spatial structure with a distribution in number, length and width along the depth of the membranes. Dead end water permeation tests reveal that the micro-channels can greatly reduce the resistance to water permeation. Furthermore, the microstructures also vary with a change in solvent, and different membrane pore sizes were observed. The initialization of the micro-channels was interpreted using the Rayleigh-Taylor Instability, driven by acceleration on the interface and facilitated by a difference in density between the suspension and the coagulant. The spacing between the micro-channels and their hierarchical structure was quantitatively mimicked using R-T Instability theory and the simulation results matched the experimental results reasonably well.

4.1 Introduction

The use of porous ceramic membranes in conventional separation technologies for water treatment such as micro- and ultrafiltration processes has shown improved long-term reliability over polymeric membranes [1]. Their many advantages such as superior chemical and thermal stabilities and mechanical robustness allow them to be cleaned easily and operated over extended periods of time. They can therefore be a reliable alternative to use in membrane bioreactors, a fast growing market in water treatment technologies [2], whereby frequent and strenuous cleaning regimes are needed. They can also be combined with ion exchange, UV disinfection or activated carbon, etc, to form other hybrid systems that are gaining attention as cost and space saving alternatives to the long conventional treatment trains for water treatments [3-6].

Currently, the main deterrent for the use of ceramic membranes in large-scale applications is their high fabrication costs when produced via the conventional multi-step fabrication method [7, 8]. The conventional multi-step method is highly time and energy consuming and contributes generously to the high capital cost of commercial ceramic membranes. Furthermore, these commercially available ceramic membranes are most often found in the tubular or flat sheet configurations, which offer much lower packing densities compared to hollow fibre or spiral-wound flat sheet polymeric membranes [7]. The micro-channel inducing phase inversion and sintering method is a relatively new method for producing asymmetric hollow fibre ceramic membranes and considerably reduces the number of steps in the fabrication process. More details on this method can be found in the literature as reviewed in Chapter 2. The steps are greatly reduced by eliminating the need to deposit additional layers on a substrate to achieve micro/ultrafiltration selectivity. This method allows facile fabrication of ceramic hollow fibre membranes, which significantly improves the packing density. Hence fabrication costs can be potentially reduced and productivity improved. Also the ability to produce a wide range of different membrane microstructures means that they can be tailored according to the application [9-25].

The morphology of the membranes formed via the micro-channel inducing phase inversion and sintering method is unique and advantageous over commercial ceramic membranes. Not only do they consist of the sponge-like structures formed by

the packing of the ceramic particles, much larger finger-like structures can also be formed in the same membrane in one step, similar to those in Loeb Sourirajan polymeric membranes [26]. For polymeric membranes, these fingers are undesired as they are generally in the form of macrovoids and can reduce the membrane performance as well as mechanical stability. However, the finger-like structures observed in ceramic membranes can resemble micro-channels, which can be long, straight, cylindrical and highly packed. In terms of filtration, these micro-channels can reduce the trans-membrane resistance to permeate flow and the sponge-like structures act as separation layers to offer the desired selectivity. Due to the advantages offered by these ordered micro-channels, they have widened the application of ceramic membranes, with examples such as hollow fibre membrane micro-reactors, solid-oxide fuel cells, membrane contactors, gas separation, etc [15, 18, 20, 23, 27]. Considering the different characteristics and roles of these finger-like voids in ceramic and polymeric membranes, the term 'micro-channels' is used for ceramic membranes in this article, and 'finger-like voids' is used for polymeric membranes, even if the origin of this structure is the same for both cases.

For the ceramic membranes made via the phase inversion and sintering method, much literature is available investigating the effects of different fabrication parameters on the range of cross-section morphologies achievable for various inorganic materials and applications [9-25]. However, an improved understanding of the formation mechanism behind these different macro- and microstructures is still needed in order to be able to accurately control and tailor the membrane characteristics according to the application. This is important in order to improve the reproducibility of the fabrication process before large-scale production of these unique asymmetric membranes can be achieved. Currently there is little consensus on the mechanisms responsible for the formation of the micro-channels.

For polymeric systems, there is a rich history of researches carried out with various different theories used to postulate and predict the formation mechanism as well as characteristics of the finger-like voids. For example, one popular hypothesis is the skin rupture theory, whereby large mechanical stresses experienced by the thin skin during immersion precipitation can lead to points of rupture in the skin from which fingers can be initiated and propagate [28]. Another popular theory attributes the fingers to the growth of nucleated polymer-lean phases in polymer solutions under the circumstance of instantaneous demixing. The theories were built upon from with

more observations and characterisations [29, 30]. However, these theories do not explain the ordered and periodic spacing between the finger-like structures as well as their hierarchical distribution along the depth of the membrane. Furthermore, with polymeric membranes, there is only very limited quantitative data available on the periodic distance between the fingers, despite the unanimous observation of this characteristic from many researchers, due to practical constraints. Therefore other theories put forward to explain the mechanisms behind finger formation also underwent the same bottlenecks with limited supporting experimental data.

Possible origins of the micro-channels are interfacial instabilities, which can arise from many different sources, such as interfacial tension gradients (marangoni instability) [31], viscosity gradients (viscous fingering) [32], or density gradients (Rayleigh-Taylor Instability (RTI) [33-35], and so on. Interfacial instabilities caused by periodic perturbations experienced by the surface of the suspension solution during immersion into another fluid medium can explain the periodic and hierarchical structure of the micro-channels. One possible type of interfacial instability that may cause the formation of the micro-channels is the Rayleigh-Taylor Instability (RTI). It is a naturally occurring phenomenon whereby periodic perturbations at the interface of two fluids with opposite pressure and density gradients destabilise the interface due to acceleration on the interface and can form finger-like structures. In later parts of this chapter, it can be seen that on the suspension/coagulant phase-inversing interface the requirements for RTI to occur are fulfilled and micro-channels can be initialised due to the instability.

This chapter aims to gain more fundamental information regarding the formation of the micro-channels in ceramic membranes by reducing the amount of parameters affecting the phase inversion process. This was achieved by fabricating flat disc ceramic membranes and investigating the effects of using five different solvents as the suspension medium on the final membrane macro- and microstructures, and in particular, the properties of the micro-channels. For the first time, the micro-channels in ceramic membranes have been quantified with their stratified pore densities and periodic distances obtained. An indication of the effect of differences in morphology on membrane performance in possible water treatment was thus investigated by looking at the water permeation fluxes of the 5 membranes. Then a possible mechanism incorporating RTI is proposed to explain the formation of the different membrane microstructures and preliminary experimental values for the

characteristic wavelengths of the different membranes were obtained. These values were mimicked using simulations based on RTI with the conditions of the suspension/solvent/non-solvent system that can be characterised. A possible direction for controlling and engineering the different microstructures is thus suggested.

4.2 Experimental

4.2.1 Materials and membrane preparation

The materials used and the experimental procedures for preparing the ceramic suspensions and disc membranes in this chapter are listed in Section 3.1, 3.2 and 3.3. The composition of the ceramic suspension is displayed in Table 4.1. The membrane precursors were heat treated and sintered at 1350 °C following the heating program described in Section 3.5. The as-obtained membranes are then denoted as Membrane-DMSO, -NMP, -DMAc, -DMF and -TEP according to the solvent used in the preparation.

Table 4.1 Alumina suspension composition for the disc membranes with the solvents: DMSO, NMP, DMAc, DMF and TEP

Component	Composition (wt.%)
Solvent	39.3
Alumina	54.8
PESf	5.5
Dispersant	0.4

4.2.2 Characterisation

The characterisation methods such as SEM, viscosity measurement, mercury intrusion porosimetry, 3-point bending, pure water permeation are listed and described in Section 3.6.

4.3 Results

4.3.1 Rheology of ceramic suspensions

Table 4.2 shows the viscosity values of the 5 suspensions consisting of different solvents at a shear rate of 0.289 s^{-1}. Suspension-TEP has a viscosity over the range at which the viscometer was capable of measuring. During the preparation process difficulty was encountered when suspending the alumina particles in TEP, and solvation of the PESf in TEP was only achieved at 80°C.

It can be seen clearly that the viscosity varies significantly when different solvents are used to disperse the alumina particles and solvate the polymer binder, despite the identical weight composition. In order to scale for the hydrodynamic effects of the different suspending media, the relative viscosities, defined as the ratio of the viscosity of the suspension to the viscosity of the pure suspending media, are also displayed in Table 4.2. The relative viscosity of the suspension increases in the order of suspension- DMF < DMAc < NMP < DMSO < TEP. This is due to the reduction in specific volume of the solvents, as seen in Table 4.2, resulting in higher volume loadings under constant weight fractions, as predicted by the Quemada model for hard sphere systems, in equation 4.1 [36].

$$\mu_r = \left(1 - \frac{\phi}{\phi_{max}}\right)^{-2} \qquad (4.1)$$

Where μ_r is the relative viscosity of the suspension, φ is the volume fraction of ceramic powder, and φ_{max} is the maximum achievable volume fraction of ceramic powder.

Table 4.2 The effect of solvent choice in the ceramic suspension on their measured viscosities and densities

	Suspension				
	DMSO	NMP	DMAc	DMF	TEP
Apparent viscosity η at 0.289 s^{-1} (mPa.s)	7580	5115	3645	1420	N/A
Viscosity of solvent (mPa.s)	1.99	1.70	1.96	0.92	1.60
Relative viscosity η/η_m	3810	3010	1860	1540	N/A
Density at standard conditions (kg/m^3)	1820	1810	1650	1660	1840
Density of solvent (kg/m^3)	1100	1030	940	944	1070

The viscosity of the suspension is an important factor in the formation of ceramic membranes. Often it can have practical implications on the fabrication process; for example, the viscosity can affect the spinnability of the suspensions [7]. Furthermore, the viscosity of the suspension can affect the cross-sectional morphology of the membrane, as high viscosities have been shown to resist the initiation and growth of the finger-like structures that are important in reducing mass transfer resistance during micro- and ultrafiltration processes [37].

4.3.2 Characteristics of micro-channels

4.3.2.1 The morphology of alumina discs

Figure 4.1 shows the cross-sectional morphologies of the 5 different sintered alumina disc membranes. Both asymmetric and symmetric membranes can be formed when the solvent in the suspension is changed. The asymmetric membranes contain sponge-like structures and micro-channels of different characteristics (Membrane-DMSO, -NMP and –DMAc in Figure 4.1a-c) whereas the symmetric membranes (Membranes-DMF and -TEP in Figure 4.1d-e) consist of a sponge-like structure across the entire cross-section. It can be seen that when different solvents are used as the suspension media and solvents for PESf, the difference in membrane morphology is drastic and this may have major effects on membrane performances, for example, the permeation flux.

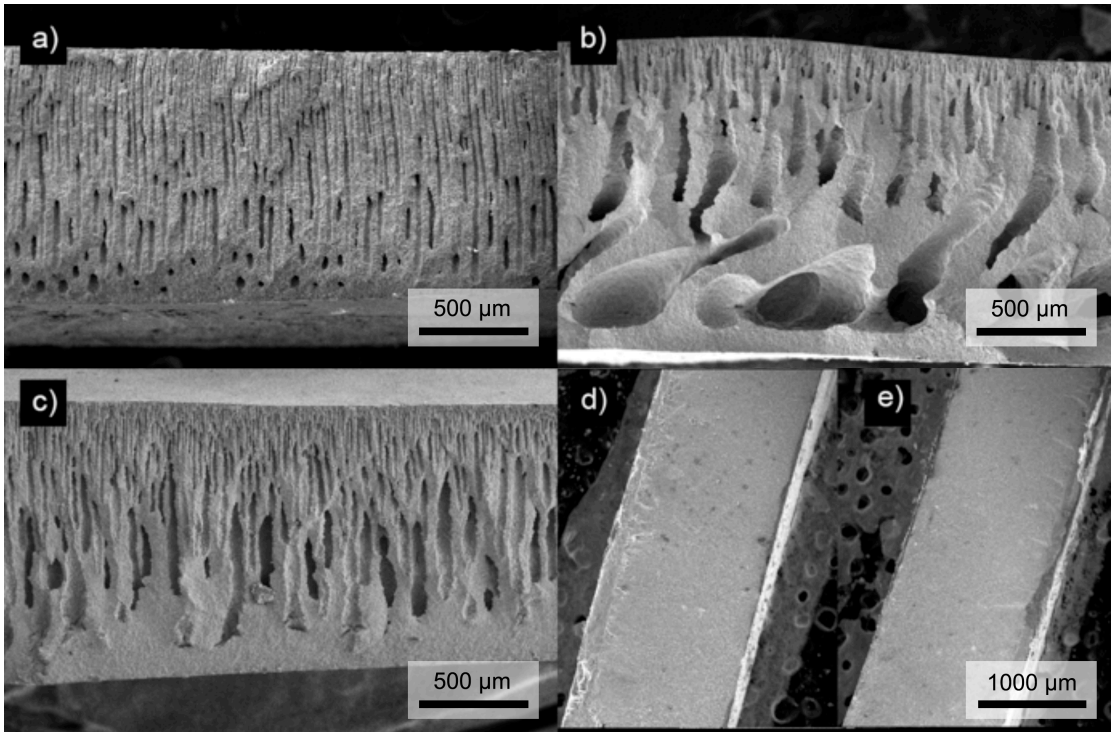


Figure 4.1 Cross-sectional SEM images of a) Membrane-DMSO, b) Membrane-NMP, c) Membrane-DMAc, d) Membrane-DMF, e) Membrane-TEP

When DMSO was used as the suspension medium and solvent, the cross-section of the membrane (Membrane-DMSO in Figure 4.1a) consists of two thin sponge-like layers sandwiching densely packed, long and narrow micro-channels. These micro-channels initiate near the top of the membrane and propagate

downwards, stopping shortly before the bottom of the membrane. When NMP was used, the membrane (Membrane-NMP in Figure 4.1b) has a cross-sectional morphology clearly different to that of Membrane-DMSO's. Although the cross-section also consists of micro-channels, their shape and quantities are quite different. The micro-channels initiate near the top region of the membrane and grow larger in size horizontally as they propagate across the cross-section, forming pear-shaped structures that bend slightly in the lower region of the membrane, as the micro-channels become influenced by the bottom surface of the mould. Figure 4.1c reveals the cross-section of the membrane formed from the suspension that has DMAc as the solvent (Membrane-DMAc). It can be seen that its morphology is similar to that of Membrane-DMSO's but the micro-channels are slightly broadened. The micro-channels initiate at the upper region of the membrane, and grow wider as they propagate the cross-section, forming slight pear-shaped structures. The micro-channels appear less wide than the ones in Membrane NMP.

4.3.2.2 Hierarchical structure of the micro-channels

Upon closer inspection of the upper regions of Membranes-DMSO, -NMP and -DMAc in Figure 4.2, it can be seen that the micro-channels in the membranes present multiple and distinctive levels, separated by their diameter, length and density. Figure 4.3 schematically shows different levels of the micro-channels in a Membrane-DMSO specimen. The micro-channels that propagate the furthest down the membranes have similar lengths and diameters, and can represent the first level. The next level consists of micro-channels that propagate the second furthest down the membrane, which also has smaller diameters, and at the next level the micro-channels are even shorter, and so on. As the levels increase the micro-channel lengths and diameters are reduced and their micro-channel lengths can be used to distinguish these different levels. Different levels of micro-channels can also overlap in the membranes, especially for the higher levels near the top region of the membranes. Furthermore, the number of levels increases in the direction from the bottom of the membrane towards the top, such that the density of the channels is extremely high at the top layer. This result is also very commonly observed in polymer phase-inversion membranes.

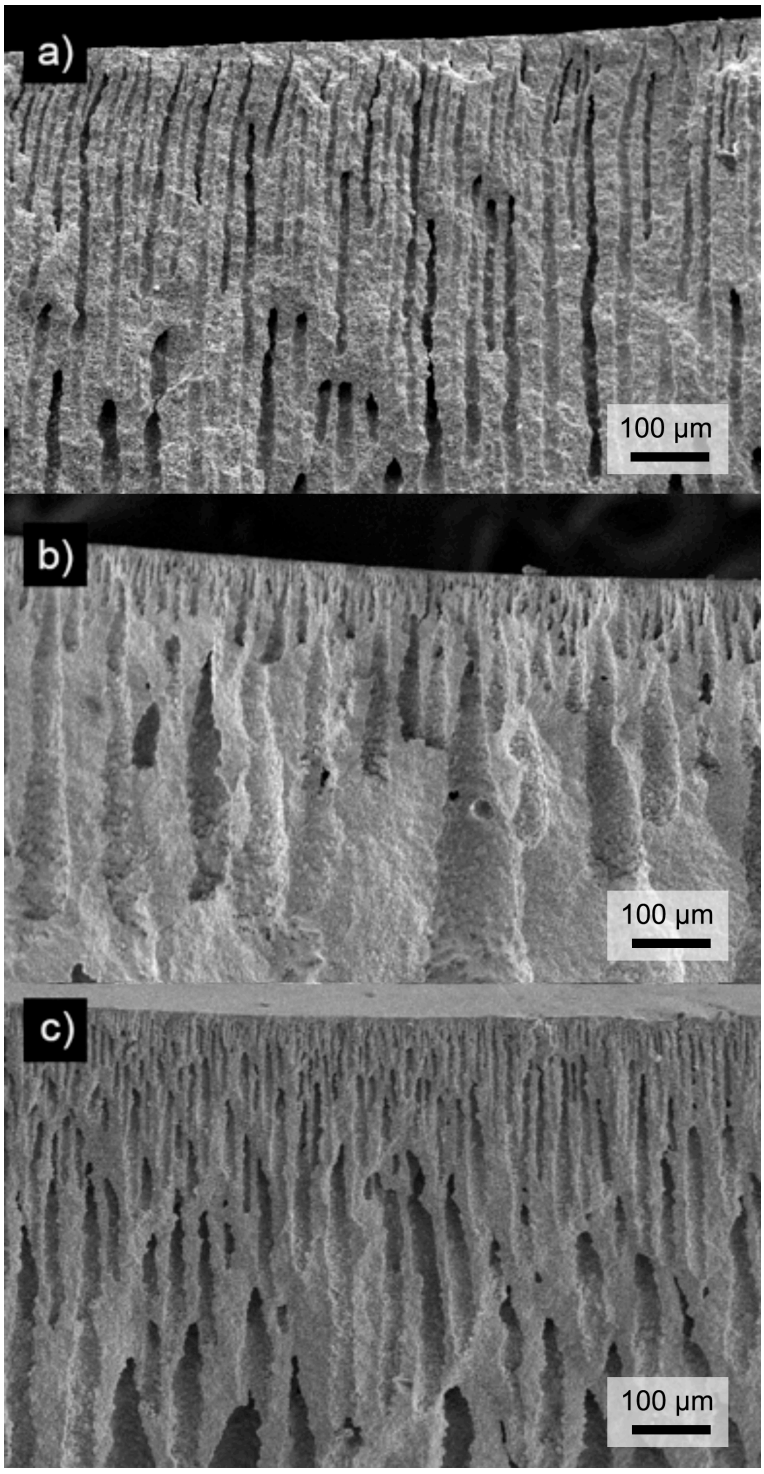


Figure 4.2 Cross-sectional SEM images of the upper region of a) Membrane-DMSO, b) Membrane-NMP and c) Membrane-DMAc

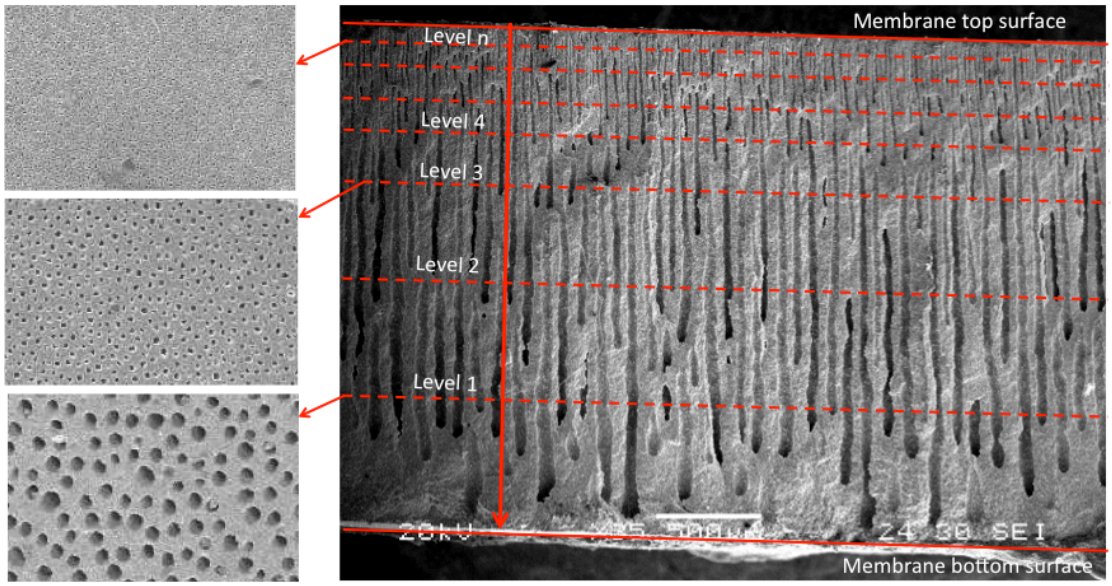


Figure 4.3 Cross-sectional image of Membrane-DMSO with the labelled hierarchical levels

In order to more clearly reveal the hierarchical feature of the micro-channels, the sintered membranes were polished from the top to remove the skin layer of the membranes and thus expose the channels. An example of such polished section close to the top is shown in Figure 4.4. From the image, at least three different sets of micro-channels can be distinguished according to their diameters. The smaller micro-channels are very intensely scattered, whereas the number of the largest micro-channels is the least. These sets of micro-channels are distributed across the plane quite evenly, showing more or less a regular pattern.

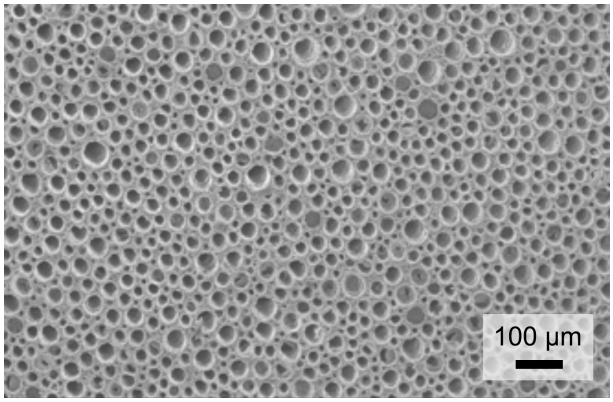


Figure 4.4 A SEM image of a polished section showing the distribution and the multi-level feature of micro-channels. The image was taken from a section close to the top surface of a Membrane-DMSO specimen.

By polishing off different proportions of the sintered membranes, a stratified micro-channel distribution was obtained, whereby the change in micro-channel characteristics along the depth of the membranes is revealed. Figure 4.5 shows the micro-channel density of the membranes on two sections that are close to the top and bottom surfaces, respectively. It is obvious from Figure 4.5 that the density of the micro-channels decline drastically along the thickness direction for each membrane type, and the diameter of the micro-channels increase considerably. Table 4.3 displays the micro-channel density extracted from SEM images at the different strata. It is worth to mention that during the practice, the minimum depth at which the micro-channels can be distinguished under SEM is 40, 30, and 10 μm for the membrane-DMSO, membrane-NMP and membrane-DMAc, respectively. The skin layer that is polished off is composed of the packing pores between the ceramic particles.

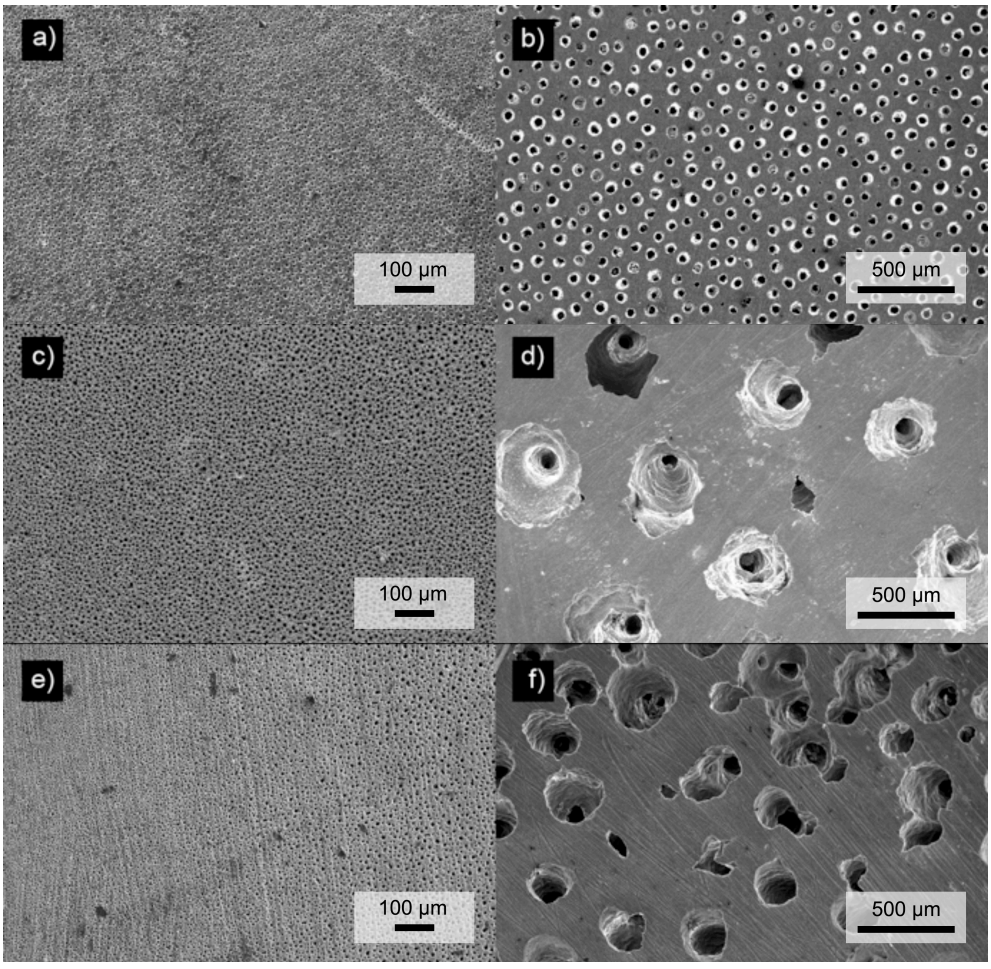


Figure 4.5 SEM images of the sections close to the membrane upper and lower surfaces. The sections were exposed after polishing off 20-30 % of the membrane thickness. (a-b) Membrane-DMSO, (c-d) Membrane-NMP and (e-f) Membrane-DMAc, respectively

Table 4.3 shows the density of the micro-channels decline along the depth direction of the membrane, with the most drastic changes close to the top surface. The rate of change of channel density is softened across the depth of the membrane. The rate of change of micro-channel density with respect to depth is compared in Figure 4.6, whereby the difference in channel density across adjacent sections is normalized with the distance between them. It can be seen that for all three membranes, the rate of channel density reduction is the highest at the top layer, and then decreases quickly at deeper positions. Interestingly, the changing rate shows roughly an exponential relation to the depth for all three membranes. An exception is found for the Membrane-DMAc samples, in which the highest changing speed is recorded at the layer between 40 and 50 μm, rather than the layer closer to the top surface between 10 and 40 μm.

Table 4.3 The density of micro-channels on sections of different depths with standard deviations of within 15 %

Membrane depth	Micro-channel density (mm^{-2})		
(μm)	Membrane-DMSO	Membrane-NMP	Membrane-DMAc
10			56700
30		12300	
40	7910	4330	32400
50		2620	11300
60			6590
70		2040	
100		1290	2910
200	2200	254	892
300	1340	177	537
400		127	278
500	735	97.5	173
1000	414		
1500	83.4		

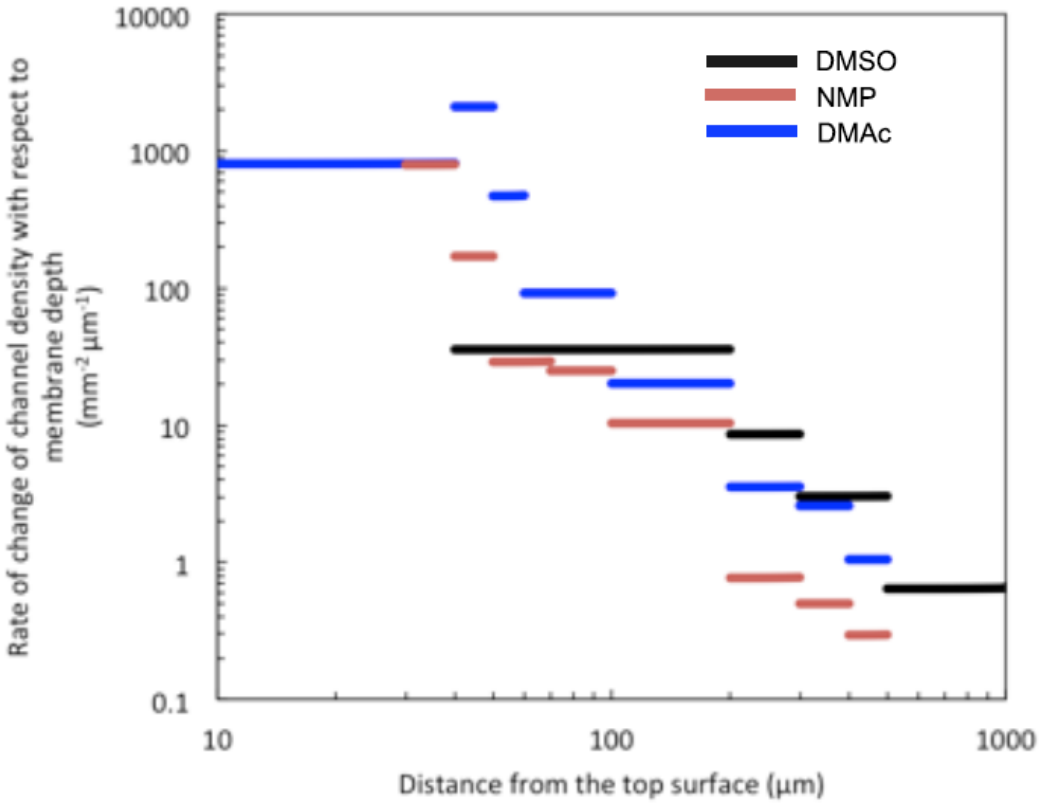


Figure 4.6 The rate of change of micro-channels density with respect to the depth of the membrane. The data were extracted from Table 4.3.

The effect of solvent in the ceramic suspension on the membrane structure is also further revealed from the different membranes' stratified micro-channel distribution, in Figure 4.6, and Table 4.3. The highest micro-channel density is found near the top of membrane-DMAc, followed by membrane-NMP, then membrane-DMSO. It can be seen that Membrane-DMAc has the most asymmetric cross-section structure, with the initial micro-channel density at the top layer being more than 300 times the density at the lower region. Membrane-NMP is also highly asymmetric with the initial micro-channel density being more than 120 times higher than the density at the lower region. Finally, the top-to-bottom micro-channel density ratio for Membrane-DMSO is around 90, slightly lower than the other two membranes.

4.3.3 Water permeation and pore structure

Table 4.4 shows the water permeation flux of the 5 membranes under dead-end filtration at 1 bar trans-membrane pressure. The rank of water permeation flux from lowest to highest goes in the order of Membrane-TEP < Membrane-DMF < Membrane-NMP < Membrane-DMAc < Membrane-DMSO. It can be seen that Membrane-DMSO has the highest water permeation flux of up to 5440 L/m^2 bar h. Membranes-DMF and TEP have the lowest water permeation flux of less than 250 L/m^2 bar h. It is apparent that the increment in water permeation flux is not linear to the decrease in membrane thickness, contrary to what is stated by the Carman-Kozeny models, due to differences in the cross-section morphology and the pore structure of the membranes. The most dramatic permeation flux increase occurs when the micro-channels are present in the membrane cross-section, i.e., in Membrane-DMSO, Membrane-NMP and Membrane-DMAc, due to the much thinner effective membrane thickness. Membrane-DMF and Membrane-TEP have very low fluxes, as there are no micro-channels in the cross-section and the effective thicknesses of the membranes are the highest. The function of micro-channels in the reduction of transport resistance of water can be evaluated by the water permeation fluxes with different configurations.

Table 4.4 Water permeation flux, thickness and average pore size of the 5 membranes with standard deviations of within 25 %

Membrane	DMSO	NMP	DMAc	DMF	TEP
Water permeation flux (L/m^{2}bar h)	5440	1010	1160	232	86.5
Membrane thickness (mm)	1.58	1.85	1.66	1.910	2.108
Average pore size (μm)	0.344	0.253	0.280	0.308	0.210

In another experiment, the lower sponge-like layer of Membrane-DMSO, Membrane-NMP and Membrane-DMAc were polished off and the water permeation flux was measured again, which are shown in Table 4.5. The water permeation fluxes

all increase remarkably with the lower sponge-like layer removed, but Membrane-DMAc underwent the largest flux increase, from 1160 L/m^2 bar h to 12300 L/m^2 bar h. In the membranes with micro-channels, the resistance to water permeation is distributed between the top and the bottom sponge-like layer as well as the middle region of micro-channels. By assuming that the majority of the permeation resistance is in the sponge-like layers, the increase of flux after removing the bottom sponge layer can be used to predict the effective thickness of the membranes, as listed in Table 4.5. The actual thickness of the bottom sponge-layer is easy to obtain from SEM images, but the top sponge-layer is hard to tell. It can be recalled from the previous section that the micro-channel openings start to appear only if the top sponge layer is polished off 40, 30, 10 μm for Membrane-DMSO, Membrane-NMP and Membrane-DMAc, respectively, thus these values can be taken as the thicknesses of the top sponge-like layer. The thicknesses of sponge layers and the ratio between the total sponge layer thickness and the top sponge layer thickness are listed in Table 4.5, together with the ratio of water fluxes before and after removing the bottom sponge layer. It is quite clear that for Membrane-DMSO and Membrane-DMAc, the two ratios are rather close, implying that the majority of the permeation resistance does distribute in the sponge-like layers, and the resistance in the region of micro-channels is minor. For Membrane-NMP, there is an obvious deviation between the two ratios, which implies a certain significant resistance in the micro-channels. It can be estimated that the resistance in the micro-channel structure of Membrane-NMP is equivalent to a 76 μm thick sponge-like layer, but only 12 and 4 μm for Membrane-DMSO and Membrane-DMAc, respectively. Even for Membrane-NMP, the effective thickness of the micro-channel region is still largely reduced compared to the apparent membrane thickness. The difference of the resistance to water permeation in the region of micro-channels between Membrane-NMP and Membrane-DMSO, Membrane-DMAc can be reasonably attributed to the structure of the micro-channels themselves. As a matter of fact, the density of micro-channels is the lowest in Membrane-NMP among the three membranes with micro-channels (in Table 4.3, by comparing the number of micro-channels on the sections with same depth), which would lead a higher resistance when compared with Membrane-DMSO and Membrane-DMAc.

Table 4.5 The correlation of water permeation (standard deviations within 25 %) and macrostructure for Membranes-DMSO, NMP and DMAc.

Sample	Water permeation flux (L/m^{2}bar h)		Ratio of the fluxes after and before the removal	Thickness of sponge-like layer (μm)		Ratio of the sponge layer thicknesses (Top+bottom)/top	Estimated membrane thickness from Ratio of fluxes (μm)
	Prior to sponge layer removal	After Bottom sponge layer removal		Top	Bottom		
DMSO	5440	8600	1.58	40	30	1.75	76
NMP	1010	1960	1.94	30	100	4.33	12
DMAc	1160	12300	10.6	10	130	14.0	4

It is worth noticing that even if the effective thickness is taken into account (the total thickness of sponge-like layers), the permeability of Membrane-DMSO is still considerably higher than Membrane-NMP and Membrane-DMAc. This can be explained by the average pore size in the sponge-like layer of the membranes. Table 4.4 also gives the average pore sizes from mercury porosimetry tests. The pore size is the largest in Membrane-DMSO, about 344 nm, which would give a 50% higher permeability of the sponge-like layer than Membrane-DMAc and an 85% higher permeability than Membrane-NMP. It is evident that the choice of solvent affects not only the macrostructure, but also the microstructure of the membranes.

The water permeation fluxes of the asymmetric membranes are compared with commercial ceramic membranes, as listed in Table 4.6. After the removal of the bottom sponge-like layer, Membrane-DMSO and Membrane-DMAc have comparable water permeation with the silicon carbide flat disc membranes from Liqtech Ltd, considering the differences in the membrane pore size. This is interesting as SiC membranes are intrinsically more hydrophilic and generally have higher water permeation fluxes than alumina membranes, which makes the asymmetric membranes with micro-channels formed in this study highly competitive in the ceramic membrane market. Compared to other alumina membranes that are used in MBRs, such as the flat sheet membranes from Meidensha Corporation, the water permeation

fluxes of Membrane-DMSO and Membrane-DMAc formed in this study are significantly higher. This means that asymmetric alumina membranes with micro-channels can potentially be competitive alternatives to use in MBRs.

Table 4.6 Comparison of the properties between the alumina membranes with micro-channels formed in this study and commercial ceramic membranes

Membrane type		Configuration	Water permeation flux (L/m^2 h) at 1 bar	Material	Pore size (μm)
Membranes with micro-channels	Membrane-DMSO	Flat disc	8, 600	α-Al_2O_3	0.34
	Membrane-DMAc (bottom layer removed)	Flat disc	12, 300	α-Al_2O_3	0.28
Commercial membranes	Liqtech Ltd [38]	Flat disc	4, 000	SiC	0.10
	Meidensha Corporation [39]	Flat sheet	1, 670	α-Al_2O_3	0.10

A tensile tester was used to gather information about the membranes' mechanical stability using the three-point bending method. It can be seen from Table 4.7 that the flexural stress of the asymmetric structures is generally lower than the symmetric ones. Overall, due to the thinness of our samples as well as the low sintering temperature used, the mechanical stability is quite low. However, the mechanical strength of these disc membranes are arbitrary and it would be unfair to compare them with commercial membranes that are usually sintered at much higher temperatures. It has been shown in this study that water permeation flux is independent to the overall membrane thickness when there are micro-channels present, and that majority of the mass transfer resistance is located at the top separation layer. Therefore, the mechanical stability of these membranes could be greatly improved by making thicker membranes with micro-channels and then

manually removing the bottom sponge-like layer. As suggested, the properties of a range of different commercial multilayer supports have been compared and added as a table in the manuscript to compare some of the experimental membranes with commercial membranes in terms of water permeation flux, pore size and material (Table 4.6).

Table 4.7 Mechanical stability of the alumina disc membranes made from different solvents with standard deviations of within 35 %

	Membrane				
	DMSO	NMP	DMAc	DMF	TEP
Flexural stress (MPa)	16.8	12.1	22.5	22.8	35.2

4.4 Discussions

4.4.1 The hierarchical micro-channel structure and linear stability theory

From the description in section 4.2.2, it is very clear that the micro-channels formed during the phase-inversion process have the following two features:

- The micro-channels distribute uniformly on the planes parallel to the surface and the channels form regular patterns;
- The micro-channels can be distinguished into multiple levels in terms of length, diameter and density.

The first feature has long been noticed in polymer phase-inversion membranes, and some researchers have related it to the periodical surface disturbing waves, which can explain the regular distribution reasonably well while other proposed mechanisms fail [40]. These theories analyse the stability of the waves, assuming the wavelength of the surface disturbance ranges linearly from zero to infinity. The major task of the linear stability analysis is to find out the most probable wavelengths, at which the instability of the wave grows the fastest, and consequently the waves disturbing the surface are amplified to initiate the micro-channels in the membrane [41]. The

instability of surface disturbances may arise from a range of different sources, such as of surface tension gradients (the Marangoni effect) [31], the difference in viscosity or density between two contact fluids [32, 35], or the gradient of solidification and shrinkage rate along the interface [42]. Inspired by Sternling and Scriven [31, 43], Frommer et al. incorporated the idea of Marangoni instability to explain the fingers in phase-inversion membranes. Sternling and Scriven had derived in their article that the gradient of surface tension led by the diffusion of mass or heat may amplify small disturbances on the interface between two fluids. In their derivation, Sternling and Scriven include the diffusivity of the species, the chemical potential gradient, the viscosity, the density, and the sign of the change of surface tension with surface species [31]. This comprehensive model comprises of the factors that are deemed important in membrane fabrication. Frommer et al. failed to use a quantitative approach to apply the theory of Marangoni instability to the phase-inversion membranes, and their interpretation was mainly qualitative. Consequently, Ray suggested that the growth of fingers in membranes induced by the Marangoni instability would be too slow, mainly due to the very high viscosity. However, in reality, the formation of fingers is very fast and hence Ray denied the Marangoni instability as the main mechanism, and proposed that another source of surface instability, the excess intermolecular potential, should be responsible for the fingers. Based on the theory, Ray derived that the distance between the longest fingers (the most probable wavelength) is 4.2 times of the membrane thickness [40]. Although in their experimental results they did get a distribution of the ratio from 2.5 - 5.1, it should be noted that Ray used the thickness of the final membrane as the reference, instead of the thickness of the cast solution that appears in the derivation. It is a common sense that the thickness of the final membrane is usually several times smaller than the cast solution, thus the actual wavelength/thickness ratios were far from 4.2, making the theory invalid here. Another theory based on interfacial instability is the viscous fingering theory, which was first introduced by Lal & Bansil and Ren et al. to interpret fingers in polymer membranes [44, 45], which was applied to the phase inversion process of ceramic/polymer/solvent suspension systems [24, 37]. The viscous fingering theory suggests that the viscosity difference is responsible for the formation of fingers, however it can be frequently found that viscosity hinders the finger to grow, thus leaves this theory questionable. Addad and Panine proposed that there is a “diffusional shock” of the interface between the solution and the

coagulant bath when both phases are in contact, which may lead to the Rayleigh-Taylor hydrodynamic instability originating from the density difference between the solution and the coagulant bath [46]. With the hypothesis, they correlated the mean distance between the finger entrances on membrane surface to the diffusivity of the solvents. Their theory did not draw much attention, but it does give light to the source of the driving force of finger initialization, though some of their theory was over simplified.

The second feature of multi-level micro-channels has also been noticed in the membrane community, but has not been clearly characterized until this research. This feature is not easy to quantify for polymer membranes because of the three-dimensional arrangement, although some preliminary studies have been done with 3-D topological techniques [47-49]. For ceramic membranes, it is much easier to do by polishing as shown in this study. Previous hypothesises using linear stability analysis only tackled the most advanced fingers and were not able to even qualitatively interpret the multi-level feature, largely because the feature itself has not been clearly revealed. In the following discussion, the multi-level feature can be seen as a projection of the solution of the instability equations.

4.4.2 The Rayleigh-Taylor Instability hypothesis

Phase inversion is an extremely complex process accompanied by plenty of mechanical, physical and chemical interactions. Focusing on the interfacial changes when the ceramic suspension contacts the coagulant, some characteristics listed below can be extracted:

- There is a difference of density, viscosity, composition across the suspension solution/coagulant interface;
- The interface moves towards the suspension side because of the extraction of solvent and the contraction of polymer;
- The interface itself starts to change because of the transfer of mass and heat, including the change of interfacial tension, viscosity, density and solidification. Gradients of such properties along the interface may appear.

Thus, the interface is a moving one between two liquids with considerable density and viscosity difference accompanied by heat and mass exchange. Many factors involved here may lead to instability of the interface separately or conjunctionally, as mentioned above. It should be pointed out that there is another important factor that has been ignored for a long time: the initial acceleration of the interface. As the interface moves towards the suspension side from still to a considerable velocity, the interface must have accelerated to reach its maximum velocity. This acceleration is actually the "diffusional shock" as has been mentioned by Added and Panine [46]. An instantaneous contraction of the interface under microscopes can often be observed when the solution is in contact with water, followed by micro-channel formation, which supports the existence of the accelerated interfacial movement.

The equation describing the moving interface during phase inversion is recalled [50]:

$$\frac{\partial X(t)}{\partial t} = J_S^{\emptyset} + J_C^{\emptyset} \tag{4.2}$$

Here X(t) is the position of the interface as a function of time, $J_S^{\emptyset}$ is the volume flux of the solvent from the solution to the coagulant, and $J_C^{\emptyset}$ is the volume flux of the coagulant diffusing to the solution. Then the acceleration of the interface would be

$$\frac{\partial^2 X(t)}{\partial t^2} = \frac{\partial J_S^{\emptyset}}{\partial t} + \frac{\partial J_C^{\emptyset}}{\partial t} \tag{4.3}$$

If the out flux of solvent is assumed to be considerably faster than the influx of the coagulant, then the magnitude of the acceleration can be estimated as Added and Panine [46].

$$\frac{\partial J_S^{\emptyset}}{\partial t} = \left[\frac{(\emptyset_S - \emptyset_C)}{1+\sqrt{D_S/D_C^H}}\right] D_S^2 \left(\frac{1}{2D_S t}\right)^{3/2} / \sqrt{2\pi} \tag{4.4}$$

Here φ_S and φ_C are the concentration of the solvent in polymer solution and coagulant bath, respectively, and D_S and D_C^H are the diffusion coefficient of the solvent in ceramic suspension/polymer solution and the coagulant bath.

At the moment when the coagulant bath contacts the solution, $t \rightarrow 0$, recommendations from Added and Panine were used, and the time needed for a diffusion process was set to 2×10^{-8}s, and D_S with a magnitude of 10^{-10} m^2/s, D_C^H with a magnitude of 10^{-9} m^2/s, which agreed with experimental values [46]. The magnitude of the interfacial acceleration is found to be around 10^5-10^7 m/s^2, which is a very high

acceleration. Note that when the outflow of the solvent is faster than the inflow of the coagulant, which is the case for most phase-inversion process, the acceleration is directed from the lighter coagulant phase to the heavier solution, and this scenario meets the requirement for facilitating the Rayleigh-Taylor instability.

Rayleigh-Taylor instability happens when there is acceleration on the interface between two fluids of different densities, to be specific, acceleration towards the heavier fluid. The instability rises from perturbing waves on the interface, where some of the waves can be amplified by the acceleration. Here the interface between the ceramic suspension and the coagulant are considered, and treated as two incompressible immiscible fluids (in real phase-inversion process, there is solvent/coagulant exchange between the polymer solution and the coagulant, strictly speaking it is not an immiscible situation. However since there is always a distinct interface between them, it can be deemed an immiscible case but with varying densities, viscosities and interfacial tension). Figure 4.7 gives a simple depiction of a two-dimensional perturbation on the interface, whose wavelength is λ and the initial amplitude is η_o.

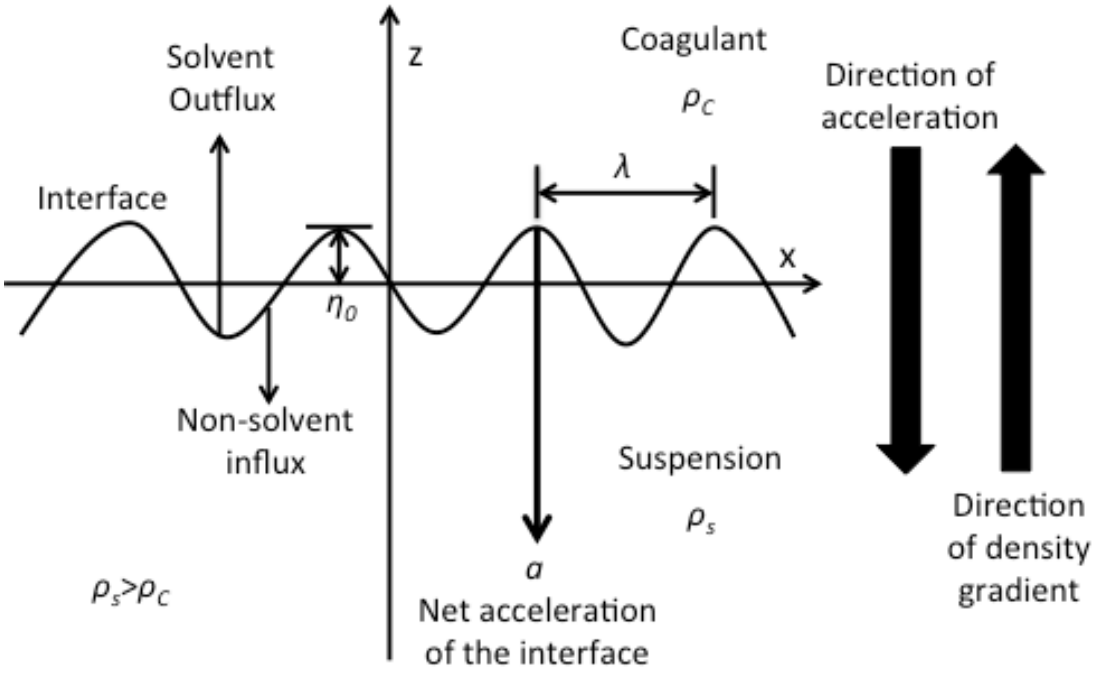


Figure 4.7 Two-dimensional perturbations on the interface of the suspension/solvent/non-solvent system during phase inversion

Under acceleration a directed towards the heavier ceramic suspension, the interface will be unstable and the perturbation will grow. Without considering the effect of viscosity, the growth rate of the perturbation will be [34]

$$\eta(t) = \eta_0 \cosh(nt) = \eta_0 \frac{e^{nt}+e^{-nt}}{2} \tag{4.5}$$

Here η(t) is the amplitude at time t, and

$$n^2 = a\left(\frac{\rho_s-\rho_c}{\rho_s+\rho_c}\right)k - \left(\frac{T}{\rho_s+\rho_c}\right)k^3 \tag{4.6}$$

Where ρ_s and ρ_c is the density of the ceramic suspension and coagulant, respectively, and T is the interfacial tension.

To allow the interface to be unstable, the right side of Equation 4.6 must be positive, thus a critical wavelength of the perturbation is required:

$$\lambda_c = \sqrt{\frac{T}{a(\rho_s-\rho_c)}} \tag{4.7}$$

A perturbation whose wavelength is shorter than the critical value would be pushed back by the interfacial tension, and longer waves will grow and lead instability of the interface. Although the critical wavelength was induced without considering viscosity, it is not affected by the viscosity, and valid for viscous conditions.

Equation 4.6 also implies a wavelength at which the disturbance grows fastest, which will dominate the growth when R-T instability happens. Without consideration of viscosity, the wavelength of the fastest growth is

$$\lambda_m = \sqrt{3}\lambda_c \tag{4.8}$$

In reality, the effect of viscosity must be considered. In this case, the equation describing the relation between the growth rate and wave number is [51]

$$-\left\{\frac{ak}{n^2}\left[(\alpha_s-\alpha_c)+\frac{k^2T}{a(\rho_s+\rho_c)}\right]+1\right\}(\alpha_c q_s+\alpha_s q_c-k)-4k\alpha_s\alpha_c+\frac{4k^2}{n}(\alpha_s\nu_s-\alpha_c\nu_c)\{(\alpha_c q_s-\alpha_s q_c)+k(\alpha_s-\alpha_c)\}+\frac{4k^3}{n^2}(\alpha_s\nu_s-\alpha_c\nu_c)^2(q_s-k)(q_c-k)=0 \tag{4.9}$$

Where ν is the kinematic viscosity, linked with viscosity μ by ν=μ/ρ,

q is defined by

$$q_s = \sqrt{k^2 + \frac{n}{\nu_s}} \tag{4.10}$$

and

$$q_c = \sqrt{k^2 + \frac{n}{\nu_c}} \tag{4.11}$$

And α is defined by

$$\alpha_s = \frac{\rho_s}{\rho_s + \rho_c} \tag{4.12}$$

and

$$\alpha_c = \frac{\rho_c}{\rho_s + \rho_c} \tag{4.13}$$

the subscript s and c denotes the phase of ceramic suspension and coagulant, respectively.

By solving equation 4.9, the wavelengths (the mean distance between micro-channels) at which the micro-channels grow faster than others can be determined. To give an impression of how the R-T instability theory predicts the pattern of micro-channels, two examples of the solution to equation 4.9 are given. Figure 4.8 and Figure 4.9 shows the k-n curve as the result of solving equation 4.9 and a simple visualisation of the membrane cross-section structure under acceleration of 10^4 m/s^2 and other conditions mimicking a typical phase-inversion system, respectively. It gives a dominating wavelength λ_m at 25.0 mm that has the highest growth number of 469, and also the secondary and the third extremums at 5.30 mm and 4.63 mm, respectively. In this circumstance, the secondary and the third extremums have a much smaller growth number than the dominating wavelength, thus micro-channels originating from these wavelengths would be much smaller than the primary micro-channels. If the precipitation front of the polymer is faster than the growth of the secondary micro-channels, these micro-channels will be frozen at the very beginning and may not appear as observable features. Therefore in this case, the pattern of micro-channels would be relatively simple, with one set of dominating micro-channels and possibly very small micro-channels close to the top. Figure 4.10 is another typical k-n curve from the solution of Equation 4.9, which was obtained under acceleration of 10^7 m/s^2 and other conditions kept the same with those in Figure 4.8 and it is apparent that it is very different. The dominating wavelength λ_m is at 271 μm,

with the highest growth number of 8.4×10^6, much higher than that in Figure 4.8. Figure 4.10 shows an oscillation feature with intensive secondary extremums at shorter wavelengths. The wavelengths of the first few secondary extremums are comparable with the dominating one, indicating that the micro-channels from these disturbing waves have shorter but comparable dimensions. There are many smaller oscillations at the high wavenumber region, indicating that there will be intensive smaller micro-channels close to the top surface.

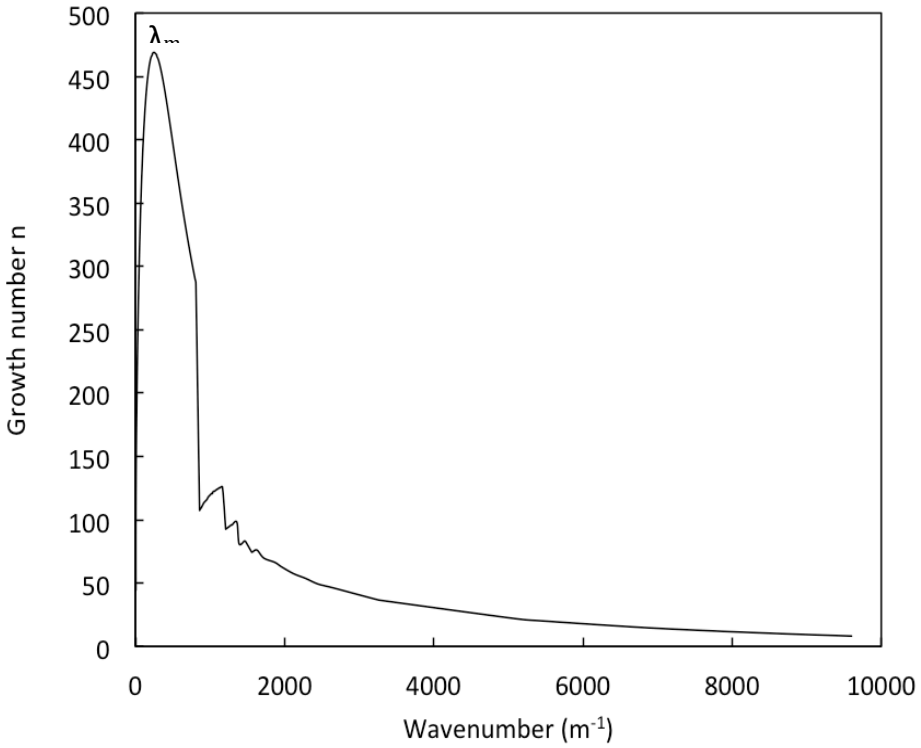


Figure 4.8 An example of the k-n curve showing the solution of the R-T Instability equation (Equation 4.9). Parameters used for the calculation: ρ_c=1000 (Kg/m^3), ρ_s=1500 (Kg/m^3), μ_c=0.001 (Pa·s), μ_s=10.000 (Pa·s), T=0.02 (N/m), and $a=1\times10^4$ (m/s^2)

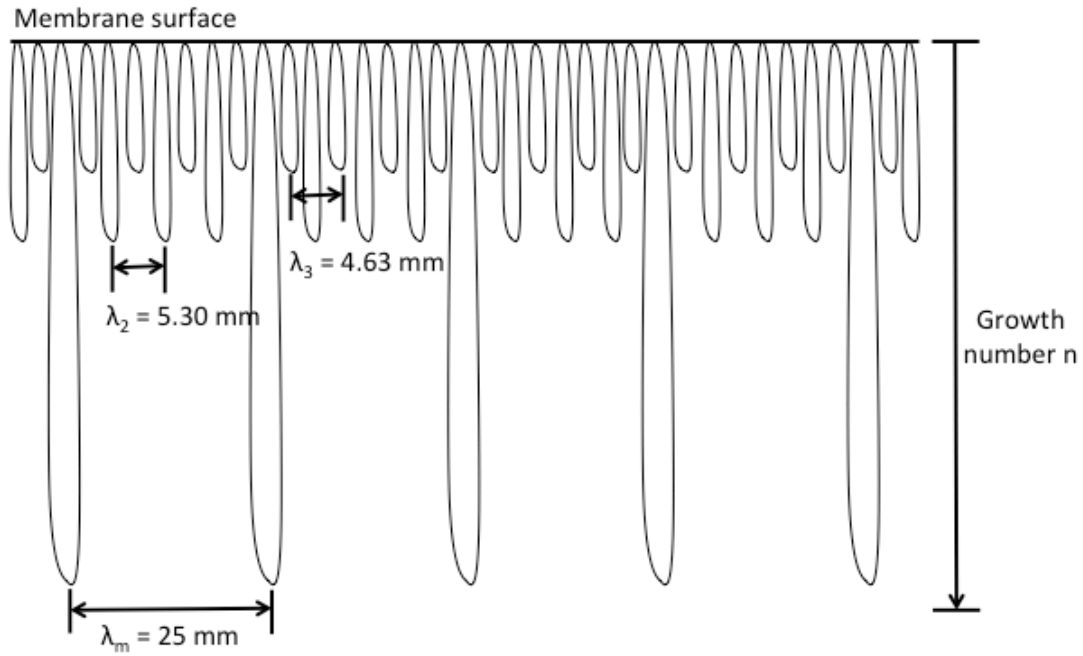


Figure 4.9 Cross-sectional schematic of a membrane formed via phase inversion with micro-channels visualising the solution in Figure 4.8

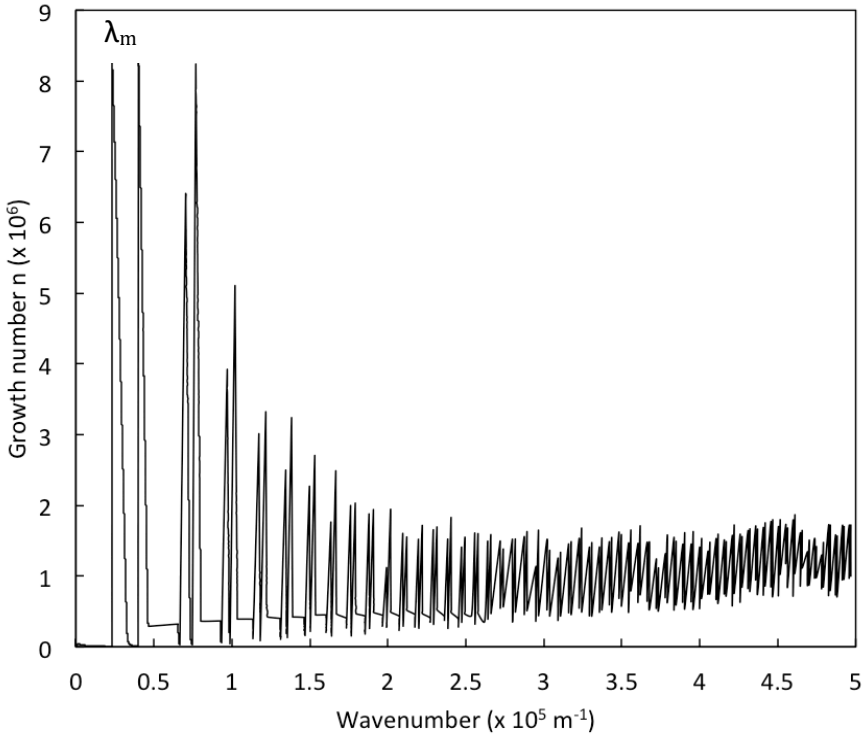


Figure 4.10 An example of the k-n curve showing the solution of the R-T Instability equation (Equation 4.9). Parameters used for the calculation: ρ_c=1000 (Kg/m^3), ρ_s=1500 (Kg/m^3), μ_c=0.001 (Pa·s), μ_s=10.000 (Pa·s), T=0.02 (N/m), and a=1×10^7 (m/s^2)

Apparently, with a higher interfacial acceleration, the number and the length of micro-channels will increase remarkably. Recall from Equation 4.4 that acceleration is directly related to the diffusion of the solvent; a faster solvent diffusion outwards often implies higher accelerations, and so it is not difficult to deduce that fast solvent diffusion often leads micro-channel formation in membranes, which has been intensively observed and discussed in the membrane community. Of course in equation 4.9, other factors such as density, viscosity, surface tension are also included, thus they will affect micro-channel formation too, and those effects can be evaluated by solving the equation.

4.4.3 Mimicking the experimental results with the RTI theory

Based on the linear stability hypothesis, each micro-channel can be deemed as the development of interfacial disturbing waves, thus the mean distance between two micro-channels can represent the wavelength, provided that micro-channels from different wavelengths can be properly distinguished. The mean distance between micro-channels (the wavelength) can be obtained from the micro-channel density (number per unit area) by assuming maximum hexagonal arrangement of the micro-channels:

$$\mathrm{d}_f = \frac{2\sqrt{3}}{3\lambda^2} \tag{4.14}$$

The hexagonal arrangement is justifiable as it has been commonly observed on interface and it is a preferred pattern of interfacial disturbance.

With Equation 4.14, micro-channel densities found on the sections of ceramic membranes (Table 4.3) can be converted to wavelengths. The converted results are listed in Table 4.8, in which the shrinkage after sintering has been considered to restore the real value in the green membranes. For all three membranes, the minimum wavelengths are similar and around 10 μm, whereas the maximum wavelength is 132 μm for Membrane-DMSO, and 227 μm, 253 μm for Membrane-NMP, Membrane-DMAc, respectively. It is worthy to point out that this conversion is rather approximate, because the multi-level micro-channel structure in the samples of present research implies overlapping of projections of different sets of micro-channels

with varied wavelengths. To minimise the influence of overlapping, the micro-channel density of each stratum is subtracted by the micro-channel density of the next stratum from the bottom of the membrane. However the overlapping between the adjacent strata still affects the accuracy of the wavelength. It is obvious that the influence of overlapping is less for the sections closer to the bottom and more severe for the sections closer to the top surface. Due to this reason, the conversion from micro-channel density to the wavelength is unlikely to be reliable for Membrane-NMP. This is because the maximum depth polished for Membrane-NMP is only 500 μm, far from the whole thickness of the membrane, which imply a severe deviation from the true value due to the overlapping effect. Counting the micro-channel number on the sections deeper than 500 μm had been impossible for Membrane-NMP. This is because the lower part of the micro-channels is severely diverted and the micro-channel wall breaks, caused by the influence of the bottom of the mould, and makes it impractical to count the actual number of micro-channels.

To verify the validity of R-T Instability model in the micro-channel formation process, the density and the viscosity of the ceramic suspensions have been measured (Table 4.2) for the input of equation 4.9. The tension of the suspension/water interface is difficult to measure as it changes too quickly, but the effect of interfacial tension can be deemed ignored in this scenario because of the high acceleration and high viscosity. The acceleration of the interface at the moment of contact is not measurable as it happens under an extremely short time scale, but as mentioned above, a typical magnitude for a micro-channel forming solvent/ceramic suspension/non-solvent system is 10^6 m/s^2, thus this value will be guessed within a reasonable deviation range to solve Equation 4.9.

Table 4.8 Wavelength converted from the density of micro-channels in Table 4.3

Membrane depth (μm)	Wavelength (μm)		
	Membrane-DMSO	Membrane-NMP	Membrane-DMAc
10			8.10
30		13.8	
40	16.0	29.8	12.2
50		50.9	18.5
60			20.8
70		45.2	
100		38.2	28.1
200	41.1	140.0	67.0
300	49.2	175.0	78.4
400		226.6	123.8
500	67.4	124.8	95.9
1000	66.5		253
1500	132.4		

Figure 4.11 gives the result of a simulation for Membrane-DMSO using an acceleration of 4×10^6 m/s^2. The simulation result shows an oscillation similar to Figure 4.10, indicating a multi-level micro-channel structure, which is true in the real membrane. In the simulation, the acceleration is chosen so that not only the wavelength, but also the order of the growth number will match the experimental results. There is a reasonable assumption that the disturbances with a larger growth number will go further from the surface of the membrane, and the order of growth number at different wavelengths can be obtained from the depth of the section in Table 4.8.

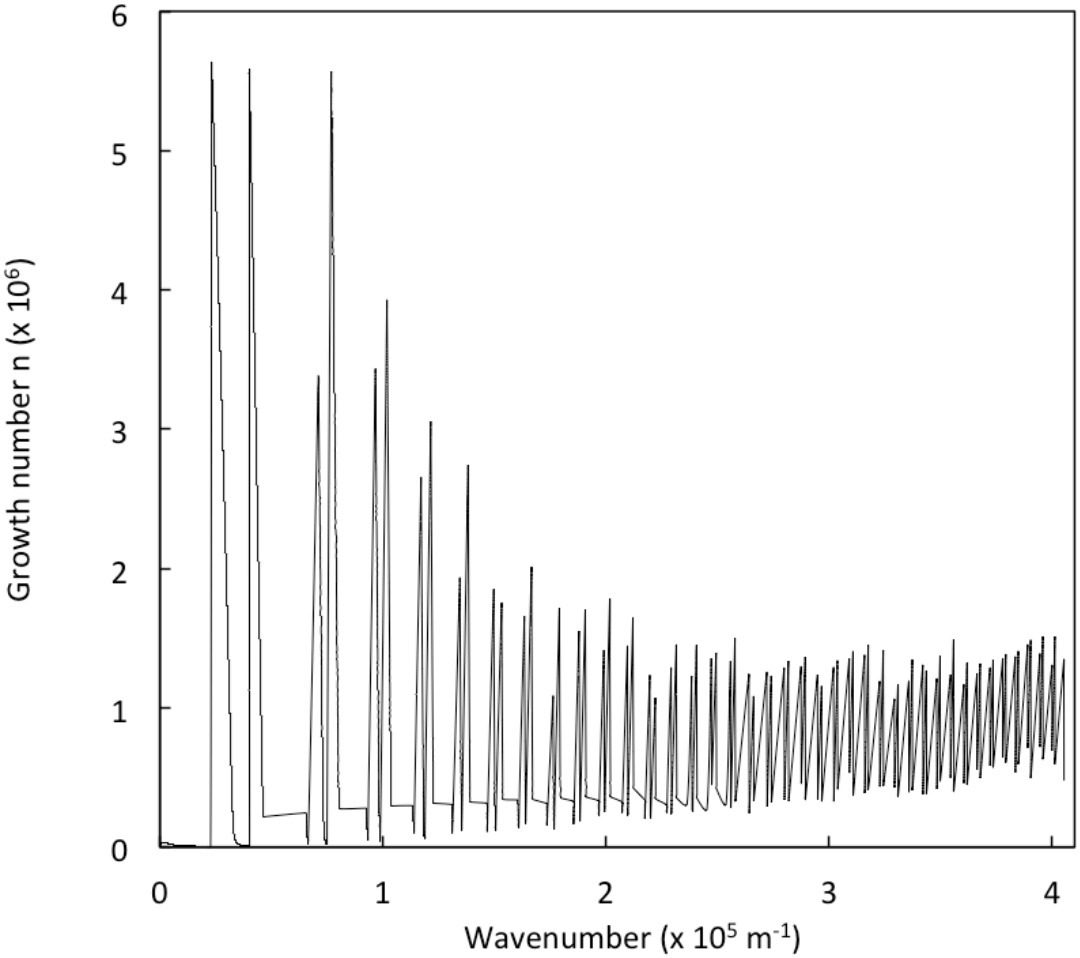


Figure 4.11 Simulation growth number vs wavenumber for Membrane-DMSO. Parameters used for the calculation: ρ_c = 1000 (kg/m^3), ρ_s = 1820 (kg/m^3), μ_c = 0.001 (Pa.s), μ_s = 7.58 (Pa.s), T = 0.02 (N/m) and a = 4x10^6 (m/s^2)

Table 4.9 gives a comparison between the simulation and the experimental results, from which both the wavelengths of interest and the order of growth number/micro-channel length match very well with errors of less than 16%. In the simulation result, the highest peak actually lies at the wavelength of 271 μm, which is missing in the experimental data because of the difficulty in choosing the section in the experiment. However, it has been found in other specimen the spacing of the longest micro-channels lie around 300 μm, very close to the theoretical wavelength.

Table 4.9 Comparison between the experimental and the simulation results of the micro-channel structure of Membrane-DMSO

Simulation results			Experimental results			% error of the wavelength
λ (μm)	n ($\times 10^6$)	rank of n	λ (μm)	depth (μm)	rank of the depth	
156.5	5.590	1	132.4	1500	1	15.4
65.0	3.432	3	67.4	500	3	3.7
61.6	3.925	2	66.5	1000	2	8.0
51.8	3.054	4	49.2	300	4	4.9
41.0	1.739	5	41.1	200	5	0.4
15.5	1.478	6	16.0	40	6	3.2

Similarly, by using a properly assumed acceleration, the structure of the micro-channels in Membrane-DMAc can be mimicked. Figure 4.12 gives the simulated k-n curve for Membrane-DMAc, the actual spacing of different sets of micro-channels and the order of length are compared with the simulated result in Table 4.9. Both wavelengths and the order of the growth number from the simulation match the experimental results very well. However, the result of the simulation for Membrane-NMP is not presented here, because the conversion from micro-channel density data to the wavelength is not reliable due to the limitations of the sample, as mentioned above. However, although it is just a very rough matching, the range of the wavelengths obtained experimentally is concurrent with the range of the simulated wavelengths, which is less than 300 μm.

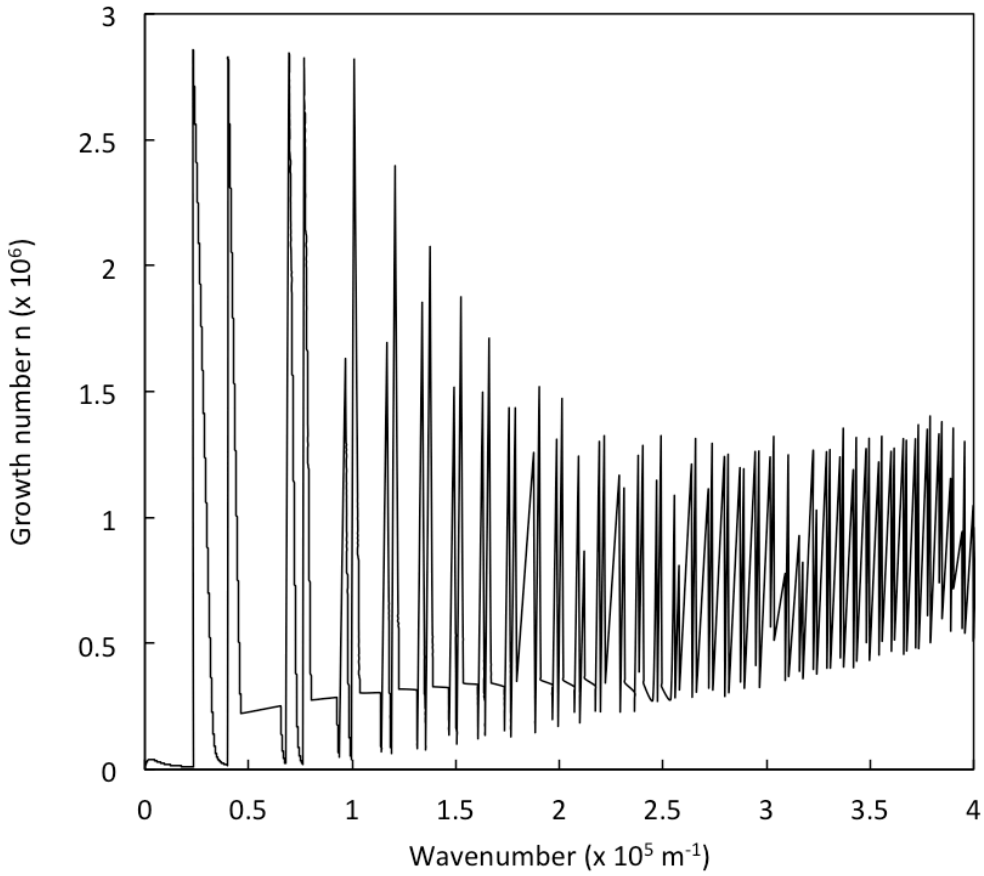


Figure 4.12 Simulation Growth number vs wavenumber for Membrane-DMAc. Parameters used for the calculation: ρ_c = 1000 (kg/m^3), ρ_s = 1650 (kg/m^3), μ_c = 0.001 (Pa.s), μ_s = 3.64 (Pa.s), T = 0.02 (N/m) and a = 5x10^6 (m/s^2)

4.4.4 The shape of micro-channels

The shape of micro-channels is determined by a multitude of factors, and detailed discussions would be beyond the scope of this chapter, and thus it will be discussed briefly. In principle, the shape can be affected by the initial momentum of the penetrating water stream, the energy dissipation from the viscosity of the suspension and the diffusional inflow of the solvent from surrounding suspension to the micro-channel. For RT instability, after the initialization of micro-channels during a very short time scale, self-similar growth of the micro-channels takes place [52]. The lateral self-similar growing process is largely affected by the initial stage of micro-channel formation and so the initial growth number is important which can be deemed

as an index of the momentum of the inflow water stream. The energy of the inflow water streams is dissipated during the micro-channel formation process because of the viscosity of the suspension until the energy is consumed. In the case of phase inversion, the viscosity of the surrounding suspension increases quickly due to the solvent/non-solvent exchange. In particular, the viscosity of the micro-channel's side wall increases quicker than the head due to a higher concentration gradient caused by shear flow. This leads to faster solvent/non-solvent exchange at the side walls. The difference in the rate of change of viscosity of the micro-channel's side wall and head is one of the reasons why the diameter of the micro-channels usually increases gradually along the length direction. Therefore, the changing rate of the viscosity influences the final dimension and the shape of micro-channels. Finally, when the inflow water stream loses its momentum, the growth of micro-channels rely more on the diffusion of the solvent from the suspension into the micro-channels. Since the diffusion is not directed, the growth of micro-channels at this stage tend to be isotropical, and the head of the micro-channels tend to be round, eventually forming the pear or tear-like micro-channels.

In this experiment, the growth numbers of the dominating micro-channels vary for different alumina suspensions, but are very high for all three types of membranes, which indicate a great momentum of the inflow water streams. In fact the micro-channels pass through the whole membrane thickness until they reach the bottom. Membrane-DMSO has slim cylindrical micro-channels, Membrane-NMP has pear-like shaped micro-channels, and Membrane-DMAc has a micro-channel shape transmitting from Membrane-DMSO to Membrane-NMP. The difference in micro-channel shape can be partially attributed to the difference in precipitation rates of PESf in the different solvents and hence the difference in the changing rate of viscosity. The Relative Energy Difference (RED) ratios of the different solvents with PESf are listed in Table 4.10, giving an indication of the PESf solubility in each solvent [53]. It is clear that DMSO would have the highest precipitation rate due to the RED being close to 1 and therefore the lowest solubility for PESf, close to its cloud point. NMP and DMAc, on the other hand, are stronger solvents for PESf with higher solubilities, hence indicate slower precipitation rates than DMSO. The high PESf precipitation rate of DMSO means rapid increase of the viscosity of the micro-channels' side walls, so that the radial growth of micro-channels is constrained, and a

slim and cylindrical shape is obtained. The viscosity at the head of micro-channels for the DMSO case also increases faster than the NMP and DMAc cases, which means a faster dissipation of the energy, thus the micro-channel's longitudinal growth in Membrane-DMSO is limited more than Membrane-NMP and Membrane-DMAc. Therefore the micro-channels stop just in front of the bottom of the membrane. On the other hand, the solubility of PESf in NMP is the greatest, and implies the slowest precipitation and the changing rate of the viscosity, thus the highest extent of radial growth is expected, resulting in pear-like shape micro-channels. A slow dissipation of the energy at the micro-channel front is also expected in Membrane-NMP, thus the micro-channels go further than that in Membrane-DMSO and due to the impact with the bottom of the mould they are diverted. This causes the micro-channels to bend, and the micro-channel heads are further enlarged, and the wall between the micro-channels become broken. Due to the prolonged mobility of the interface surrounding the micro-channels in Membrane-NMP, diffusional flow of the solvent from the surrounding suspension may contribute to the growth of the micro-channels as well, and leads to the more evident radial growth at the micro-channel heads. The solubility of PESf in DMAc is slightly higher than DMSO but considerably lower than NMP, thus the shape of micro-channels is in between Membrane-DMSO and Membrane-NMP, but closer to Membrane-DMSO.

Table 4.10 Hansen Solubility parameters for the five solvents and their relative energy difference with PESf

	Energy from dispersion forces δ_d ($MPa^{1/2}$)	Energy from permanent dipole-permanent dipole forces δ_p ($MPa^{1/2}$)	Energy from hydrogen bonding δ_h ($MPa^{1/2}$)	Relative Energy Difference
DMSO	18.4	16.4	10.2	0.996
DMF	17.4	13.7	11.3	0.915
DMAc	16.8	11.5	10.2	0.924
NMP	18.0	12.3	7.2	0.655
TEP	16.7	11.4	9.2	0.940
PESf	19.6	10.8	9.2	
Water	15.5	16	42.3	5.564

4.5 Conclusions

The influence of the solvent on the structure of phase-inversion ceramic disc membranes and the formation of micro-channels in them has been investigated. Directly from the experimental results, we may summarize the effects of the solvents as the following:

1. The choice of the solvent determines the macrostructure of the membranes, cylindrical micro-channels were formed when DMSO is the solvent, and pear or tear-like micro-channels were formed when NMP or DMAc are the solvent. Symmetric micro-channel-free membranes were formed when DMF and TEP were used as solvents.
2. The micro-channels have a hierarchical structure where the length, width and number of micro-channels change along the depth direction. The distribution of the micro-channels shows a regular and periodical feature. These characteristics are also affected by the choice of the solvent. The micro-channels in the membranes greatly reduce the resistance to water permeation.
3. The choice of solvent also affects the microstructure of phase-inversion ceramic membranes, leading to changes in the membranes' pore sizes.

The initialization of micro-channels is interpreted by the Rayleigh-Taylor Instability theory. It is assumed that upon contact between the ceramic suspension and the coagulation bath, the inter-diffusion of the solvent and the non-solvent leads to rapid accelerated movement of the suspension/coagulant interface, and the R-T Instability occurs during which the lighter coagulant invades into the heavier ceramic suspension. The spacing and the hierarchical structure of the micro-channels are quantitatively mimicked in this work by using the R-T Instability theory, and the simulation results match the experimental results reasonably well. Following the R-T theory, the shape of the micro-channels can be qualitatively interpreted through the combination of the hydrodynamic and the physical-chemical processes. It is suggested that during the growing process of the micro-channels, the initial momentum of the invading coagulant streams, the rate of change of viscosity, and the diffusion of the solvent from the suspension towards the micro-channels would determine the shape of the micro-channels.

The interpretation to the formation of micro-channels includes comprehensive factors, in which the inter-diffusion of the solvent and the non-solvent is the most influential. According to the R-T Instability theory, micro-channels form easily if the outflow of the solvent is considerably faster than the inflow of the non-solvent, and so the diffusion rate of the solvent often influences the tendency of micro-channel formation, which matches the empirical rules in the phase-inversion process. Viscosity matters in the R-T Instability theory, but it does not always give a monotonic change. Instead, the influence of viscosity is affected by the acceleration of the moving interface. This also agrees with the experience in phase-inversion membranes that the effects of the viscosity are complicated. Density is another important factor in the theory but has been largely ignored in the past. It is required in the R-T Instability theory that the density of the suspension or the polymer solution should be heavier than the coagulant to induce micro-channels, otherwise the R-T instability will not occur. It is also true that in literature, fingers normally will not occur if a light solvent such as acetone is used, unless the concentration of the polymer is high enough to reverse the direction of the density gradient across the interface [54]. In few cases, it has been found that the addition of certain surfactants can turn membranes from finger-free structures to structures yielding fingers, even if the polymer solution is lighter [55]. But it is arguable that in this situation, the surfactant actually greatly increases the solvent/non-solvent exchange rate [55], thus the density gradient at the interface is instantaneously reversed whilst the acceleration of the moving interface is still high, and so R-T Instability still occurs. The R-T instability theory can also be used to interpret the dependence of thickness on the formation of micro-channels during phase-inversion, which has been commonly noticed in the practice [56-59]. It can be referenced from the R-T Instability theory that when the thickness of the membrane is comparable to the wavelength, the growth number is proportional to the cube of the thickness, and thus the tendency of micro-channel formation reduces quickly when the membrane thickness is reduced [60].

Although in this study it is believed that the R-T instability can be used to interpret many fingering phenomena during phase-inversion process, other mechanisms of finger formation are not excluded. As mentioned before, interfacial instability can be introduced by many different sources, such as the Marangoni effect or other gradient of interfacial properties, and may be synergetic to one another to

further enhance the micro-channel formation process. For example, it has been observed that the fingers in ceramic membranes can branch out and form highly porous structures [24]. It is believed that it can be interpreted by the Kelvin-Helmholtz instability [61, 62], which occurs when the shear flow of the invading coagulant stream acts on the wall of the main fingers, and likely acts simultaneously with the R-T instability.

Like other mechanisms proposed before, to accurately predict the number and dimensions of micro-channels is difficult. Although it has been shown here that the spacing and the relative lengths of micro-channels can be reproduced based on the R-T Instability theory, it is hard to obtain the exact value of the acceleration of the interface. This is due to the complexity of the inter-diffusion of such multiphase systems; especially in this case whereby the addition of large amounts of ceramic powder would greatly influence the diffusion process. Besides, the non-Newtonian feature of the ceramic suspension makes it tricky to apply a proper value of the viscosity even if it can be measured under ideal conditions. These problems would be the tasks of future research.

References

1. Mallada, R. and M. Menéndez, *Inorganic Membranes: Synthesis, Characterization and Applications: Synthesis, Characterization and Applications*. 2008: Elsevier Science
2. Judd, S., *The MBR Book: Principles and Applications of Membrane Bioreactors for Water and Wastewater Treatment*. 2010: Elsevier Science
3. Calvert, P.D., et al., *Dispersion of Ceramic Particles in Organic Liquids.* MRS Online Proceedings Library, 1986. **73**: p. null-null.doi:10.1557/PROC-73-579
4. Zhang, X., D.K. Wang, and J.C. Diniz Da Costa, *Recent progresses on fabrication of photocatalytic membranes for water treatment.* Catalysis Today, 2014. **230**: p. 47-54
5. Oh, H.K., et al., *Removal of organics and viruses using hybrid ceramic MF system without draining PAC.* Desalination, 2007. **202**(1-3): p. 191-198

6. Kabsch-Korbutowicz, M. and A. Urbanowska, *Water treatment in integrated process using ceramic membranes.* Polish Journal of Environmental Studies, 2010. **19**(4): p. 731-737
7. Li, K., *Ceramic Membranes for Separation and Reaction*. 2007: Wiley
8. Buekenhoudt, A., et al., *1.11 - Basic Aspects in Inorganic Membrane Preparation*, in *Comprehensive Membrane Science and Engineering*, E. Drioli and L. Giorno, Editors. 2010, Elsevier: Oxford. p. 217-252.http://dx.doi.org/10.1016/B978-0-08-093250-7.00011-6
9. Liu, S., K. Li, and R. Hughes, *Preparation of porous aluminium oxide (Al2O3) hollow fibre membranes by a combined phase-inversion and sintering method.* Ceramics International, 2003. **29**(8): p. 875-881.http://dx.doi.org/10.1016/S0272-8842(03)00030-0
10. Wei, C.C., et al., *Ceramic asymmetric hollow fibre membranes—One step fabrication process.* Journal of Membrane Science, 2008. **320**(1–2): p. 191-197.http://dx.doi.org/10.1016/j.memsci.2008.04.003
11. Yang, N., X. Tan, and Z. Ma, *A phase inversion/sintering process to fabricate nickel/yttria-stabilized zirconia hollow fibers as the anode support for micro-tubular solid oxide fuel cells.* Journal of Power Sources, 2008. **183**(1): p. 14-19.http://dx.doi.org/10.1016/j.jpowsour.2008.05.006
12. Kingsbury, B.F.K. and K. Li, *A morphological study of ceramic hollow fibre membranes.* Journal of Membrane Science, 2009. **328**(1–2): p. 134-140.http://dx.doi.org/10.1016/j.memsci.2008.11.050
13. Wang, T., et al., *Preparation and characterization of alumina hollow fiber membranes.* Frontiers of Chemical Engineering in China, 2009. **3**(3): p. 265-271.10.1007/s11705-009-0010-2
14. Zhang, X., et al., *Asymmetric porous cordierite hollow fiber membrane for microfiltration.* Journal of Alloys and Compounds, 2009. **487**(1–2): p. 631-638.http://dx.doi.org/10.1016/j.jallcom.2009.08.028
15. Kingsbury, B.F.K., Z. Wu, and K. Li, *A morphological study of ceramic hollow fibre membranes: A perspective on multifunctional catalytic membrane reactors.* Catalysis Today, 2010. **156**(3–4): p. 306-315.http://dx.doi.org/10.1016/j.cattod.2010.02.039

16. Zhang, X., et al., *Highly permeable porous YSZ hollow fiber membrane prepared using ethanol as external coagulant.* Journal of Alloys and Compounds, 2010. **494**(1–2): p. 366-371.http://dx.doi.org/10.1016/j.jallcom.2010.01.048
17. Han, L.-F., et al., *Preparation, characterization and permeation property of Al2O3, Al2O3–SiO2 and Al2O3–kaolin hollow fiber membranes.* Journal of Membrane Science, 2011. **372**(1–2): p. 154-164.http://dx.doi.org/10.1016/j.memsci.2011.01.065
18. Kanawka, K., et al., *A dual layer Ni/Ni-YSZ hollow fibre for micro-tubular SOFC anode support with a current collector.* Electrochemistry Communications, 2011. **13**(1): p. 93-95.http://dx.doi.org/10.1016/j.elecom.2010.11.022
19. Luiten-Olieman, M.W.J., et al., *Porous stainless steel hollow fibers with shrinkage-controlled small radial dimensions.* Scripta Materialia, 2011. **65**(1): p. 25-28.http://dx.doi.org/10.1016/j.scriptamat.2011.03.023
20. Rahman, M.A., et al., *Development of a catalytic hollow fibre membrane micro-reactor for high purity H2 production.* Journal of Membrane Science, 2011. **368**(1–2): p. 116-123.http://dx.doi.org/10.1016/j.memsci.2010.11.025
21. Tan, X., et al., *Morphology control of the perovskite hollow fibre membranes for oxygen separation using different bore fluids.* Journal of Membrane Science, 2011. **378**(1–2): p. 308-318.http://dx.doi.org/10.1016/j.memsci.2011.05.012
22. Luiten-Olieman, M.W.J., et al., *Towards a generic method for inorganic porous hollow fibers preparation with shrinkage-controlled small radial dimensions, applied to Al2O3, Ni, SiC, stainless steel, and YSZ.* Journal of Membrane Science, 2012. **407-408**: p. 155-163.10.1016/j.memsci.2012.03.030
23. Othman, M.H.D., et al., *Dual-layer hollow fibres with different anode structures for micro-tubular solid oxide fuel cells.* Journal of Power Sources, 2012. **205**(0): p. 272-280.http://dx.doi.org/10.1016/j.jpowsour.2012.01.002

24. Wang, B. and Z. Lai, *Finger-like voids induced by viscous fingering during phase inversion of alumina/PES/NMP suspensions.* Journal of Membrane Science, 2012. **405-406**: p. 275-283.10.1016/j.memsci.2012.03.020
25. Wu, Z., et al., *A controlled sintering process for more permeable ceramic hollow fibre membranes.* Journal of Membrane Science, 2013. **446**(0): p. 286-293.http://dx.doi.org/10.1016/j.memsci.2013.05.040
26. Loeb, S. and S. Sourirajan, *Sea Water Demineralization by Means of an Osmotic Membrane*, in *Saline Water Conversion?II*. 1963, AMERICAN CHEMICAL SOCIETY. p. 117-132.doi:10.1021/ba-1963-0038.ch009 10.1021/ba-1963-0038.ch009
27. Koonaphapdeelert, S., Z. Wu, and K. Li, *Carbon dioxide stripping in ceramic hollow fibre membrane contactors.* Chemical Engineering Science, 2009. **64**(1): p. 1-8.http://dx.doi.org/10.1016/j.ces.2008.09.010
28. Strathmann, H., et al., *The formation mechanism of asymmetric membranes.* Desalination, 1975. **16**(2): p. 179-203.http://dx.doi.org/10.1016/S0011-9164(00)82092-5
29. Stropnik, Č. and V. Kaiser, *Polymeric membranes preparation by wet phase separation: mechanisms and elementary processes.* Desalination, 2002. **145**(1–3): p. 1-10.http://dx.doi.org/10.1016/S0011-9164(02)00322-3
30. Prakash, S.S., L.F. Francis, and L.E. Scriven, *Microstructure evolution in dry–wet cast polysulfone membranes by cryo-SEM: A hypothesis on macrovoid formation.* Journal of Membrane Science, 2008. **313**(1–2): p. 135-157.http://dx.doi.org/10.1016/j.memsci.2008.01.006
31. Sternling, C.V. and L.E. Scriven, *INTERFACIAL TURBULENCE - HYDRODYNAMIC INSTABILITY.* AIChE Journal, 1959. **5**(4): p. 514-523
32. Saffman, P., *Viscous Fingering in Hele-Shaw Cells.* J Fluid Mech, 1986. **173**: p. 73-94
33. Lewis, D., *The instability of liquid surfaces when accelerated in a direction perpendicular to their planes. II.* Proceedings of the Royal Society of London. Series A, Mathematical and Physical Sciences, 1950: p. 81-96
34. Taylor, G., *The Instability of Liquid Surfaces when Accelerated in a Direction Perpendicular to their Planes. I.* Proceedings of the Royal Society of London.

Series A. Mathematical and Physical Sciences, 1950. **201**(1065): p. 192-196.10.1098/rspa.1950.0052

35. Sharp, D.H., *An Overview of Rayleigh-Taylor Instability.* Physica D, 1984. **12**(1-3): p. 3-18.Doi 10.1016/0167-2789(84)90510-4
36. Zhou, Z., P.J. Scales, and D.V. Boger, *Chemical and physical control of the rheology of concentrated metal oxide suspensions.* Chemical Engineering Science, 2001. **56**(9): p. 2901-2920.http://dx.doi.org/10.1016/S0009-2509(00)00473-5
37. Kingsbury, B.F.K. and K. Li, *A Morphological Study of Ceramic Hollow Fibre Membranes.* Journal of Membrane Science, 2009. **328**(1-2): p. 134-140
38. LiqTech International, I. *DYNAMIC CROSS FLOW FILTRATION SILICON CARBIDE MEMBRANE DISCS*. FUTURE FILTRATION [cited 2014 10/01]; Available from: http://liqtech.com/img/user/file/SiC-Disc-Sheet_V1.pdf.
39. Corporation, M. *Ceramic Membrane Unit*. 2013 [cited 2014 04/02]; Available from: http://water-solution.meidensha.co.jp/download/img/bb60-3163.pdf.
40. Ray, R., W. Krantz, and R. Sani, *Linear-stability Theory Model for Finger Formation in Asymmetric Membranes.* Journal of Membrane Science, 1985. **23**(2): p. 155-182
41. Normand, C., Y. Pomeau, and M.G. Velarde, *Convective Instability - Physicists Approach.* Reviews of Modern Physics, 1977. **49**(3): p. 581-624.DOI 10.1103/RevModPhys.49.581
42. Neogi, P., *Mechanism of Pore Formation in Reverse-Osmosis Membranes during the Casting Process.* Aiche Journal, 1983. **29**(3): p. 402-410.DOI 10.1002/aic.690290309
43. Scriven, L.E. and C.V. Sternling, *The Marangoni Effects.* Nature, 1960. **187**(4733): p. 186-188
44. Lal, J. and R. Bansil, *Effects of Gelation on Morphology of Spinodal Decomposition and Viscous Fingering.* Physica A, 1992. **186**(1-2): p. 88-96.Doi 10.1016/0378-4371(92)90367-Y
45. Ren, J.Z., Z.S. Li, and F.S. Wong, *Membrane structure control of BTDA-TDI/MDI (P84) co-polyimide asymmetric membranes by wet-phase inversion*

process. Journal of Membrane Science, 2004. **241**(2): p. 305-314.DOI 10.1016/j.memsci.2004.06.001

46. Addad, J.P.C. and P. Panine, *Pore generation in asymmetric polymeric membranes - Correlation with solvent mobilities.* Polymer Bulletin, 1999. **42**(3): p. 345-352
47. Remigy, J.C. and M. Meireles, *Assessment of pore geometry and 3-D architecture of filtration membranes by synchrotron radiation computed microtomography.* Desalination, 2006. **199**(1-3): p. 501-503.DOI 10.1016/j.desa1.2006.03.193
48. Viguie, J., et al., *Characterisation of 3D porous macrostructure of hollow fibre membranes using X-ray tomography-Effects of some spinning process conditions.* Journal of Membrane Science, 2013. **435**: p. 11-20.DOI 10.1016/j.memsci.2013.01.062
49. Fang, H., et al., *Phase-inversion tape casting and synchrotron-radiation computed tomography analysis of porous alumina.* Journal of the European Ceramic Society, 2013. **33**(10): p. 2049-2051.DOI 10.1016/j.jeurceramsoc.2013.02.032
50. Reuvers, A.J., J.W.A. Vandenberg, and C.A. Smolders, *Formation of Membranes by Means of Immersion Precipitation .1. A Model to Describe Mass-Transfer during Immersion Precipitation.* Journal of Membrane Science, 1987. **34**(1): p. 45-65.Doi 10.1016/S0376-7388(00)80020-4
51. Chandrasekhar, S., *Hydrodynamic and Hydromagnetic Stability*. 1961: Courier Dover Publications
52. Dalziel, S.B., P.F. Linden, and D.L. Youngs, *Self-similarity and internal structure of turbulence induced by Rayleigh-Taylor instability.* Journal of Fluid Mechanics, 1999. **399**: p. 1-48.Doi 10.1017/S002211209900614x
53. Hansen, C.M., *Hansen solubility parameters: a user's handbook*. 2012: CRC press
54. Smolders, C., et al., *Microstructures in Phase-inversion Membranes. Part 1. Formation of Macrovoids.* Journal of Membrane Science, 1992. **73**(2-3): p. 259-275
55. Lin, F.C., et al., *Effect of surfactants on the structure of PMMA membranes.* Journal of Membrane Science, 1997. **123**(2): p. 281-291

56. Ren, J., J. Zhou, and M. Deng, *Morphology transition of asymmetric polyetherimide flat sheet membranes with different thickness by wet phase-inversion process.* Separation and Purification Technology, 2010. **74**(1): p. 119-129.10.1016/j.seppur.2010.05.014

57. Widjojo, N. and T.S. Chung, *Thickness and air gap dependence of macrovoid evolution in phase-inversion asymmetric hollow fiber membranes.* Industrial & Engineering Chemistry Research, 2006. **45**(22): p. 7618-7626.Doi 10.1021/Ie0606587

58. Li, D.F., et al., *Thickness dependence of macrovoid evolution in wet phase-inversion asymmetric membranes.* Industrial & Engineering Chemistry Research, 2004. **43**(6): p. 1553-1556.Doi 10.1021/Ie034264g

59. Vogrin, N., et al., *The wet phase separation: the effect of cast solution thickness on the appearance of macrovoids in the membrane forming ternary cellulose acetate/acetone/water system.* Journal of Membrane Science, 2002. **207**(1): p. 139-141.Pii S0376-7388(02)00119-9
Doi 10.1016/S0376-7388(02)00119-9

60. Fermigier, M., et al., *2-Dimensional Patterns in Rayleigh-Taylor Instability of a Thin-Layer.* Journal of Fluid Mechanics, 1992. **236**: p. 349-383.Doi 10.1017/S0022112092001447

61. Kim, H., J.C. Padrino, and D.D. Joseph, *Viscous effects on Kelvin-Helmholtz instability in a channel.* Journal of Fluid Mechanics, 2011. **680**: p. 398-416.Doi 10.1017/Jfm.2011.206

62. Funada, T. and D.D. Joseph, *Viscous potential flow analysis of Kelvin-Helmholtz instability in a channel.* Journal of Fluid Mechanics, 2001. **445**: p. 263-283

Chapter 5: High flux micro-channelled ceramic disc membranes for water treatments and spinning of microfibres

Chapter 5 *studies the effects of more fabrication parameters on micro-channel growth and development in alumina disc membranes in search for the morphology that will provide the most improved flux and proposes a potential new application of the membranes for the spinning of microfibres*

Abstract

Micro-channel embedded disc membranes with superior water permeation rates have been fabricated by the combined phase inversion and sintering method. The micro-channel properties such as density (the number per unit area), length, diameter and shape can be tailored according to the application and can be designed and controlled by applying the Rayleigh-Taylor Instability theory. Physical parameters such as alumina loading, coagulation bath temperature and membrane thickness were manipulated to achieve a wide range of micro-channel density and lengths. After removing the bottom redundant layer via manual polishing, the water permeation flux of the membrane with 30 wt.% loading reached values of up to 321, 000 $L/m^2 \cdot h \cdot bar$, with an overall membrane thickness of 1.80 mm, and an average pore size of 0.778 μm. A new application of ceramic disc membranes was also discussed for the spinning of microfibres through the micro-channels, and YSZ fibres were successfully fabricated.

5.1 Introduction

Reducing the thickness of ceramic membranes is the most straightforward and efficient way to improve permeation fluxes. However, due to the brittle nature of ceramic materials, ceramic membranes have to be thick enough to hold external

impacts. The trade-off can be overcome by engineering the structure of ceramic membranes whilst keeping the membrane thick, so that the transport resistance inside membrane body can be minimised and the effective thickness is greatly reduced. Such a strategy has been implemented in the previous Chapter 4 by introducing micro-channels in ceramic bodies via an adapted phase-inversion method. In particular, by using DMSO in the ceramic suspension, well-organised micro-channels can be introduced into ceramic membranes. These micro-channels can provide close-to-negligible transport resistance in the supporting layer, and thus helps to enhance the water permeation fluxes of the ceramic hollow fibre membranes [1-4].

In Chapter 4, it has been found the micro-channels can significantly improve the water permeation rate of flat discs; therefore it is of great interest to explore the possibility of using micro-channelled flat sheet ceramic membranes in a plate-and frame unit, which may greatly enhance the efficiency of relevant water treatment plants. In this chapter, various fabrication parameters such as alumina loading in the suspension, membrane thickness and coagulation temperature were systematically changed to tune the structure of micro-channelled flat sheet alumina MF membranes, to achieve extraordinary water permeation fluxes of up to 321,000 L m^{-2} h^{-1} bar^{-1} with an average pore size of 0.778 μm, which was non-achievable previously with other conventional methods. The Rayleigh-Taylor instability theory was then used to help explain how the fabrication parameters influence the characteristics of the micro-channels. Finally, an additional application of the ceramic disc membranes was proposed: for the continuous spinning of microfibres such as YSZ fibres through the micro-channels and preliminary characterisations of the fibres were achieved.

5.2 Experimental

5.2.1 Materials and Preparation of ceramic suspensions

The materials used and ceramic disc fabrication methods are listed in Section 3.1, 3.2 and 3.3. The composition of the membranes made in this chapter are listed in Table 5.1 below. For different membrane thicknesses and coagulation temperatures, the composition for the suspension with 55 wt.% alumina loading was used. The composition of the YSZ suspension for spinning microfibres is listed in Table 5.2.

Table 5.1 Alumina suspension compositions for disc membranes

Component	Alumina loading and the other compositions (wt. %)				
	30	36	45	55	65
DMSO	61.3	56.1	48.0	39.3	30.3
Alumina	30.0	35.8	45.0	54.8	65.0
PESf	8.5	7.8	6.7	5.5	4.2
Dispersant	0.2	0.3	0.3	0.4	0.5

Table 5.2 YSZ suspension composition for making thin microfibres

Component	Composition (wt.%)
DMSO	43.5
YSZ	45.0
PESf	10.9
Dispersant	0.6

5.2.2 The preparation of alumina discs

The set-up for fabricating the alumina disc precursors and general method is given and explained in Section 3.3. The dimensions of the different moulds are as follow: stainless steel moulds of 1 mm thickness and 30 mm diameter, 2 mm thickness and 30 mm diameter, 4 mm thickness and 30 mm diameter, and a PTFE mould of 30 mm thickness and 30 mm diameter. For membranes that were less than 1 mm thick, the volume of suspension required to fill up the 1 mm thickness moulds to the desired thickness was calculated and injected using 5 mL syringes. For the testing of different coagulation temperatures, the glass coagulation bath was placed on a heating plate with a thermometer inserted to control the phase inversion temperature. The membrane precursors were then dried in air and underwent heat treatment to remove the organic components and sintered at 1350 °C.

5.2.3 Spinning of YSZ microfibres

Firstly, 30 wt.% loading alumina disc membranes were sintered at 1600 °C and mechanically polished with 1200 grit sanding paper to remove the top and bottom sponge-like regions. Then, the membrane was attached to a stainless steel vessel with epoxy resin. The vessel was filled with the YSZ suspension and a pressure of 20 bar was applied to extrude the suspension through the micro-channels of the membrane and into a coagulation bath where precipitation occurs and the continuous YSZ microfibres were formed (Figure 5.1). The microfibres were then dried under ambient conditions and heat treated and sintered at 1300 °C.

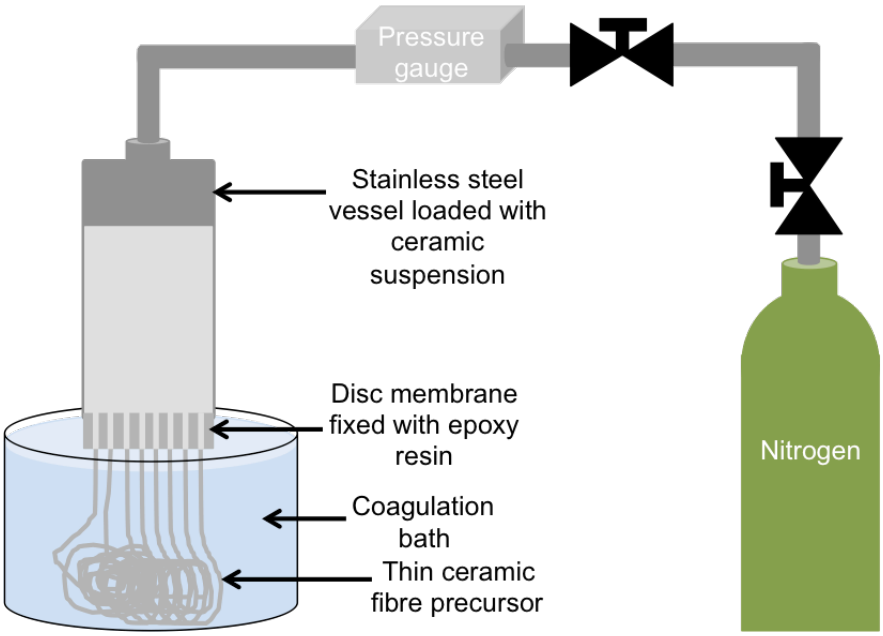


Figure 5.1 Schematic of the set-up for fabricating thin fibres by spinning through micro-channelled ceramic membranes

5.2.4 Characterisation

All characterisation methods such as morphological characterisation using SEM, gas-liquid displacement, micro-channel quantification, 3-point bending and pure water permeation tests are described and explained in Section 3.6. The tensile strength of the YSZ microfibres were measured using a Deben Microtest stage controller with a

200 N load cell. Samples 2.0 cm in length were prepared and held in place with superglue and card paper at the two ends and 6 samples were taken with a standard deviation of within 35 %.

5.3 Results

5.3.1 Morphological characteristics

Figure 5.2a-e displays the cross-sectional morphology of the 2 mm thick alumina membranes with different ceramic loadings ranging from 30 wt.% to 65 wt.% (Table 5.1). For all five loadings it can be seen that the membranes consist of densely packed, cylindrical and long micro-channels that extend across the membrane cross-section, sandwiched between two denser layers of packed ceramic particles. The denser layers' pore sizes can be manipulated to provide the membrane with its selectivity. The long micro-channels can reduce mass transfer resistance but maintain essential mechanical stability for the membrane, as shown in Chapter 4. At low loadings, the micro-channels are much more densely packed, with smaller diameters (5-15 μm at the top region for 30 wt.% powder loading compared to 20-45 μm at the top region for 65 wt.% loading) (Figure 5.3, Figure 5.2f-j, and Table 5.3). At higher loadings, in particular, from 55 wt.% to 65 wt.%, the micro-channel density is noticeably reduced, and less micro-channels were able to penetrate to the bottom of the membranes. Thus, the average micro-channel length is reduced as the loading is increased. From 30 wt.% - 55 wt.% loading, the micro-channels propagate through the entire membrane, whereas for 65 wt.% loading, the micro-channels terminate at around 40 % of the membrane thickness.

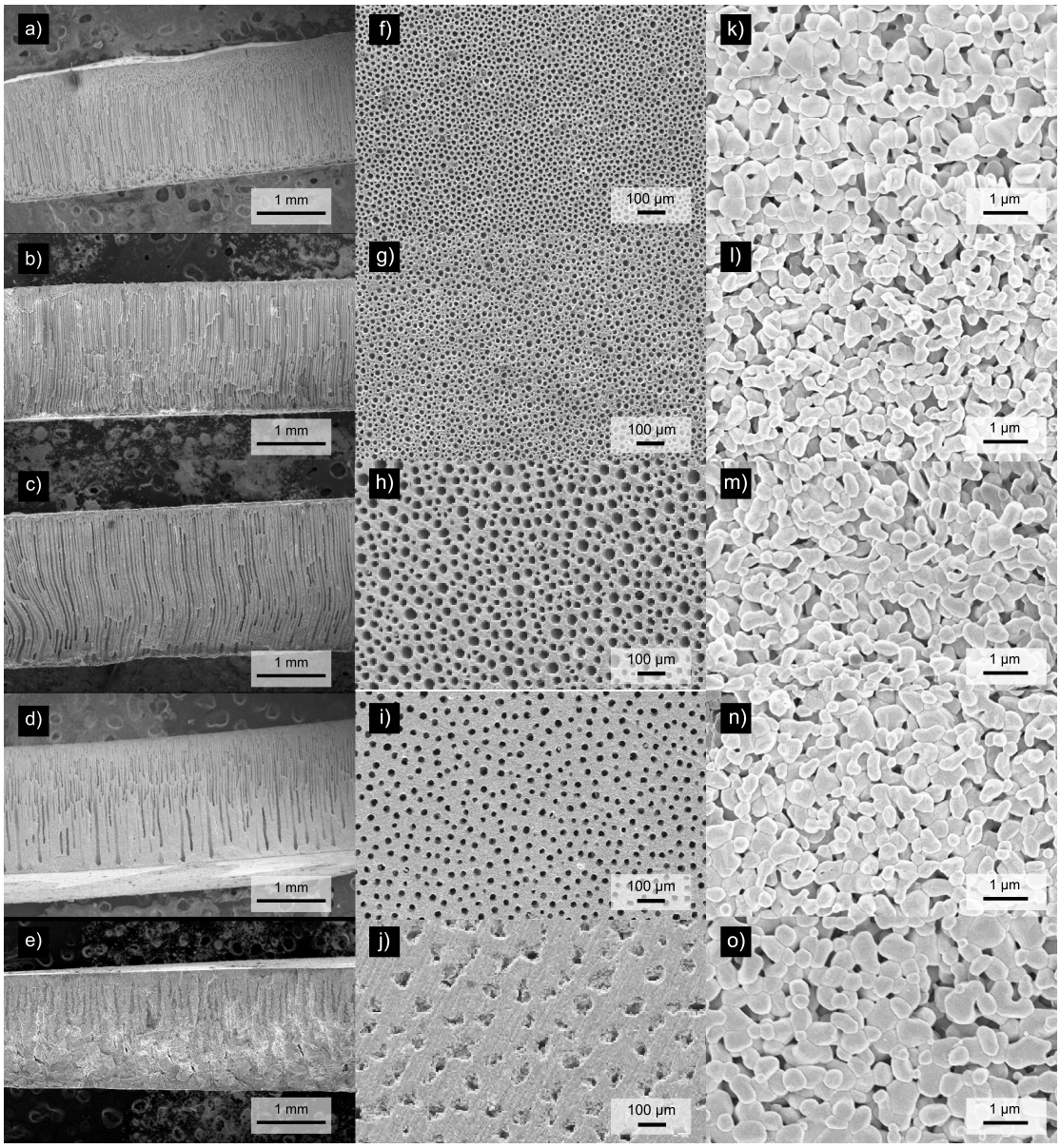


Figure 5.2 SEM images of membranes made from suspensions with different alumina loadings of 30 wt.% (a, f, k), 36 wt.% (b, g, l), 45 wt.% (c, h, m), 55 wt.% (d, I, n), and 65 wt.% (e, j, o). The left column (a-e) shows the whole view of cross-section, the middle column (f-j) shows the micro-channel openings on a section parallel to the surface after removal of 500µm from the top of membranes, and the right column (k-o) gives high-resolution SEM images of the top surface

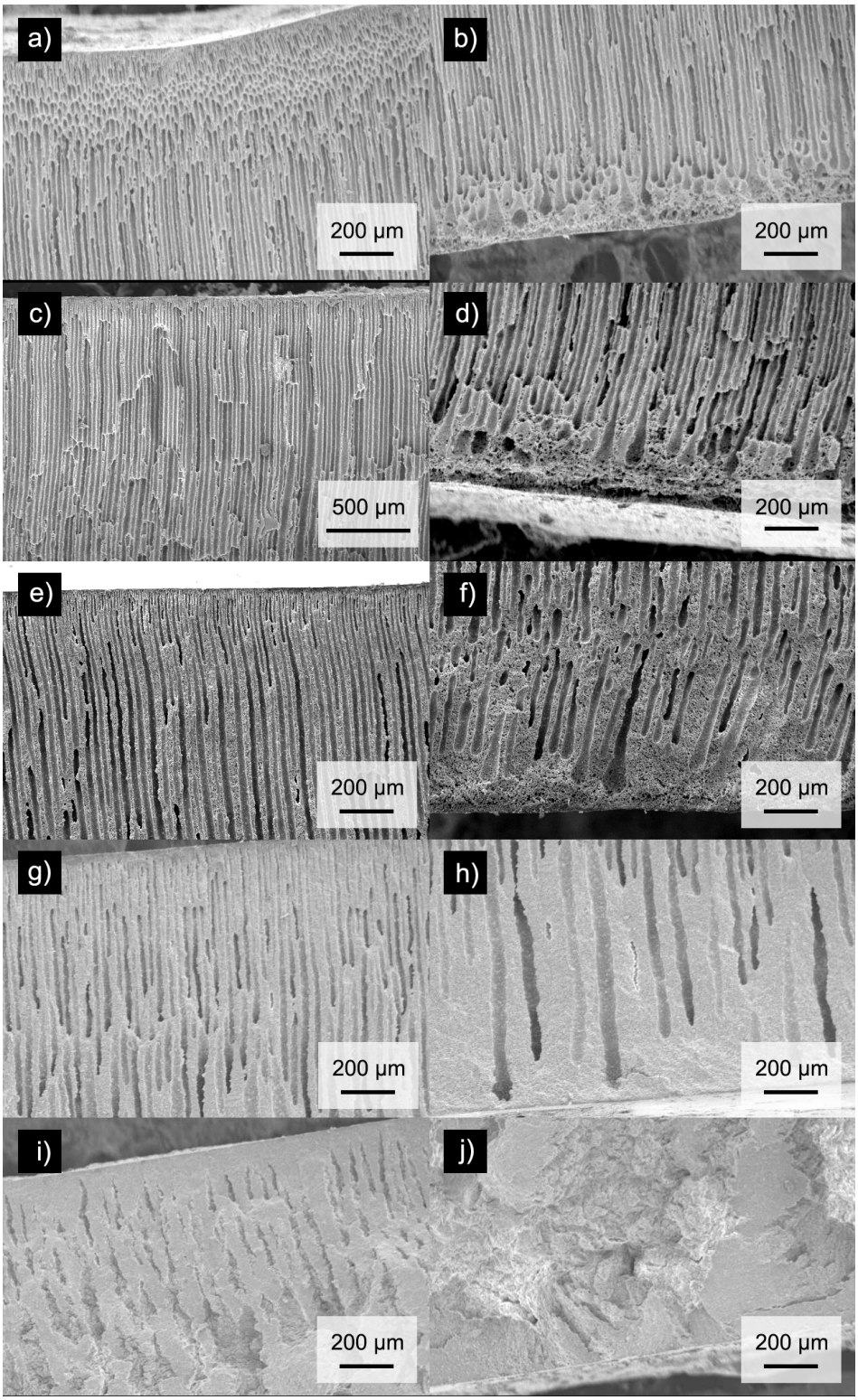


Figure 5.3 Close up cross section SEM images of (left) the top regions and (right) the bottom regions of membranes made from suspensions of different alumina loadings (a-b) 30 wt.%, (c-d) 36 wt.%, (e-f) 45 wt.%, (g-h) 55 wt.%, and (i-j) 65 wt.%

Table 5.3 Micro-channel densities from different strata of the membranes made with different alumina loadings with standard deviations of within 20 %

Distance from top of membrane (μm)	Micro-channel density (/mm^2)				
	Membrane-30 wt.%	Membrane-36 wt.%	Membrane-45 wt.%	Membrane-55 wt.%	Membrane-65 wt.%
40	14, 100	8, 160	8, 530	7, 910	-
100	2, 570	3, 570	2, 500	1, 760	-
200	2, 410	1, 400	1, 490	2, 200	-
300	2, 370	1, 460	1, 440	1, 340	-
500	2, 510	3, 180	464	735	90.1
1000	2, 150	908	306	414	23.3
1500	1, 510	1, 150	367	83.4	-

The micro-channel structure shown in Figure 5.2 resembles the well-known anodic alumina membranes (AAMs) [5-8]. AAMs also have well-arranged long straight channels, but the channel diameter is much smaller, normally from 0.01 μm to 0.4 μm. In AAMs, liquid permeation fluxes essentially follow the Hagen-Poiseuille equation and is proportional to the square of channel diameter and the inverse of membrane thickness [9], therefore there is always obvious trade-offs of permeation flux vs. channel size and membrane thickness. In practice, free-standing AAMs need to be at least tens of microns thick (typically thicker than 60 μm) to be mechanically stable for handling. Combining the small channel diameter and the long transport passage, water permeation flux through commercial AAMs is limited to less than a few thousand litres per square meter membrane area per hour under one bar pressure difference (L/ m^2 h bar^{-1}) [10, 11]. On the other hand, AAMs need prolonged time to make it thick enough to meet the mechanical stability for industrial applications, and current commercial AAM thickness is normally less than 200 μm, which limits their uses to laboratory only. And it is also worth to mention that AAMs, which are composed of amorphous alumina material, are unstable in water [9], therefore unlikely to be used for water treatments. Unlike AAMs, the micro-channelled alumina membranes presented here have much bigger channels whose size is tens of microns,

therefore the transport resistance in the channelled supporting layer is negligible and the permeation fluxes are mainly limited by the denser separation layers.

Figure 5.4 displays the cross-section morphology of membranes prepared from the 55 wt.% suspension with different thicknesses. It can be clearly seen that there is a transition from a combination of denser layers and micro-channels, to the one with a homogenous structure formed by packing of alumina particles. In a 30 mm thick membrane (Figure 5.4a), which is thick enough for the micro-channels to grow without the interference from the mould bottom during formation, the micro-channels are intensive at the top layer and then separated to different sets by their lengths at lower parts. The longest channels can be clearly distinguished from others, and the average space between them, which reflects the wavelength of the most advancing wave, is around 500 μm. For thinner membranes of 4 mm, 1 mm thickness (Figure 5.4b & 5.4c), and 2 mm thick membrane shown in Figure 5.2, intensive micro-channels are present in most part of the cross section and then stopped by the mould bottom. For the 380 μm thick membrane (Figure 5.5d), which is thinner than the wavelength of the longest micro-channels in the 30 mm thick membrane, it is obvious that the number of the micro-channels is much less than in the thicker membranes (Table 5.4), but the momentum of the channels was still high enough to by impacted by the mould bottom and the interaction led the channels to bend severely. However, when the membrane thickness is reduced to 250 μm (Figure 5.4e), the micro-channels completely disappeared. It is therefore evident that there is a critical thickness whereby the formation of micro-channels will be supressed.

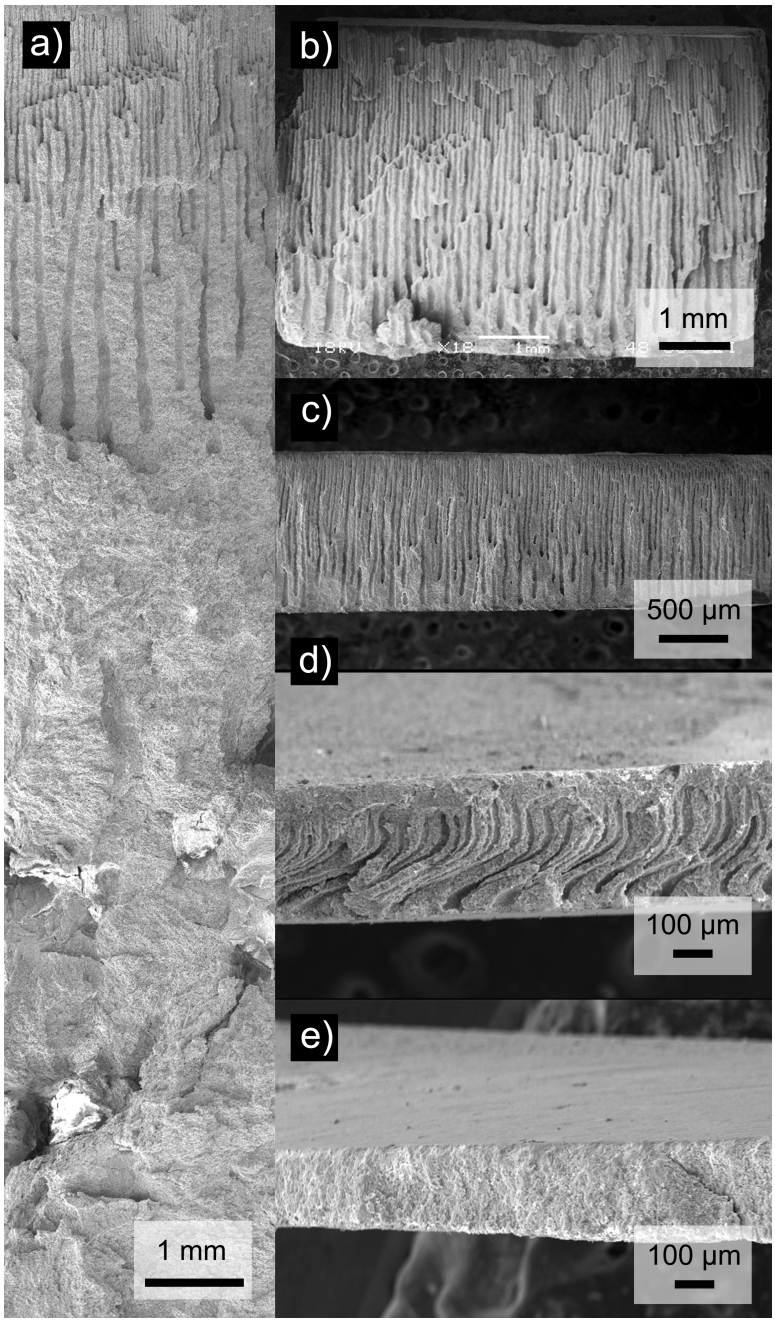


Figure 5.4 Cross-section SEM images of the alumina membranes made from the 55 wt.% suspension with different membrane thicknesses. a) 30 mm, b) 4 mm, c) 1 mm, d) 380 µm and e) 250 µm

Table 5.4 Micro-channel densities from different strata of the membranes of different thicknesses with standard deviations of within 30 %

Distance from top of membrane (μm)	Micro-channel density (/mm^2)			
	1 mm	2 mm	4 mm	30 mm
40	45, 700	7, 910	2, 260	1, 390
100	1, 250	1, 760	1, 510	-
200	1, 080	2, 200	-	-
300	712	1, 340	-	-
500	415	735	773	-
700	78.0	-	-	-
1000	-	414	414	-
1500	-	83.4	174	-
2700	-	-	122	-
3200	-	-	28.9	-
3600	-	-	14.0	-

The temperature at which phase inversion occurs at is also likely to make substantial changes to membrane morphology, as can be seen in Figure 5.5. Different coagulation temperatures led to an increase in the length of the micro-channels, from approximately 4.7 mm to 5.5 mm and 5.8 mm from 20 °C to 30 °C and 50 °C, respectively, which coincides with what has been found in integral polymeric systems [12]. The increase in micro-channel length is most likely attributed to a combination of increase in the mutual diffusion coefficient and reduction in suspension viscosity, causing an increase in the interfacial acceleration as well as reduced resistance to micro-channel growth, respectively. However, this increase in micro-channel length is not very drastic, most likely due to the almost instantaneous closure of the micro-channel entrance due to the suspension's surface tension. This means a continuous denser structure on the top layer is formed quickly, which dramatically reduces the solvent and non-solvent exchange rate and thus reducing the acceleration of the interface. Apart from micro-channel length, the micro-channel density also increased with increasing coagulation temperature (Table 5.5).

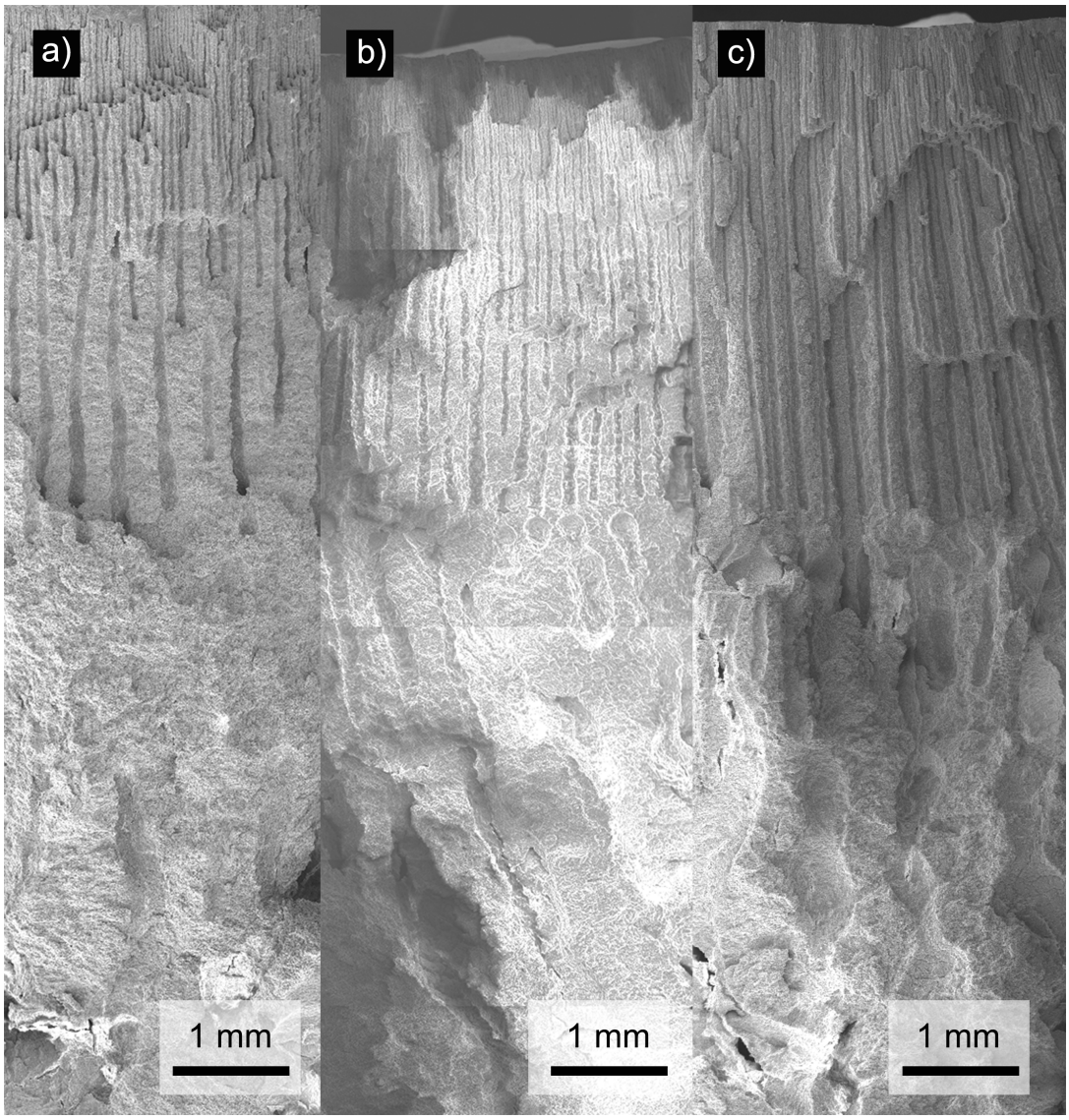


Figure 5.5 Cross-section SEM images of the alumina membranes with different coagulation temperatures a) 20 °C, b) 30 °C, c) 50 °C

Table 5.5 Micro-channel densities for membranes made in different coagulation temperatures after removing 40 μm of the membranes' top surfaces with standard deviations of within 30 %

	Coagulation temperature		
	20 °C	30 °C	50 °C
Micro-channel density (/mm^2) at 40 μm from the top surface	1210	2260	4810

5.3.2 Water permeation and pore size

Table 5.6 displays the water permeation flux of the membranes made with different ceramic loadings and their top layer pore size measured by gas-liquid displacement method. The bottom denser layer was mechanically removed and the overall thickness was kept at around 1.80 mm. This removed the redundant denser layer at the bottom which only acts to increase mass transfer resistance, as shown in a previous study [3]. It can be seen that as the loading is reduced, the water permeation flux is increased dramatically. Although the average pore size increases significantly as well, the corresponding change in water permeation flux is not proportional to the change in pore size. Instead, the change in flux is mainly attributed to the decreasing thickness of the top layer (Figure 5.3), as well as the increased micro-channel density with decreasing loading (Figure 5.2). The water permeation flux is significantly higher than commercial flat disc ceramic membranes, and can be potentially be great candidates for use in membrane bioreactors.

Figure 5.6 reveals the pore size distribution for each alumina loading. The pore size as well as porosity is dramatically reduced when the loading is increased, as expected due to increased tightness of the alumina particle packing, and this is corroborated by the high resolution SEMS (Figure 5.2k-o). At the lowest loadings such as from 30 – 36 wt.%, the average pore size could be up to 4 times bigger than membrane 65 wt.%. All loadings provide the separation layer with pore sizes in the micro-filtration range.

Table 5.6 Dead-end water permeation fluxes of 5 membranes made from different ceramic loadings under 1 bar trans-membrane pressure with standard deviations of within 25 %

Membrane	30 wt.%	36 wt.%	45 wt.%	55 wt.%	65 wt.%	SiC Flat disc [13]
Water permeation flux (L/m^2 h bar)	321, 000	144, 000	14, 000	9, 350	1, 700	10, 000
Pore size of the separation layer (μm)	0.778	0.603	0.353	0.188	0.175	1.0

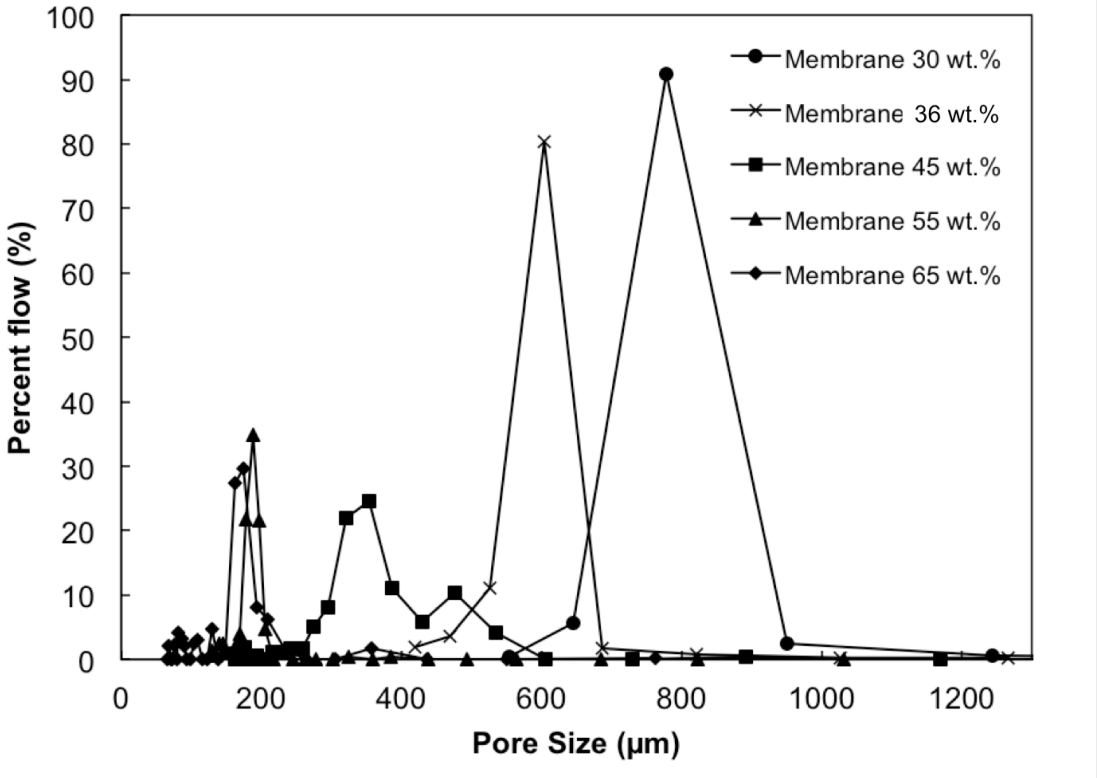


Figure 5.6 Gas-liquid displacement porosimetry data for the membranes made from suspensions of different loadings after the removal of the bottom sponge layer

The disc membranes fabricated in this study have superior water permeation fluxes compared with commercially available disc membranes. When compared to SiC disc membranes (Table 5.6), which are intrinsically much more hydrophilic than alumina, the membranes made with the lowest loading (30 wt%) is significantly higher than the SiC membranes.

5.3.3 Mechanical stability

3-point bending tests were carried out to explore the mechanical stability of the membranes formed with different ceramic loadings. Table 5.7 displays the breaking stress of the membranes. It can be seen that ceramic loading does have a significant impact on the mechanical strength of the membrane, but only up to a certain degree in this experiment. Below a certain ceramic loading (45 wt.%), increasing the ceramic loading led to a drastic improvement in breaking stress, due to much improved contact between the alumina particles, and hence provided more effective sintering, as well as the increasing thickness of the sponge-like structure. Above this loading, there begins to be a slight decrease in breaking stress, which is most likely caused by the difference in cross-section morphology. As seen in Figure 5.2, Membrane 65 wt.% is the most asymmetric in terms of cross-section morphology, with three distinctly different membrane sub-structures.

Table 5.7 Mechanical stability of the membranes made from different ceramic loadings under 3-point bending configuration with standard deviations of within 35 %

Membrane	30 wt.%	36 wt.%	45 wt. %	55 wt.%	65 wt.%
Average breaking stress (MPa)	4.70	6.54	16.7	15.8	13.3

The alumina membranes formed in this study are not mechanically strong enough for industrial applications, but can be greatly improved by adjusting other membrane properties such as the membrane thickness without compromising the water permeation flux, or increasing the sintering temperature. A thicker membrane

consisting of a thin denser selective layer supported by micro-channels is anticipated to have improved mechanical stability without sacrificing permeation flux.

5.4 Discussion

5.4.1 Influencing factors

There have been many different theories and interpretations on the origin of the micro-channels that appear in phase inversion induced membranes. However, the general consensus is that the finger-like structures are formed by periodical surface disturbing waves, which have a wide range of different sources, such as surface tension gradients, viscosity or density differences, or the gradient of solidification and shrinkage rate along the interface [14-17] One particular theory to explain the initiation and growth of the micro-channels is the Rayleigh-Taylor Instability [18], with promising results when used to mimic the micro-channel characteristics [3], as explained in Chapter 4.

The Rayleigh-Taylor instability occurs when there is an acceleration of the interface from a lighter fluid towards a heavier one, amplifying the periodic perturbations at the interface to form finger-like patterns [18]. During phase inversion, there is a complex network of different processes that occur at the interface in parallel to each other in the form of mechanical, physical and chemical interactions. When the suspension is immersed into the non-solvent bath, there is a difference in density, viscosity and composition across the suspension solution and non-solvent interface. During the phase inversion process solvent and non-solvent exchange occurs at the interface, and due to the extraction of solvent as well as contraction of the polymer, the interface moves towards the suspension side. The mass and heat transfer across the system leads to the transient nature of this process, and there will be interfacial tension, viscosity, density and solidification gradients along the interface, which can all act to destabilise the interface. The wavelengths of the perturbations with sufficient growth numbers will grow into finger-like structures that are solidified as micro-channels in the membranes, with specific diameters as well as densities.

There are therefore many factors during the preparation and fabrication steps that can affect the formation of the micro-channels in these flat disc membranes, such

as: the density and viscosity of the suspension solution and coagulant, the mutual diffusion coefficient of the solvent and non-solvent, the precipitation rate of the polymer binder, etc. Indirect parameters during fabrication can affect a number of the abovementioned factors, such as ceramic loading, solvent and polymer binder choice as well as composition, coagulation temperature, non-solvent choice, membrane thickness, etc.

5.4.2 Simulation

As established in a previous study, Rayleigh-Taylor simulations were applied onto the ceramic membrane system, in effort to mimic the micro-channel characteristics in these membranes, with promising results [3]. Here the effect of different parameters was investigated with the same simulation. When the ceramic loading in the suspension was changed, various different parameters in the system were changed, such as the density, viscosity, and acceleration of the interface. Two different simulations were carried out to make the effect of the different parameters clearer. The simulations were achieved by linear stability analysis, as explained in detail in a Chapter 4, which solves for the wavenumbers k and their corresponding growth numbers n, displayed as k-n curves in Figures 5.7 and 5.8. The wavenumber can be related to the distance between each micro-channel, whereas the growth number can give insight into the growth rate and final length of the micro-channels. Figure 5.7 displays the result from simulations carried out with changing viscosities and densities, but constant acceleration, whereas Figure 5.8 displays the results for changing accelerations and constant viscosity and density.

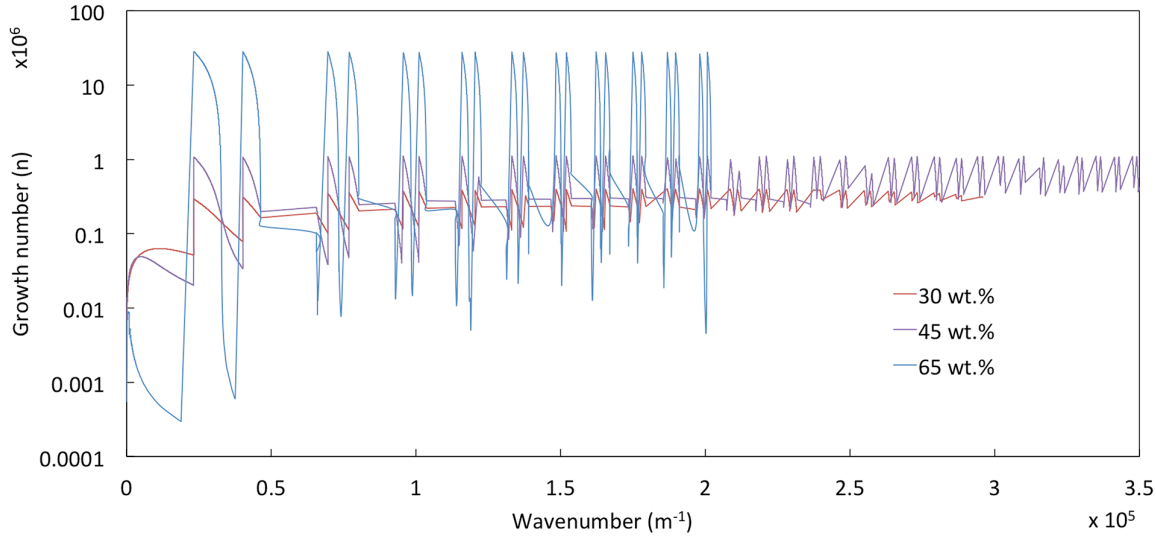


Figure 5.7 Simulation growth number vs wavenumber for 3 different alumina suspension loadings. Parameters used for the calculation: ρ_c = 1000 (kg/m^3), ρ_s = 1440, 1660 and 1850 (kg/m^3), μ_c = 0.001, (Pa.s), μ_s = 0.309, 1.38 and 37.8 (Pa.s), T = 0.02 (N/m) and a = 4x10^6 (m/s^2) for loadings 30, 45, and 65 wt.%, respectively

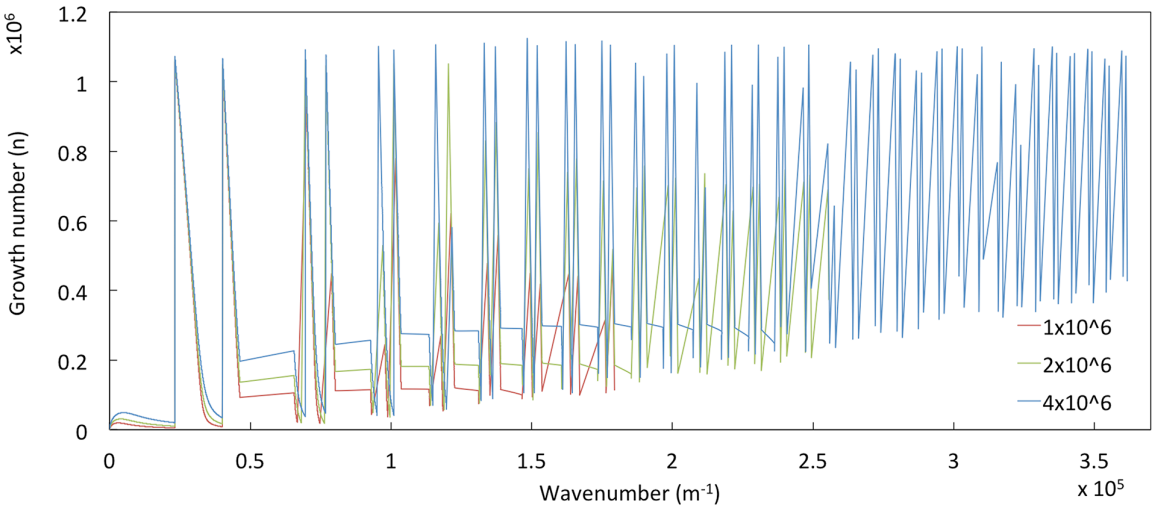


Figure 5.8 Simulation Growth number vs wavenumber for 3 different alumina suspension loadings. Parameters used for the calculation: ρ_c = 1000 (kg/m^3), ρ_s = 1660 (kg/m^3), μ_c = 0.001 (Pa.s), μ_s = 1.38 (Pa.s), T = 0.02 (N/m) and a = 1x10^6, 2x10^6 and 4x10^6 (m/s^2)

The k-n curve in Figure 5.7 reveals that as the ceramic loading is increased, the number of small wavelength (large wavenumbers) perturbations decreases, as the increasing viscosity led to increased finger growth resistance. This is clear in SEM diagrams as the micro-channels for the high loadings (65 wt%) are most sparsely

spaced apart (Figure 5.2), and the experimental wavelengths obtained also support this (Table 5.8). It is also apparent that there are far fewer distinct levels of micro-channels of different wavelengths, when compared with 30 wt.% loading (Figure 5.2). In addition, as the viscosities and densities increase, the simulation shows a vast increase in the perturbations' growth numbers, which suggests that the micro-channels will propagate further. However, due to the influence of the bottom of the mould on the micro-channel growths, it was not possible to fairly compare the final lengths of the micro-channels in the disc membranes for the case of different ceramic loadings. However, the micro-channels in Membrane 65 wt.%, as shown in Figure 5.2, appear to have terminated before reaching the bottom of the membrane. This contradicts with the simulation results at a high interfacial acceleration. This is because the change in viscosity would also indirectly cause changes to other parameters in the complicated phase inversion process. The increase in viscosity is caused by the increase in solid loading in the suspensions, and increasing the loading would also reduces the diffusion of the solvent and thus the acceleration of the interface, which was not measured and hence neglected in the simulation of Figure 5.7. A few arbitrary acceleration values were chosen to look at the effect of acceleration on the perturbations, and it is apparent that lower acceleration is accompanied with lower growth number, as shown in Figure 5.8. Figure 5.8 also shows how increasing acceleration can cause a dramatic increase in growth number of mostly the small wavelength perturbations. This explains how the micro-channel wavelengths are much smaller for the membranes made from the low loadings (Table 5.8). Unlike in Chapter 4, it was difficult in this chapter to gather information about the micro-channels across the different levels, due to the practical limitations of the experimental procedure. It was difficult to accurately polish off layers of ceramic material by hand, especially at the top layers for the low loading membranes, and the acceleration of the interface was arbitrarily chosen, hence the simulations were only used as a guideline to explain the changes in micro-channel properties, rather than to predict and mimic them.

Table 5.8 Comparison between the experimental and simulation results of the micro-channel structure of membranes made from different alumina loadings

Membrane	Distance from top of membrane (μm)	Experimental wavelength (μm)	Simulated wavelength (μm)	Error (%)
30 wt.%	40	11.7	19.0	38.4
	1500	32.3	28.7	12.5
45 wt.%	40	15.7	14.2	10.6
	1500	63.5	21.4	197
55 wt.%	40	16.0	15.5	3.2
	1500	132	156.5	15.4
65 wt.%	500	131	156	16.0
	1000	223	271	17.7

In light of the Rayleigh-Taylor instability theory, which points out that the initial growth speed of the micro-channels will be proportional to the cube of the membrane thickness when the thickness is close to the wavelength of the growing wave [19], we can expect that the tendency of micro-channel formation reduces quickly when the membrane thickness is reduced. On the other hand, the speed of precipitation increases quickly when the membrane thickness decreases [20]. Hence, when the membrane is thinner than a critical thickness, the precipitation front will overrun the front of the micro-channels and thus, the formation of micro-channels is supressed (Table 5.4).

For increasing temperature, the viscosity and acceleration of the interface are expected to change most substantially. At higher temperatures the viscosity is reduced, but the acceleration of the interface should be higher, and therefore, from looking at Figure 5.8, the growth numbers of the small wavelength perturbations would be higher, hence the higher the micro-channel density (Table 5.5).

The models have helped explain the phenomena of micro-channel formation in inorganic phase inversion membranes. However, it is difficult to accurately predict the micro-channel characteristics, due to technical and practical limitations. In terms of practicality, it is difficult to control accurately the mechanical reduction of the membrane thickness via manual polishing. Furthermore, due to how intensely packed

the micro-channels are in some of the membranes, it is difficult to distinguish the different micro-channel levels from one another to know accurately how much to remove for each level. In terms of the simulation, it is based on Newtonian fluids but the ceramic suspensions do not exhibit Newtonian behaviour, especially at the high ceramic loadings. It was also not possible to experimentally estimate an interfacial acceleration, and arbitrary values were taken as reference points. However, some improved understanding was achieved, and the simulations can be potentially used to help design and control the specific types of micro-channels desired.

5.4.3 Potential new application of micro-channel enhanced ceramic disc membranes - continuous and facile spinning of microfibres

Micro- or nanofibres have enormous surface areas per unit mass and have an extensive span of applications that range from filters to reinforcement materials to tissue engineering. The only promising method that can produce continuous organic and inorganic micro- and microfibres is electrospinning. However, the electrospinning method depends on many different variables and can be hard to precisely control, as well as having low efficiency, and therefore is not widely industrialised for mass-producing these very thin fibres.

In order for the mass production of ultra thin fibres in the micro- or nano-range, a fabrication method that is facile, easy to control and operate, efficient, precise and cost-effective is desired. Using ceramic membranes with open micro-channels as a medium through which a polymeric or inorganic dilution is extruded through can potentially be used to produce ultra-thin fibres in large quantities.

The alumina disc membranes fabricated in this study were used (30 wt.% solid loading) after being sintered at 1600 °C and having their top and bottom sponge-like layers mechanically removed. They were then used to spin YSZ fibres by extruding a YSZ suspension containing 1 μm YSZ particles with a polymer additive and DMSO solvent into a coagulation bath, whereby the polymer will act as binder and precipitate, forming solid fibre precursors. After calcination and sintering the binder is removed, leaving pure YSZ fibres (Figure 5.9). After heat treatment and sintering at 1300 °C the final YSZ fibres have diameters of approximately 90 μm, and tensile

breaking strengths of 313 MPa. This method is flexible and can be easily expanded to fabricate other types of inorganic fibres as well as polymeric microfibres.

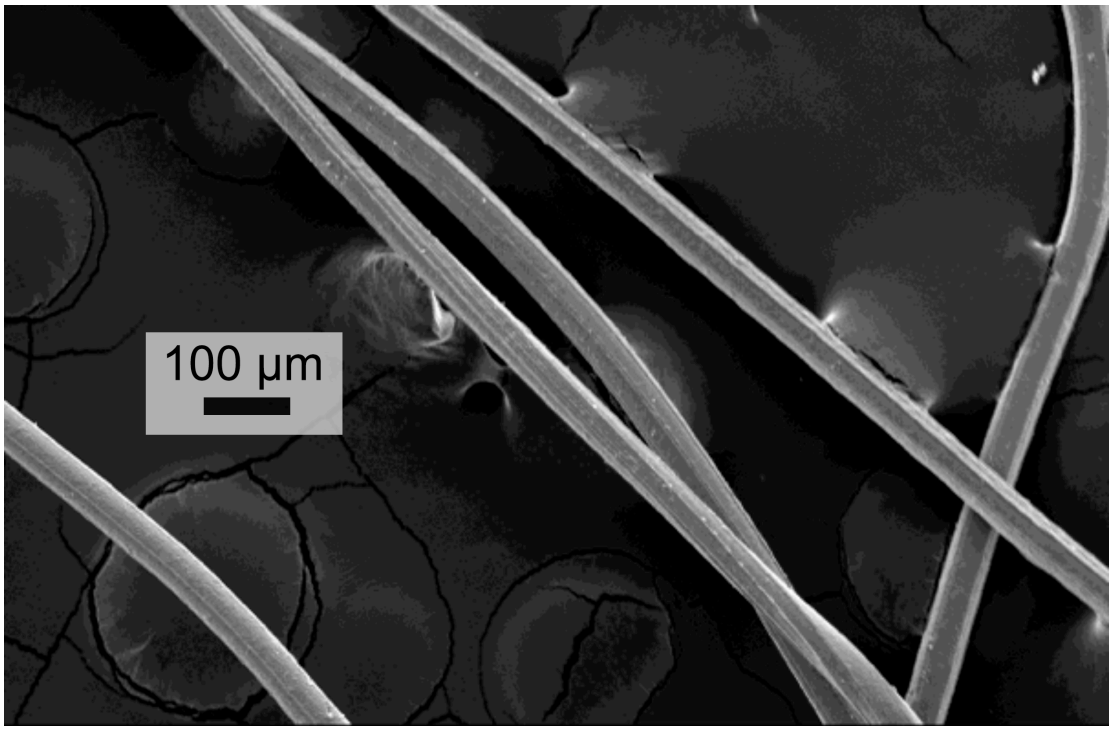


Figure 5.9 SEM image of YSZ microfibres sintered at 1300 °C fabricated by extrusion through alumina disc membranes with open micro-channels

5.5 Conclusions

The effects of alumina solid loading, membrane thickness, and coagulation temperature on the initiation and development of micro-channels in alumina disc membranes have been investigated. It was found that the alumina loading has major effects on the micro-channel density and surface pore size. Low loadings lead to much more densely packed micro-channels with smaller diameters but the average pore sizes are much bigger. By removing the redundant sponge-like layer via manual polishing, the water permeation flux of the membrane with the lowest loading of 30 wt.% achieved water permeation flux values of up to 321, 000 $L/m^2 \cdot h \cdot bar$ with an average pore size of 0.778 µm and a membrane thickness of 1.80 mm, which is significantly higher than typical commercial flat disc membranes which have fluxes of around 10, 000 $L/m^2 \cdot h \cdot bar$ with a similar pore size. However, the mechanical

stability is low for these highly asymmetric membranes due to their very thin sponge-like layers. There is potential to improve the mechanical stability without losing the high permeation flux, by increasing the micro-channel lengths whilst keeping the sponge-like layer the same thickness. It was also found that there is a threshold membrane thickness of around 400 μm whereby the cross-section structure transitions from a continuous, sponge-like structure to one with micro-channels. The temperature at which phase inversion is carried out at also made significant changes to the micro-channel density and length. From 20 °C to 50 °C, the longest micro-channel length increased from 4.7 m to 5.8 mm. Overall, there are many factors that influence the formation of micro-channels in ceramic membrane systems, mainly the density and viscosity of the suspension and coagulant and the acceleration of the interface. Simulations based on the Rayleigh-Taylor instability theory was used explain the micro-channel characteristics in these membranes. The models were able to help explain the general trends of micro-channel growth with the different fabrication parameters, but accurate mimicking was not possible due to technical and practical imitations. In the future improvements include using a more accurate method for removing ceramic materials, using SEMs to identify the distinct layers of micro-channels and then used as a guideline for how much to mechanically remove, and using high-speed cameras to gain an approximate value for the acceleration of the interface. Furthermore, a new application of these flat disc membranes was discussed: for spinning ultra-thin polymeric or inorganic fibres. YSZ fibres of 90 μm in size were successfully fabricated by extruding through the open micro-channels of the membranes made with 30 wt.% alumina loading.

References

1. Kingsbury, B.F.K., Z. Wu, and K. Li, *A morphological study of ceramic hollow fibre membranes: A perspective on multifunctional catalytic membrane reactors.* Catalysis Today, 2010. **156**(3–4): p. 306-315.http://dx.doi.org/10.1016/j.cattod.2010.02.039
2. Lee, M., et al., *Micro-structured alumina hollow fibre membranes – Potential applications in wastewater treatment.* Journal of Membrane Science, 2014. **461**: p. 39-48.http://dx.doi.org/10.1016/j.memsci.2014.02.044
3. Lee, M., et al., *Formation of micro-channels in ceramic membranes – Spatial structure, simulation, and potential use in water treatment.* Journal of Membrane Science, 2015. **483**: p. 1-14.http://dx.doi.org/10.1016/j.memsci.2015.02.023
4. Kingsbury, B.F.K. and K. Li, *A morphological study of ceramic hollow fibre membranes.* Journal of Membrane Science, 2009. **328**(1–2): p. 134-140.http://dx.doi.org/10.1016/j.memsci.2008.11.050
5. Masuda, H. and K. Fukuda, *Ordered Metal Nanohole Arrays Made by a Two-Step Replication of Honeycomb Structures of Anodic Alumina.* Science, 1995. **268**(5216): p. 1466-1468
6. Masuda, H., et al., *Highly ordered nanochannel-array architecture in anodic alumina.* Applied Physics Letters, 1997. **71**(19): p. 2770-2772.doi:http://dx.doi.org/10.1063/1.120128
7. Li, A.P., et al., *Hexagonal pore arrays with a 50–420 nm interpore distance formed by self-organization in anodic alumina.* Journal of Applied Physics, 1998. **84**(11): p. 6023-6026.doi:http://dx.doi.org/10.1063/1.368911
8. Lee, W., et al., *Structural engineering of nanoporous anodic aluminium oxide by pulse anodization of aluminium.* Nat Nano, 2008. **3**(4): p. 234-239.http://www.nature.com/nnano/journal/v3/n4/suppinfo/nnano.2008.54_S1.html
9. Itaya, K., et al., *Properties of porous anodic aluminium oxide films as membranes.* Journal of Chemical Engineering of Japan, 1984. **17**(5): p. 514-520.10.1252/jcej.17.514
10. Song, C., et al., *pH-sensitive characteristics of poly(acrylic acid)-functionalized anodic aluminum oxide (AAO) membranes.* Journal of

Membrane Science, 2011. **372**(1–2): p. 340-345.http://dx.doi.org/10.1016/j.memsci.2011.02.017

11. Sang Won, L., et al., *Transport and functional behaviour of poly(ethylene glycol)-modified nanoporous alumina membranes.* Nanotechnology, 2005. **16**(8): p. 1335
12. Amirilargani, M., et al., *Effects of coagulation bath temperature and polyvinylpyrrolidone content on flat sheet asymmetric polyethersulfone membranes.* Polymer Engineering & Science, 2010. **50**(5): p. 885-893.10.1002/pen.21603
13. A/S, L.I. *Future Filtration Silicon Carbide Ceramic Membranes*. [cited 2016 06/01]; Available from: http://www.liqtech.com/img/user/file/SiC-Disc-Sheet_V1.pdf.
14. Wang, B. and Z. Lai, *Finger-like voids induced by viscous fingering during phase inversion of alumina/PES/NMP suspensions.* Journal of Membrane Science, 2012. **405-406**: p. 275-283.10.1016/j.memsci.2012.03.020
15. Neogi, P., *MECHANISM OF PORE FORMATION IN REVERSE OSMOSIS MEMBRANES DURING THE CASTING PROCESS.* AIChE Journal, 1983. **29**(3): p. 402-410
16. Saffman, P.G., *VISCOUS FINGERING IN HELE-SHAW CELLS.* Journal of Fluid Mechanics, 1986. **173**: p. 73-94
17. Sternling, C.V. and L.E. Scriven, *Interfacial turbulence: Hydrodynamic instability and the marangoni effect.* AIChE Journal, 1959. **5**(4): p. 514-523.10.1002/aic.690050421
18. Sharp, D.H., *An overview of Rayleigh-Taylor instability.* Physica D: Nonlinear Phenomena, 1984. **12**(1–3): p. 3-18.http://dx.doi.org/10.1016/0167-2789(84)90510-4
19. Fermigier, M., et al., *Two-dimensional patterns in Rayleigh-Taylor instability of a thin layer.* Journal of Fluid Mechanics, 1992. **236**: p. 349-383.doi:10.1017/S0022112092001447
20. Lee, H., W.B. Krantz, and S.-T. Hwang, *A model for wet-casting polymeric membranes incorporating nonequilibrium interfacial dynamics, vitrification and convection.* Journal of Membrane Science, 2010. **354**(1–2): p. 74-85.http://dx.doi.org/10.1016/j.memsci.2010.02.066

Chapter 6: Micro-structured alumina hollow fibre membranes

Chapter 6 *transfers the knowledge gained from Chapters 4 and 5 to hollow fibre membranes to fabricate 3 distinct cross-section morphologies in search for a design suitable for potential water treatment processes*

Abstract

In this chapter, three types of micro-structured alumina hollow fibre membranes, i.e. Membranes 1, 2 and 3, have been developed and characterised for potential use in wastewater treatments. They consist of two basic structures: finger-like micro-channels for reduced transmembrane resistance, and sponge-like layer(s) for micro-filtration (MF). They have been fabricated via a combined phase-inversion and sintering technique, whereby the interfacial instability at the suspension and coagulant interface leads to the formation of a plurality of finger-like voids or micro-channels within the membranes. The three internal coagulants used were hexane, DMSO and tap water with air gaps of 0 or 30 cm. Mechanical strength and water permeation flux were found to be sensitive to changes in membrane morphology, while pore size distribution of the separation layer(s) were less affected and were all in the microfiltration range. Membrane 2, with just one very thin separation layer, exhibited the highest water permeation flux of 1874 L/(m^2 h) at 0.1 MPa. Effects of sintering temperature on pore size distribution, mechanical property and water permeation of the three membranes, in particular Membrane 2, were systematically investigated. Sintering temperatures between 1300 °C and 1350 °C are suggested for Membrane 2, taking into consideration of the reduced water permeation at higher sintering temperatures and the lowered mechanical strength at lower sintering temperatures.

6.1 Introduction

The scarcity of ceramic membranes in wastewater treatments has historically been due to their high fabrication costs and intrinsic brittleness, as well as sealing difficulties and lower packing densities. The most common ceramic membrane configurations employed in water treatment are the tubular, monolith and honey-comb architectures, produced by extrusion techniques [1]. However, when compared with the hollow fibre configuration, (surface area to volume up to 9000 $m^2 \cdot m^{-3}$) [2], the much lower membrane area provided by the common ceramic membranes can make them less competitive.

Although extrusion techniques are not inherently energy intensive and expensive, they can only be used to achieve symmetric membranes. However, asymmetric membranes with a thin selective layer on top of thicker and more porous sub-layers made of larger particles are desired for MF and UF applications in order to reduce the resistance to permeate flow. Conventionally, asymmetric membranes are achieved by coating a membrane substrate with multiple layers of ceramic particles of different sizes, which are sintered after each layer coating in order to form a membrane with a gradated pore structure. These additional steps increase the time and costs of the overall fabrication process considerably.

The combined phase inversion and sintering technique can produce asymmetric ceramic membranes with significantly reduced number of steps. This method can form membrane precursors with a range of different micro-channels and their surface properties that can be tailored, as demonstrated in Chapters 4 and 5. The disc membranes with long and intensively packed micro-channels provided much enhanced water permeation fluxes. However, as mentioned above, the disc configuration has low packing densities. On the other hand, hollow fibres enhanced with micro-channels could potentially produce highly compact and productive membrane modules.

In this study, three distinct membrane morphologies with just one layer of micro-channels and sponge-like separation layer(s) were designed and delivered by manipulating the spinning conditions, in particular the bore fluid choice and air gap. The three types of membranes were characterised and the effects of different ceramic membrane morphologies on properties such as pore size, pore size distribution,

mechanical strength and pure water permeation flux were systematically investigated. The membrane morphology most promising for potential applications in aqueous microfiltration was further characterised looking at the effects of sintering temperature on membrane properties.

6.2 Experimental

6.2.1 Materials and alumina suspension preparation

The materials used and the alumina suspension preparation steps are listed in Section 3.1 and 3.2. The composition of the hollow fibres made in this chapter is listed in Table 3.3.

Table 6.1 Alumina suspension composition for single-layered hollow fibre membrane Designs 1, 2 and 3

Layer	Composition (wt.%)		
	Design 1	Design 2	Design 3
Ceramic layer	DMSO	28.3	
	Alumina	64.0	
	PESf	6.4	
	Dispersant	1.3	
Bore fluid	Hexane	DMSO	Water

6.2.2 Preparation of alumina hollow fibres

The spinning process is described in Section 3.2, and in this chapter a dual-layer spinneret was used, as shown in Figure 6.1. This is a typical spinneret design consisting of an inner annulus for delivering the internal precipitant, and an outer annulus for extruding the ceramic suspension. The two annuli keeps the precipitant and ceramic suspension separated until they are both extruded from the spinneret. This dual-orifice spinneret can be used in conjunction with different bore fluids and external coagulation conditions to form different hollow fibre designs. Membrane Designs 1, 2 and 3 were fabricated using this spinneret with the following conditions

(Table 6.2). The dried hollow fibre precursors were heat treated and sintered at temperatures from 1204 °C to 1455 °C.

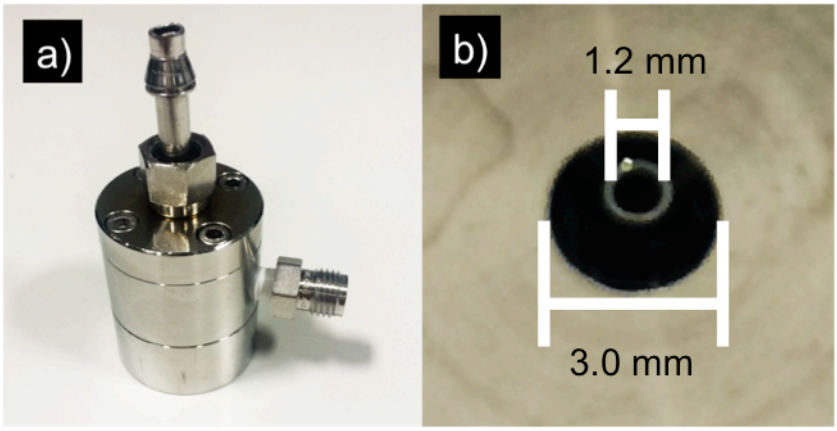


Figure 6.1 Photograph of the double-orifice spinneret for extruding single-layered hollow fibre membranes

Table 6.2 Fabrication parameters for hollow fibre designs 1, 2 and 3 by changing the bore fluid and air gap

Spinning parameter	Design 1	Design 2	Design 3
Extrusion rate (ml/min)	7	7	7
Bore liquid rate (ml/min)	10	10	10
Air gap (cm)	0	0	30

6.2.3 Characterisation

The characterisation methods such as SEM, mercury intrusion porosimetry, gas-liquid displacement, 3-point bending and pure water permeation are described in Section 3.6.

6.3 Results and Discussion

6.3.1 Morphology and microstructure of Membrane 1

From Figure 6.2a-b, it can be seen that when hexane, an "inert" bore fluid that is immiscible with the solvent (DMSO) in the alumina suspension, is used, a morphology consisting of two thin sponge-like layers sandwiching one layer of micro-channels is formed. The micro-channels originate from the outer surface and extend towards the inner surface and across most of the cross-section. As a result of zero air gap, phase inversion commences immediately at the outer region of the nascent fibre as the suspension is extruded through the spinneret. Upon immersion into the water bath, solvent and non-solvent exchange and polymer precipitation commences, which leads to an acceleration of the nascent fibre and water interface. The perturbations at the interface with longer wavelengths than the critical wavelength will cause an interfacial instability and grow into finger-like micro-channels, which penetrate the membrane cross-section. The bore fluid is inert and therefore does not contribute to the solvent and non-solvent exchange at the inner region of the nascent fibre and only acts to provide adequate hydrodynamic force to form and maintain the shape of the membrane's hollow centre. For the same reason, the micro-channels do not break through the membrane and are terminated next to the inner surface.

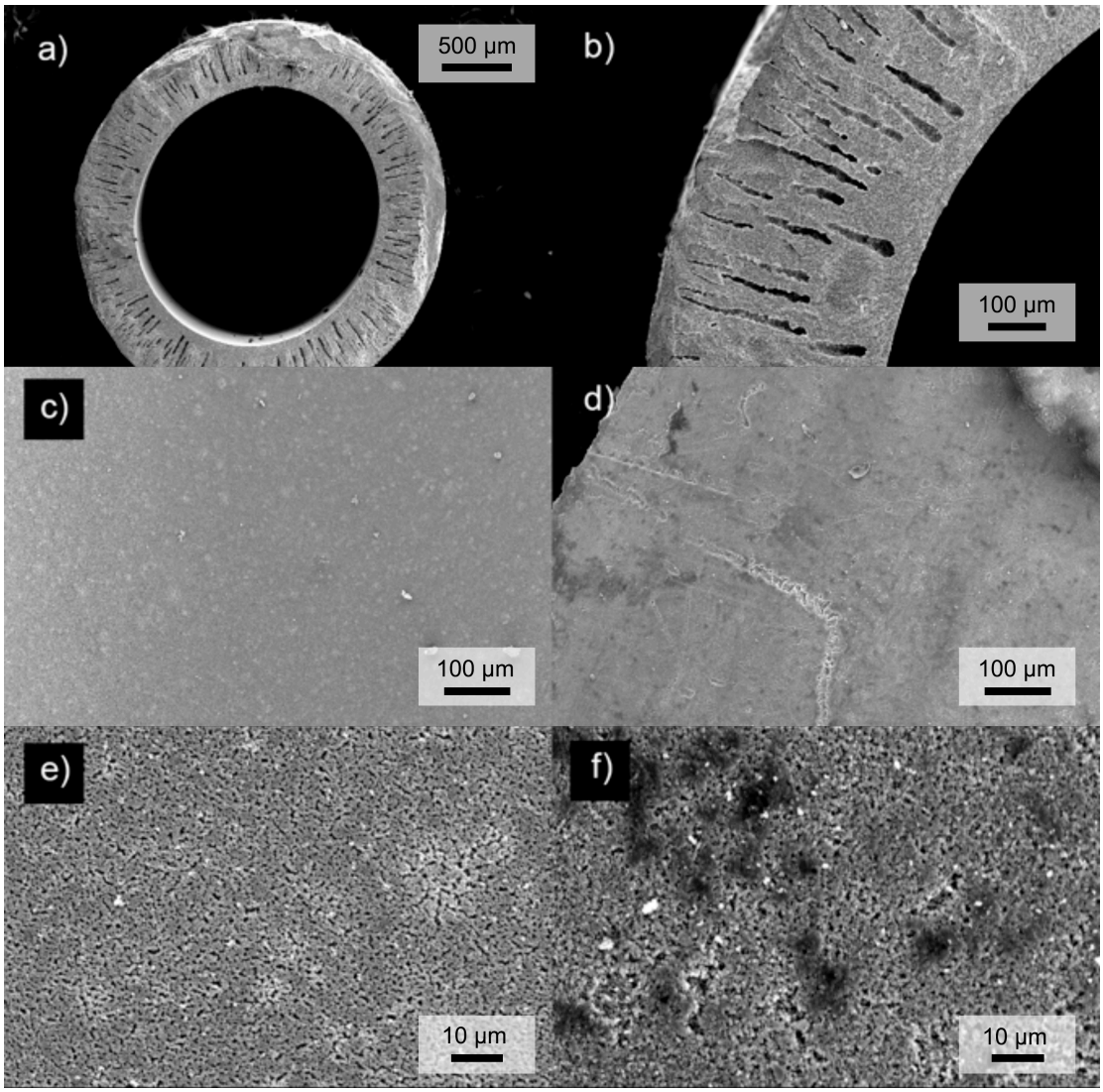


Figure 6.2 SEM images of a) whole view, b) close-up cross-sectional view, c) inner surface at low magnification, d) outer surface at low magnification, e) inner surface at high magnification and f) outer surface at high magnification of Membrane 1 sintered at 1342 °C

Figure 6.2c-f shows the inner and outer surface morphologies of Membrane 1. At low magnification of 150x, the two surfaces show no observable differences. However, upon closer inspection at 1200x, the packing pores at the outer surface appear to be slightly larger than the ones at the inner surface. This means that the pore size distribution in Figure 6.3a, obtained using the bubble point method, represents the typical pore structure of the inner surface of Membrane 1, which is appromimately 0.1 µm in size. The counterpart in Figure 6.3b, obtained from mercury intrusion method, reveals pore size to be approximately 0.23 µm, and changes slightly with different sintering temperatures. During mercury intrusion the mercury will fill the

largest surface pores first; hence the 0.23 μm peak should represent the pores at the outer surface. After all the larger surface pores have been filled, the micro-channels will be then filled, and subsequently the packing pores between the alumina at the finger peripherals will be filled. Therefore the presence of a pore size gradient across the membrane may have dampened the presence of the pores on the inner surface. Of course, such difference in pore size may be due to the different characterization methods. Moreover, due to the presence of two sponge-like layers, micro-channels inside Membrane 1 are not differentiable in Figure 6.3. In addition, due to the similarities in pore size of the two skin layers at the inner and outer surfaces, this Membrane 1 can potentially operate in both inside-out and outside-in configurations.

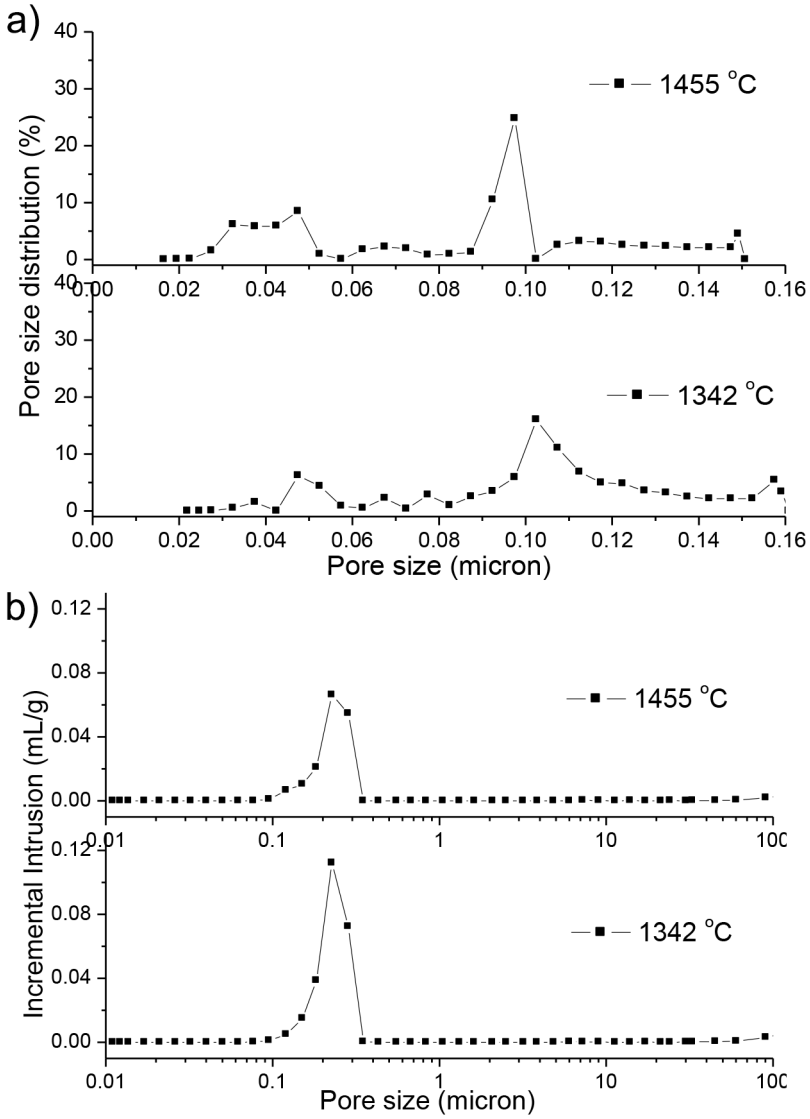


Figure 6.3 Bubble point method data a) and mercury intrusion data b) for Membrane 1 sintered at 1342 and 1455 °C

6.3.2 Morphology and microstructure of Membrane 2

Figure 6.4a-f shows the cross-sectional morphology and surface structures of Membrane 2, fabricated using DMSO as the bore fluid, which is highly miscible with the non-solvent (water). From Figure 6.4a-b, it can be seen that the cross-section of membrane 2 consists of long micro-channels originating from the outer surface, which penetrate through the membrane and are open at the inner surface. The outer region of the membrane consists of a thin sponge-like structure. Similar to Membrane 1, zero air gap allows instantaneous precipitation at the outer surface. The use of a solvent as the bore liquid means that proper solvent-non-solvent exchange across the membrane is maintained and precipitation or increased local viscosity at the inner surface is prevented before the solvent is finally exhausted. This allows continuous growth of the finger-like micro-channels until they penetrate the inner surface of Membrane 2. As a result, the separation layer of Membrane 2 is at the outer surface (or outer thin sponge-like layer), and the highly porous micro-channel packed layer beneath it would generate little resistance to water permeation. Similar morphologies have been fabricated for perovskite hollow fibre membranes targeted for oxygen permeation by using a different solvent: over 70 wt.% NMP mixed with water or ethanol as the bore fluid [3, 4].

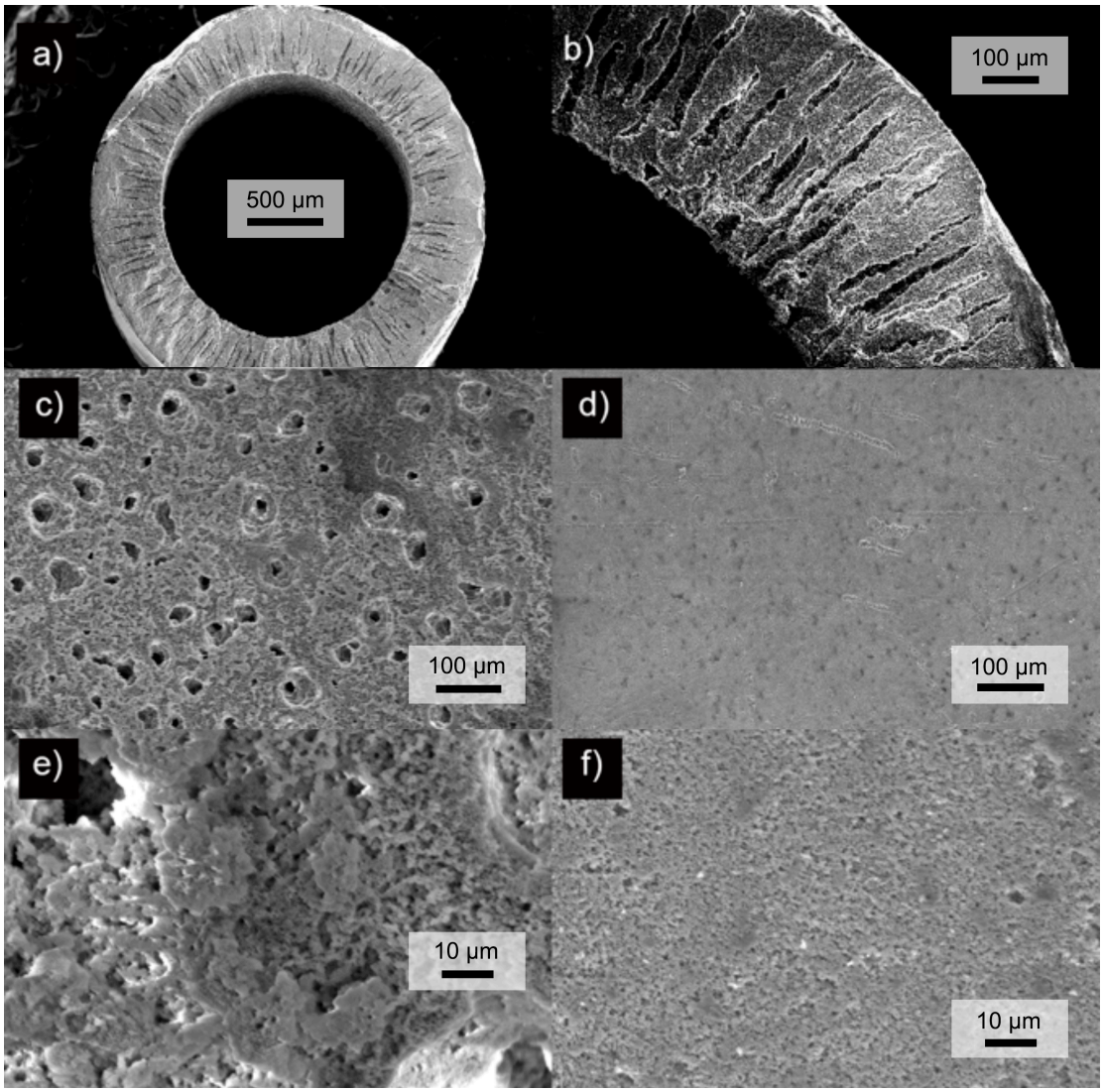


Figure 6.4 SEM images of a) whole view, b) close-up cross-sectional view, c) inner surface at low magnification, d) outer surface at low magnification, e) inner surface at high magnification and f) outer surface at high magnification of Membrane 2 sintered at 1342 °C

From Figure 6.4c-f, the inner surface appears to be much more porous than the outer surface. The pores at the inner surface are much larger than the pores at the outer surface and upon closer magnification at 1200x, it can be seen clearly that the small packing pores surround these large pores. Compared to Membrane 1, the inner surface of Membrane 2 appears rougher due to the fact that DMSO has been used as both the bore liquid and solvent in the suspension.

The larger secondary pores are the openings to the micro-channels across the membrane and can act to reduce the mass transfer resistance across the entire membrane during water permeation. Pore size distribution of Membrane 2's

separation layer is similar but wider than Membrane 1's (Figure 6.5a), due to the fact that there is only a very thin surface and sponge-like layer acting as the separation layer for Membrane 2. The mercury intrusion data in Figure 6.5b reveals a bimodal distribution, one at 0.23 μm and another between 5 and 20 μm. The much larger pores should belong to the inner surface openings of the large micro-channels, and the peaks for the smaller primary pores of both the outer thin separation layer and those between micro-channels are much narrower, implying a more even pore size distribution. Due to the much larger pores at the inner surface, Membrane 2 will most preferably operate in the outside-in configuration.

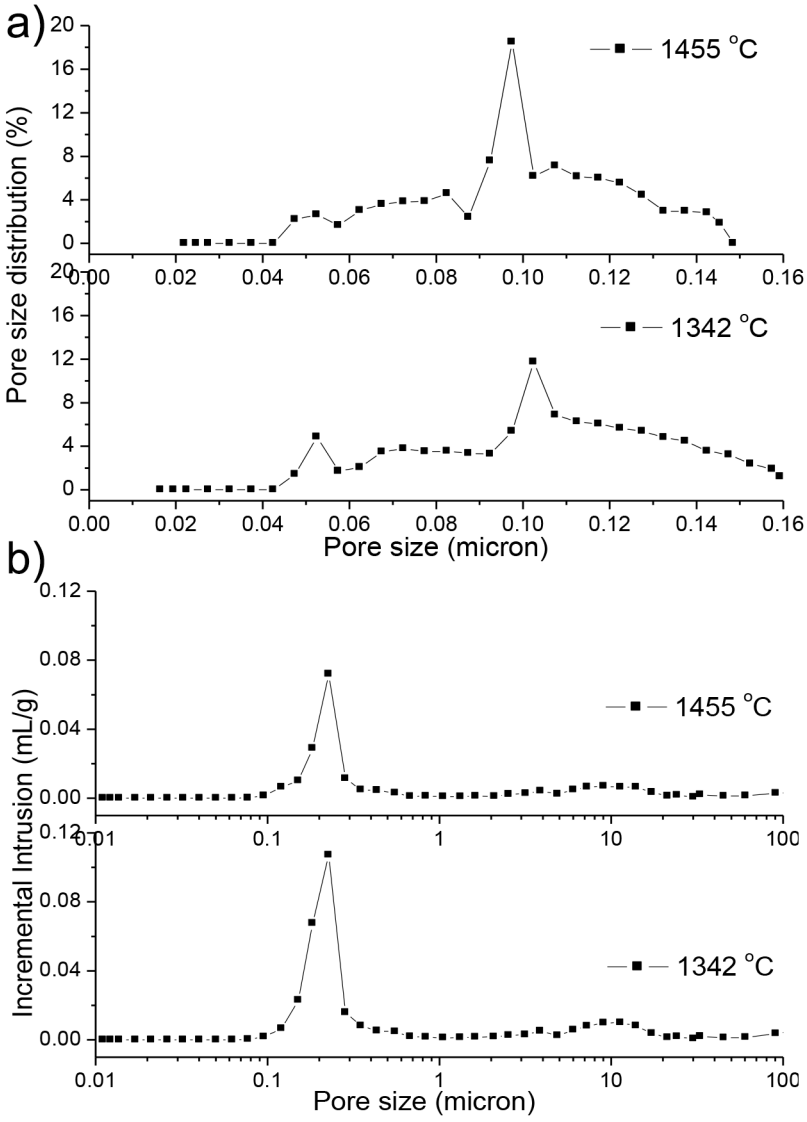


Figure 6.5 Bubble point method data a) and mercury intrusion data b) for Membrane 2 sintered at 1342 and 1455 °C

6.3.3 Morphology and microstructure of Membrane 3

In contrast to Membranes 1 and 2, when water is used as the inner coagulant, together with an air gap of 30 cm, the cross-sectional structure of Membrane 3, as shown in Figure 6.6, is formed. The morphology consists of two sponge-like layers of different thicknesses (sponge-like layer is much thicker at the outer region) sandwiching one layer of micro-channels (Figure 6.6a and b). 0 cm air gap with water as bore fluid has been previously reported to give a sandwich-like structure with two layers of finger-like voids and hence in this study 30 cm was chosen for the formation of long finger-like voids, in effort to reduce membrane resistance to water filtration[5]. As the suspension is extruded, the inner surface is in contact with the non-solvent earlier than the outer surface; hence phase inversion and the formation of micro-channels are initiated there. Meanwhile, the outer surface is in contact with air and solvent evaporation and polymer precipitation induced by the moisture in the air would contribute to an increase in local viscosity at the outer surface. As the nascent fibre enters the water bath the growth of micro-channels is inhibited from the outer region due to the area's increased viscosity. Solvent and non-solvent exchange at the outer surface further increases the local viscosity and the micro-channels originating from the lumen side are thus terminated. Due to elongation of the nascent fibre before entering the water bath, the outer diameter of Membrane 3 (Figure 6.6a) is smaller than Membrane 1 and 2's.

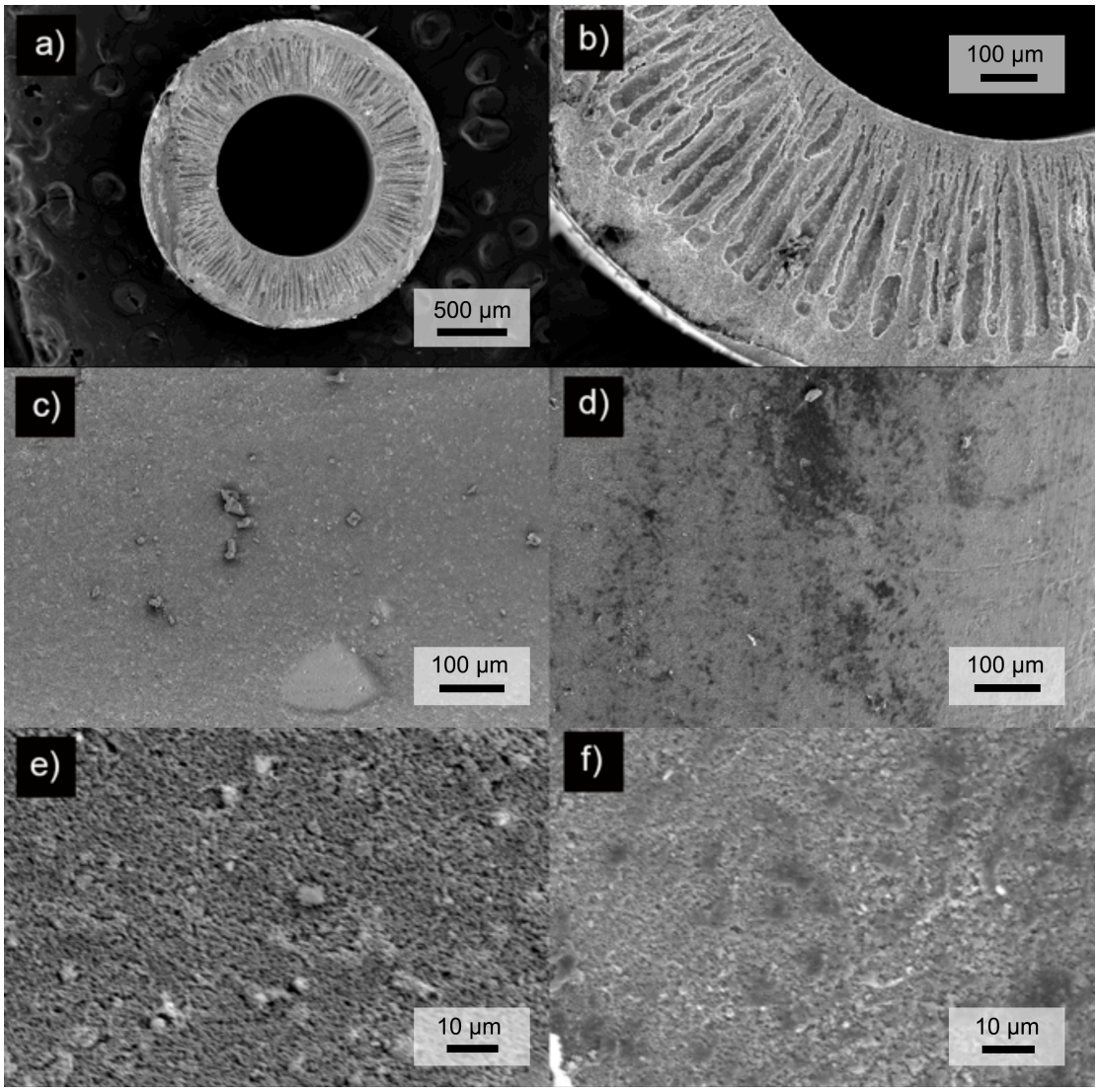


Figure 6.6 SEM images of a) whole view, b) close-up cross-sectional view, c) inner surface at low magnification, d) outer surface at low magnification, e) inner surface at high magnification and f) outer surface at high magnification of Membrane 3 sintered at 1342 °C

Figure 6.6c-f shows the surface morphology of Membrane 3. At low magnification, both the inner and outer surfaces appear to be tightly packed with no large pores, similar to Membrane 1 (Figure 6.2c and d). Upon higher magnification at 1200x, it can be observed that the packing pores at the inner surface are slightly larger than the ones at the outer surface. This indicates that the pore size distribution in Figure 6.7a (bubble point method) represents the pore structure of the outer thicker sponge-like separation layer, which is around 0.10 µm. The two peaks (0.23 µm and 0.54 µm respectively) in Figure 6.7b (mercury intrusion method) indicate the penetration of mercury from both the inner and outer surfaces, filling the micro-

channels, corresponding well to the high magnification SEM images in Fig 6.6(e) and (f). However, the cumulative intrusion of the 0.54 μm peak is around half of the one at 0.23 μm, because the latter represents the pore volume of both the outer sponge-like layer and those between the finger-like micro-channels. Membrane III may be able to operate in both outside-in and inside-out configurations, depending on the feed quality and the permeate specification.

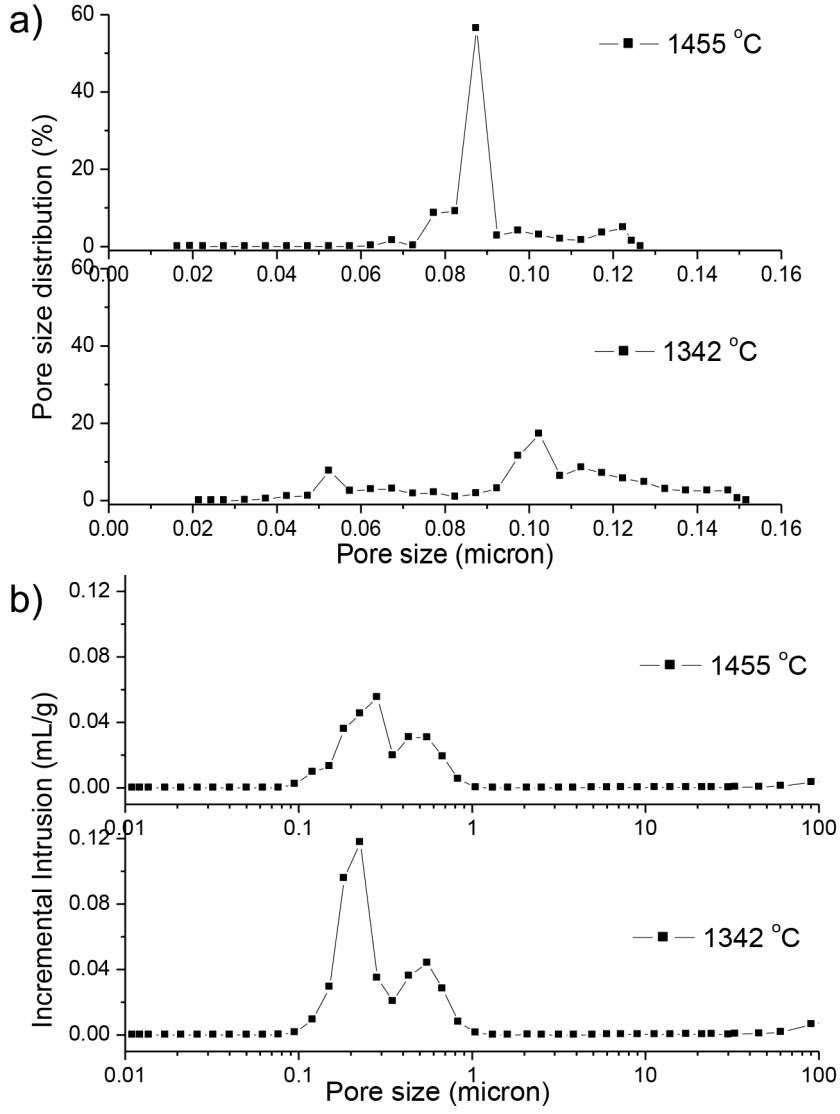


Figure 6.7 a) Bubble point method data and b) mercury intrusion data for Membrane 3 sintered at 1342 and 1455 °C

Figures 6.2, 6.4 and 6.6 show that the morphologies of the fabricated alumina hollow fibre membranes varies dramatically with changes in the spinning parameters. By changing the type of bore fluid and the length of air gap used during spinning, the separation layer thickness can be altered. The sponge-like sub-structures are formed

by the tightly packed ceramic particles immobilised by the precipitated polymer and the large micro-channels are formed from interfacial instabilities such as the Rayleigh-Taylor instabilty. The proportion and position of these different sub-structures within the cross-section can be altered by manipulating with the spinning conditions, such as: air gap, bore fluid choice, external coagulant choice, extrusion and bore fluid flow rates, etc. The sponge-like structures can be made very thin, forming the selective layer of the membrane. By using a solvent as the bore fluid, it has been observed here that finger-like micro-channels can be designed and formed. These micro-channels may be able to reduce trans-membrane resistance and improve mass transfer during filtration. The bubble point method data in Figures 6.3a, 6.5a and 6.7a revealed all three membranes to have separation layer pore sizes of below 0.20 μm. This means that they all are suitable for microfiltration. In contrast to the bubble point method, which reveals information on the open through pores, mercury intrusion method measures both dead and through pores; hence it can be used to probe more information about the overall pore structure of the membranes.

6.3.4 Mechanical Strength and Water Permeation Flux

As can be seen from Table 6.3, the membrane morphology has significant influence on the mechanical properties. Besides the increased mechanical strength at elevated sintering temperatures for all three membranes, Membrane 1 is slightly stronger than Membrane 2 with a similar OD, due to the presence of two sponge-like layers. Membrane 3 has the smallest OD, due to elongation effects during dry-wet spinning, and the thickest sponge-like layer, but the lowest mechanical strength. In general, larger micro-channels and thinner sponge-like layers are expected to reduce the membrane's mechanical strength. However, there are other factors that may have reduced Membrane III′s mechanical strength, such as a gradient pore size across the membrane cross-section and the difference in finger-like micro-channel densities inside the membrane. However, it is comparable with previous counterparts of similar morphologies [6, 7].

Table 6.3 Mechanical properties of the three membranes sintered at different temperatures with standard deviations of within 35 %

Sintering	Peak loading (N)			Mechanical Strength (MPa)		
Temperature (°C)	1	2	3	1	2	3
1342	12.0	8.6	4.2	58.3	41.8	39.7
1455	18.1	16.6	7.7	116.5	96.3	88.2

Pure water permeation of the three membranes was also tested as shown in Table 6.4. It can be seen that as the sintering temperature is decreased, the water permeation flux increases, agreeing well with morphologies and microstructures discussed above. Due to the presence of one thin sponge-like separation layer (outer surface), as well as highly porous micro-channels beneath it, Membrane 2 exhibits a higher water permeation flux (1874 L/(m^2·h) measured at 1 bar) compared with Membrane 1 where the separation layer is slightly thicker and is located at the inner sponge-like layer. In contrast, Membrane 3 with the thickest sponge-like separation layer gives the lowest water permeation, although its pore size distribution is quite similar to the other two membranes. The water permeation fluxes obtained for Membrane 2 at both sintering temperatures are above 1000 L/(m^2·h·bar), which is the general threshold value for microfiltration membranes [8].

Table 6.4 Water permeation of the three membranes sintered at different temperatures with standard deviations of within 25 %

Sintering	Water Permeation Flux (L/(m^2·h·bar))		
Temperature (°C)	1	2	3
1342	1069	1874	997
1455	753	1088	664

From these preliminary characterisations, it may be deduced that Membrane 2 would be more promising for usage in aqueous microfiltration treatment with superior water permeation flux. Further characterisations were then carried out on this

membrane, i.e. sintered in a wider range of temperatures (1204 - 1455 °C) and the results are given below.

Mercury intrusion data in Figure 6.8 shows that as the sintering temperature is increased, the intensity of the first peak, which indicates how porous the sponge-like structures are at the separation layer, reduces to almost half. Meanwhile, the pore size shifts from 0.18 μm to 0.23 μm. The second peak representing the open micro-channels reduces from approximately 17 μm to 9 μm when the sintering temperature is increased from 1204 to 1455 °C.

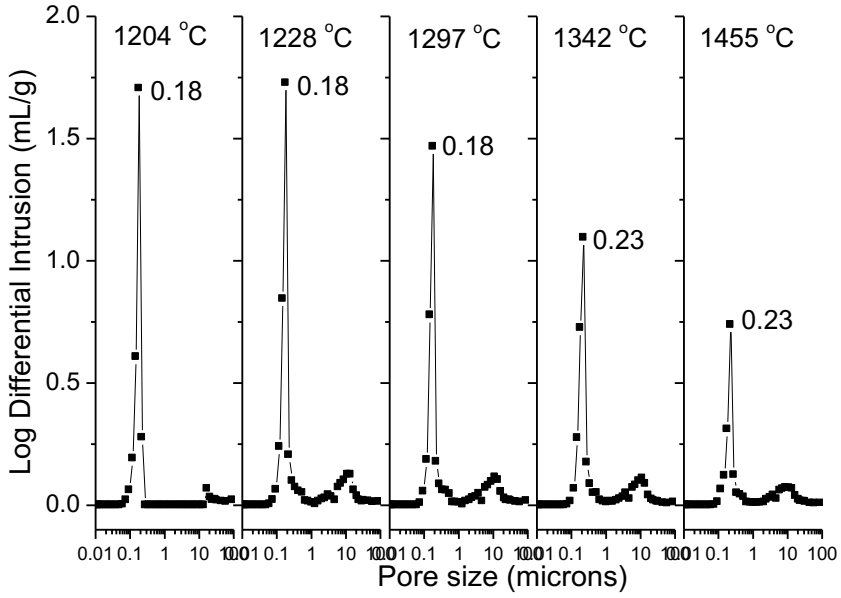


Figure 6.8 Mercury intrusion data for Membrane 2 sintered at 5 different temperatures

Figure 6.9 shows that as the sintering temperature is increased from 1204 °C to 1445 °C, the mechanical strength also increases. In particular, from 1350 °C onwards the mechanical strength increases more dramatically, but is compromised with a significant drop in water permeation flux. Similar trends have been observed in previous studies [6, 7].

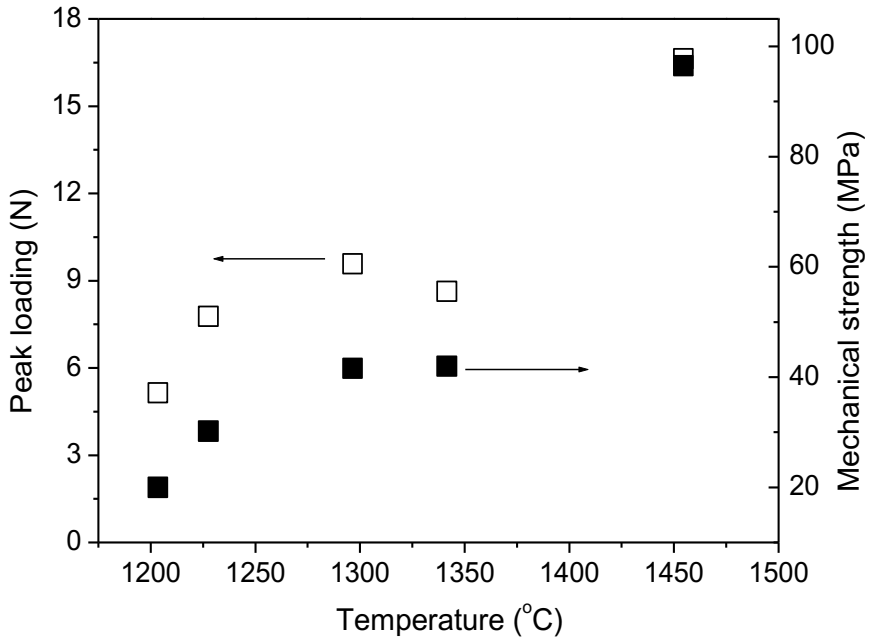


Figure 6.9 Peak loading and mechanical strength data for Membrane 2 sintered at 5 different temperatures with standard deviations of within 35 %

In general, sintering temperature affects porosity, pore size and thickness of a membrane, which subsequently affects its water permeation. From 1204 to 1297 °C, there is no significant change in the sponge-like structure (Fig 6.8), although the O.D. is smaller. This indicates that the slightly reduced separation layer thickness may lead to the increased water permeation in this temperature range (Fig 6.10). With further increased sintering temperatures (1342–1455 °C), the more significant changes in the sponge-like structure (Fig 6.8) and reduced surface pore size (Fig 6.5(a)) indicate a less permeable membrane (Fig 6.10), even if its separation layer is supposedly thinner than the one at lower sintering temperatures. It should also be noted here that, mercury intrusion data in Fig 6.8 represents the change of sponge-like structure throughout the Membrane II at various sintering temperatures, which can be slightly different from the pore structure of its separation layer (outer skin-like sponge-like layer). Further investigations focusing on the pore structure and actual thickness of this separation layer will reveal more details of how to further improve its water permeation.

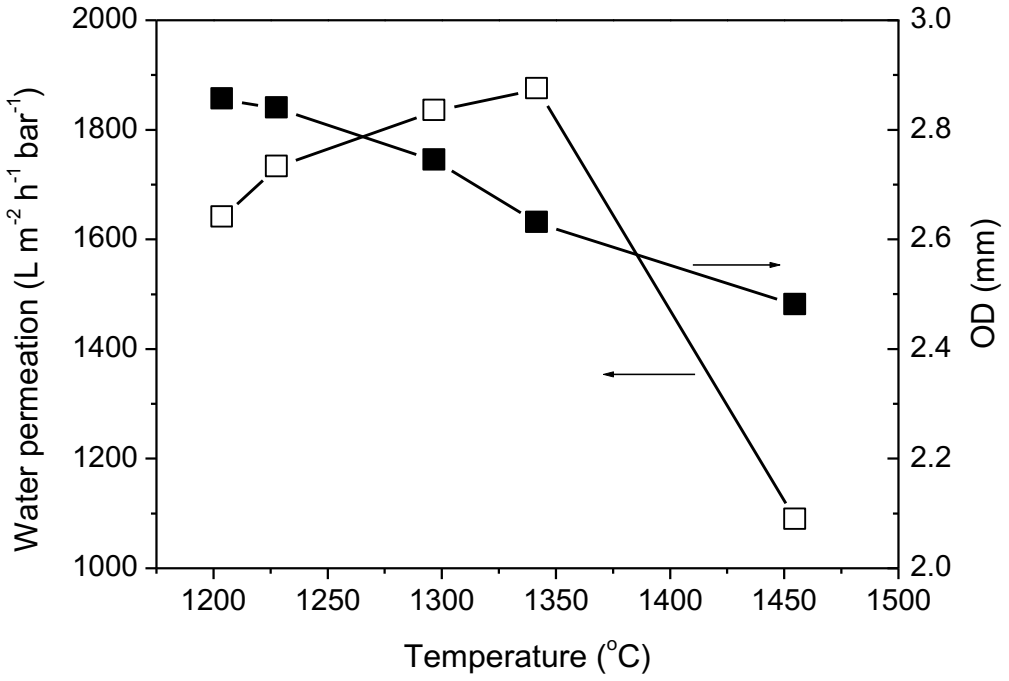


Figure 6.10 Water permeation flux data measured at 1 bar difference and the outer diameters of Membrane 2 sintered at 5 different temperatures with standard deviations of within 25 %

Overall, sintering conditions can be used to alter the water permeation flux and mechanical strength of the hollow fibre membranes. A compromise is required in order for the water permeation flux to be adequately high for water filtration purposes without losing its mechanical stability. From the results, sintering temperatures between 1300 °C and 1350 °C should be employed for the alumina hollow fibre membranes before the membrane undergoes a dramatic dip in water permeation flux.

6.4 Conclusions

Three different membrane morphologies have been achieved in one step via the combined phase inversion and sintering method. The manipulation of different spinning conditions such as air gap and bore fluid choice was used to create asymmetric membranes by altering the thicknesses of the sponge-like structures formed by the tight packing of ceramic particles and micro-channels formed by interfacial instabilities. When the ceramic suspension is extruded through the spinneret with no air gap, the choice of bore fluid has significant impact on the inner

surface structure. When an inert and immiscible fluid such as hexane is used as a bore fluid during wet spinning, two thin layers of sponge-like structures are formed at the inner and outer regions, sandwiching a layer of micro-channels. When a miscible solvent such as DMSO is used as the bore fluid, the thin sponge-like layer at the inner region is eliminated and micro-channels are formed. When water was chosen as the bore fluid with a 30 cm air gap, two layers of sponge-like structures of different thicknesses sandwiching one layer of finger-like voids is formed. The pore sizes at the surface of the separation layer(s) of all three types of membranes are less than 0.20 μm, falling in the microfiltration range. Membrane 2 exhibits the highest water permeation flux of up to 1874 L/(m^2·h) at 1 bar. This membrane would be expected to excel in water treatment applications compared to the other structures. This type of morphology was further characterised and it was found that different sintering temperatures could be used to alter its water permeation flux and mechanical stability. A sintering temperature of between 1300 °C and 1350 °C is recommended in order to have a trade-off between the water permeation flux and mechanical stability.

References

1. Zhang, T.C., et al., *Membrane Technology and Environmental Applications*. 2012: American Society of Civil Engineers
2. Li, K., *Ceramic Membranes for Separation and Reaction*. 2007: Wiley
3. Wang, Z., et al., *Preparation and Oxygen Permeation Properties of Highly Asymmetric La0.6Sr0.4Co0.2Fe0.8O3−α Perovskite Hollow-Fiber Membranes.* Industrial & Engineering Chemistry Research, 2008. **48**(1): p. 510-516.10.1021/ie8010462
4. Tan, X., et al., *Morphology control of the perovskite hollow fibre membranes for oxygen separation using different bore fluids.* Journal of Membrane Science, 2011. **378**(1–2): p. 308-318.http://dx.doi.org/10.1016/j.memsci.2011.05.012
5. Kingsbury, B.F.K. and K. Li, *A morphological study of ceramic hollow fibre membranes.* Journal of Membrane Science, 2009. **328**(1–2): p. 134-140.http://dx.doi.org/10.1016/j.memsci.2008.11.050

6. Liu, S., K. Li, and R. Hughes, *Preparation of porous aluminium oxide (Al2O3) hollow fibre membranes by a combined phase-inversion and sintering method.* Ceramics International, 2003. **29**(8): p. 875-881.http://dx.doi.org/10.1016/S0272-8842(03)00030-0
7. Wu, Z., et al., *A controlled sintering process for more permeable ceramic hollow fibre membranes.* Journal of Membrane Science, 2013. **446**(0): p. 286-293.http://dx.doi.org/10.1016/j.memsci.2013.05.040
8. Van Der Bruggen, B., et al., *A review of pressure-driven membrane processes in wastewater treatment and drinking water production.* Environmental Progress, 2003. **22**(1): p. 46-56.10.1002/ep.670220116

Chapter 7: New open micro-channelled alumina hollow fibre membrane structures toward broadened applications

***Chapter** 7 provides a novel method for producing ceramic hollow fibre membranes with open-micro-channels at any desired surface(s) via the use of polymeric sacrificial layers with potential widened applications*

Abstract

In this chapter, three structural designs for ceramic membranes have been achieved for the first time through the co-extrusion of polymeric and ceramic layers. During co-extrusion, micro-channels are initiated due to the Rayleigh-Taylor instability and they propagate through the different layers. The polymeric layer(s) is then calcined off during the heat treatment step, which opens the micro-channels and following sintering a ceramic membrane with open micro-channels ranging from a few to a few tens of micrometres in diameter can be formed. These long, straight and non-tortuous micro-channels can be controlled to be open at any or all of the surfaces. Design 4 has open micro-channels passing through the entire membrane wall, Design 5 has a separation layer at the lumen and open micro-channels at the shell side, and Design 6 has open micro-channels from both lumen and shell sides sandwiching a separation layer of sponge-like structure. Aside from having much improved mass transfer property due to the reduced effective membrane thickness, they can be easily incorporated into hybrid systems with anticipated improvements in unit compactness and performance. The pure water permeation of Design 5 reached up to 159, 000 L/m^2 h bar with pore sizes in the micro-filtration range. The micro-channels are easily accessible from the shell/lumen side; therefore catalysts or adsorbents can be easily deposited into the micro-channels. Examples of possible applications include a high-efficiency dispersing device realised with Design 4; a gas chromatography column for

gas separation with very low pressure drop realised with Design 5 and a highly compact membrane micro-reactor for consecutive reactions proposed with Design 6.

7.1 Introduction

The combined phase inversion and sintering method is a promising method for creating ceramic membranes that have shown various advantages over traditional methods in Chapter 6. The ability to form finger-like micro-channels in the membranes due to interfacial instabilities not only reduces mass transfer resistance, giving rise to competitive pure water permeation fluxes, but also widens the possible applications of these ceramic membranes [1-8].

In Chapter 6, by eliminating the redundant dense surface and sponge-like layer, the pure water flux of the membranes can be increased. Furthermore, the micro-channels are desirable crevices where catalysts or other active components can be deposited or coated to form hybrid systems [9], but the existence of the dense surfaces prohibit access to these micro-channels unless solution techniques are employed.

For flat disc membranes, it is very simple to mechanically open the micro-channels via sanding off the dense surface and/or the sponge-like layer. However, this is much more difficult to do in hollow fibre membranes. So far, only openings on hollow fibre inner surfaces have been achieved by incorporating a solvent into the bore fluid in Chapter 6 as well as in literature [10, 11]. However, there may be applications whereby other configurations are desired, for example, open micro-channels at the outer surface only, or open channels throughout the entire membrane cross-section. The flexibility of the combined phase inversion and sintering method means that the cross-sectional structure of hollow fibres can be designed and tailored as desired. In this study, three significantly different membrane cross-sectional structures with open micro-channels have been designed and fabricated via the co-extrusion of polymeric and ceramic layers. The co-extrusion of multiple of layers has been used extensively in both polymeric and ceramic membranes, broadening their applications whilst reducing fabrication costs [12-15]. Different materials can be used in the different layers to increase the functionality of the membranes. Dual-layered polymeric membranes have found use in applications such as pervaporation and membrane distillation and triple-layered membranes in solid oxide fuel cells [16, 17].

However, the multi-layered membranes in literature are mostly entirely organic, or inorganic, and the finger-like structures in these membranes are still enclosed inside the membranes. In this study, polymeric and ceramic layers were co-extruded, and following heat treatment the polymeric layer(s) are removed, leaving unique single-layered ceramic membrane structures. For the first time, ceramic hollow fibres with open micro-channels at the desired surface(s) have been formed in a single spinning step as shown in Figure 7.1 and their properties such as cross-sectional morphology, pore size distribution, mechanical stability and pure water flux were systematically investigated and their potential applications were discussed.

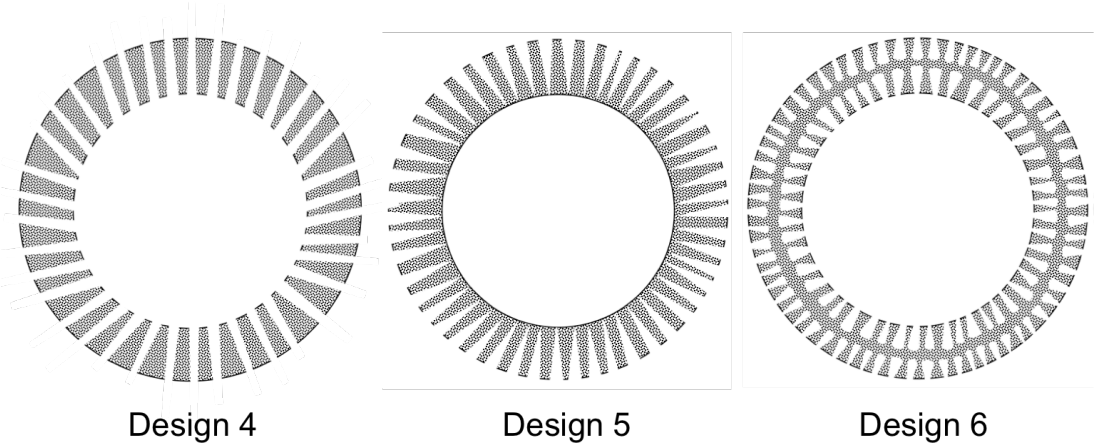


Figure 7.1 Schematic of the three types of hollow fibre cross-section structural designs achievable through co-extrusion of ceramic and polymeric layers

7.2 Experimental

7.2.1 Materials and preparation of alumina suspensions

The materials and prepraration method for the alumina suspensions are listed in Section 3.1 and 3.2. The composition of the alumina suspension for the hollow fibre designs 4, 5 and 6 are listed in Table 7.1. The composition of the polymer dope for the membrane emulsion experiment is described in Table 7.2.

Table 7.1 Alumina suspension composition for hollow fibre membranes Designs 4, 5 and 6

Layer	Composition (wt.%)							
	Design 4		Design 5		Design 6		Design 3	
Ceramic layer	NMP	33.6	DMSO	33.6	NMP	33.6	DMSO	33.6
	Alumina	60.0	Alumina	60.0	Alumina	60.0	Alumina	60.0
	PESf	6.0	PESf	6.0	PESf	6.0	PESf	6.0
	A135	0.4	A135	0.4	A135	0.4	A135	0.4
Polymeric layer	NMP	80.0	TEP	80.0	NMP	80.0	N.A.	
	PESf	20.0	PESf	20.0	PESf	20.0		
Bore fluid	NMP	70.0	Water	100.0	Water	100.0	Water	100.0

Table 7.2 Polymer dope composition for membrane emulsion experiment

Component	Composition (wt.%)
DMSO	90.0
PAN	10.0

7.2.2 Preparation of alumina hollow fibres

The general method for spinning alumina hollow fibres is described in Section 3.4. Table 7.3 lists the spinning parameters used and Figure 7.2 displays the photographs of the triple- and quadruple-orifice spinnerets for fabricating multi-layered ceramic membranes. These spinnerets have multiple concentric annuli, and can extrude many layers at the same time. The triple-orifice spinneret consists of 3 annuli, and the quadruple-orifice spinneret consists of 4 annuli. Ceramic and polymeric layers can be extruded simultaneously to form unique membrane morphologies. Figure 7.2 also displays the schematics explaining the components of each layer for hollow fibre designs 4, 5 and 6, and The alumina hollow fibre precursors were then dried and underwent heat treatment and sintering at 1350 °C, 1450 °C, 1500 °C and 1600 °C.

Table 7.3 Fabrication parameters for hollow fibre designs 4, 5 and 6

		Design 4	Design 5	Design 6	Common single layer hollow fibre
Flow rate (mL/min)	Inner polymeric layer	N.A.	N.A.	0.75	N.A.
	Ceramic layer	16	7	16	7
	Outer polymeric layer	1	4	1	N.A.
	Bore fluid	25	15	25	15
Air gap (cm)		0	25	0	25

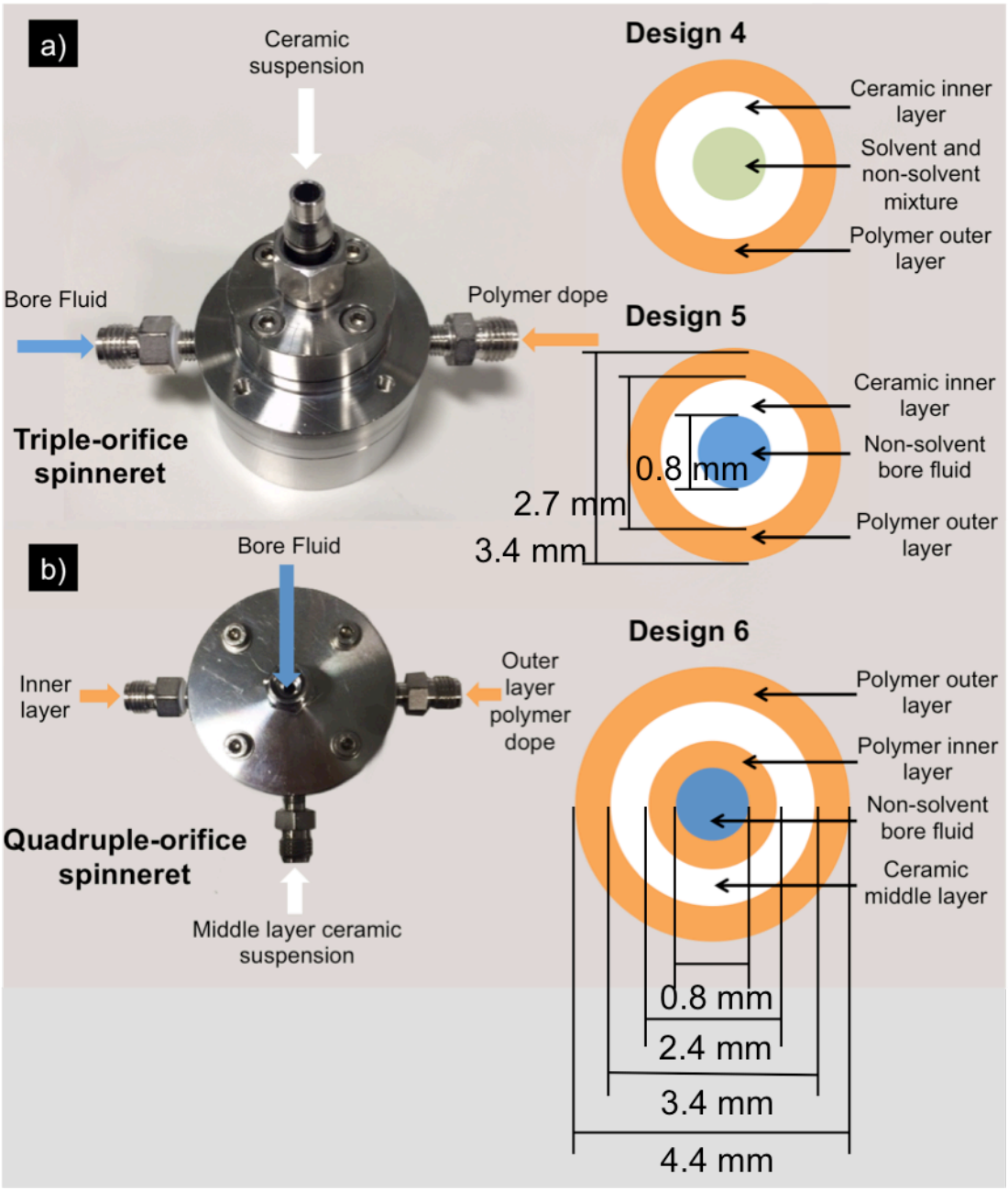


Figure 7.2 Photographs of the triple-orifice and quadruple-orifice spinnerets for extruding dual-layered and triple-layered hollow fibre membranes

7.2.3 Preliminary application experiments

7.2.3.1 Hollow fibre membrane emulsion experiment

Firstly hollow fibres of Design 4 were sintered at 1600 °C and then fitted onto ¼ inch NPT male connectors and sealed with epoxy resin at both the connector and at the

hollow fibre end. The hollow fibre was then connected to a syringe filled with PAN dope, which is controlled by a syringe pump. The rate of dope extrusion was fixed at 0.1 mL/min and the hollow fibre was immersed into a beaker of hexane whilst it was being constantly mechanically stirred. The solvent in the PAN dope was immiscible with hexane and hence the hexane turns from clear to cloudy as the amount of PAN emulsion in hexane is increased. Then the hollow fibre is removed and under continuous stirring, ethanol is added to the solution. The PAN is insoluble in ethanol and hence begins to precipitate, forming small polymeric microspheres (Figure 7.3).

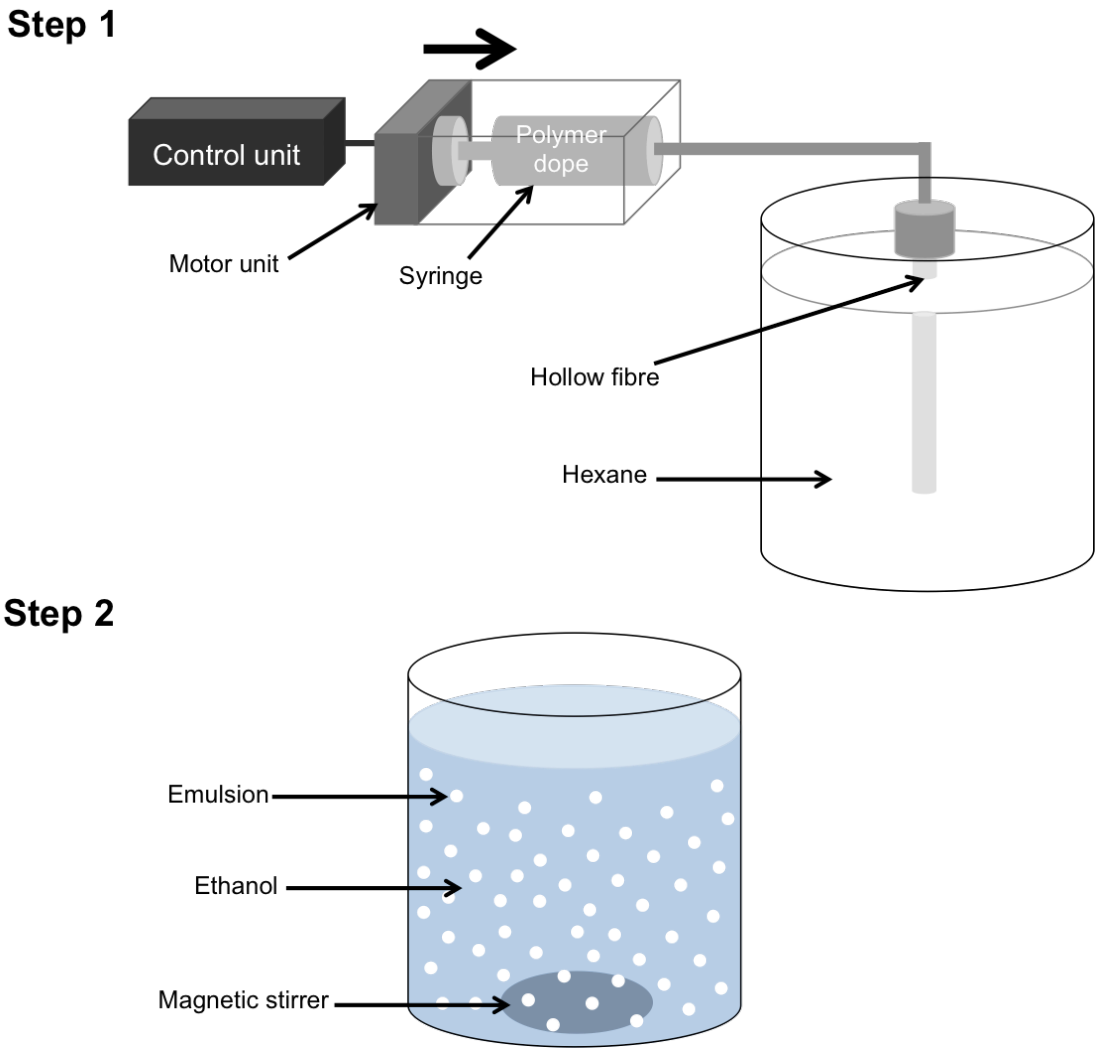


Figure 7.3 Schematic of the set-up for the hollow fibre membrane emulsion experiment

7.2.4 Characterisation

The characterisation methods such as SEM, gas-liquid displacement, 3-point bending, pure water permeation are descibed in Section 3.6.

7.3 Results

7.3.1 Cross-sectional morphology of the micro-structured hollow fibre membranes

7.3.1.1 Design 4

The cross-sectional structure of Design 4's membrane precursor is displayed in Figures 7.4a and 7.4b. Here the outer layer consists of a polymer, and the inner layer the ceramic material. The micro-channels can be seen to initiate from the polymeric layer at the shell side (Figure 7.4b) upon contact with the non-solvent in the coagulant bath at zero air gap, and propagated through the ceramic layer into the weak non-solvent bore fluid, leaving an open lumen. The polymeric layer was then subsequently removed during the heat session. This design is achieved via the use of a triple-layered spinneret, to co-extrude a layer of ceramic suspension inside a polymeric layer. In this case the choice of bore fluid and solvent for the polymer dope are vital to ensure open micro-channels at both the lumen and shell sides are achieved. The polymeric layer needs to be able to form intensive micro-channels that will have enough momentum to protrude through both layers. Therefore, NMP was chosen to solvate the PESf in both the outer polymeric and inner ceramic layers, according to Chapter 4. The bore fluid was chosen to be a mixture of non-solvent and solvent in order to reduce the precipitation rate at the lumen side, to prevent closure of the micro-channels in order to form an open lumen.

After calcination and sintering, the final membrane is left with open micro-channels at both the lumen and shell sides, as can be seen in Figure 7.4c-f. As the micro-channels are initiated from the shell side, their size at the outer layer is significantly smaller than the openings at the inner layer. The size and density of the openings at the shell side can be controlled via adjusting the polymeric, ceramic layers' and bore fluid composition as well as membrane thickness. There are many theories that different researchers have adopted for the source of these micro-channels, such as: the rapture of membrane surface [18], the growth of polymer-lean nuclei [19], viscosity gradient [20, 21], surface tension gradient [21-23], or the gradient of solidification and shrinkage rate along the interface [24]. As discussed in a previous study, the formation of the micro-channels may also be attributed to the

Rayleigh-Taylor Instability, which occurs when there is an acceleration on the interface between two fluids of different masses, and arises from perturbing waves at the interface (Chapter 4 and 5) Possible sources of acceleration that can cause interfacial instabilities include the solvent and non-solvent exchange and polymer precipitation, which leads to the accelerated movement of the interface towards the polymer solution/ceramic suspension side. The general trends of micro-channel growth have been recorded, explained and quantitatively mimicked in this previous study, which explains the effect of different solvents in the ceramic suspension on the micro-channel lengths, shape and density. For Design 4, it can be therefore predicted that by using a solvent with a high mutual diffusion coefficient with the coagulant bath combined with a significant density gradient across the polymer and non-solvent interface, higher micro-channel densities at both the lumen and shell sides can be achieved. On the other hand, the polymeric layer thickness would also affect the micro-channel size and density. A thicker polymeric layer would mean larger micro-channel openings at the shell side, as the micro-channels would have had longer time to develop in both length and width before meeting the ceramic suspension. However this thickness cannot be too high such that the micro-channels lose all of their momentum before being able to protrude through the lumen. Design 4 can be used as a substrate from which additional membrane layers can be deposited upon, with much reduced mass transfer resistance due to the open-channelled structure. Furthermore, due to the long, cylindrical and non-tortuous micro-channels of Design 4, another possible application would be as a high-efficiency mixing device to produce emulsions or dispersions of one liquid phase in another immiscible liquid phase.

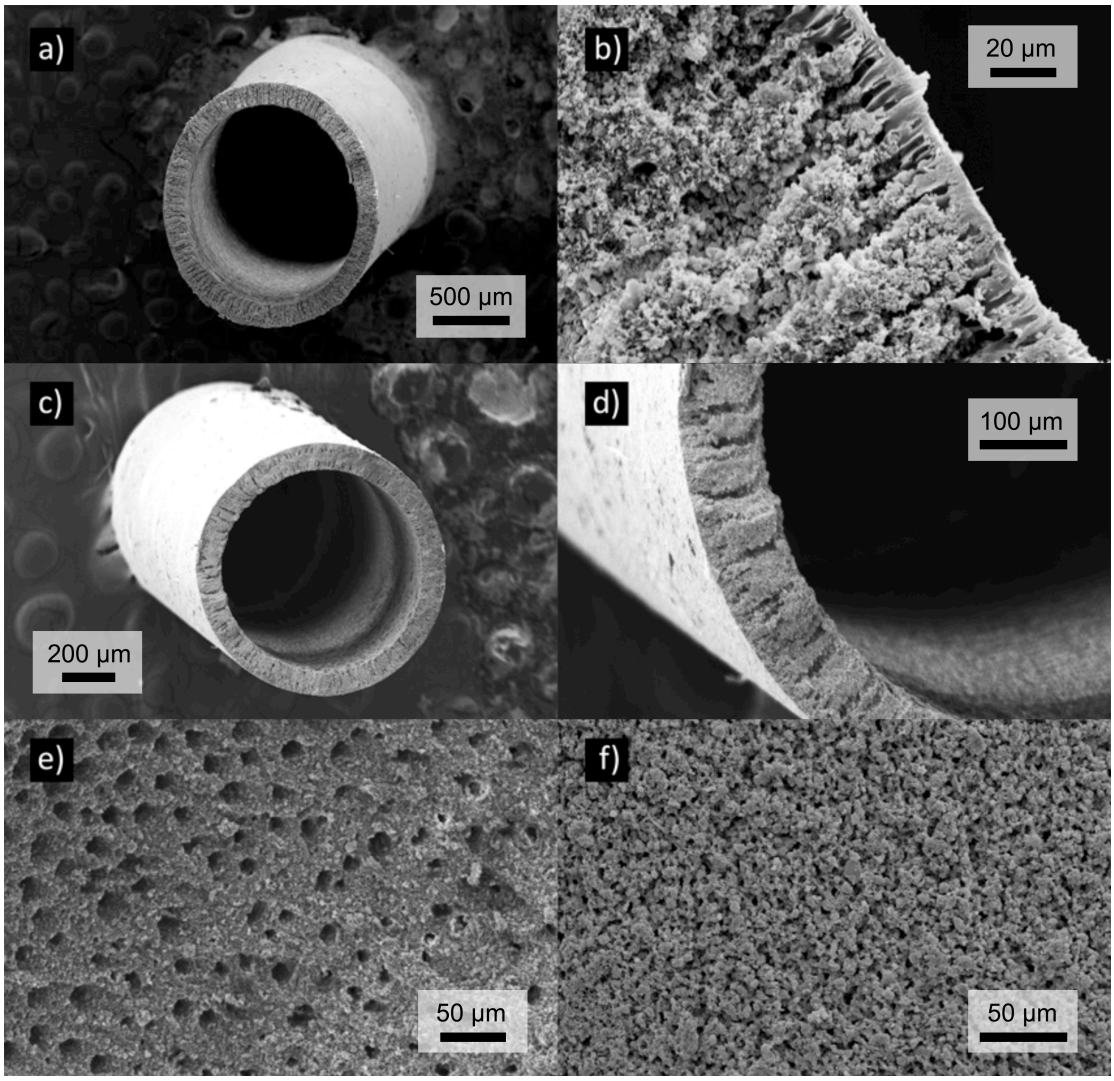


Figure 7.4 SEM cross-section images of the Design 4's dual-layered membrane precursor (a-b), sintered fibre at 1500 °C (c-d) and the inner and outer surfaces of the sintered fibre at 1500 °C (e-f), respectively

7.3.1.2 Design 5

Figure 7.5 displays the cross-sectional morphology of Design 5. From Figure 7.5a and 7.5b, a dual-layered membrane can be seen; this is the membrane precursor for Design 5. The inner layer consists of alumina particles, immobilised by the precipitated polymer binder, surrounded by an outer polymeric layer. All of the micro-channels originate from the lumen side upon contact with the non-solvent bore fluid, and propagates across the ceramic layer towards the shell, protruding through into the polymeric layer, as can be seen in the close up SEM (Figure 7.5b). After the

heat treatment, the polymeric outer layer is removed, leaving an open outer surface. This type of design is created via the use of triple-layered spinnerets to simultaneously spin a ceramic layer inside a polymeric layer. During spinning, the lumen and shell sides will be in contact with the water non-solvent, and phase inversion will commence at both sides at different times by the use of a long air gap. The air gap gives time for the micro-channels to develop from the lumen before the outer polymeric layer comes into contact with the water bath, and here the choice of solvent in the polymer dope is vital to realise the designed structure. The outer polymeric layer needs to precipitate slowly enough for the micro-channels to break through at the ceramic suspension and polymeric layer interface, and to ensure that the polymer outer layer forms a continuous sponge-like structure near the shell side. Therefore, in this case, TEP was chosen to solvate the PESf for the outer polymeric layer. A previous study has shown that no micro-channels are formed during phase inversion when TEP is used as the solvent, and its precipitation rate is slower than other common solvents (Chapter 4). The solvent chosen for dispersing the alumina particles and solvating the PESf for the inner layer is also important, as the acceleration of the interface at the lumen side needs to be high enough to initiate the micro-channels as well as to provide enough momentum for the micro-channels to propagate through the entire ceramic layer and into the polymeric layer. The theory behind the origin of the micro-channels can be found in the same previous study mentioned above in Chapters 4 and 5. Based on this previous study, DMSO was chosen as the solvent to facilitate the growth of long, regular and densely packed micro-channels.

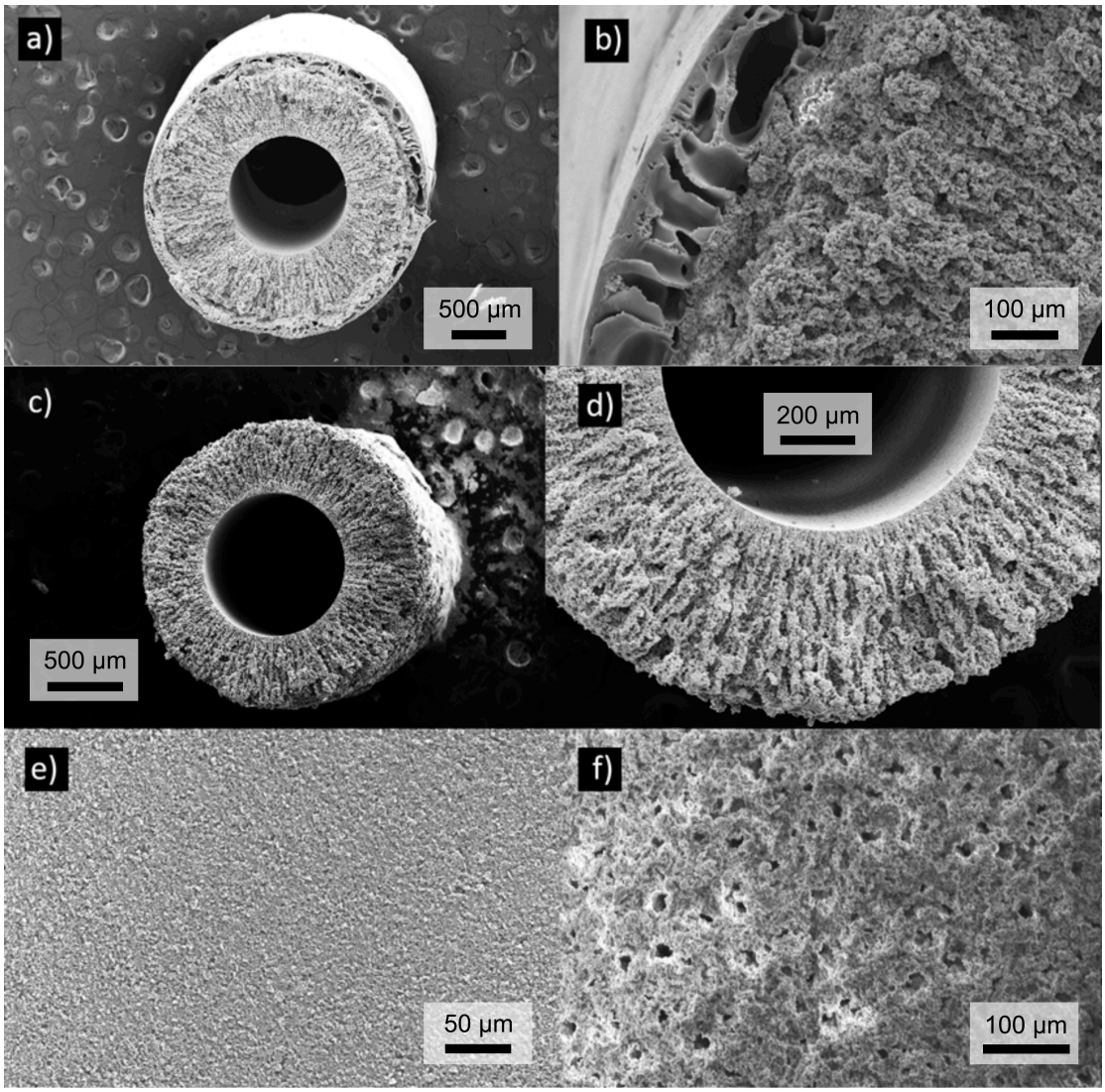


Figure 7.5 SEM cross-section images of Design 5's dual-layered membrane precursor (a-b), sintered fibre at 1500 °C (c-d) and the inner and outer surfaces of the sintered fibre at 1500 °C (e-f), respectively

Following debinding and sintering, the polymeric layer is eliminated and the ceramic inner layer is consolidated, as shown in Figure 7.5c and 7.5d. Here it can be seen that the membrane thickness is reduced significantly (from around 2580 µm precursor diameter to 1870 µm final diameter after sintering at 1500 °C). The lumen surface is dense and can thus act as a separation barrier, whereas the shell side surface consists of intensively arranged open micro-channels and together they reduce the mass transfer resistance of the membranes. The pore size and pore size distribution of the separation surface can be controlled using different suspension compositions as well as sintering conditions, and pore size can range from completely dense to

micrometre-scaled. The size of the micro-channel openings at the shell side can be controlled by various factors. One method would be to change the composition of ceramic suspension and bore liquid to provide different driving forces for the initialisation and growth of the micro-channels, which may result in varied channel densities and channel sizes. Detailed explanations on the formation of the micro-channels can be found in Chapters 4 and 5. Another method would be to change the ceramic layer thickness, with thicker membranes leading to larger micro-channel openings, as the micro-channels grow in both their length and lateral width across the radial direction. Due to the ease of access of these micro-channels from the shell side, catalysts or adsorbents can be easily deposited into these pockets of space, opening a broad range of different applications, such as water treatment hybrid systems, membrane micro-reactors, gas separation columns, etc.

7.3.1.3 Design 6

Figure 7.6a and 7.6b display the cross-sectional morphology of the triple layered membrane precursor for Design 6, which has three layers: two polymeric layers sandwiching a layer of ceramic material. The inner polymeric layer could not be seen in the SEM diagram as the polymer shrinks and delaminates from the fibre immediately after the spinning process. This design is created via the use of a quadruple-layered spinneret (shown in Figure 7.2). During spinning, phase inversion will occur at both the lumen and shell sides, starting from the polymeric layers. In this case, it is desired for the micro-channels to be formed from the polymer sides and into the ceramic layer. Therefore, similar to Design 4, NMP was chosen for the polymeric and ceramic layers, and the micro-channels can be seen to originate from both the shell and lumen sides, breaking through to the ceramic layer, meeting in the middle.

Following debinding and sintering, a ceramic hollow fibre membrane with open micro-channels at both the lumen and shell sides is formed (Figure 7.6c-f). The opening sizes of the micro-channels at the inner layer are significantly smaller than the ones at the outer layer. The size of these micro-channels can again be controlled, using the methods mentioned for Designs 4 and 5. Furthermore, the sponge-like separation layer's pore size can also be tailored without significantly affecting the micro-channel sizes during sintering. Such a design could be used in applications such

as a highly compact and efficient membrane micro-reactor for multiple reactions, whereby two catalytic reactions can take place in series in the catalyst-containing micro-channels at the different sides of the membrane.

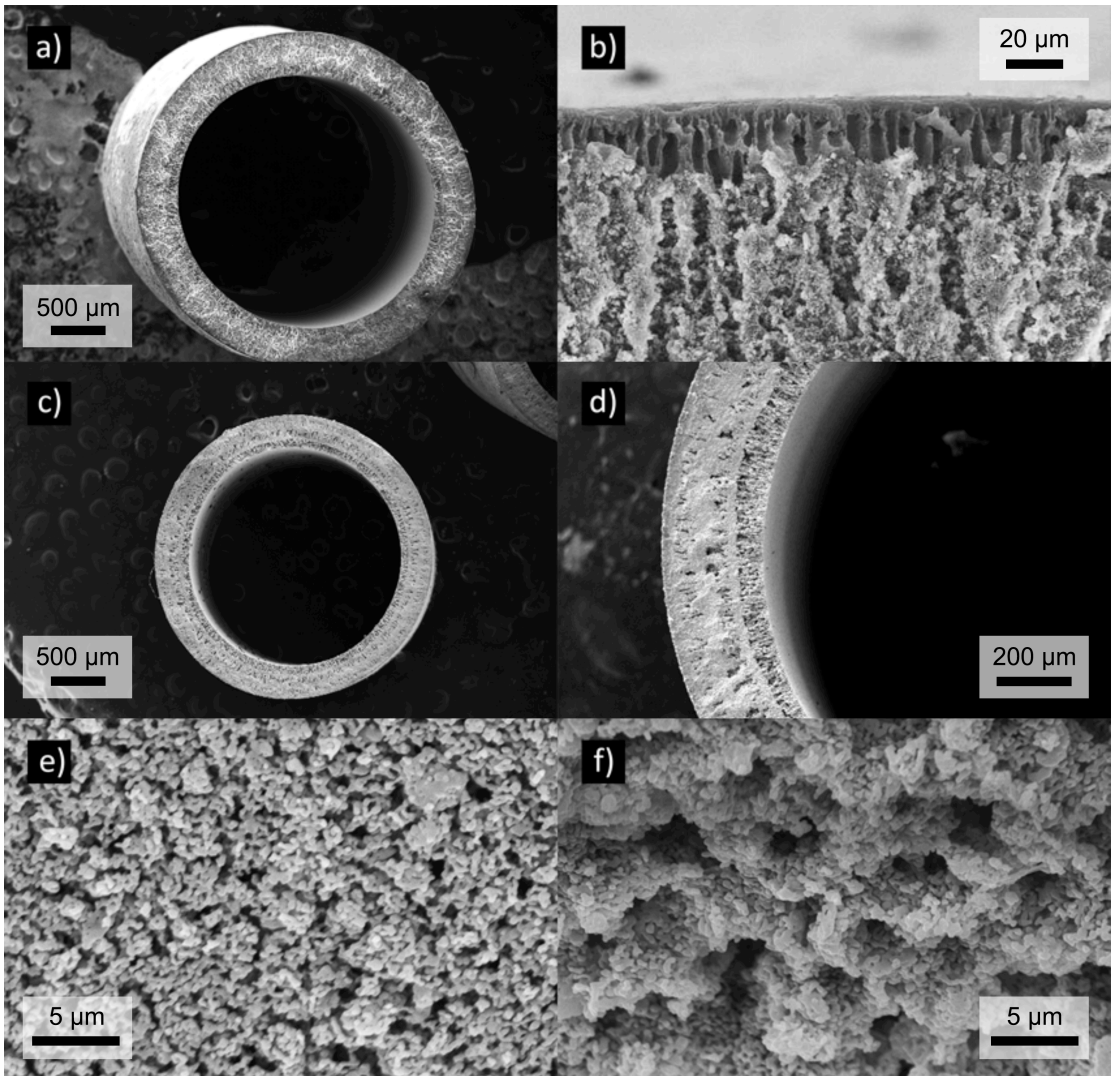


Figure 7.6 SEM cross-section images of Design 6's triple-layered membrane precursor (a-b), sintered fibre at 1500 °C (c-d) and the inner and outer surfaces of the sintered fibre at 1500 °C (e-f), respectively

7.3.2 Pore size, pore size distribution and micro-channel size

Gas-liquid displacement porosimetry was used to probe information regarding the through pores of Designs 4 and 5. This method measures the smallest size of the channels; therefore the results give the opening size on the outer surface for Design 4 and the pore size on the inner separation surface for Design 5. Figure 7.7 reveals the size distribution of the micro-channel openings on the outer surface of Design 4. The

graph shows a main peak at 3.41 μm and a smaller peak at 1.65 μm, which may be attributed to different sets of micro-channels in the outer polymeric layer. From the SEM images (Figure 7.4e) the inner layer has much larger micro-channel openings of up to 40 μm in diameter. For Design 5, Figure 7.8 reveals the pore size of the inner separation surface, which is at around 1 μm and the micro-channel openings at the outer surface can be seen to range from 10 μm to 40 μm from SEM images (Figure 7.5f). Figure 7.9 shows the mercury intrusion result of Design 6, whereby the sponge-like layer pore size distribution and the size of the openings for Design 6 can be seen. The sponge layer pore sizes lie between 0.25-0.30 μm, and the bigger pore size distribution from 1-5 μm, which peaked at 3.2 μm can be attributed to the openings on the inner and outer surfaces. The result is concurrent with the SEM images, which confirms that the micro-channel openings for Design 6's inner layer mostly range between 1-2 μm (Figure 7.6e), whereas the outer layer micro-channel openings are in the range of between 3-5 μm (Figure 7.6f).

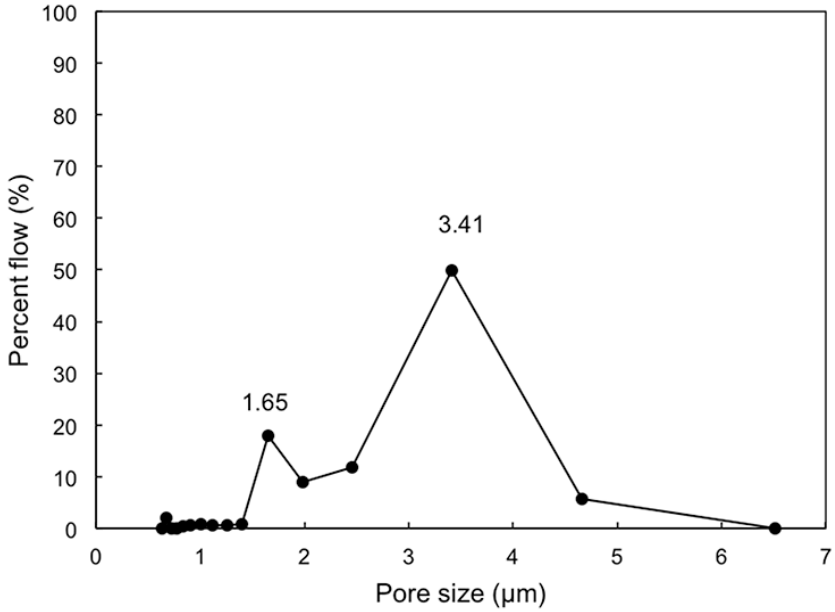


Figure 7.7 Gas-liquid displacement porosimetry data for membrane Design 4

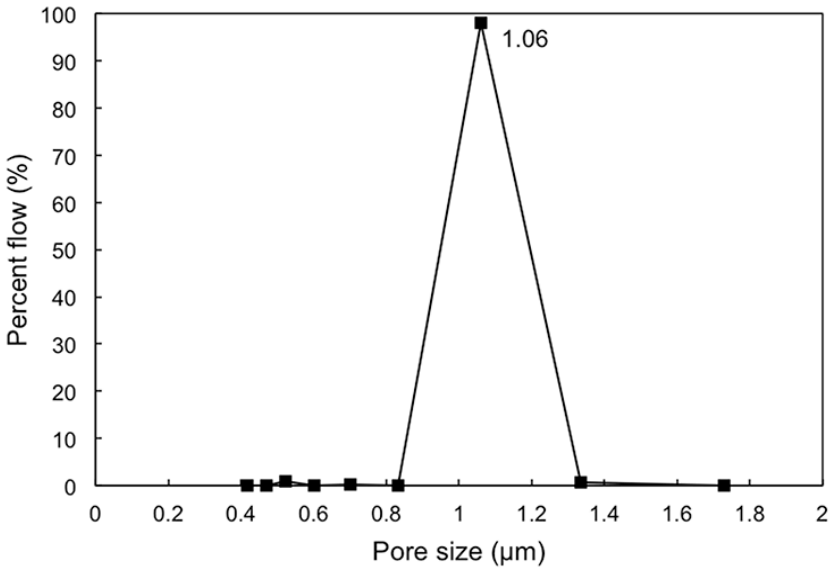


Figure 7.8 Gas-liquid displacement porosimetry data for membrane Design 5

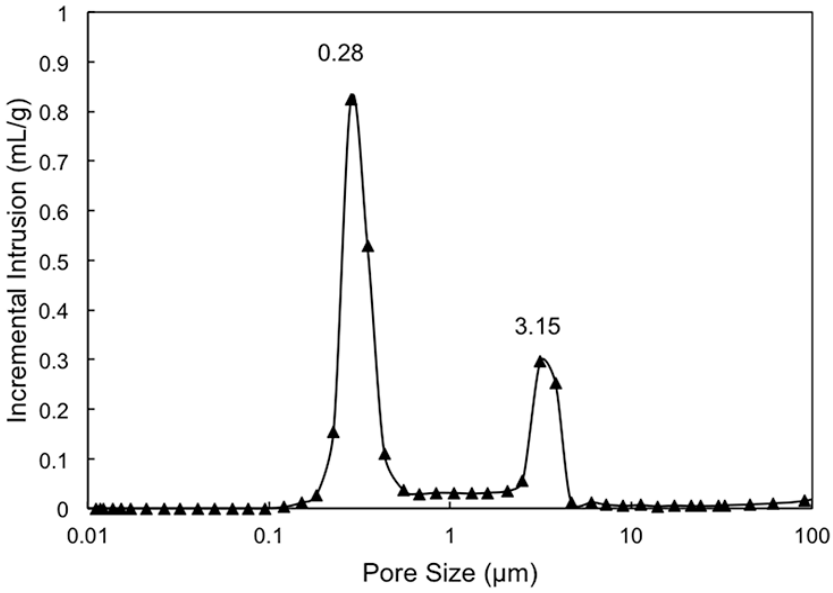


Figure 7.9 Mercury intrusion porosimetry data for membrane Design 6

7.3.3 Water permeation

In water treatment applications, it is desired for the clean water permeation rate to be as fast as possible. Design 5 has only one very thin separation layer, and its water

permeation flux is evidently superior to common asymmetric hollow fibres fabricated in this study and also elsewhere [25], as can be seen in Table 7.4. Design 5 has fluxes that are about 60 times higher than an asymmetric hollow fibre membrane with denser inner and outer surfaces and sponge-like layers, reaching fluxes as high as 159,000 L/m^2 h bar. This is due to the ultra-thin effective separation layer in Design 2, whose average pore size is around 1 μm, providing sufficient selectivity for microfiltration applications. The long and open micro-channels provide the membranes with adequate mechanical stability to be used continuously under a trans-membrane pressure of 1 bar, which is sufficient for microfiltration. On the other hand, the pure water permeation fluxes of Design 4 and 6 were omitted, as their designs are not intended for single-phase microfiltration applications. It can also be noticed that this flux is dramatically higher than the water permeation flux of Design 2's in Chapter 6. Although the pore size of Design 5 (sintered at 1450 °C) is only 4 times larger than the pore size of Design 2 (sintered at 1342 °C), the flux is around 85 times higher. This is because for Design 5, the separation layer is much thinner and the micro-channel density much higher, when compared with Design 2, due to the choice of solvent and lowered ceramic loading in this study.

Table 7.4 Water permeation flux of Design 5 sintered at different temperatures under 1 bar trans-membrane pressure operated under dead-end filtration mode with standard deviations of within 25 %

Sintering Temperature (°C)	Water permeation flux (L/m^2 h bar)		
	Design 5	Design 3	Phase inversion alumina hollow fibre from literature[25]
1450	159,000	2500	340
1500	121,000	1872	-

7.3.4 Mechanical property

Table 7.5 displays the 3-point bending strength of the 3 designs. It is apparent that the cross-sectional morphology, composition of the different layers in the precursors, and sintering temperature can have dramatic influence on the membrane's mechanical

stability. Design 4 has comparable bending strength to a typical asymmetrical ceramic hollow fibre formed by phase inversion in this study, especially at the lower sintering temperatures. Design 5 has the lowest bending strength out of all of the fibres fabricated in this study. Compared with Design 4, although both designs eliminate the sponge-like layer, the number of micro-channels and thus the porosity in Design 5 is significantly higher than Design 4's, and hence the mechanical property of Design 5 is much weaker, and this should be improved in future studies. Design 6 can be recognised to have the highest bending strength out of all of the fibres compared in this experiment at all sintering temperatures, due to fact that the design has a thick sponge-like layer, which give a strong support to the fibre. However, in general the mechanical stability is lower than others in literature, that have much thicker densely packed structures [25], and improving mechanical stability should be the focus of future works.

Table 7.5 3-point bending strength of the 3 designs sintered at different temperatures with standard deviations of within 35 %

Sintering Temperature (°C)	Bending Strength (MPa)				
	Design 4	Design 5	Design 6	Design 3	Phase inversion alumina hollow fibre from literature[25]
1350	14.8	2.61	32.6	12.5	-
1450	48.0	6.8	74.5	30.9	130
1500	50.0	10.71	117.4	89.8	150

7.4 Discussions

7.4.1 Propagation of micro-channels at the two-layer interface

The initiation and growth of micro-channels during phase inversion have been pointed out to be the consequence of interfacial instability in Chapters 4 and 5. We have studied the flat disc cases of alumina membranes and found that a quantitative prediction of the development of micro-channels can be achieved by using the

Rayleigh-Taylor Instability theory. According to the R-T Instability theory, for the single layer cases, when water comes into contact with the polymer solution or ceramic suspension, the density difference and the interfacial acceleration would drive interfacial disturbances to grow quickly at certain wavelengths, and water streams penetrate into these growing points with a high initial speed, and the momentum of water streams may lead to the development of long and slim micro-channels in the membrane. In this study, whereby there were two higher density layers in contact with the lighter non-solvent, the interface between the two layers lies in the way of proceeding micro-channels, and various scenarios could be met and the propagation of micro-channels would occur differently.

In the case of Designs 4 and 6, the micro-channels grow from the polymeric layer into the ceramic layer, which means that the momentum of the water stream in the proceeding micro-channels is partially dissipated in the polymeric layer first, before meeting the interface. The momentum must be adequate after passing the interface to push the micro-channels into the ceramic suspension, which has a higher viscosity and resistance to micro-channel growth. This means that if the thickness of the polymeric layer is increased, dissipation of the momentum in the polymeric layer will be higher. The remaining momentum that can work onto the ceramic suspension is smaller, and fewer micro-channels will have the adequate initial momentum to pass through to the ceramic layer, and the openings will be larger in size but more sparsely distributed. If the thickness of the polymeric layer is further increased, there will be no water streams with sufficient momentum to pass the ceramic layer, and no micro-channels would propagate through. In case of Design 5, micro-channels start from the ceramic layer and proceed towards the polymeric layer, and at the interface the viscosity and resistance decrease suddenly, making the front of micro-channels an easier way to out, and therefore the micro-channels cross over the interface easily, leaving big open pores on the surface of the ceramic layer when the polymer is removed after sintering.

7.4.2 Potential applications of the three unique structured hollow fibres

7.4.2.1 Design 4

As mentioned briefly in the results, the different micro-structures can be used for different applications, depending on the process and their different requirements. Design 4 has no active separation layer and therefore cannot be used directly for separation applications such as micro/ultrafiltration. Its unique structure consists of straight micro-channels that are open at both the lumen and shell sides, and their size and amount can be controlled during the spinning process. A potential application of this structural design would be membrane emulsification, a method that uses low pressure to force the dispersed phase to permeate through a porous membrane with a uniform pore size distribution into the continuous phase. This is much simpler, and requires lower energy requirements and less surfactant when compared with conventional methods that uses colloid mills, rotor-stator systems, and high pressure homogenizers [26]. Currently, membrane emulsification faces limitations due to their low fluxes, intrinsically due to the membranes available on the market. Another method is called micro-channel emulsification, which uses chips with micro-channel arrays made via etching, and can produce highly uniform-sized droplets, but main drawback once again includes low production rates [27]. Design 4 has both the advantages of membrane and micro-channel emulsification, as it has a fairly uniform micro-channel size, and very low mass transfer resistance, as well as being able to form highly compact hollow fibre bundles. The dispersed phase can be pushed through the micro-channels from the lumen and enter the continuous phase to form the emulsions, as can be seen in Figure 7.10. As the micro-channel sizes can be tailored accordingly, a range of different sized droplets can potentially be formed. Furthermore, the membranes can be produced easily in large quantities, and hence scale-up would be simple by combining the membranes in modules and can potentially be used to mass-produce emulsions. Figure 10 displays polyacrylonitrile spheres formed using a Design 5 hollow fibre membrane in a preliminary study to first form a continuous emulsion and then followed by precipitation in a non-solvent. The resulting spheres were successfully fabricated with an average diameter of around 0.1 μm.

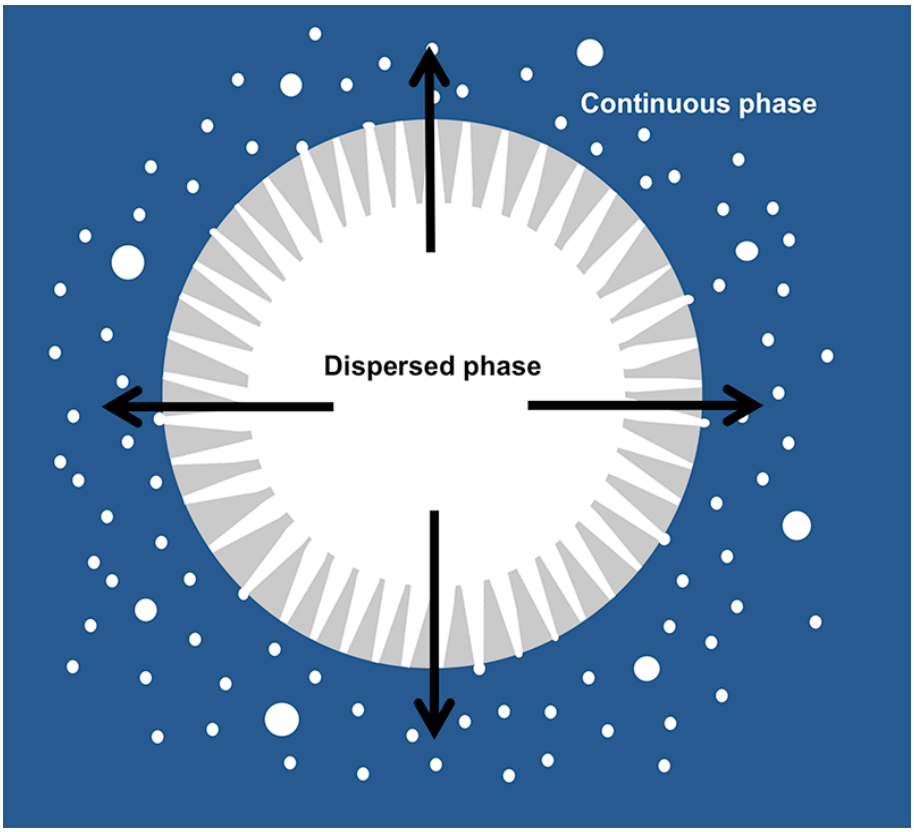


Figure 7.10 Schematic of a membrane emulsification process that can be realised with Design 4

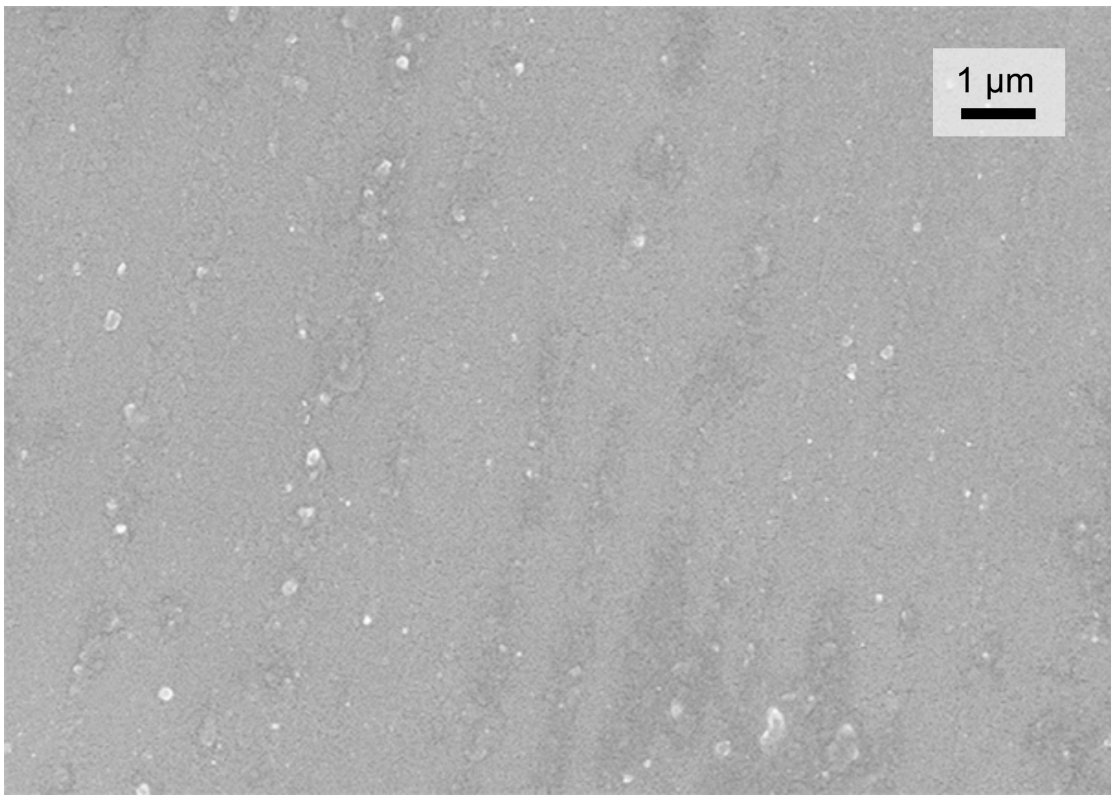


Figure 7.11 SEM of PAN spheres formed from membrane emulsification using Design 4 followed by phase inversion

7.4.2.2 Design 5

For Design 5, there is only one very thin separation layer at the lumen, and its advantages include very low mass transport resistance and extremely high geometric surface area. This makes them desirable for a wide range of applications, such as micro/ultrafiltration, micro-reactor, membrane hybrid systems, gas chromatography, etc. For micro/ultra-filtration, the membranes can be used on their own to provide selectivity against contaminants in wastewater such as sand and large particulates, colloids, bacteria, volatile organic components, etc. Furthermore, as the micro-channel densities are very high, these membranes provide an exceptional amount of accessible geometric surface area and volume, forming pockets in which other functional materials can be deposited. This opens up an extensive list of possible applications, such as: membrane micro-reactor with catalysts deposited into the micro-channels, one-step membrane hybrid system for heavy metal adsorption or a gas chromatography column by depositing adsorbents into the micro-channels, as depicted in Figure 7.12. The use of Design 5 membranes for the abovementioned applications will all potentially reduce a large amount of space required for the same amount of productivity, forming highly compact systems.

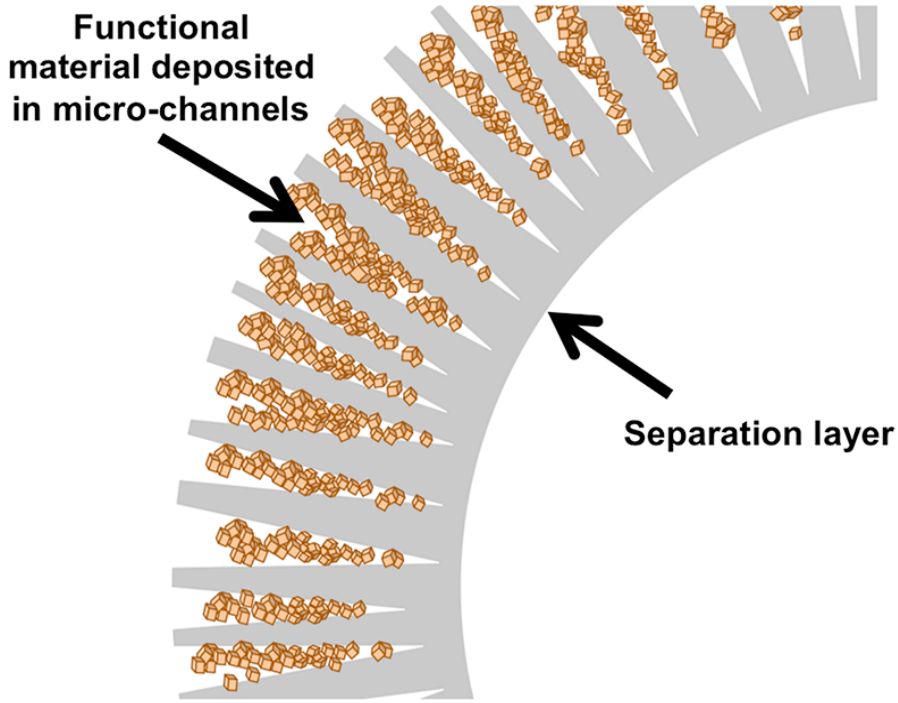


Figure 7.12 Schematic of membrane Design 5 with deposited functional material in the micro-channels

7.4.2.3 Design 6

Design 6 has no smooth separation layer that is in direct contact with the feed, and would therefore not be additionally beneficial in micro/ultra-filtration processes as large contaminants can get deposited into the micro-channels, and would be difficult to clean. Instead, this design can possibly be used as a highly compact and efficient membrane micro-reactor for multiple reactions. As there are two sets of open micro-channels that are separated by a sponge-like layer, two different reactions can take place in series at the different sides of the membranes. For example, Design 6 can potentially be used to combine the methanol reforming reaction with the water gas shift (WGS) reaction in one hollow fibre membrane reactor to produce hydrogen that is suitable for fuel cells, as illustrated in Figure 7.13. In this configuration, one side is packed with methanol reforming catalysts in the micro-channels, and when the feed of methanol and water vapour pass through the membrane, it will be converted to H_2, CO_2 and a small amount of CO. The products then flow into the packed WGS catalysts in the micro-channels of the other side and react with the water vapour fed from the other side to minimise the concentration of CO, so that the produced hydrogen will be safe to use in polymer electrolyte membrane (PEM) fuel cells. Such a compact and highly efficient design would be especially useful to provide quality hydrogen for mobile devices, in which the space is very much limited.

And since the fabrication technique is applicable to other materials, the sponge-like layer in the middle of the Design 6 can be made to be selective to one of the products of the up-stream reaction, and take full advantages of the unique membrane structure. For example, if the membrane is made of a mixed ion and electron conducting (MIEC) material that only allow oxygen to permeate but not others, a decomposition reaction of an oxygen-containing compound and an oxygen-consuming reaction can be coupled seamlessly. A typical case for the up-stream reaction would be the catalytic decomposition of CO_2, which produces O_2 and CO at high temperatures with low equilibrium conversion rate; if the other side of the membrane is packed with catalysts for partial oxidation of methane (POM) or oxidative coupling of methane (OCM), which consumes oxygen from the other side through the middle separation layer, the equilibrium limit of the CO_2 decomposition can be broken due to the removal of the oxygen product.

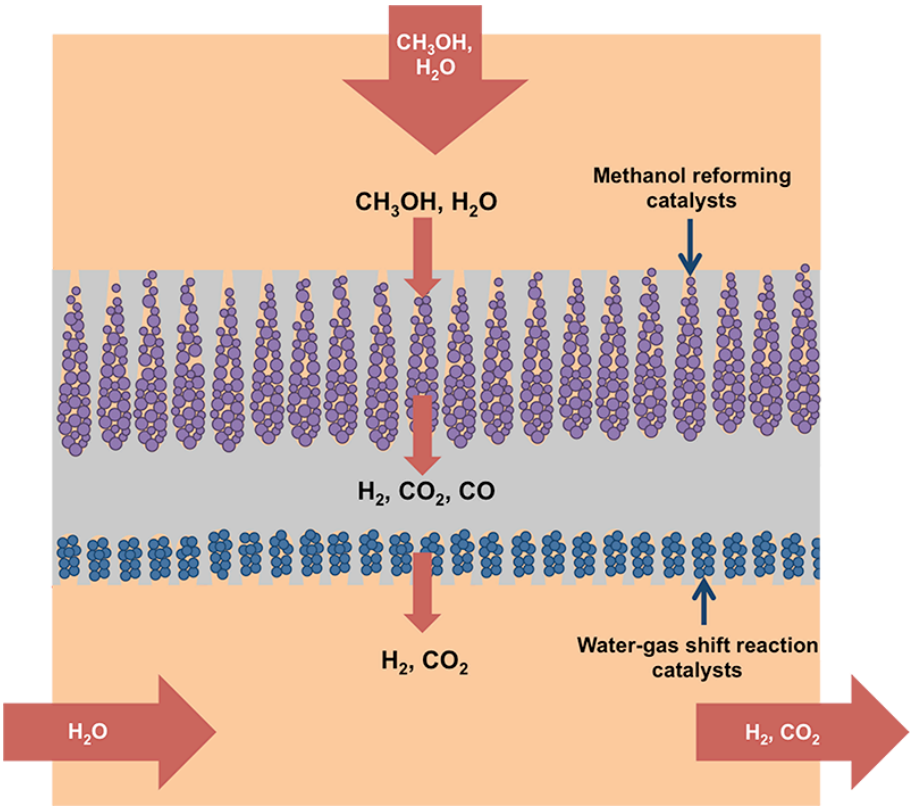


Figure 7.13 Schematic of a combined methanol reforming and water shift reaction process that can be realised with Design 6

7.5 Conclusions

Three new ceramic membrane structural designs have been performed and fabricated in this study, with long, cylindrical and non-tortuous micro-channels that can be arranged to be open at either the inner or outer surfaces, or both surfaces via a single-step co-extrusion method. Design 4, with long, straight and non-tortuous open micro-channels at both surfaces can potentially be used in membrane emulsification. Design 5 has open micro-channels on the outer surface that greatly reduce the mass transfer resistance of the membrane, due to the impressively reduced effective membrane thickness. This was evident in the pure water permeation flux of Design 5, which reached values as high as 159, 000 L/m^2 h bar. Due to the very low mass transfer resistance combined with an exceptional amount of surface area offered by the micro-channels, Design 5 can potentially be used in a wide range of applications such as: micro-filtration for water treatment, membrane hybrid systems whereby adsorbents can be easily deposited into the micro-channels for heavy metal removal, or as a gas

chromatography column with adsorbents in the micro-channels for gas separation. Design 6 has open micro-channels on both the inner and outer surfaces, with a sponge-like layer in the centre. This design can potentially be used as a membrane micro-reactor for consecutive reactions, whereby the micro-channel at the different sides of the sponge-like layer can perform different reactions by the deposition of different catalysts. The micro-channel properties such as opening size as well as the selective layer pore size can be easily tailored according to the application by adjusting the spinning parameters. The main drawback of these new designs is the lower mechanical stability, which can be improved in future studies by increasing the overall membrane thickness whilst maintaining the very thin separation layer.

References

1. Fang, H., et al., *Hydrophobic porous alumina hollow fiber for water desalination via membrane distillation process.* Journal of Membrane Science, 2012. **403–404**: p. 41-46.http://dx.doi.org/10.1016/j.memsci.2012.02.011
2. Huang, H., et al., *Facile one-step forming of NiO and yttrium-stabilized zirconia composite anodes with straight open pores for planar solid oxide fuel cell using phase-inversion tape casting method.* Journal of Power Sources, 2015. **274**: p. 1114-1117.http://dx.doi.org/10.1016/j.jpowsour.2014.10.190
3. Zhang, J.-W., et al., *Preparation and characterization of silicon nitride hollow fiber membranes for seawater desalination.* Journal of Membrane Science, 2014. **450**: p. 197-206.http://dx.doi.org/10.1016/j.memsci.2013.08.042
4. Huang, H., et al., *Phase-inversion tape-casting preparation and significant performance enhancement of Ce0.9Gd0.1O1.95–La0.6Sr0.4Co0.2Fe0.8O3−δ dual-phase asymmetric membrane for oxygen separation.* Materials Letters, 2014. **137**: p. 245-248.http://dx.doi.org/10.1016/j.matlet.2014.09.016
5. Zhuang, S., et al., *Dense composite electrolyte hollow fibre membranes for high temperature CO2 separation.* Separation and Purification Technology, 2014. **132**: p. 712-718.http://dx.doi.org/10.1016/j.seppur.2014.06.025
6. Zhang, X., et al., *Fabrication of nanostructured TiO2 hollow fiber photocatalytic membrane and application for wastewater treatment.* Chemical

Engineering Journal, 2014. **236**: p. 314-322.http://dx.doi.org/10.1016/j.cej.2013.09.059

7. Othman, N.H., Z. Wu, and K. Li, *An oxygen permeable membrane microreactor with an in-situ deposited Bi1.5Y0.3Sm0.2O3−δ catalyst for oxidative coupling of methane.* Journal of Membrane Science, 2015. **488**: p. 182-193.http://dx.doi.org/10.1016/j.memsci.2015.04.027
8. Gouveia Gil, A., et al., *A highly permeable hollow fibre substrate for Pd/Al2O3 composite membranes in hydrogen permeation.* International Journal of Hydrogen Energy, 2015. **40**(8): p. 3249-3258.http://dx.doi.org/10.1016/j.ijhydene.2015.01.021
9. Othman, N.H., Z. Wu, and K. Li, *A micro-structured La0.6Sr0.4Co0.2Fe0.8O3−δ hollow fibre membrane reactor for oxidative coupling of methane.* Journal of Membrane Science, 2014. **468**: p. 31-41.http://dx.doi.org/10.1016/j.memsci.2014.05.051
10. Tan, X., et al., *Morphology control of the perovskite hollow fibre membranes for oxygen separation using different bore fluids.* Journal of Membrane Science, 2011. **378**(1–2): p. 308-318.http://dx.doi.org/10.1016/j.memsci.2011.05.012
11. Liu, N., et al., *Honeycomb-structured perovskite hollow fibre membranes with ultra-thin densified layer for oxygen separation.* Separation and Purification Technology, 2011. **80**(2): p. 396-401.http://dx.doi.org/10.1016/j.seppur.2011.04.014
12. de Jong, J., et al., *Towards single step production of multi-layer inorganic hollow fibers.* Journal of Membrane Science, 2004. **239**(2): p. 265-269.http://dx.doi.org/10.1016/j.memsci.2004.02.039
13. Zhu, J., L. Jiang, and T. Matsuura, *New insights into fabrication of hydrophobic/hydrophilic composite hollow fibers for direct contact membrane distillation.* Chemical Engineering Science, 2015. **137**: p. 79-90.http://dx.doi.org/10.1016/j.ces.2015.05.064
14. Bonyadi, S. and T.S. Chung, *Flux enhancement in membrane distillation by fabrication of dual layer hydrophilic–hydrophobic hollow fiber membranes.* Journal of Membrane Science, 2007. **306**(1–2): p. 134-146.http://dx.doi.org/10.1016/j.memsci.2007.08.034

15. Fu, F.-J., S. Zhang, and T.-S. Chung, *Sandwich-structured hollow fiber membranes for osmotic power generation.* Desalination, 2015. **376**: p. 73-81.http://dx.doi.org/10.1016/j.desal.2015.08.018
16. Li, T., Z. Wu, and K. Li, *Co-extrusion of electrolyte/anode functional layer/anode triple-layer ceramic hollow fibres for micro-tubular solid oxide fuel cells–electrochemical performance study.* Journal of Power Sources, 2015. **273**: p. 999-1005.http://dx.doi.org/10.1016/j.jpowsour.2014.10.004
17. Jamil, S.M., et al., *Recent fabrication techniques for micro-tubular solid oxide fuel cell support: A review.* Journal of the European Ceramic Society, 2015. **35**(1): p. 1-22.http://dx.doi.org/10.1016/j.jeurceramsoc.2014.08.034
18. Strathmann, H., et al., *Formation Mechanism of Asymmetric Membranes.* Desalination, 1975. **16**(2): p. 179-203.Doi 10.1016/S0011-9164(00)82092-5
19. Smolders, C.A., et al., *Microstructures in Phase-Inversion Membranes .1. Formation of Macrovoids.* Journal of Membrane Science, 1992. **73**(2-3): p. 259-275.Doi 10.1016/0376-7388(92)80134-6
20. Kingsbury, B.F.K. and K. Li, *A morphological study of ceramic hollow fibre membranes.* Journal of Membrane Science, 2009. **328**(1–2): p. 134-140.http://dx.doi.org/10.1016/j.memsci.2008.11.050
21. Matz, R., *Structure of Cellulose-Acetate Membranes .1. Development of Porous Structures in Anisotropic Membranes.* Desalination, 1972. **10**(1): p. 1-&.Doi 10.1016/S0011-9164(00)80243-X
22. Sternling, C.V. and L.E. Scriven, *INTERFACIAL TURBULENCE - HYDRODYNAMIC INSTABILITY.* AIChE Journal, 1959. **5**(4): p. 514-523
23. Frommer, M.A. and R.M. Messalem, *Mechanism of Membrane Formation .6. Convective Flows and Large Void Formation during Membrane Precipitation.* Industrial & Engineering Chemistry Product Research and Development, 1973. **12**(4): p. 328-333.DOI 10.1021/i360048a015
24. Neogi, P., *Mechanism of Pore Formation in Reverse-Osmosis Membranes during the Casting Process.* Aiche Journal, 1983. **29**(3): p. 402-410.DOI 10.1002/aic.690290309
25. Xu, G., et al., *SiC nanofiber reinforced porous ceramic hollow fiber membranes.* Journal of Materials Chemistry A, 2014. **2**(16): p. 5841-5846.10.1039/C3TA15348G

26. Charcosset, C., I. Limayem, and H. Fessi, *The membrane emulsification process—a review.* Journal of chemical technology and biotechnology, 2004. **79**(3): p. 209-218

27. Vladisavljević, G., I. Kobayashi, and M. Nakajima, *Production of uniform droplets using membrane, microchannel and microfluidic emulsification devices.* Microfluidics and nanofluidics, 2012. **13**(1): p. 151-178

Chapter 8: Micro-structured alumina multi-channel capillary tubes and monoliths

Chapter 8 *describes a method for increasing the mechanical stability of ceramic tubular membranes by fabricating multi-channel capillary tubes and monoliths in attempt to gain both high strength and flux simultaneously*

Abstract

In this chapter, a continuous and single-step fingering inducing phase-inversion process for fabricating micro-structured alumina multi-channel capillary tubes and monoliths, which consist of a plurality of radial micro-channels, has been developed. In addition to the geometrical similarity to conventional ceramic monoliths, the unique radial micro-channels created in the walls of the multi-channel capillary tubes (or monoliths) can reduce hydraulic resistance and increase surface area, which are critically important factors for filtration and catalytic reactions. Furthermore, the enlarged cross section area of the multi-channel configuration enhances the resistance to external impacts. The technique described in this study not only can be scaled up for fabricating monoliths of commercial sizes, but can also be scaled down to make multi-channel capillary tubes, solving the issue of insufficient mechanical property in current ceramic hollow fibres.

8.1 Introduction

The presence of radial micro-channels significantly greatly reduces the permeation resistance to fluids as a membrane, and increases their accessible surface area, which is critically important for catalytic reactions when employed as a catalyst substrate. However, these radial micro-channels compromise the membrane's mechanical

property, as seen in the previous chapters. Generally it is preferred to bundle the hollow fibres/capillary tubes of this type together in order to meet industrial expectations.

To increase the tube strength to resist external impacts, the most efficient way is to increase the cross section area of the ceramic tubes. Two strategies can be adopted to achieve this: one is to use a single-channel configuration and increase the area of the cross section by increasing the diameters and/or the wall thickness; and the other option is to use a multi-channel configuration. The former strategy seems straightforward but in practice faces problems during the phase-inversion fabrication process. When the thickness or the diameter exceeds a certain value, the precipitation rate of the nascent fibre reduces quickly and the suspension cannot be solidified in time, hence the fibre will not be maintained in the desired dimensions because of severe elongation induced by gravity. Due to this reason, the diameter and the thickness of ceramic hollow fibres are limited. In fact, even if larger ceramic hollow fibre/capillary tubes can be made, it will compromise the surface area to volume ratio as well as their transport convenience.

Multi-channel ceramic monoliths, or sometimes known as ceramic honeycombs, have been widely studied and used in industries [1], especially in the fields of catalyst substrates and membrane filtration. Its current fabrication process is largely based on extruding a ceramic paste through a die or mould, similar to the way that commercial ceramic tubes are fabricated. The multi-channel monoliths fabricated through this method have symmetric-structured walls. Even though the monoliths obtained in such a way can have high surface area to volume ratios, it is still low when compared with the requirements of a catalyst carrier, and thus an extra coating of γ-alumina is often washed onto the inner surface of the channels to further enhance the surface area. Thus, the resistance of mass/heat transfer is also significantly increased due to its microstructure.

Applying the micro-channel inducing phase-inversion technique to the multi-channel configuration is theoretically advantageous from aspects of both the fabrication process and the performance of the multi-channel monoliths. In this chapter, the idea of multi-channel monolith membranes via the micro-channel inducing phase-inversion method is implemented by delicately designed spinnerets as described in Section 8.2. The designed spinnerets use certain numbers of well-arranged parallel nozzles to deliver the internal coagulant, and the rest of the

encompassed circular area is filled with the ceramic suspension. With such multi-channel spinneret configurations, the problem of slow precipitation in larger-dimension single-channel hollow fibres will no longer be an issue, because the thickness of the internal walls between the channels and the outer wall has been largely reduced. Furthermore, the internal walls come into contact with the internal coagulant on both sides, thus the precipitation rate of the suspension is further improved. With the multi-channel spinnerets, it is now possible to produce ceramic monolith/capillary tubes of large dimensions. It is also expected that multi-channel ceramic monoliths produced through this method will minimise the drawbacks of traditional monoliths by introducing self-organised radial micro-channels in the cross section of the walls, which will not only reduce the resistance of mass/heat transfer, but also greatly increase the geometric surface area, which will be beneficial for catalytic reactors.

Aiming to combine the advantages of phase-inversion induced asymmetric structures and multi-channel monolith tubes, in this prove-of-principle study, 1-channel and 3-channel hollow fibres as well as 7-channel and 19-channel capillary/monolith tubes were successfully fabricated through the micro-channel inducing phase-inversion method. The macro- and micro-structures of the multi-channel tubes were characterised, the mechanical property was investigated, and the mass transport property of the tubes was evaluated from water permeation results. This chapter also theoretically explored the influence of the macro-structure to the mechanical property, as well as a feasible route of improving water permeation through optimised sealing patterns of the multi-channel tubes.

8.2 Experimental

8.2.1 Materials and alumina suspension preparation

The materials used and the alumina suspension preparation procedure is described in Section 3.1 and 3.2. The composition of the alumina suspensions are listed in Table 8.1.

Table 8.1 Alumina suspension composition for multi-channel membranes

Component	Composition (wt.%)
DMSO	31.4
Alumina	62.0
PESf	6.2
Dispersant	0.4

8.2.2 Preparation of alumina hollow fibres, multi-channel tubes and monoliths

The spinning process is described in Section 3.4. Table 8.2 and Figure 8.1 display the spinneret design and spinning parameters for fabricating multi-channel hollow fibres/tubes/monoliths. The smaller annuli are where the bore fluid is extruded, and surrounding them is the ceramic suspension. During spinning, multi-channels of bore fluid is extruded with the ceramic suspension simultaneously, forming multi-channel membrane precursors. The membrane precursors were heat treated and sintered at temperatures 1300 °C, 1350 °C, 1400 °C and 1450 °C.

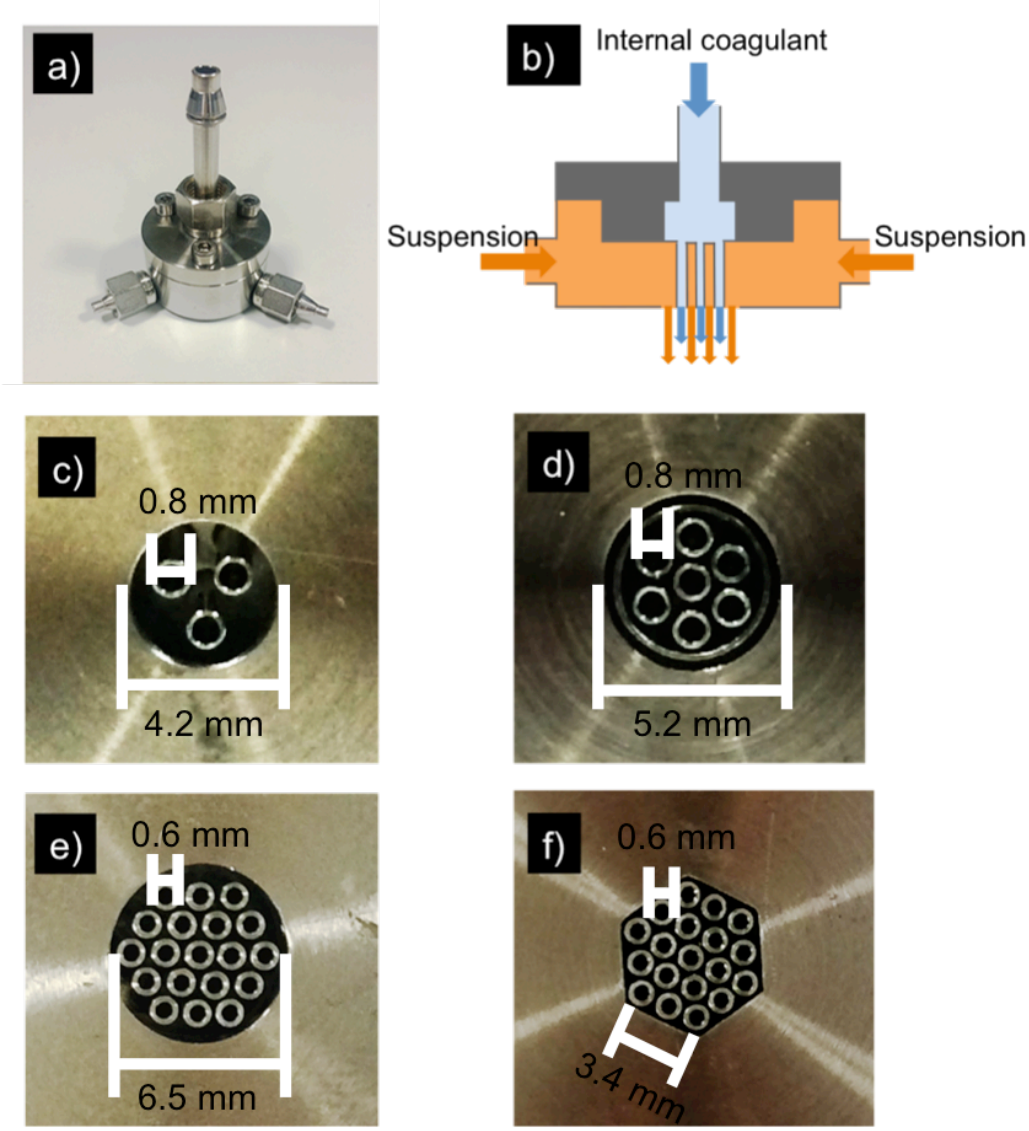


Figure 8.1 Photograph and schematic of the multi-channel spinnerets for extruding multi-channel hollow fibre/tubular/monolithic membranes

Table 8.2 Fabricating parameters of micro-structured multi-channel alumina tubes

Spinning parameter	Single-channel	3-channel	7-channel	19-channel
Extrusion rate (ml/min)	8	10	16	11
Bore liquid rate (ml/min)	10	14	16	18
Air gap (cm)	1	1	1	0

8.2.3 Characterisation

The characterisation methods such as SEM, optical microscopy, mercury intrusion porosimetry, 3-point bending and pure water permeation tests are described in Section 3.6.

8.3 Theoretical analysis of the geometrical influence to the fractural loading

Long, slim shaped materials are most likely to be damaged by a shear force perpendicular to the longitude direction, which is particularly important for brittle materials like ceramics. Hence for the case of ceramic hollow fibres and capillary tubes, the resistance to a bending force is one of the most important mechanical properties. This resistance can be properly evaluated by three-point bending tests, which give the maximum bending force needed to fracture a ceramic sample. In general, a three-point-bending fractural stress of a circular bar with a symmetric cross section is determined by

$$\sigma_{max} = \frac{M \times R}{I} \tag{8.1}$$

Here σ_{max} is the fractural stress which is determined by the material and the microstructure and irrelevant to the geometry of the sample. R is the outer diameter of the sample. M is the bending moment which is determined by the fractural loading force F and the span L used during the test:

$$M = \frac{F \times L}{4} \tag{8.2}$$

And I is the second moment of area defined by

$$I = \int y^2 dA \tag{8.3}$$

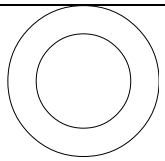
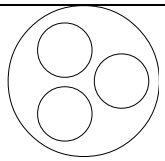
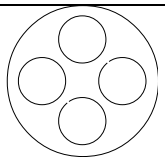
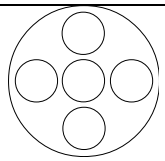
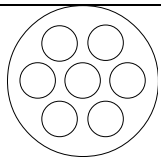
y is the coordinate of the force direction relative to the centre of the cross section, and the integral over the solid area of the cross section. Apparently I is geometry dependent. Hence the fractural loading F is expressed by

$$F = \frac{4I \times \sigma_{max}}{L \times R} \tag{8.4}$$

It would be useful to analyse how the geometry of the cross section affect the fractural loading of the ceramic tubes. For comparison, the multi-channel and single-channel tubes of same material with a fixed outer diameter R were considered, so that the

fractural loading only varies with I. To be fair, the area of the cross section was also fixed so that the fractural loadings obtained were from the same amount of material. A typical dimension of a single-channel ceramic capillary tube was adopted, say, the outer diameter of 4 mm and the inner diameter of 2.5 mm for this case study. Correspondent radius of the channel of a multi-channel tube was set so that the area of the cross section was the same as the single-channel tube. The configuration of each tube and the relative fractural loading compared to the single-channel tube are listed in Table 8.3. It can be seen from the calculation that the fractural loading of multi-channel tubes is actually lower than the single-channel tube with same cross section area. The 19-channel monolith is not included in Table 8.3, because the second moment of area I is difficult to calculate due to the complexity of the cross section geometry. Shi et al. also experimentally studied the mechanical property of 4-channel alumina hollow fibres and claimed that the 4-channel configuration itself may contribute to the improved fractural loading compared with single-channel configuration [2], but the theoretical analysis in this study suggested that this is not the case.

Table 8.3 Relative fractural loading of multi-channel tubes.

Configuration*					
Internal radius (mm)	1.25	0.7217	0.6250	0.5590	0.4725
Distance between the tube and channel centres (mm)	N/A	1.0	1.0	1.3	1.2
Relative fractural loading (%)**	100	88.96	90.46	83.25	86.98

* The outer diameter of the tube is 4 mm;

** The fractural loading is normalized by the value of the single-channel tube.

It is worth mentioning that in the above analysis, the OD and ID of the single-channel tube were set to 4 mm and 2.5 mm, respectively. The wall had to be set to be as thick as 0.75 mm to achieve a fair comparison, otherwise the 5-channel and 7-channel configurations would not be possible to construct whilst the area of the cross section was maintained. However in reality, such dimensions of single-channel tubes are difficult to maintain during the phase-inversion process due to the reduced precipitation rate of the ceramic suspension and the consequent elongation of the nascent tube. The viscosity of the suspension could be increased to a very high value to minimize the elongation and maintain the dimensions, but the radial micro-channel feature in the walls will be lost due to the high viscosity [3]. Thus a typical alumina hollow fibre which has an outer diameter of 2 mm and an inner diameter of 1 mm was considered, and the fractural loading was calculated to be 13.83% of the 4/2.5 mm single-channel tube, and 15.90% of the 7-channel capillary tube in Table 8.3, assuming they have same microstructure at the walls. Based on the above analysis, if the multi-channel configurations can effectively enlarge the cross section area of the phase-inversion monolithic and capillary tubes, which is otherwise unachievable with the single-channel configuration, the resistance of the tubes to the bending force will be effectively enhanced.

The arrangement of the channels also affects the fractural loading as can be shown by calculations. Taking the 7-channel capillary tube in Table 8.3 as an example, if the distance between the channel centre and the tube centre is changed, the effect of the distance on the fractural loading can be evaluated, as shown in Figure 8.2. It is obvious that when the channels move towards the shell, the fractural loading decreases. Whereas it can be expected that the resistance of mass transport will be reduced when the channels are closer to the outer surface. Hence a careful design of the spinneret is required to achieve a balance between the mechanical and the mass transport properties.

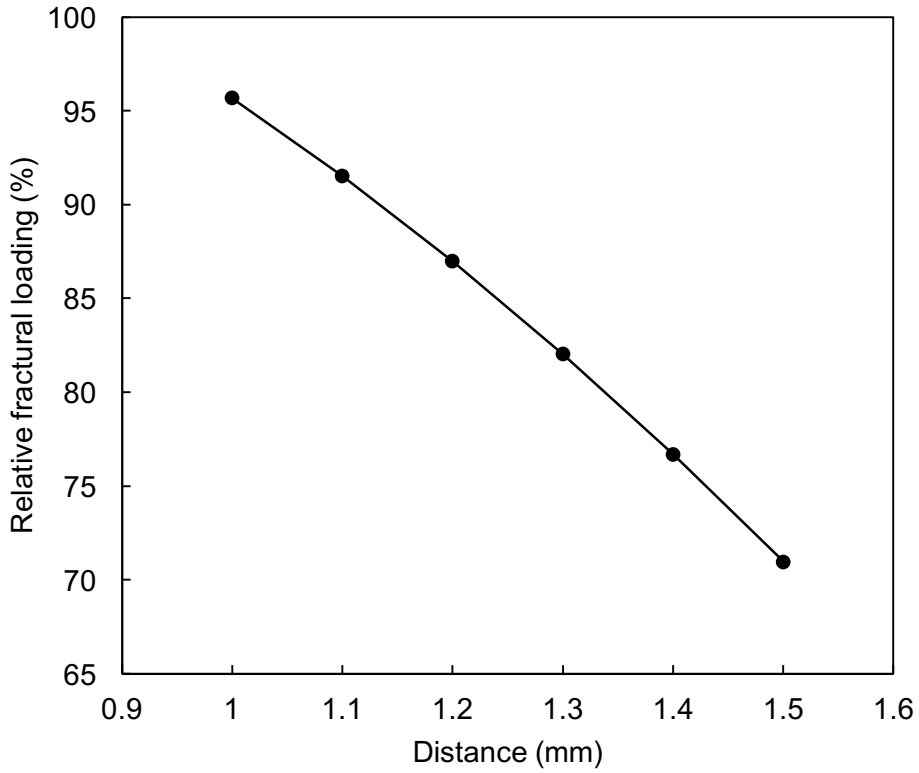


Figure 8.2 The effect of the distance between the channel centre and the tube centre on the relative fractural loading of a 7-channel capillary tube listed in Table 8.3. The outer diameter of the tube is 4 mm and the internal diameter of the channels is 0.945 mm.

8.4 Results and discussions

8.4.1 Structure of the multi-channel alumina tubes

Benefiting from the fingering inducing phase-inversion process, micro-structured alumina monolith tubes consisting of 19 parallel channels obtained after sintering at 1350 °C for 4 h in both cylindrical and hexagonal configurations are shown in Figure 8.3(a-b). The green tube for the cylindrical monolith had an outer diameter of 6.62 mm, and it reduced to 5.68 mm after sintering, which is considerably larger than the single-channel ceramic hollow fibres available in literatures. The 19 uniform channels are organised in the same way as the spinneret design (Figure 8.1), leaving a thin continuous wall around these channels (Figure 8.3c-d). In the wall between the channels (Figure 8.3c), and the regions between the channels and the outer surface of the monolith (Figure 8.3d), a plurality of self-organised micro-channels can be

observed, which is formed due to the growth of interfacial instability at the suspension/non-solvent interface [3, 4]. Similar to the conventional ceramic monoliths [1], the parallel multi-tubular channels would allow ideal flow of fluids. Meanwhile, the radial micro-channels self-organised inside the walls [5, 6] can lead to additional benefits, such as higher geometric surface area and reduced mass transfer resistances, which are beneficial characteristics for catalysis related applications.

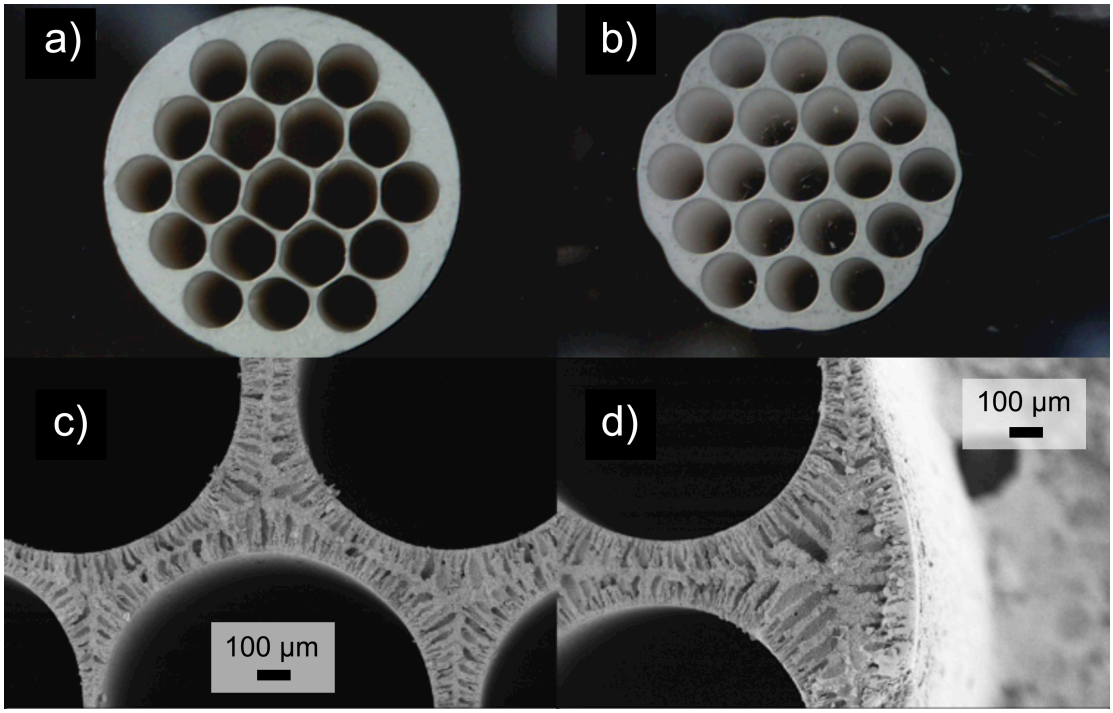


Figure 8.3 Photographic pictures of 19-channel alumina monolith a) with cylindrical geometry, b) with hexagonal geometry, and SEM images of the c) wall structure between channels and d) wall structure between channel and outer surface of the hexagonal alumina monolith

The pore structure of the 19-channel cylindrical monolith sintered at 1350 °C was determined by mercury porosimetry, as depicted in Figure 8.4. There is a minor peak at 0.554 µm, but the majority of the pore volume lies at 0.183 µm. Similar bimodal pore size distributions have also been observed previously in single-channel hollow fibres using NMP as the solvent [5, 6], whereby the hollow fibres had a dominating peak at 7-10 µm and then a minor peak at around 0.16 µm. The smaller pores found at 0.183 µm or at 0.16 µm are believed to represent the inter-granule packing pores between the alumina particles, whereas the bigger pores found at 0.554 µm or at 7-10 µm represent the size of the micro-channel entrances in the membrane wall [5, 6]. It is obvious that in the current study, the entrance size (0.554 µm) is

much smaller than in previous studies (7-10 μm), and the corresponding pore volume is also much lower. The differences can be interpreted from the formation process of the micro-channels and the structure of the tubes. It has been experimentally verified that the micro-channels are the consequence of invading streams of the coagulant and are initiated by interfacial instability [4]. The size of the initial entrance represents the wavelength of the characteristic interfacial disturbance, which is from tens of microns to more than a hundred microns as determined in Chapters 4 and 5. The entrance shrinks during the formation process of the micro-channels due to the surface tension of the suspension, until the suspension surrounding the entrance precipitates due to the solvent/non-solvent exchange. Hence, the final size of the entrance of the micro-channels is largely determined by the precipitation speed of the suspension surrounding the entrance (and the shrinking speed of the entrance, of course, which in turn is affected by the interfacial tension of the suspension). Compared with the suspensions used in previous chapters [5, 6], the suspension used in the current study contains more ceramic powder (62 wt% vs 58-59 wt%), which would have reduced the solvent/non-solvent exchange rate and thus prolonged the duration needed for precipitation to occur, and consequently led to further shrinkage of the micro-channel entrances to a smaller size, or the eventual enclosure of the entrances completely. From Figure 8.4, it can be seen that most pore volume is located at 0.183 μm, which represents the inter-granule packing pores, rather than at 0.554 μm, which is believed to represent the entrance of the micro-channels. However, the SEM images in Figure 8.3 show a large volume fraction of the micro-channels in the tube walls. The simple reason is that most entrances of the micro-channels were completely closed during the formation process, and the volume of these micro-channels is presented as the surrounding inter-granule packing pores instead. There was only a small fraction of micro-channels that were not completely closed, and they left a narrow entrance at 0.554 μm, hence their corresponding pore volume is also small. These narrow openings, in the opinion of the author, lie on the very thin inner walls (thinner than 100 μm at some places) as shown in Figure 8.3, and can be attributed to the faster precipitation rate of these very thin walls when compared with other parts of the monolith tube. This is because for the very thin walls, less solvent in the suspension can be supplied to compensate the loss of solvent at the surface, which leads the micro-channel entrances to precipitate faster than those on thick walls.

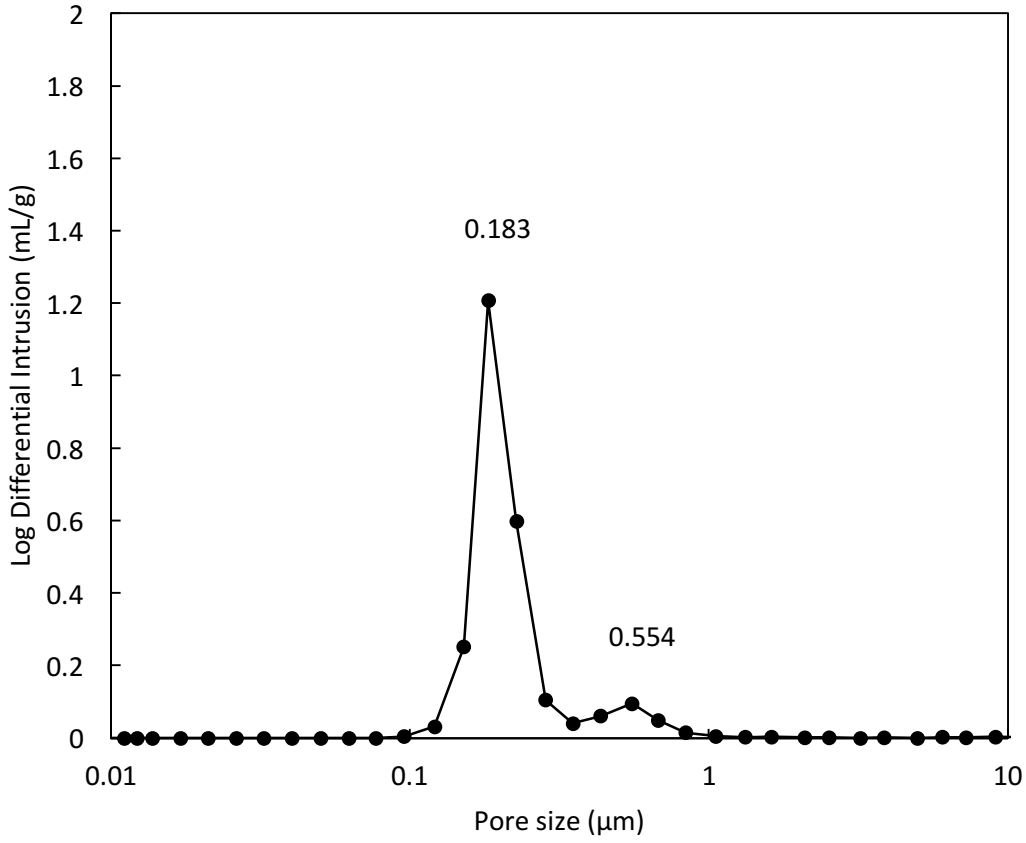


Figure 8.4 Pore size distribution of 19-channel alumina monoliths sintered at 1350 °C for 4 h

Figure 8.5 presents the cross-section structure of the single-channel and 3-channel hollow fibres and 7-channel capillary tube sintered at 1350 °C. The OD of the green single-channel hollow fibre was 2.88 mm and it was reduced to 1.94 mm after sintering at 1350 °C for 4 h. The OD of the green 3-channel hollow fibre was reduced from 2.89 mm to 2.57 mm after sintering under the same conditions and finally, the OD of the green 7-channel was reduced the least proportionally from 3.65 mm to 3.32 mm. It is worthwhile to note that after sintering, the radial shrinkage of the multi-channel tubes is considerably lower than the single-channel hollow fibre, which was 11.1%, 9.0% and 14.2% for the 3-channel, 7-channel and 19-channel tubes, respectively, and 32.6% for the single-channel hollow fibre. The obvious difference seems to be caused by changes in the membrane geometries. However, it is still too early to speculate the reason for this phenomenon.

The single-channel hollow fibre (Figure 8.5a) has a typical structure of a membrane formed via phase-inversion. Due to the presence of a 1 cm air gap, the finger-like micro-channels from the lumen and shell sides have different lengths

(Figure 8.5b), as explained in previous literature [3]. The channels in the 3-channel hollow fibre (Figure 8.5c) are evenly distributed over the cross-section but have an oval shape. The non-circular characteristic of the channels may be attributed to the geometry-related non-uniform resistance to the hydraulic pressure around the channels when the bore liquid applies a pressure onto the nascent fibre. The elongation of the nascent fibre during spinning into the coagulation bath might also contribute to the oval shape. For the 7-channel capillary tube, the central channel appears to be more circular than the other 6 channels (Figure 8.5e), which might be linked to the fact that it had more "symmetric" resistance to the hydraulic pressure around the channel than the other 6 channels surrounding it. On the other hand, the 6 channels at the outer region of the 7-channel tube have an egg-like shape and the thin ends point to the rim, where the resistance to the hydraulic pressure is the least. Similar to the single-channel phase-inversion ceramic hollow fibres, in the 3-channel and 7-channel tubes, self-organised finger-like micro-channels appear in the regions between channels and the outer surface, as well as between the channels themselves (Figure 8.5d and Figure 8.5f), which has also been seen in the 19-channel tubes as revealed above.

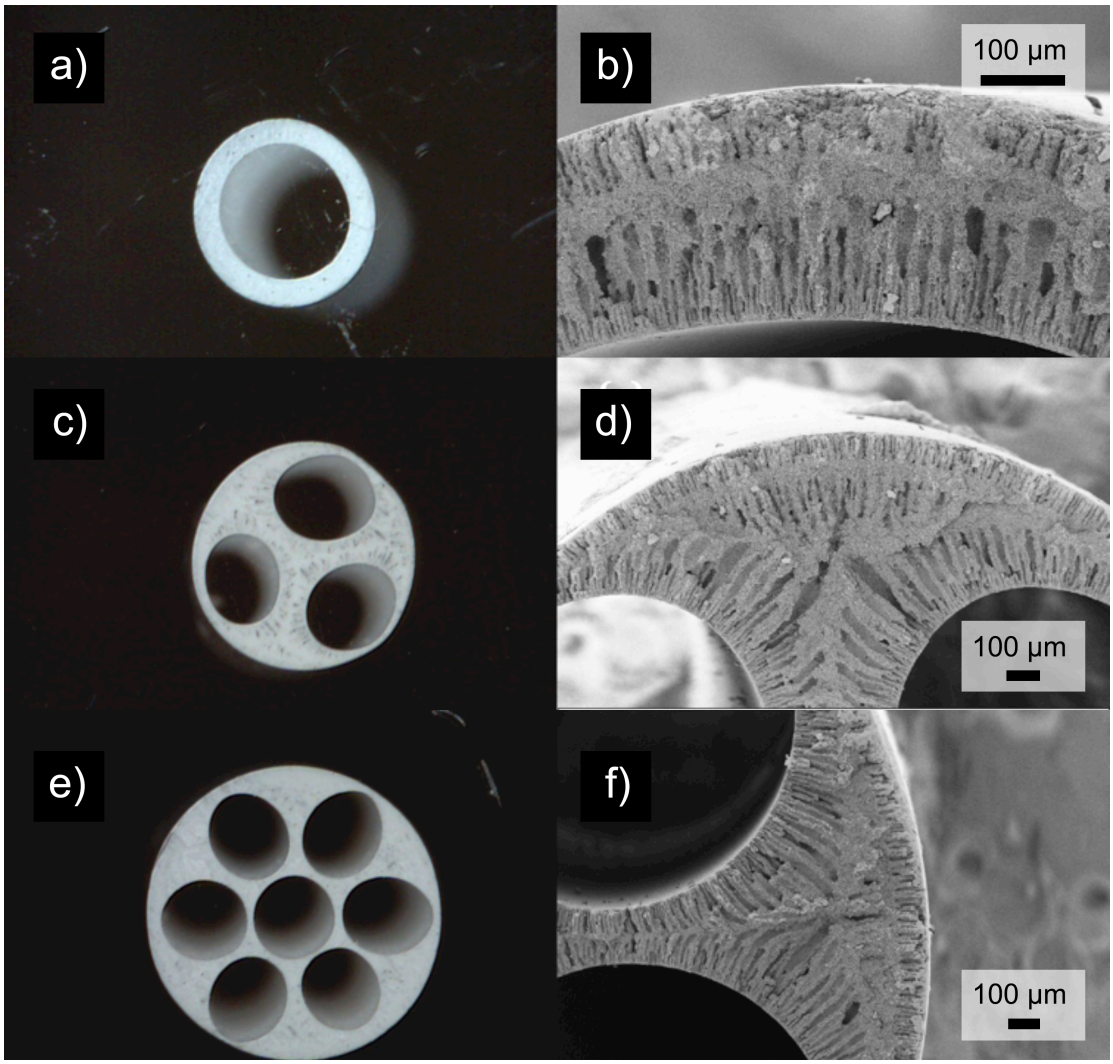


Figure 8.5 Photographic pictures of (a, c, e) the single-channel, 3-channel hollow fibres and 7-channel capillary tube respectively and SEM images of (b, d, f) close-up of the cross section of single-channel, 3-channel hollow fibres and 7-channel capillary tube respectively

From mercury porosimetry results, it was observed that the single-channel hollow fibre and 3- and 7-channel tubes have a single peak and the same pore size at each sintering temperature, as represented by the single-channel hollow fibre whose pore size distribution is depicted in Figure 8.6. The single peak represents the size of the inter-granule packing pores between the alumina particles, and the peak representing the entrances of the micro-channels in the 19-channel tube (as shown in Figure 8.4) is not observable here, which suggests that the micro-channels shown in Figure 8.5 are all enclosed. This is not a surprise, as the walls in the 1, 3, 7-channel tubes are all thicker than the walls in the 19-channel tube, which leads to slower precipitation of the micro-channel's entrances, allowing enough time for all of the

micro-channels to close, as discussed before. As expected, the sintering temperature significantly influences the pore size distribution and porosity of the membrane. From 1300 °C to 1350 °C, the size of the inter-granule packing pores is the same at around 0.183 μm, but with reduced quantity. From 1350 °C to 1450 °C, the pore size begins to change and increases with increasing sintering temperature, but reduces in quantity. Meanwhile the pore size distribution broadens when the sintering temperature is increased. These results have been widely found in ceramics, because both pore densification and pore growth occur during sintering, and generally the pore geometry determines whether it will shrink or grow. Normally when convex sides surround a pore (at higher coordination numbers), the centre of curvature is away from the pore, and the pore grows during sintering. Therefore as the sintering temperature is increased, the rate of pore growth also increases, and led to a pore size of up to 0.284 μm at 1450 °C. At the same time, the smaller packing pores in the green membranes that have concave sides and low coordination numbers have a centre of curvature towards the pore, and so they shrink and densify with increasing sintering temperature, and led to reduction of the final membrane porosity.

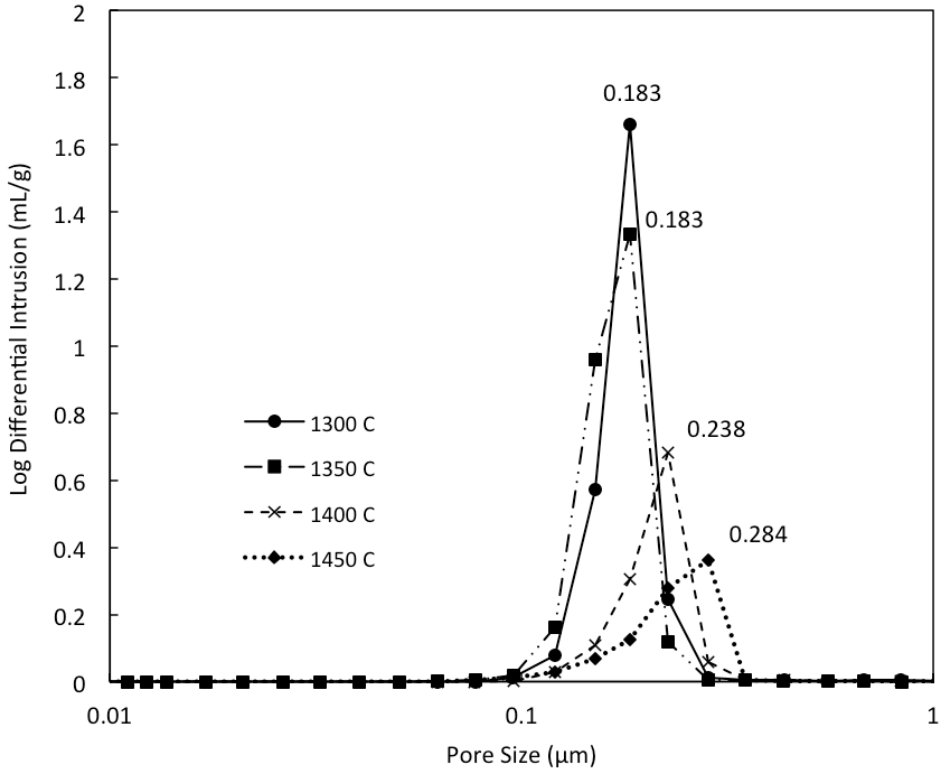


Figure 8.6 Pore size distribution of the single-channel hollow fibre sintered at different temperatures between 1300 – 1450 °C for 4 h

8.4.2 The mechanical property

Three-point bending tests show that, as expected, the fracture loading of the membranes increase with increasing dimensions of the tubes, due to the larger area of the membrane cross section, and all tubes show enhanced fractural loading when the sintering temperature is increased (Figure 8.7). The fracture loadings of the hexagonal 19-channel monolith are almost identical to the cylindrical 19-channel monolith, due to the fact that their cross section areas are very close, thus only the results of the hexagonal monolith is presented in Figure 8.7 for simplicity. The 19-channel monolith has the largest cross section area, and hence the fractural loading is significantly higher than the other types of membranes fabricated in this study. The fractural loading reduces in the order of 7-, 3-, and single-channel membrane. As an example, after sintering at 1450 °C, the fracture loads of the 19-channel monolith and 7-channel capillary tubes reached 42.2 N and 21.7 N, respectively, followed by 9.7 N and 6.8 N of the 3-channel and single-channel alumina hollow fibres, respectively. Based industrial experience, a fractural loading of 21 N (with a 60 mm span) is already comparable to a commercial alumina capillary tube that has been proven to be sustainable under microfiltration/ultrafiltration working conditions. The 7-channel tube sintered at 1450°C, and the 19-channel monolith sintered at a temperature higher than 1350°C, has met the criterion.

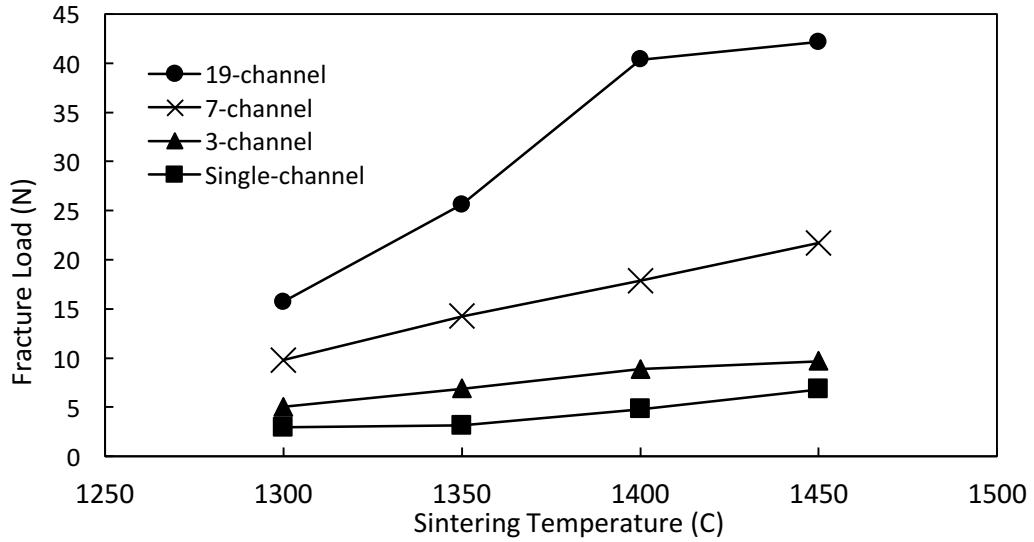


Figure 8.7 Fracture load of the single-channel hollow fibre and multi-channel monoliths sintered at different temperatures between 1300 – 1450 °C with standard deviations of within 35 %

This study shows that an easy way to considerably improve the mechanical property of these monolith membranes is to elevate the sintering temperature, but this may also cause adverse effects on the performance of the membranes due to the reduced porosity as seen in the mercury porosimetry results earlier on Figure 8.6. Besides using larger dimensions or higher sintering temperatures, another approach from the aspect of membrane material can also be considered to improve the fractural loading. It is worthwhile to note that the fractural loading of the 7-channel capillary tube reported in this research is considerably higher than the 4-channel alumina capillary tubes with similar diameters reported elsewhere [2] (the results are compared based on the same testing span), which is likely to be due to the smaller alumina powder used in this research and hence the finer microstructure. Of course, it is also reasonable to expect that, by designing the spinneret, the dimensions of the monoliths can be further enlarged and the quantity of the parallel channels steered towards those of commercial ceramic monoliths, based on the great flexibility and sustainability of the phase-inversion process. Thus better mechanical properties can be foreseen with larger phase-inversion monoliths.

8.4.3 Water permeation

It is well known that multi-channel configurations will potentially compromise the permeation flux in filtration processes because of the longer transport routes of the permeate when compared with single-channel tubes. However, this reduction of the flux can be largely compensated in the phase-inversion multi-channel tubes by the reduced internal resistance due to the radial micro-channels formed during the fabrication process.

Water permeation of 1, 3, 7-channel membranes was evaluated under a dead-end mode as shown in Figure 3.4 and the results are presented in Figure 8.8. The 19-channel monolith was not tested because in the view of the author, due to the lower packing density per unit volume, such a high channel number would be more suitable for other purposes, such as catalytic convertor, rather than for filtration purposes. For the 1, 3, 7-channel membranes, the permeation flux of the membranes increases when the number of channels increases, because the actual permeation area is larger. Furthermore, all of the membranes show a permeation flux linear to pressure up to 4 bar. The 7-channel capillary tube had the highest water permeation flux of up to 1550

$L \cdot m^{-2} \cdot h^{-1} \cdot bar^{-1}$ under a sintering temperature of 1300 °C. This is higher than some commercial monolith microfiltration alumina membranes with a similar pore size [7], but the fractural loading is only 9.8 N, far below the 21 N criterion needed for industrial use.

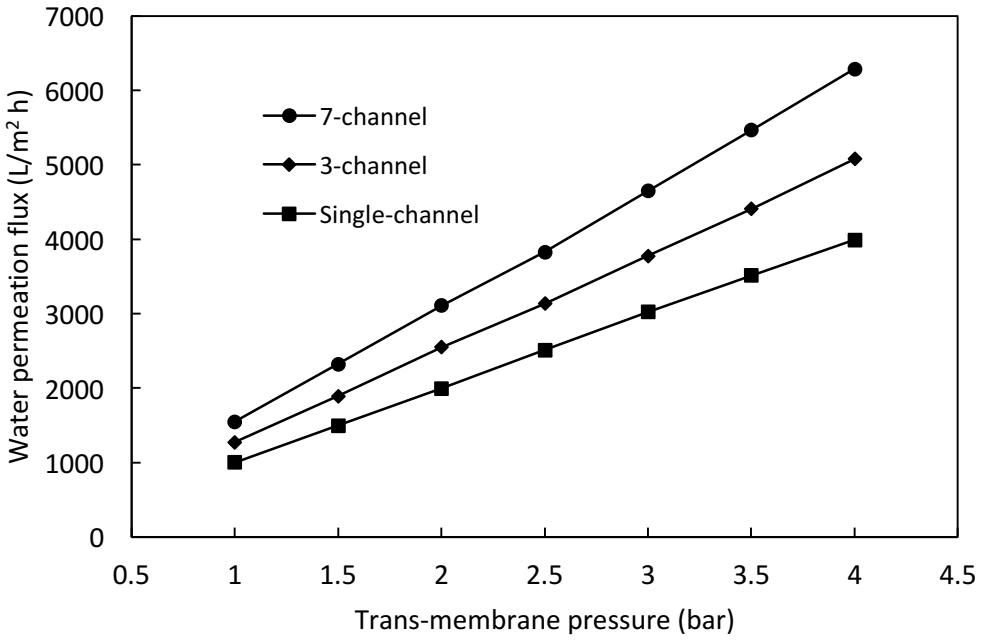


Figure 8.8 Pressure dependent dead-end water permeation of the single-channel hollow fibre and multi-channel monoliths sintered at 1300 °C carried out in the out-in configuration with standard deviations of within 25 %

Improving the sintering temperature leads to higher mechanical property, but changes the membrane porosity and pore size, leading to degradation of the membrane's water permeation properties. Figure 8.9 displays both the fracture load and water permeation flux of the 7-channel capillary tubes sintered at different temperatures. A sintering temperature of around 1350 °C is therefore recommended for the membranes in this research in order to achieve a reasonable balance between the mechanical property and the permeation flux. At this point the permeation flux is around 1070 $L \cdot m^{-2} \cdot h^{-1} \cdot bar^{-1}$, and the fractural loading is 14.3 N, both are at an acceptable level, although the fractural loading is still lower than the stringent industrial requirement. Benefiting from the flexibility of the phase-inversion method, the mechanical property and the permeability of the multi-channel membranes can possibly be tuned by changing the fabrication parameters. For example, Chapter 4 has shown that the permeation property can be enhanced significantly by using other

solvents in the ceramic suspension, such as DMSO and DMAc rather than NMP, and these possibilities will be explored in future works.

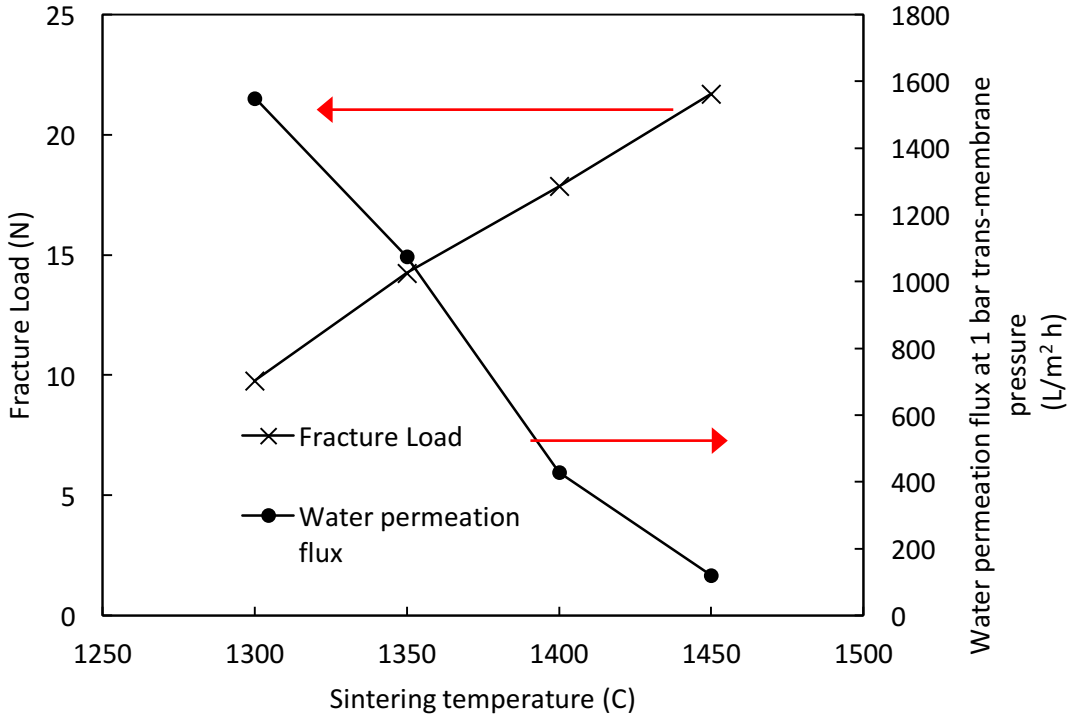


Figure 8.9 Fracture load (standard deviation 35 %) and water permeation flux (standard deviation 25 %) of the 7-channel capillary tube sintered at different temperatures between 1300 – 1450 °C

Furthermore, sealing the 7-channel capillary tube selectively can enhance the water permeation flux, which increases the actual permeation area. Figure 8.10 displays the water permeation flux after the centre channel of a 7-channel capillary tube sintered at 1350 °C was selectively sealed, and the sealing pattern is also shown in the figure. The water permeation flux increased by around 25% after selective sealing and reached up to 1330 $L \cdot m^{-2} \cdot h^{-1} \cdot bar^{-1}$, which is quite meaningful for applications where compact modules are preferred. Under such an operation mode, which applies a considerable pressure difference across the internal walls, the mechanical strength of the walls may be of concern due to their reduced thickness. As can be seen from Figure 8.9, the membranes remained intact under a pressure difference of up to 4 bar, which is high enough for microfiltration processes, and the water permeation is nearly proportional to the pressure difference. Moreover, water permeation flux at the same pressure repeated well during the course of increasing and decreasing the pressure difference between 1 and 4 bar. This indicates that there

is proper mechanical strength of the walls between the channels, which was further consolidated via pressure shock tests. In the pressure shock tests the pressure difference was swung quickly between 0 and 3 bar for 10 cycles, with only small changes in water permeation observed, which can be attributed to mild fouling.

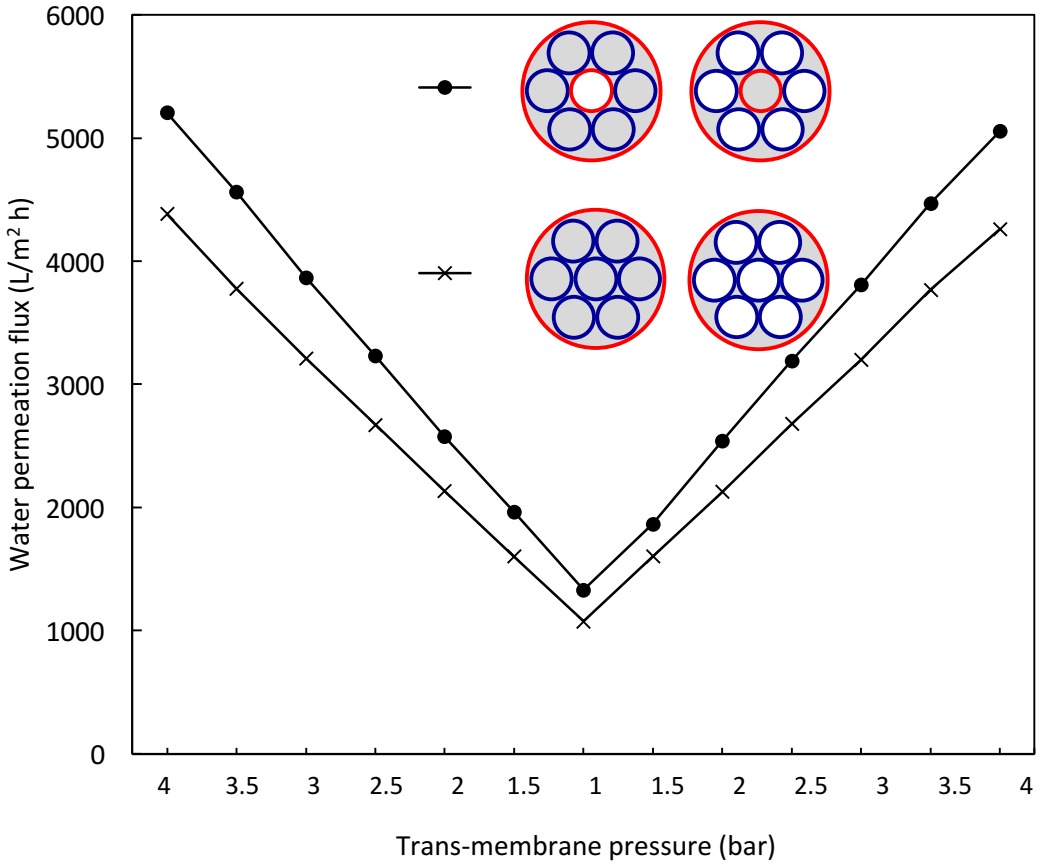


Figure 8.10 Stepwise decrease and subsequent increase in trans-membrane pressure on dead-end water permeation (standard deviation 25 %) of the 7-channel capillary tube with a selectively sealed channel sintered at 1350 °C and carried out in the out-in configuration. Note: For the selected sealing patterns, red lines indicate physical regions of feed side, blue lines indicate physical regions of permeate side, shadows indicate the blockage to the channel ends of feed side

8.5 Conclusions

Apart from a wide range of single-channel ceramic hollow fibres, the continuous fingering inducing phase-inversion process is potentially a productive route for developing micro-structured multi-channel ceramic monolithic and capillary tubular membranes. Besides flexible control over both the microstructure and the

macrostructure via the phase-inversion method, the monolithic structure leads to considerably improved mechanical property, which is currently the most outstanding challenge of single-channel ceramic hollow fibres/capillaries for practical applications. Moreover, the well-reserved radial micro-channels self-organised inside the walls lead to higher surface area and reduced mass transfer resistances, all of which show promising benefits in applications such as water filtration and possibly for catalytic reactions.

References

1. Avila, P., M. Montes, and E.E. Miro, *Monolithic reactors for environmental applications - A review on preparation technologies.* Chemical Engineering Journal, 2005. **109**(1-3): p. 11-36.10.1016/j.cej.2005.02.025
2. Shi, Z., et al., *Preparation and characterization of α-Al2O3 hollow fiber membranes with four-channel configuration.* Ceramics International, 2014.10.1016/j.ceramint.2014.09.065
3. Kingsbury, B.F.K. and K. Li, *A morphological study of ceramic hollow fibre membranes.* Journal of Membrane Science, 2009. **328**(1–2): p. 134-140.http://dx.doi.org/10.1016/j.memsci.2008.11.050
4. Wang, B. and Z. Lai, *Finger-like voids induced by viscous fingering during phase inversion of alumina/PES/NMP suspensions.* Journal of Membrane Science, 2012. **405-406**: p. 275-283.10.1016/j.memsci.2012.03.020
5. Kingsbury, B.F.K. and K. Li, *A morphological study of ceramic hollow fibre membranes.* Journal of Membrane Science, 2009. **328**(1-2): p. 134-140.10.1016/j.memsci.2008.11.050
6. Kingsbury, B.F.K., Z.T. Wu, and K. Li, *A morphological study of ceramic hollow fibre membranes: A perspective on multifunctional catalytic membrane reactors.* Catalysis Today, 2010. **156**(3-4): p. 306-315.10.1016/j.cattod.2010.02.039
7. *CeraMem® Full-size Membrane Modules*. 2013 [cited 2013 21/08]; Available from: http://www.veoliawaterst.com/ceramem/en/fullsizemodulesceramem.htm.

Chapter 9: A high-capacity open bore GC column based on alumina hollow fibres

Chapter 9 *studies into more detail a potential application of the newly designed hollow fibre design with open micro-channels for use as the support for a high-capacity gas chromatography column*

Abstract

A new gas chromatography (GC) column configuration has been designed, fabricated and executed for the separation of gases. The design consists of ceramic hollow fibres with intensively self-arranged open micro-channels in its wall as the carrier, and the stationary phase is packed inside the micro-channels. The hollow lumen leads to negligible pressure drop along the GC column that is similar to the common capillary columns, whilst the intensively distributed micro-channels provide spacious volume for packing the stationary phase to realise much enhanced capacity that is close to common packed columns. Using alumina hollow fibre as an example, this novel design has been demonstrated as GC columns packed with 5Å molecular sieve particles and used to separate nitrogen and oxygen successfully. Such a GC column with a length of 8 m was able to separate O_2 and N_2 completely, with an injection volume of 90 μL, which is 20 -30 times higher than a typical capillary column, and a negligible pressure drop of only 0.01 bar. The theoretical plate number of this column for oxygen is up to almost 20 times higher than a commercial packed column's, and and for nitrogen it is almost 8 times higher.

9.1 Introduction

Packed and open capillary columns currently dominate the gas chromatography (GC) industry, and albeit both have their own advantages, they each have their unique shortcomings as well [1-3]. The traditional packed columns are cheap, easy to set up as well as to operate but are prone to heterogeneities and are often limited in their lengths. The open capillary columns are highly efficient but their sampling capacities are very low, for example, typically 3 - 5 μL injection volume for a 0.32 mm x 30 m column [4] and requires complex GC systems with an extra sample splitting unit.

In attempt to combine the advantages of the existing column designs as well as to negate their disadvantages, asymmetric ceramic hollow fibres are looked at for inspiration. Ceramic hollow fibres offer high chemical, thermal and mechanical stability as well as high packing densities [5-7]. The common asymmetric ceramic hollow fibres possess intensive self-arranged micro-channels, which in filtration applications can reduce the mass transfer resistance, and can potentially be used to contain a wide range of functional materials to form various functional devices [8].

In Chapters 6 and 7, ceramic hollow fibres with open micro-channels at either the inner and/or outer surfaces have been achieved, allowing easy access to these free spaces [9, 10]. In considering the new design of GC columns, these open micro-channels can act as crevices and pockets of space where the stationary phases such as molecular sieves can be stored and packed, increasing the capacity of the column significantly, and will be able to withstand high injection sample capacities, like a packed column. Such columns based on ceramic hollow fibres also have a hollow bore in the centre, which massively reduces pressure drop along the column, like a capillary column. In essence, the design of this column is an upgraded open capillary column, with functional materials packed in the hollow fibre walls, and an open bore in the centre, combining the high capacity of packed columns and low pressure drop of open capillary columns. The configurations of the three mentioned columns are illustrated in Figure 9.1.

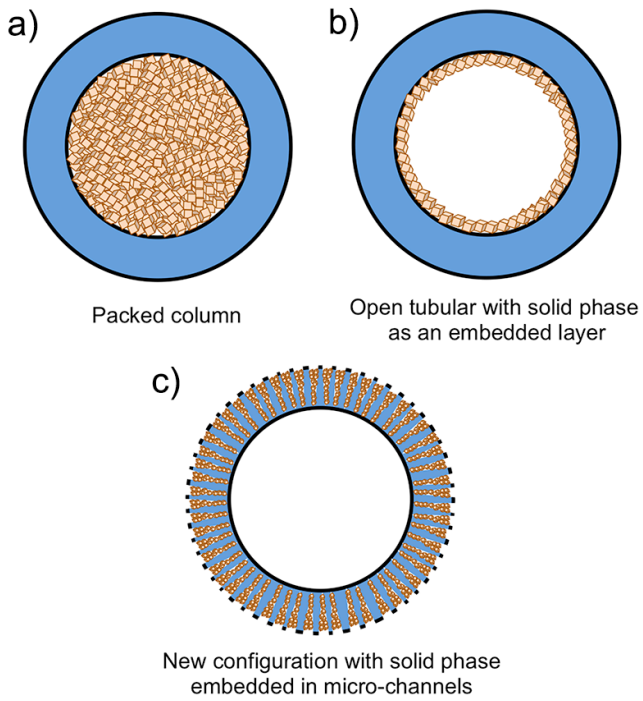


Figure 9.1 Common gas chromatography configurations (a-b), and the proposed new configuration using packed micro-channels in hollow fibres c)

In this study, for the first time, alumina hollow fibres with open micro-channels have been designed and set up as a GC column. The micro-channels in the hollow fibres were packed with 5Å molecular sieve particles and the hollow fibres were assembled in stainless steel tubes, which were connected with a mass spectrometer acting as the detector to demonstrate its capability to separate oxygen and nitrogen in air with minimal pressure drop. The effects of various operating parameters such as column length and sample gas flow rate on separation properties were investigated.

9.2 Experimental

9.2.1 Materials and alumina hollow fibre preparation

The materials used for the alumina hollow fibre membranes in this chapter are listed in Section 3.1. 5Å molecular sieve was purchased form Sigma Aldrich, UK. The Argon carrier gas was purchased from BOC, UK. The preparation of the alumina

suspensions is described in Section 3.2. The alumina hollow fibres with open micro-channels on the shell side were fabricated using the general spinning procedure as described in Section 3.4. The method adopted in this chapter is a slightly altered version of the method used in Chapter 7. The same quadruple-layer spinneret as described in Chapter 7 was used but instead of using a polymer sacrificial layer on the outer annuli, a layer of NMP solvent was used instead. The composition is the same as Design 5's in Chapter 7, and the ceramic extrusion rate, bore fluid, and NMP outer layer flowrates were 10 mL/min, 40 mL/min, and 5 mL/min, respectively. The alumina membranes were heat treated and sintered at 1500 °C, following the treatment programme listed in Section 3.5.

9.2.2 Deposition of 5Å particles into the micro-channels of alumina hollow fibres

The sintered hollow fibres were potted into ¼ inch NPT male connectors and sealed with epoxy resin. On the other hand, 5Å molecular sieve particles were dispersed in water (1.2 g/L) under mechanical stirring. The fibre was then connected to a vacuum filtering flask connected to a vacuum pump, as shown in Figure 9.2. A vacuum is applied from the lumen of the hollow fibre, suctioning the molecular sieve particles into the micro-channels and clear water through the membrane and into the flask. The hollow fibres were then dried in ambient conditions. The hollow fibres were broken from the NPT male connectors and packed into 20 cm long stainless steel tubes with 1/8 inch outer diameter and 1.75 mm inner diameter, which were connected by 1/16 inch tubes to form the gas chromatography column, as displayed in Figure 9.3. Prior to using the columns for gas separation, the entire column was placed in an oven overnight at 200 °C with argon gas purging through at 30 mL/min to activate the zeolite as well as to remove the water and air entrapped in the fibres and the molecular sieve.

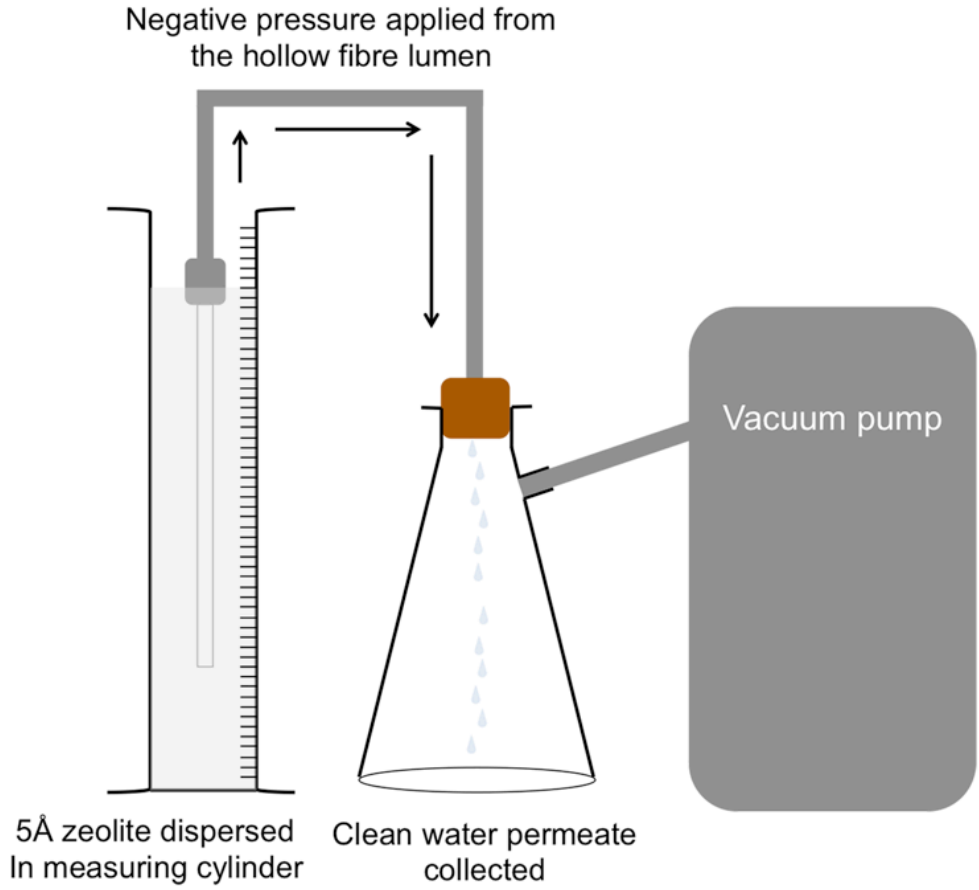


Figure 9.2 Schematic of the deposition process for loading zeolite particles into the hollow fibres' micro-channels



Figure 9.3 Photograph of the gas chromatography column

9.2.3 Gas chromatograph experiment

The separation of nitrogen and oxygen in air was carried out using the set up in Figure 9.4 at room temperature (22 ± 1 °C), whereby argon was used as the carrier gas, air was used as the sample gas, and a mass spectrometer was used to detect the gases. The GC column inlet was connected to a 6-way valve whereby the sample gas was injected and mass flow controllers (Omega FMA-2600A) were used to control its composition. The outlet of the GC column was then connected to the mass spectrometer (FLIR Griffin 400) to analyse the flue gas. The column efficiency (theoretical plate number) was calculated from the chromatograph results using the following equation:

$$N_A = 5.545 \left(\frac{t_R(A)}{w_h(A)}\right)^2 \quad (9.1)$$

where N_A is the number of theoretical plates for analyte A, t_R is the retention time for analyte A and w_h is the peak width at half-height of analyte A.

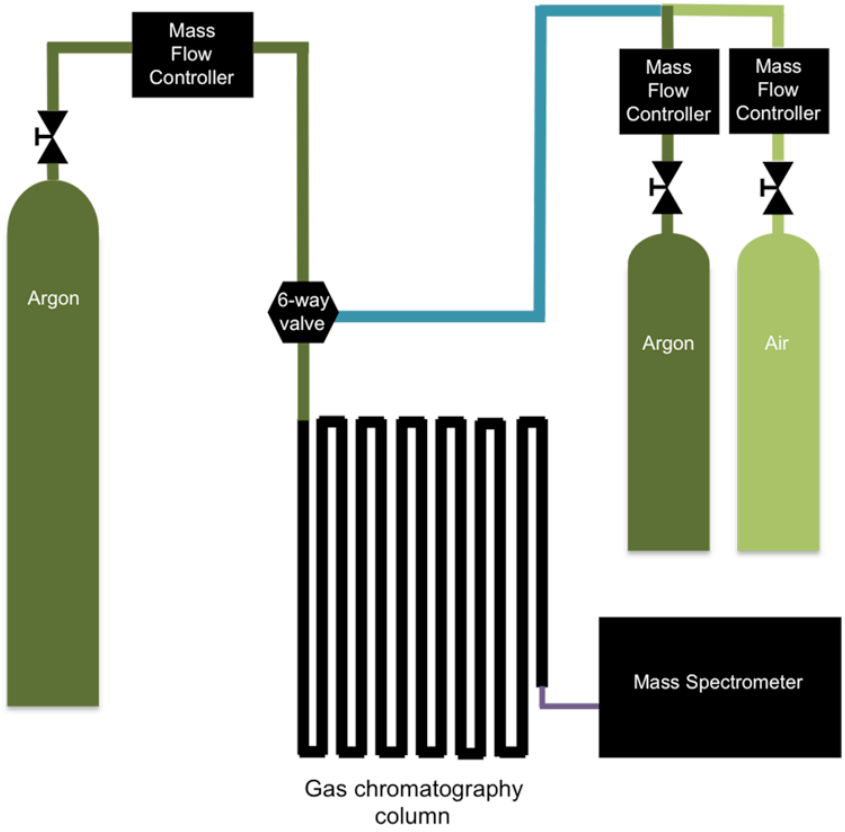


Figure 9.4 Gas chromatography column paired with a mass spectrometer using argon as the carrier gas and air as the sample gas

9.2.4 Characterisation

All membrane characterisation methods such as SEM and gas-liquid displacement are described in Section 3.6

9.3 Results

9.3.1 GC column morphology

The alumina hollow fibre used in the GC column is unique in that it is asymmetric in structure with densely self-arranged, 300 μm long and cylindrical micro-channels; with micro-channel openings of between 20 – 35 μm, and micro-channel densities of around 560 openings per mm^2 as displayed in Figure 9.5. Furthermore, the micro-channels are open on the outer surface (Figure 9.5b), which allows easy access to the extensive free volume offered by the micro-channels. At the lumen side there is a thin layer of continuously packed alumina particles that form a skin layer which prevents anything larger than the layer's pore size to pass through. This design was achieved by the interfacial instability-induced micro-channelling method, whereby micro-channels can be formed in a wide range of materials during a phase inversion process. In this experiment, a concentric triple-layered spinneret was used to deliver three components: a water coagulant in the centre, then a ceramic suspension, followed by a solvent outer layer into a non-solvent water bath. During spinning, the micro-channels were initiated from the lumen side, and propagated through to the shell side. At the same time, the polymer additive also began to precipitate, in the direction from the lumen to the shell side. Due to the presence of a solvent layer surrounding the shell side of the nascent ceramic fibre, phase inversion is delayed at the ceramic suspension and solvent interface and the micro-channels had time to reach the shell side before immersion into the water bath. With sufficient momentum, the micro-channels crossed the ceramic suspension and solvent interface, and left large openings on the outer surface.

The openings of the micro-channels are in the range between 20 to 35 μm in diameter, which is big enough for the molecular sieve particles of approximately 3 to

5 µm in size to enter. The molecular sieve particles were carried by water and entered the micro-channels by the means of vacuum-facilitated filtration, and were retained inside the micro-channels by the inner surface, which has an average pore size of around 1 µm (Figures 9.5c-d and Figure 9.6). Figure 9.5e and 9.5f show an even distribution of the molecular sieve particles in the micro-channels.

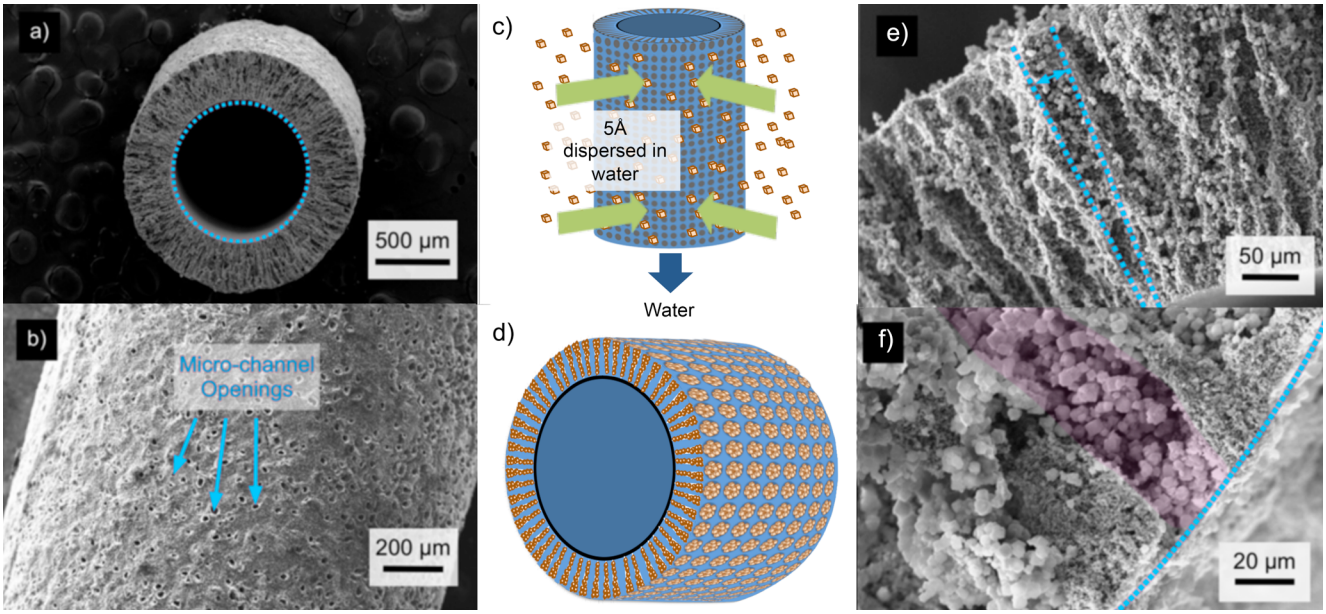


Figure 9.5 SEM of the hollow fibres a) the hollow fibre cross-sectional overview, the dashed line highlights the inner skin layer; b) the outer surface of the hollow fibre with micro-channel openings, the arrows indicates open micro-channels; c) a schematic of the deposition process to pack the 5Å molecular sieve particles into the micro-channels; d) an illustration of the hollow fibre with packed molecular sieve particles; e) the cross-sectional view in which the dashed line highlights a micro-channel capsuling molecular sieve; and f) a close-up cross-sectional view, the dashed line highlights the open shell side of the hollow fibre, and the pink shading highlights the example of an area where molecular sieve particles were deposited

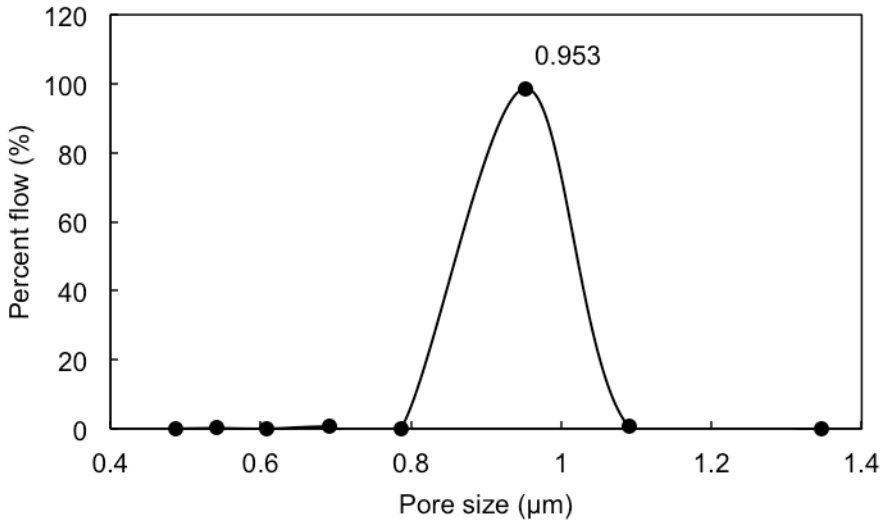


Figure 9.6 Pore size distribution of the hollow fibre membrane obtained by the gas-liquid displacement method

9.3.2 Separation performance of nitrogen and oxygen

Figure 9.7 displays the air separation characteristics of the GC column at different column lengths. A sample size of 90 μL was injected with an argon carrier gas flow rate of 10 mL min^{-1}. It can be seen that separation of oxygen and nitrogen could be effectively improved with longer columns. The degree of the separation can be evaluated by the resolution of two peaks, The chromatograph resolution can be calculated using the following equation [1]:

$$R_{AB} = 2\frac{t_R(B)-t_R(A)}{w_h(B)+w_h(A)} \qquad (9.2)$$

where R_{AB} is the resolution, $t_R(A)$ and $t_R(B)$ are the retention times of analytes A and B, and $w_h(A)$ and $w_h(B)$ are the peak width at half-height of the analytes. The separation results shown in Figure 9.4 give resolutions of 0.40, 0.50, 0.69 and 0.82 for the oxygen and nitrogen peaks when the column lengths were 2, 4, 6 and 8 m, respectively.

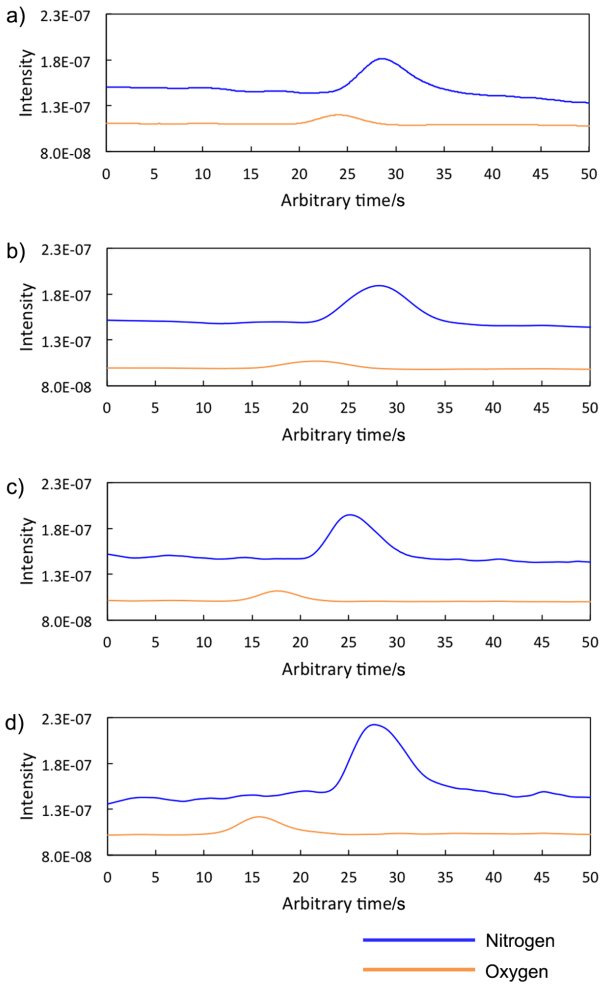


Figure 9.7 Mass spectrographs of nitrogen and oxygen through a a) 2 m, b) 4 m, c) 6 m and d) 8 m long GC columns with 10 mL min^{-1} argon carrier gas and 90 µL air injection volume

When the injection volume is reduced to 45 µL, a resolution of 1.03 for the oxygen and nitrogen peaks was obtained. It is suggested that a resolution of 1 represents 94% separation of two symmetric peaks of same height, and such degree of separation will be adequate for most GC analysis [1]. Therefore, an 8 m column is almost good enough for usual purposes, and the resolution can be easily improved by using longer columns if stringent separation is needed. Besides, the entire prototype column at 8 m long has an extra-column dead volume of around 1.2 mL generated by the connections (Figure 9.3), which can cause broadening of the peaks but can be negated by reducing or eliminating the connection lengths by better industrial designs in the future to get better resolutions.

As expected, the flow rate of the argon carrier gas also makes significant changes to the column's separation capabilities. It can be seen in Figure 9.8 that with an 8 m

long column and an injection volume of 45 µL, the separation property of the column increased with decreasing flow rate, and the resolution decreased from 1.03 to 0.57, 0.47 and 0.23 when the carrier gas flow rate increased from 10 to 20, 30 and 40 mL min^{-1}, respectively. However, the slower the carrier gas flow rate, the analytes are more likely to experience back diffusion and thus cause wider peaks. In order to achieve sharper peaks with even better resolution, the dead volume within the column need to be reduced, as mentioned above, and longer columns at higher carrier gas flow rates could be required. It should also be noted that the pressure drop across the columns were very small. At 8 m and a flow rate of 10 mL min^{-1}, a pressure drop of only 0.01 bar was experienced, whereas in literature, micropacked and packed capillary columns can experience pressure drops per meter of between 0.51 – 203 bar [2].

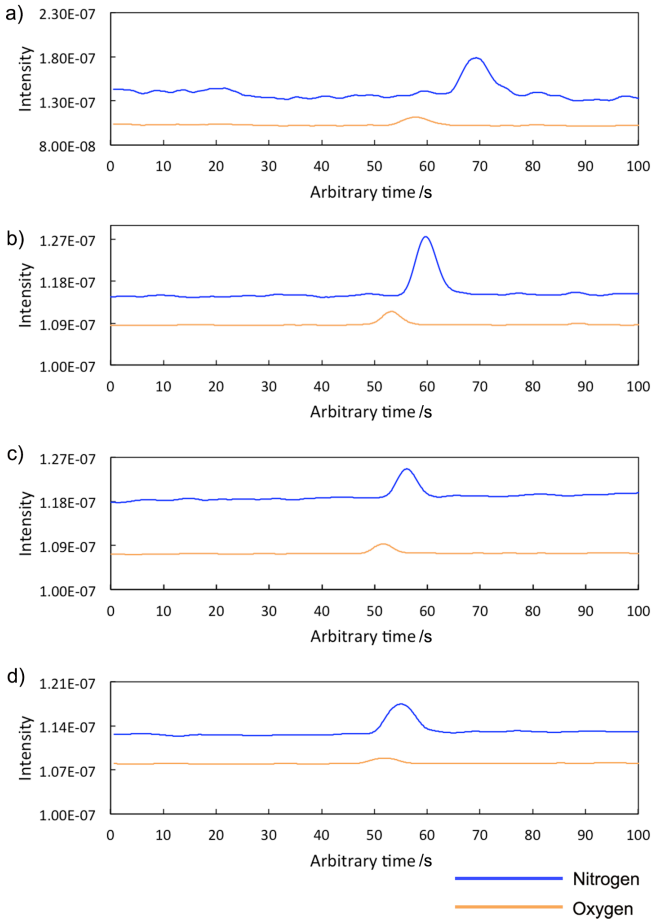


Figure 9.8 Mass spectrographs of nitrogen and oxygen through an 8 m column with 45 µL air injection volume and argon carrier flow rates of a) 10 mL min^{-1}, b) 20 mL min^{-1}, c) 30 mL min^{-1} and d) 40 mL min^{-1}.

9.4 Discussion

This chromatography column configuration is essentially an upgraded open-tubular column with much higher loading rates of stationary phase, which is due to the unique structure of the ceramic hollow fibre that provide larger accessible free volume. During the deposition process, approximately 46 mg is loaded into every metre of fibre and a total loading of around 370 mg of molecular sieve in an 8 m long column. On the contrary, the porous layer of the stationary phase in commercial porous-layer open tubular (PLOT) columns is often only less than 15 μm thick. Taking a commercial PLOT column with 5Å molecular sieve as the stationary phase that is 30 m long with an inner diameter of 0.32 mm and 12 μm thick stationary layer as an example [4], it has a total 5Å molecular sieve loading of around 2.8 mg per metre of column, and 84 mg for the entire column, which is significantly smaller than the column presented here.

The length of the micro-channels is about 300 μm, and it would be of interest how this length may affect the separation performance. It can be estimated from the diffusion coefficients that the oxygen and nitrogen molecules can diffuse through a distance of around 4 mm in every second, which is significantly higher than the outer radius of the hollow fibres (around 0.80 mm). The big pore size, which is around 1 μm, and the highly porous structure of the hollow fibre would not slow down the diffusion significantly, as studied previously [11]. This means that the mass transfer resistance for the analytes to reach the stationary phase should not affect the separation performance, too much. Such an assumption is supported by the theoretical plate numbers and plate heights calculated from the experimental results, as displayed in Table 9.1. A comparison with commercial packed column and PLOT column is also made in Table 9.1. The hollow fibre configuration achieved efficiencies (plate height) that are comparable with a packed and a capillary column. Although the packed column can have much higher plate numbers if the length is increased, limitations such as high pressure drops place a practical threshold on their lengths at a few metres. On the other hand, capillary columns can be assembled to up to 100 m long, due to their hollow bores, although in practice they are most commonly found at 30 m or 60 m length. Capillary columns can have high plate numbers due to their long lengths but can only take on very small sample loads due to the very low amount of

stationary phase layered on the capillary walls. The hollow fibre configuration with the solid phase packed into the micro-channels has an empty bore with minimal pressure drop, and hence can withstand high carrier flow rates like the capillary columns. On the other hand, large-volume stationary phase is offered by the micro-channels that are exposed for adsorption, and hence the hollow fibre columns can handle large sample sizes, like the packed columns.

In this prototype column, some technical limitations were imposed due to the brittleness of the alumina material, such as the interruption of the column's continuity due to the number of connections, which not only reduce the separation efficiency of the column, but also increase the difficulty of preparing longer columns. However, the beauty of this column fabrication method is its flexibility, and can be applied easily to other materials, such as metals like nickel and stainless steel, or polymer materials that can withstand high temperatures, for example, polybenzimidazole (PBI), which can be easily coiled and form very long columns. With these alternative materials, continuous columns with unlimited lengths can be easily obtained, and the column diameter can also be easily reduced during the spinning fabrication process, therefore the separation resolution can be significantly improved.

Table 9.1 Comparing the properties and performance of the packed micro-channel hollow fibres and commercial GC columns using 5Å molecular sieve as the stationary phase

	Packed column [12]	Open capillary column [4]	Packed hollow fibre column
Column length (m)	1	30	8
Carrier gas	H_2	He	Ar
Carrier gas flow rate (mL min^{-1})	30	2	10
O^2 retention time (min)	0.43	1.88	2.08
N_2 retention time (min)	0.82	2.55	2.28
Column inner diameter (mm)	2	0.32	1.6
Theoretical plate number for O_2	121	14600	2368
Theoretical plate number for N_2	248	11900	1931
Theoretical plate height for O_2 (mm)	8.28	2.05	3.38
Theoretical plate height for N_2 (mm)	4.03	2.52	4.14

9.5 Conclusions

In conclusion, this study provided promising results for a proof-of-concept for a new gas chromatography column design. This design consists of alumina hollow fibres with intensively arranged micro-channels as the carrier whereby the stationary phase is packed into the micro-channels. This design has an open-tubular structure, and compared with normal capillary columns, the loaded stationary phase is substantially increased due to the large free volume provided by the micro-channels. This design combines the advantages of both traditional packed columns for allowing large

sample injection volumes with the open tubular columns with low pressure drop and high effectiveness. Through additional tweaking and optimisation, the performance of this new column configuration is expected to improve further. The results of this study can potentially make a significant step for gas chromatography configurations, and also could be potentially advantageous when used alongside other important gas chromatography developments, such as multidimensional gas chromatography [13] and chromatography with supercritical fluids [14, 15]. It is also worthwhile to emphasise that this column design is a generic template, and can be applied to liquid chromatography applications as well when the effect of mass transfer is minimized by using smaller column diameters and optimised operation conditions.

References

1. Poole, C.F., *The essence of chromatography*. 2003: Elsevier
2. Poole, C.F. and S.K. Poole, *Chromatography today*. 2012: Elsevier
3. Bruno, T.J., *A review of capillary and packed column gas chromatographs.* Separation & Purification Reviews, 2000. **29**(1): p. 27-61
4. Vickers, A. *PLOT Column Selection*. 2000 [cited 2016 05/01]; Available from: https://http://www.agilent.com/cs/library/eseminars/Public/PLOT Column Selection.pdf.
5. Li, K., *Ceramic Membranes for Separation and Reaction*. 2007, Chichester: John Wiley & Sons Ltd
6. Leo, A., et al., *High performance perovskite hollow fibres for oxygen separation.* Journal of Membrane Science, 2011. **368**(1–2): p. 64-68.http://dx.doi.org/10.1016/j.memsci.2010.11.002
7. Li, W., et al., *Ce0.8Sm0.2O2−δ−La0.8Sr0.2MnO3−δ Dual-Phase Composite Hollow Fiber Membrane for Oxygen Separation.* Industrial & Engineering Chemistry Research, 2009. **48**(12): p. 5789-5793.10.1021/ie9002624
8. Kingsbury, B.F.K. and K. Li, *A morphological study of ceramic hollow fibre membranes.* Journal of Membrane Science, 2009. **328**(1–2): p. 134-140.http://dx.doi.org/10.1016/j.memsci.2008.11.050
9. Zydorczak, B., Z. Wu, and K. Li, *Fabrication of ultrathin La0.6Sr0.4Co0.2Fe0.8O3–δ hollow fibre membranes for oxygen permeation.*

Chemical Engineering Science, 2009. **64**(21): p. 4383-4388.http://dx.doi.org/10.1016/j.ces.2009.07.007

10. Yin, W., et al., *Highly asymmetric yttria stabilized zirconia hollow fibre membranes.* Journal of Alloys and Compounds, 2009. **476**(1–2): p. 566-570.http://dx.doi.org/10.1016/j.jallcom.2008.09.079
11. Li, K., J. Kong, and X. Tan, *Design of hollow fibre membrane modules for soluble gas removal.* Chemical engineering science, 2000. **55**(23): p. 5579-5588
12. RESTEK. *Permanent Gases on Molecular Sieve 5A and Molecular Sieve 13X.* [cited 2015 17/11]; Available from: http://www.restek.com/chromatogram/view/GC_PC00166/5a%7C7782-44-7.
13. Meinert, C. and U.J. Meierhenrich, *A New Dimension in Separation Science: Comprehensive Two-Dimensional Gas Chromatography.* Angewandte Chemie International Edition, 2012. **51**(42): p. 10460-10470.10.1002/anie.201200842
14. Gere, D.R., R. Board, and D. McManigill, *Supercritical fluid chromatography with small particle diameter packed columns.* Analytical Chemistry, 1982. **54**(4): p. 736-740
15. Klesper, E., *Chromatography with Supercritical Fluids.* Angewandte Chemie International Edition in English, 1978. **17**(10): p. 738-746.10.1002/anie.197807381

Chapter 10: Conclusions and future works

Chapter 10 *concludes the achievements made in this thesis compared with the initial aims and provides suggestions for improvements and future work*

10.1 Introduction

This thesis focused on designing and tailoring micro-channel enhanced alumina membranes for more tailored as well as widened applications. To achieve this, the thesis was assembled to gain a fundamental understanding of the formation of micro-channels in ceramic membranes systems, to design and predict different micro-channel structures, to realise the different structures in hollow fibre membranes, to explore the novel and new designs in new applications, and to control membrane geometry to improve their mechanical stability. Ceramic membranes have been viewed as robust, reliable and great performing options for membrane processes that can potentially alleviate the problems encountered by organic membranes, as well as taking membrane technologies to new frontiers by expanding their applications. Therefore, the studies in this thesis sought to negate current bottlenecks with ceramic membranes, such as their low mechanical stability and packing densities, as well as to introduce novel and new membrane morphologies to extend their potentials. This chapter presents the achievements made throughout the thesis, which includes the research objectives that have been addressed in each chapter, the implications and impacts of the results, the limitations and difficulties of the research, and finally ideas and suggestions for future work. The conclusions are first presented in a general format, and then in more detail for each chapter.

10.2 General conclusions

Micro-channel enhanced alumina membranes have been successfully designed and fabricated throughout this thesis. The micro-channel inducing phase inversion and sintering method was used to form asymmetric ceramic membranes with intensively arranged micro-channels. Firstly, an improved fundamental understanding of the formation of micro-channels in disc membranes was achieved. Various factors such as ceramic suspension composition, membrane thickness, and coagulation temperature were tested and a fundamental understanding of the range of dimensions and densities of micro-channels that can be produced was achieved. For the first time, the micro-channel densities were exposed, quantified and compared with simulation results based on the proposed Rayleigh-Taylor instability theory with fairly good agreements. The micro-channel enhanced disc membranes were also found to dramatically improve pure water permeation fluxes and were suggested for potential use in water treatments. A new application of micro-channel enhanced disc membranes was suggested for spinning polymeric or inorganic fibres that can be down to micrometre-sized. Next, the knowledge gained from the fundamental study was transferred to hollow fibre membranes, whereby 6 unique membrane structures were designed and realised. An important development included the formation of open micro-channels at the desired surface(s) by the use of different bore fluids and sacrificial polymer layers. With open micro-channels and only one very thin separation layer, water permeation flux was massively increased. Furthermore, these designs added a completely new function to ceramic hollow fibres. The vast amount of accessible free volume allowed easy deposition and storage of functional materials to potentially form highly compact and efficient hybrid systems, such as chromatography and adsorption columns, and micro-reactors for consecutive reactions. The design with no separation layer but completely open micro-channel was discussed for use in membrane emulsification. Using one of the hollow fibre designs with one separation layer and open micro-channels on the outer surface, a gas chromatography prototype column was developed and investigated for the separation of nitrogen and oxygen in air, by depositing 5Å molecular sieve particles into the intensively arranged micro-channels. The two gases were successfully separated and the column efficiencies exceed those of a commercial packed column, and similar to

those of capillary columns, with a much-lowered adsorbent loading required. Finally, due to the compromise of mechanical strength with the presence of micro-channels, a method to improve mechanical stability whilst keeping the benefits of the micro-channels was proposed and executed in the form of multi-channel hollow fibres/tubes/monoliths, which expanded the cross-sectional area of the membranes, with significant improvements.

10.3 Chapter by chapter conclusions

10.3.1 Chapter 4

An improved fundamental understanding of the micro-channel formation mechanisms in ceramic membranes was achieved. Flat disc membranes were fabricated from different alumina suspensions with 5 different solvents, and a range of different micro-channels and different selective layer pore sizes were achieved. Micro-channel shapes ranged from intensively packed, straight, long, and cylindrical, to sparsely distributed tear-shaped structures. The membranes with long and cylindrical micro-channels have the best performance in terms of water permeation flux for microfiltration, and after removal of the bottom sponge-like layer to reveal open micro-channels, the permeation flux increased significantly. A major development achieved in this study is the stratified quantification of the micro-channels, and the mimicking of their wavelengths using a simulation based on the Rayleigh-Taylor Instability theory achieved fairly good agreements.

10.3.2 Chapter 5

In this chapter, a larger range of fabrication parameters and their effects on micro-channel properties of disc-shaped alumina membranes were studied. Factors such as alumina loading, membrane thickness, and coagulation temperature were varied. It was discovered that lowering the alumina loading led to the formation of extremely thin and intensively packed, long, and straight micro-channels, which had excellent water permeation properties. It was also discovered that a threshold membrane

thickness exists before micro-channel development commenced and increasing coagulation temperature increases the micro-channel lengths and density. The stratified micro-channel densities for membranes of different alumina loadings were also quantified and explained using the simulation based on the Rayleigh-Taylor instability theory. Although there are some agreements with the simulations, both technical and practical limitations prevented accurate and intricate prediction of micro-channel properties. In addition, a potential new application of the micro-channel enhanced flat disc membranes was proposed: to spin polymeric or ceramic microfibres. Preliminary results provided the fabrication of 100 μm thick YSZ fibres made by extruding through the micro-channels of the disc membranes and phase inversion in a coagulation bath.

10.3.3 Chapter 6

The knowledge gained from the previous chapters regarding the factors that can produce the most desired micro-channels was taken and applied to hollow fibres in this chapter. Single-layered asymmetric hollow fibres of 3 distinctly different cross-section structures were fabricated by using different bore fluids and air gap. The design with one separation layer and open micro-channels on the inner surface had superior water permeation flux due to the elimination of a redundant sponge-like layer and is the most promising choice for use in aqueous microfiltration. A series of different sintering temperatures were tested for this design and finally, a sintering temperature between 1300 °C and 1350 °C was recommended for the optimum condition without sacrificing too much of the water permeation flux for increased mechanical stability.

10.3.4 Chapter 7

In this chapter, a polymer sacrificial layer was incorporated into the spinning process to form 3 types of hollow fibre membranes with different open micro-channel arrangements. Micro-channels could be formed open at the inner, outer, or both surfaces of a hollow fibre. The structure with an open outer surface had dramatically improved water permeation flux due to the very thin effective separation layer. As the

micro-channel bodies are now easy to access, they can be used to store functional materials such as adsorbents or catalysts. 3 potential types of applications also stemmed from the 3 designs and were discussed: membrane emulsification, chromatography/adsorption column, and membrane micro-reactor for consecutive reactions. However, potential larger-scale use of these membranes was limited by their weak mechanical stability, due to their very thin densely packed layer.

10.3.5 Chapter 8

This chapter targeted at improving the mechanical stability of micro-channel enhanced hollow fibres by increasing the cross-section area of the membranes. 3-channel, 7-channel, and 19-channel multi-channel hollow fibres, tubes, and monoliths with micro-channels were fabricated with a significant increase in mechanical stability. This configuration allows simultaneous existence of both micro-channels and high mechanical stability. It was also found that by selectively sealing some of the channels, water permeation flux was increased.

10.3.6 Chapter 9

In this chapter, one of the potential applications of the hollow fibre structure with open micro-channels on the outer surface was studied. A prototype for a new configuration of gas chromatography column was constructed from this type of membrane and tested for separating nitrogen and oxygen in air as an example. 5Å molecular sieve particles were deposited into the micro-channels and the hollow fibres were arranged in stainless steel tubes to form columns ranging from 2 m to 8 m long. An 8 m long column was able to completely separate nitrogen and oxygen at an argon carrier gas flow rate of 10 mL/min. This column configuration had a column efficiency superior to that of a traditional packed column, and an adsorbent loading capacity much lower than that of a capillary column. The resolution, however, could be improved by extending the column length.

10.4 Future work

10.4.1 Morphology design

10.4.1.1 Highly smooth ceramic membrane surfaces

This thesis focused on designing and fabricating different cross-section morphologies within the alumina disc and hollow fibre membranes. The new designs offered an alternative way to combine functional materials into the ceramic membranes: deposition into the micro-channel cavities. However, the surface morphology has been neglected in this thesis. Ceramic membranes have been commonly used as substrates or support materials to improve the performance or change the functionality of the membrane. When an additional layer of functional material is coated on top of a ceramic membrane, good conformity between the two layers can improve their adhesion to each other and also heat and mass transfer. A study in literature has found that increasing the surface roughness of the substrate reduces the adhesion of the membrane [1]. It is therefore desired to fabricate membrane substrates with smooth surfaces to form well-adhered and uniform membrane layers.

Smooth membrane surfaces can potentially be achieved by spinning hollow fibres through a quadruple-orifice spinneret, with a coagulant bore liquid followed by the ceramic suspension, then a lubricant layer followed by a polymer protection layer (Figure 10.1). This way phase inversion commences from the inner layer and micro-channels are initiated there, and at the shell side the hollow fibre is in contact with a lubricant layer which does not cause phase inversion, and is immiscible with the ceramic suspension, and can reduce the movement of ceramic particles away from the fibre during the spinning process. Outside this lubricant layer a polymeric layer is also extruded, and it phase inverts as soon as it reaches the coagulation bath, preventing contact between the ceramic suspension and water.

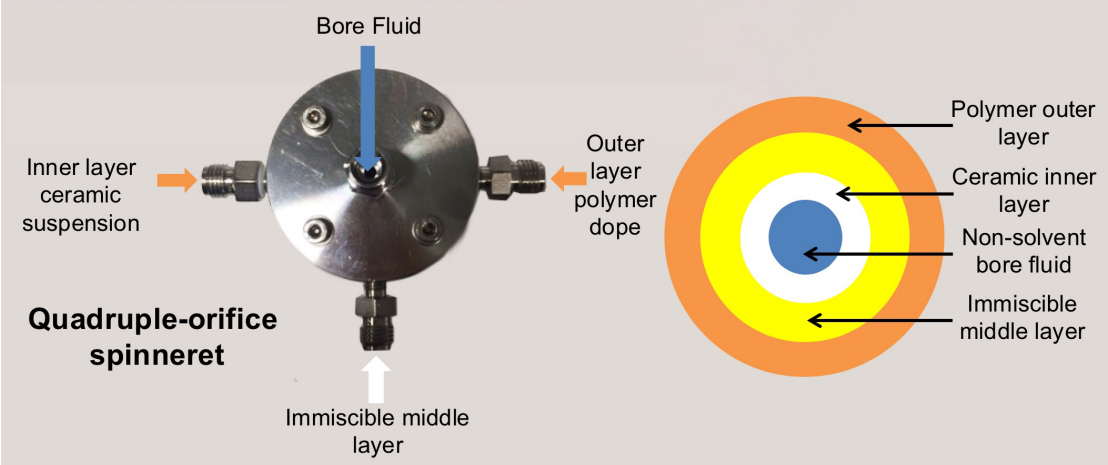


Figure 10.1 Schematic of the quadruple-orifice spinneret and the different layers that are spun for very smooth ceramic membranes

10.4.1.2 Combined phase inversion and sintering for ultrafiltration ceramic membranes

Currently in this thesis, membranes in the microfiltration selectivity range were fabricated. It would be of interest to fabricate hollow fibre membranes with finer selectivity, that is, in the ultrafiltration and nanofiltration range in a single-step phase inversion process. This can be achieved by adjusting the suspension composition and fabrication parameters. Ceramic particles of smaller diameters or different materials can be used to achieve smaller packing pores. Furthermore, multi-layered ceramic membranes can be spun with finer ceramic particles in the outer layer and large particles in the inner layer to reduce the cost of using fine particles for the entire hollow fibre.

10.4.2 Other membrane materials

Due to the versatility of the cross-section design of the micro-channel enhanced hollow fibres and the extensive surface area offered by the micro-channels, they can potentially be applied to a much broader range of applications. As a wider range of industries look to incorporate membranes in their systems, there will be new demands

for the membrane materials, for expanding their functions, or for enhanced thermal, chemical, or mechanical stability.

10.4.2.1 Improving mechanical stability

The mechanical stability remains a challenge for industrialisation of micro-channel enhanced alumina membranes. Although the formation of micro-channels in ceramic membranes reduces the mass transfer resistance significantly, the mechanical stability was also reduced. For improving mechanical stabilities, stronger ceramic materials such as zirconia or silicon carbide, or metal materials such as stainless steel can be used to fabricate membranes via the micro-channel inducing phase inversion and sintering method to form micro-channel enhanced hollow fibres. For ceramic membranes, some attempts have been made to improve mechanical stability by reinforcing the membranes with nanofibres to bridge cracks. SiC was found to improve the mechanical stability by 40 % (sintered between 1450-1510 °C) with additional improvements in water permeation flux as well [2]. YSZ particles were also added to alumina membranes in a study and it was found that the mechanical stability was slightly improved [3]. A potential work would be to systematically test a range of nanofibres such as other ceramic fibres or metal fibres (titanium carbide, stainless steel, etc) and investigate the effects of the type of fibre, fibre size, and concentration on the mechanical stability of the final membrane.

10.4.2.2 Broadening applications

10.4.2.2.1 Water treatment

Semi-conducting materials such as titanium, zinc oxide, and ferric oxide can be made into hollow fibres easily through spinning. They can be used to degrade and inactivate organic contaminants. If the semi-conducting materials were made into micro-channel enhanced hollow fibres with the Design 5, there would be no compromise between the photocatalytic activity and membrane flux due to the very thin separation layer, unlike the common multi-layered TiO_2 membranes. Other functional materials such as

adsorbents can also be packed into the micro-channels to form highly compact and productive water treatment systems.

10.4.2.2.2 Energy generation

Inorganic hollow fibres with open micro-channels can be potentially used to form compact single-cell microbial fuel cells to provide electricity and treat wastewater simultaneously. The micro-channel inducing phase inversion and sintering method can be used to produce special hollow fibres fit for this purpose: a dual-layered membrane consisting of an anode layer and a proton exchange layer. Electro-active bacteria are coated in the micro-compartments offered by the open micro-channels and transfer electrons from the organic waste to the anode layer via anaerobic respiration. During this process protons are also produced, and they are transported through the proton exchange layer into the cathode, which is the lumen of the hollow fibre. The electrons flow from the anode through to the cathode via an external resistance, and in the cathode, they react with oxygen and protons to form water and an electrical potential difference. The schematics of the hollow fibre design and the electricity generation process are depicted in Figure 10.3. The inorganic hollow fibre microbial fuel cell can potentially be a highly compact and productive system due to their high packing density and the vast surface area offered by the micro-channels for biofilm growth.

Future works can concentrate on choosing the most suitable materials for the anode and proton exchange layers. The anode must be highly conductive, gas permeable, and show good adhesion for microbes. The proton exchange layer must be dense and have high proton conductive properties at ambient temperatures, and low conductive properties for electrons and other ions. Not only do the materials have to fulfil the abovementioned requirements, their thermal expansion coefficients must be similar to prevent cracking or delamination during sintering, as well as being economical. Potential candidates for the anode layer include stainless steel and titanium, or inorganic composite materials, and potential materials for the proton exchange membrane include oxide glasses and clayware-based materials.

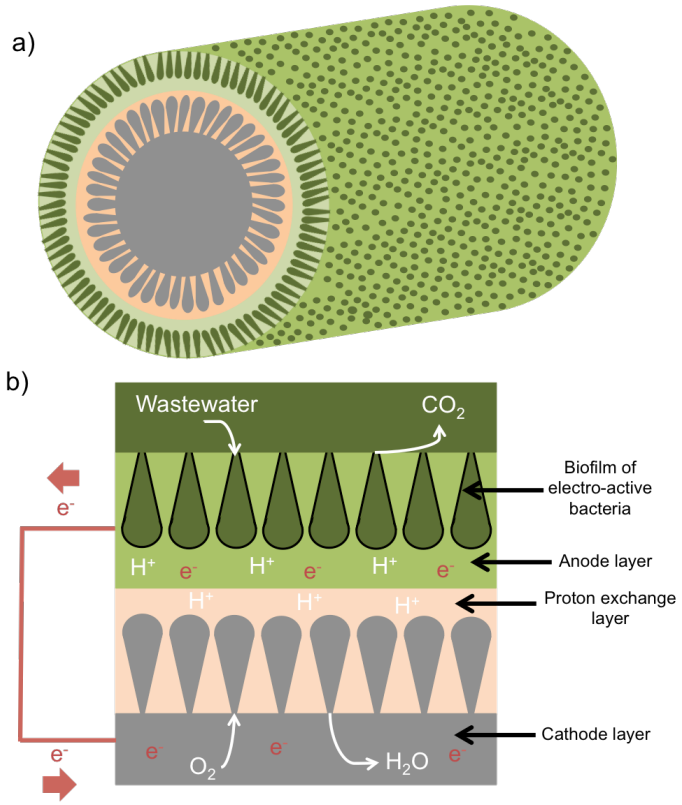


Figure 10.2 Schematic of a) the cross sectional structure of the hollow fibre potentially suitable for microbial fuel cells and b) the processes happening across the membrane layers to generate electricity

10.4.3 Potential applications

In this study, the potential applications were only briefly discussed and results from preliminary studies of one prototype were given. The early results were promising and reveal the vast amount of possible applications that can arise from tailoring the sub-structures, mainly the micro-channels, for much-improved performance. The applications discussed in this thesis include water treatment, membrane emulsification, and membrane micro-reactor for consecutive reactions. Further investigations are required regarding the applications such as membrane emulsification and membrane micro-reactor for multiple reactions. In terms of membrane emulsion, improvements in the pore size distribution of the micro-channels are required, to produce uniform-sized dispersions. A more systematic study on membrane emulsion is required. In terms of membrane micro-reactor, reactions such as the water-shift reaction can be studied using the new membrane design. Palladium

catalysts could be deposited into the micro-channels in the shell side, whereas nickel-based catalysts are deposited in the micro-channels in the lumen side.

References

1. Swain, P.S. and D. Andelman, *The influence of substrate structure on membrane adhesion.* Langmuir, 1999. **15**(26): p. 8902-8914
2. Xu, G., et al., *SiC nanofiber reinforced porous ceramic hollow fiber membranes.* Journal of Materials Chemistry A, 2014. **2**(16): p. 5841-5846.10.1039/C3TA15348G
3. Wang, B., M. Lee, and K. Li, *YSZ-Reinforced Alumina Multi-Channel Capillary Membranes for Micro-Filtration.* Membranes, 2016. **6**(1): p. 5

List of Publications

Publications

Journal Articles

1. Lee, M., et al., *Micro-structured alumina hollow fibre membranes – Potential applications in wastewater treatment.* Journal of Membrane Science, 2014. **461**: p. 39-48.http://dx.doi.org/10.1016/j.memsci.2014.02.044
2. Lee, M., et al., *Formation of micro-channels in ceramic membranes – Spatial structure, simulation, and potential use in water treatment.* Journal of Membrane Science, 2015. **483**: p. 1-14.http://dx.doi.org/10.1016/j.memsci.2015.02.023
3. Lee, M., et al., *Micro-structured alumina multi-channel capillary tubes and monoliths.* Journal of Membrane Science, 2015. **489**: p. 64-72.http://dx.doi.org/10.1016/j.memsci.2015.03.091
4. Lee, M., B. Wang, and K. Li, *New designs of ceramic hollow fibres toward broadened applications.* Journal of Membrane Science, 2016. **503**: p. 48-58.http://dx.doi.org/10.1016/j.memsci.2015.12.047
5. Wang, B., M. Lee, and K. Li, *YSZ-Reinforced Alumina Multi-Channel Capillary Membranes for Micro-Filtration.* Membranes, 2016. **6**(1): p. 5

Book Chapter

1. Lee, M., Z. Wu, and K. Li, *2 - Advances in ceramic membranes for water treatment A2 - Basile, Angelo*, in *Advances in Membrane Technologies for Water Treatment*, A.C.K. Rastogi, Editor. 2015, Woodhead Publishing: Oxford. p. 43-82.http://dx.doi.org/10.1016/B978-1-78242-121-4.00002-2

Conference Oral Presentation

1. Lee, M., et al., *Formation of micro-channels in ceramic membranes – Spatial structure, simulation, and potential use in water treatment,* presented at 10th International Congress on Membrane and Membrane Processes, 20th – 25th July, 2014, Suzhou, China

Conference Poster Presentation

1. Lee, M., B. Wang, and K. Li, *New designs of ceramic hollow fibres toward broadened applications,* presented at Euromembrane Conference, 7th – 10th September, 2015, Aachen, Germany